Probabilistic Strain-Based Fracture Mechanics Analysis of Weldments

by

Rakesh Ranjan

A thesis
presented to the University of Waterloo
in fulfillment of the
thesis requirement for the degree of
Doctor of Philosophy
in
Civil Engineering

Waterloo, Ontario, Canada, 2019

Examining committee Membership

The following persons served on the examining committee for this thesis. The decision of the examining committee is by majority vote.

External Examiner	**Professor Colin MacDougall** Department of Civil Engineering, Queen's University, Kingston, Ontario, Canada
Supervisor	**Professor Scott Walbridge** Civil and Environmental Engineering, University of Waterloo, Ontario, Canada
Internal Member	**Professor Emeritus Timothy Topper** Civil and Environmental Engineering, University of Waterloo, Ontario, Canada
Internal-external Member	**Professor Emeritus Grzegorz Glinka** Mechanical and Mechatronics Engineering, University of Waterloo, Ontario, Canada
Internal-external Member	**Professor Norman Zhou** Mechanical and Mechatronics Engineering, University of Waterloo, Ontario, Canada

Author's Declaration

This thesis consists of material all of which I authored or co-authored: see Statement of Contributions included in the thesis. This is a true copy of the thesis, including any required final revisions, as accepted by my examiners.

I understand that my thesis may be made electronically available to the public.

Statement of Contributions

This thesis is comprised of six chapters including three main chapters. At the time of submission of this thesis, three journal papers and two conference papers were published based on this thesis work. The content presented in Chapter 5 will be submitted for review in a peer-reviewed journal. The paper manuscripts have been modified and expanded in each chapter to fit the style of the thesis. I am the primary author in two journal papers and one conference paper, second author in one conference paper, and third author in one journal paper. Prof. Scott Walbridge has reviewed each manuscript. There are several co-authors on the manuscripts who have contributed to the work. The contributions from the co-authors are as follows:

Chapter 3

Ranjan, R., de Oliveira Miranda, A. C., Guo, S. H., Walbridge, S., & Gerlich, A. (2019). Fatigue analysis of friction stir welded butt joints under bending and tension load. *Engineering Fracture Mechanics*, *206*, 34-45.

I performed all of the analysis, writing, and revision work. I also performed 50% of the fatigue tests with assistance from S.H. Guo. and A.C. Miranda who conducted the other 50% of the fatigue tests and all the fatigue crack growth rate tests. Prof. Walbridge and Prof. Gerlich provided editorial support and technical guidance.

Guo, S., Shah, L., **Ranjan, R.**, Walbridge, S., & Gerlich, A. (2019). Effect of quality control parameter variations on the fatigue performance of aluminum friction stir welded joints. *International Journal of Fatigue*, *118*, 150-161.

I performed 30% of the fatigue tests and 100% of the fracture mechanics analysis. S. Guo conducted 70% of the fatigue tests and performed the hardness tests. L. Shah fabricated all of the specimens and performed all of the metallurgical analysis. Prof. Walbridge and Prof. Gerlich provided editorial support and technical guidance.

Chapter 4

Ghahremani, K., **Ranjan, R.**, Walbridge, S., & Ince, A. (2015). Fatigue strength improvement of aluminum and high strength steel welded structures using high-frequency mechanical impact treatment. 6th Fatigue Design Conference, Senlis, France.

I performed 90% of the fatigue tests. K. Ghahremani performed the first 10 % of the fatigue tests while training me and he also wrote the manuscript. Prof. Walbridge provided editorial support and technical guidance. Prof. Ince provided editorial support.

Ranjan, R., Ghahremani, K., Walbridge, S., & Ince, A. (2016). Testing and fracture mechanics analysis of strength effects on the fatigue behavior of HFMI-treated welds. *Welding in the World*, *60*(5), 987-999.

I performed 90% of the fatigue tests, the materials tests, the fatigue crack growth rate tests, 100% of the fracture mechanics analysis, and wrote the manuscript. K. Ghahremani performed the remaining 10% of the fatigue tests. Prof. Walbridge provided editorial support and technical guidance. Prof. Ince provided editorial support.

Ranjan, R., Walbridge, S. (2017). Crack shape effects on the fatigue behaviour of HFMI treated welds under variable amplitude loading conditions. International Conference on Shot Peening (ICSP-13), Montreal, Canada.

I performed the analysis and wrote the paper. Prof. Walbridge provided editorial support.

Chapter 5

Ranjan, R., Walbridge, S. (2019). Probabilistic fracture mechanics analysis of HFMI treated welded joints. (to be submitted)

I performed the analysis and wrote the paper. Prof. Walbridge provided editorial support.

Abstract

Welded joints are considered to be one of the most critical locations in structural components from a fatigue perspective because of high stress concentrations near the weld toe region, the presence of tensile residual stresses, and defects from the welding process. New welding techniques like friction stir welding (FSW) and post-weld treatment technologies like high-frequency mechanical impact (HFMI) treatment have a strong potential to improve the fatigue performance of welded joints. However, it is essential to carefully examine the effectiveness and limitations of these new welding techniques and treatment technologies to ensure their reliable fatigue performance in service. Often, new technology is not employed until it has been proven to be reliable through years of performance under real-life service conditions. The design of welded joints fabricated using new technologies poses another challenge for structural engineers, which is, how to design a component for which there are no design codes or code-specified quality control criteria. In the absence of such design codes, designers often refer to non-compulsory guidelines, which may only be applicable to components fabricated with older technologies. This can result in overly conservative designs. In the absence of specific quality control criteria for components fabricated with new welding technologies like FSW, existing design codes usually recommend quality control criteria based on "best practice" rather than relating defect size to fatigue performance. Against this background, this thesis aims to study FSW joints and HFMI treated joints, from a fracture mechanics perspective, which will contribute to the development of performance-based design provisions and quality control criteria for welds employing these technologies.

FSW joints have been found to have better fatigue performance than arc welded joints. While the tolerance window for the FSW process is wide, there is a possibility of having defects in these joints, which can severely affect the fatigue performance. In this study, a comprehensive testing program was carried out to study the fatigue performance of FSW joints with intentionally introduced defects including angular misalignment, toe flash, lack of penetration or "kissing bond", and wormhole defects. As fatigue testing becomes time-consuming and expensive, numerical modelling and simulation provide complementary ways to assess the effects of parameter variations on fatigue performance. With this in mind, a previously-developed strain-based fracture mechanics (SBFM) model is improved and extended in this thesis to study the fatigue behavior of FSW aluminum joints.

In its previous form, the employed SBFM model was capable of performing a one-dimensional (1D) crack propagation analysis. For each crack size, the crack shape was allowed to evolve using a pre-defined crack shape evolution function. In the current work, the existing 1D model was first programmed in MATLAB and then improvements in the existing model related to failure criteria were made. Subsequently, the model was extended to perform 2D fracture mechanics analysis. This improved 2D SBFM model is applied to assess the fatigue behaviour of HFMI treated A514 steel and 5083 aluminum welds (welded using metal inert gas welding process). Fatigue tests of as-welded and HFMI treated specimens were carried out to validate the prediction capability of the 2D SBFM model. A comprehensive material testing program was also carried out to estimate the input parameters required by the 2D model. With inputs obtained from material tests, the 2D model shows a reasonably good agreement between the fatigue life obtained from the model and the experiments. A sensitivity analysis is performed with the 2D model to identify the most important parameters, which affect the behaviour of HFMI treated welds.

Following the deterministic SBFM analysis of FSW and HFMI treated joints, the 2D SBFM model is extended to a probabilistic framework to obtain probabilistic stress-life curves (i.e. curves associated with a specific survival probability). To do this, statistical distributions of the input parameters are first defined. The resulting probabilistic stress-life curves are then compared with the available design curves and the differences are highlighted.

The presented probabilistic analysis demonstrates how the 2D SBFM model can serve as a useful analytical tool for developing quality control guidelines and reliability-based design curves for the HFMI treatment technology, which is applicable to a broad range of materials (e.g. various grades of steel and aluminum), scales, and cyclic loading conditions, beyond what can be practically investigated in a purely experimental program.

Acknowledgments

I would like to offer my deepest gratitude to my thesis supervisor, Prof. Scott Walbridge, who has guided me during this research work and provided technical and financial help all the way. His guidance and encouragement during my doctoral study played a vital role in shaping this thesis to this level. I feel fortunate to have had the opportunity to interact with Prof. Timothy Topper, who has not only provided guidance in experimental aspects of my research work but also explained basic concepts of fatigue elegantly. I also feel privileged to have had discussions with Prof. Grzegorz Glinka on the weight function method and its implementation schemes.

I would like to thank Prof. Norman Zhou for serving as a committee member for this thesis. I would also like to thank Prof. Colin MacDougall for being the external examiner for this thesis.

I would like to thank my research collaborators Prof. Antonio Miranda, Prof. Adrian Gerlich, Shi Hui Guo, and Luqman Shah for collaborating on friction stir welding (FSW) project. I would like to thank Dr. Kasra Ghahremani and Prof. Ahyan Ince for their collaboration on the high frequency mechanical impact (HFMI) treatment project.

I am grateful to the Natural Sciences and Engineering Research Council of Canada (NSERC), Ministry of Transportation of Ontario (MTO), and General Dynamics Land Systems (GDLS) Canada for providing financial support during my doctoral research work. A significant amount of computation time during probabilistic analysis was saved because of the computing facility provided by Compute Canada (www.computecanada.ca).

Thanks are due to my friends at the University of Waterloo including Rajdip, Luqman, Carol, Melanie, Laurent, Spencer, and Ali, with whom I have spent happy moments during social events.

Last but not the least, I am grateful for my parents, brother Rajeev Ranjan, sister Rashmi Bharti, and my wife Sandhya Patel who have always been there for me in the ups and downs of my life.

Dedication

To my parents

Table of Contents

List of Figures

List of Tables

List of Symbols

$(a/c)_{initial}$	initial crack or defect aspect ratio
a_i	initial crack depth
A	area of cross-section
a	crack depth
A	deepest point of a crack
a/c	crack aspect ratio
a/t	normalized crack depth
a_0	small crack growth correction factor
a_{crit}	critical crack depth
a_f	final crack depth
a_i	initial crack or defect depth
A_{net}	area of the net section
A_{qe}	area of quarter-elliptical crack
A_{se}	area of semi-elliptical crack
B	surface point of a crack
c	half crack width
C	Paris Erdogan law constant
C'	intercept of S-N curve
d	a particular depth below surface
D_{avg}	weld toe geometry dimension
D_b	indent depth because of HFMI treatment
Dw	weld toe geometry dimension
e_{cl}	combined local elastic strain
E	elastic modulus
K	stress intensity factor
K_{el}	elastic stress based stress intensity factor
K'	cyclic Ramberg Osgood constant
K'_m	monotonic Ramberg Osgood constant
K_{max}	maximum stress intensity factor
K_{min}	minimum stress intensity factor
K_{op}	stress intensity factor corresponding to crack opening strain
L	length of the specimen in between the grip

$\log(C')_{\mu}$	mean value of $\log(C')$
$\log(C')_{d}$	design value of $\log(C')$
m	Paris Erdogan law constant
m'	slope of S-N curve
$m(x,t)$	weight function coefficient
N	number of cycles (fatigue life)
n'	cyclic Ramberg Osgood constant
n'_m	monotonic Ramberg Osgood constant
R	load or stress ratio (min/max)
R_w	radius of the weld toe
S	nominal stress range
S_0	crack opening stress
S_{cl}	combined local elastic stress
S_{cu}	crack opening stress for the current cycle
S_{el}	local elastic stress
S_{max}	maximum nominal stress
S_{min}	minimum nominal stress
S_{opss}	steady-state crack opening stress
S_y	cyclic yield strength
t	thickness of the component
w	width of the component
Y	geometry correction factor

List of Greek Symbols

σ_y	monotonic yield strength
$(\sigma_r)_{max}$	maximum residual stress
$(\sigma_r)_{toe}$	residual stress at the weld toe
μ_{op}	crack closure build-up parameter
α	plastic constraint factor
ΔK_{eff}	effective SIF range
ΔK_{th}	threshold SIF range
ΔS	nominal stress range
ΔS_{eq}	equivalent stress range
$\Delta\varepsilon$	local inelastic strain range
$\Delta\sigma$	local inelastic stress range
ε	local inelastic strain
$\sigma_{app}(x)$	non-uniform applied stress distribution
$\sigma'_{app}(x)$	equivalent uniform applied stress distribution
σ_{max}	maximum local inelastic stress
σ_{min}	minimum local inelastic stress
σ_{net}	stress at the net section
σ_r	residual stress
$\sigma_r(x)$	non-uniform residual stress distribution
$\sigma'_r(x)$	equivalent uniform residual stress distribution
θ	angle at the weld toe / angular misalignment

List of Acronyms

1D	one dimensional
2D	two dimensional
A5PW	5083 aluminum alloy, properly welded
A5WH	5083 aluminum alloy, wormhole
A6KB	6061 aluminum alloy, kissing bond
A6LJ	6061 aluminum alloy, lap joint
A6PW	6061 aluminum alloy, properly welded
A6TF	6061 aluminum alloy, toe flash
A6WH	6061 aluminum alloy, wormhole
AS	advancing side of the weld
ADM	aluminum design manual
AWS	American welding society
AW	as-welded
BM	base metal
CSA	Canadian standard association
Cat.	category
CT	compact tension
CNC	computer numeric control
CA	constant amplitude
CA-UL	constant amplitude with underload
FAT	fatigue class in IIW
FE	finite element
FL	failure location
FSW	friction stir welding
HAZ	heat affected zone
HCF	high cycle fatigue
HFMI	high frequency mechanical impact
IIW	international institute of welding
ISO	international organization of standardization
JLR	joint line remnant
LCF	low cycle fatigue
MIG	metal inert gas (welding)
NDE	non-destructive evaluation
NZ	nugget zone
QC	quality control
QE	quarter-elliptical (crack)

R-O	Ramberg-Osgood
RS	retreating side of the weld
HRC	Rockwell hardness scale
SE	semi-elliptical (crack)
SBFM	strain-based fracture mechanics
SCF	stress concentration factor
SIF	stress intensity factor
S-N	nominal stress range-number of cycles
UIT	ultrasonic impact treatment
VA	variable amplitude
VHCF	very high cycle fatigue
HVN	Vicker ′s hardness number
WR	weld root
XRD	x-ray diffraction

Chapter 1
Introduction

Welded joints (weldments) are considered to be one of the most critical locations in structural components from a fatigue perspective because of the presence of tensile residual stress, high stress concentration, and defects from the welding process. The structural performance of welded components strongly depends on weld quality. Engineering assessment of critical welded structural components is important to provide support for material selection, design and fabrication, in-service assessment, and failure analysis (Smallbone 2008). New welding techniques and post-weld treatment technologies have a strong potential to improve the fatigue performance of welded joints. However, it is essential to carefully examine their effectiveness and limitations to ensure their reliable fatigue performance in service.

1.1 Background and motivation

Several new welding techniques have been developed in the last few decades such as laser beam welding, electron beam welding, magnetic pulse welding, and friction stir welding (FSW). FSW is a relatively new solid-state joining process. Because of the solid-state nature of FSW, it overcomes several issues associated with conventional arc welding such as weld distortion, solidification-related porosities and solidification-related cracking (Lohwasser and Chen 2009). FSW has been found to produce a low concentration of defects and is very tolerant of variations in welding process parameters (Dialami et al. 2017). Nevertheless, defects have been found in FSW joints, such as lack of penetration (kissing bond), toe flash, wormhole, and geometric misalignment.

The effect of these welding defects on fatigue performance of welded joints has not been quantified yet in terms of reduction in fatigue performance. There is a need to study the effect of the presence of misalignment defects (of specific magnitude) and welding defects (of specific size and location) on the fatigue performance of FSW joints to develop quality control criteria based on fatigue performance rather than on the basis of "best practice" in the welding industry. Although FSW has been applied in the shipbuilding, robotics, aerospace, and automotive industries, it has

not yet found widespread use for structural applications such as bridges and other metallic civil infrastructure. For civil engineering applications, it is challenging to implement a new welding technology until it has gone through years of testing and design code provisions have been developed and approved. Often, the lack of fatigue test data and design guidelines work as a barrier to implementing new welding technologies into practice.

When a welded component is fabricated using a conventional welding process such as metal inert gas welding process, there is high tensile residual stress near the weld toe region, possibility of weld distortion, presence of welding defects and the possibility of weaker material properties (e.g. in the case of aluminum) at the weld toe, which is the common cause for the poor fatigue performance of arc welded joints in the as-welded (i.e. without application of post-weld treatment) condition. There are several post-weld treatment technologies available, including high-frequency mechanical impact (HFMI) treatment. Post-weld treatment using HFMI results in compressive residual stress at the weld toe, reduced stress concentration at weld toe because of improved weld toe geometry, and enhanced material properties at the weld toe because of local work hardening. HFMI treatment is known to improve the fatigue performance of welded joints that are already in service, as well as in new components. However, the treatment effectiveness has not been precisely quantified yet on a wide range of materials, under variable amplitude loading conditions, and on large components considering all of the uncertainties involved in the treatment process.

1.1.1 Friction stir welding

FSW involves moving a rapidly rotating tool along a joint, which heats the material by friction to the extent that the materials on each side of the joint are softened and stirred, causing fusion of the joint. A schematic of the FSW process is shown in Figure 1.1. There are three locations in FSW joints at which surface defects can be present: the weld root, advancing side of the weld, and retreating side of the weld. The advancing side of the weld is where the direction of tool rotation is the same as the welding direction and the retreating side is where the direction of tool rotation is opposite to the welding direction as shown in Figure 1.1. Since FSW is a relatively new welding technique, process-specific fatigue design guidelines, and quality control criteria are

currently not available. Recent ISO (ISO 25239 2011) and AWS (AWS-D17.3/D17.3M:200X 2010) standards now include broad provisions for the quality control and pre-qualification of FSW joints. The technical committee for the Canadian code (CAN/CSA W59.2 2018) for welding of aluminum structures has adopted similar provisions.

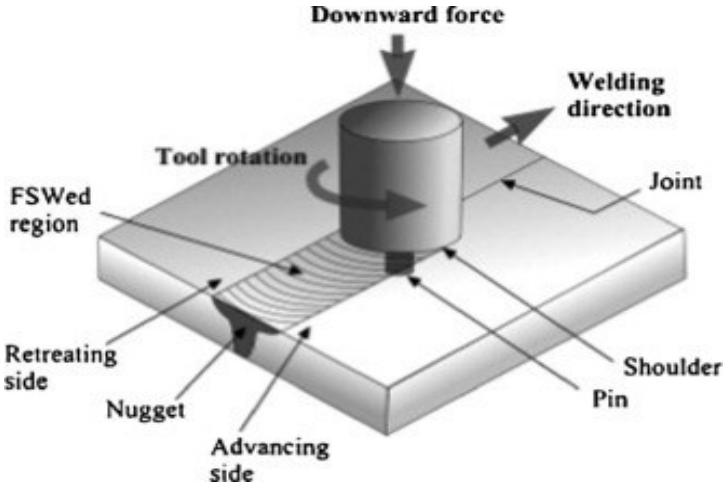

Figure 1.1: Friction stir welding process (He, Gu, and Ball 2014)

From the review of previous research on FSW joints undertaken in (Miranda, Gerlich, and Walbridge 2015), it is apparent that a number of gaps in the state-of-the-art in this area remain unaddressed. Specifically, the existing design codes – in North America particularly – have taken the very cautious approach of assuming that the fatigue life of the FSW joint is equal that of the geometrically similar conventional arc welded joint. Secondly, the tolerance limits on the various defect types do not seem to be related to fatigue performance but rather on "best practice" in the welding industry, which is concerning. There is a need to develop improved "performance-based" code provisions for the quality control (QC) and fatigue design of FSW joints for emerging aluminum structural applications such as bridge decks. Other research gaps include a lack of fatigue test data under variable amplitude (VA) loading condition in the long-life domain (> 10^7 cycles).

1.1.2 Post-weld treatment technology

Post-weld treatment technologies are mainly categorized as either residual stress-based methods or weld geometry improvement methods. HFMI treatment is generally categorized as a

residual stress-based method. An HFMI tool along with several types of indenters are shown in Figure 1.2 (a) and Figure 1.2 (b). A typical weld toe profile in the as-welded condition and after HFMI treatment is shown in Figure 1.2 (c) and Figure 1.2 (d) respectively. The weld toe groove created by HFMI treatment at the weld toe can be seen in Figure 1.2 (d). This groove reduces the component thickness slightly in the treated area. However, the negative effect of this thickness reduction is less than the benefit from the corresponding reduction in the stress concentration after the treatment. Depending on the yield strength of the material and size of the indenter, the optimum groove depth varies from 0.2 mm to 0.6 mm and the groove width varies between 3 mm and 6 mm (Marquis and Barsoum 2016).

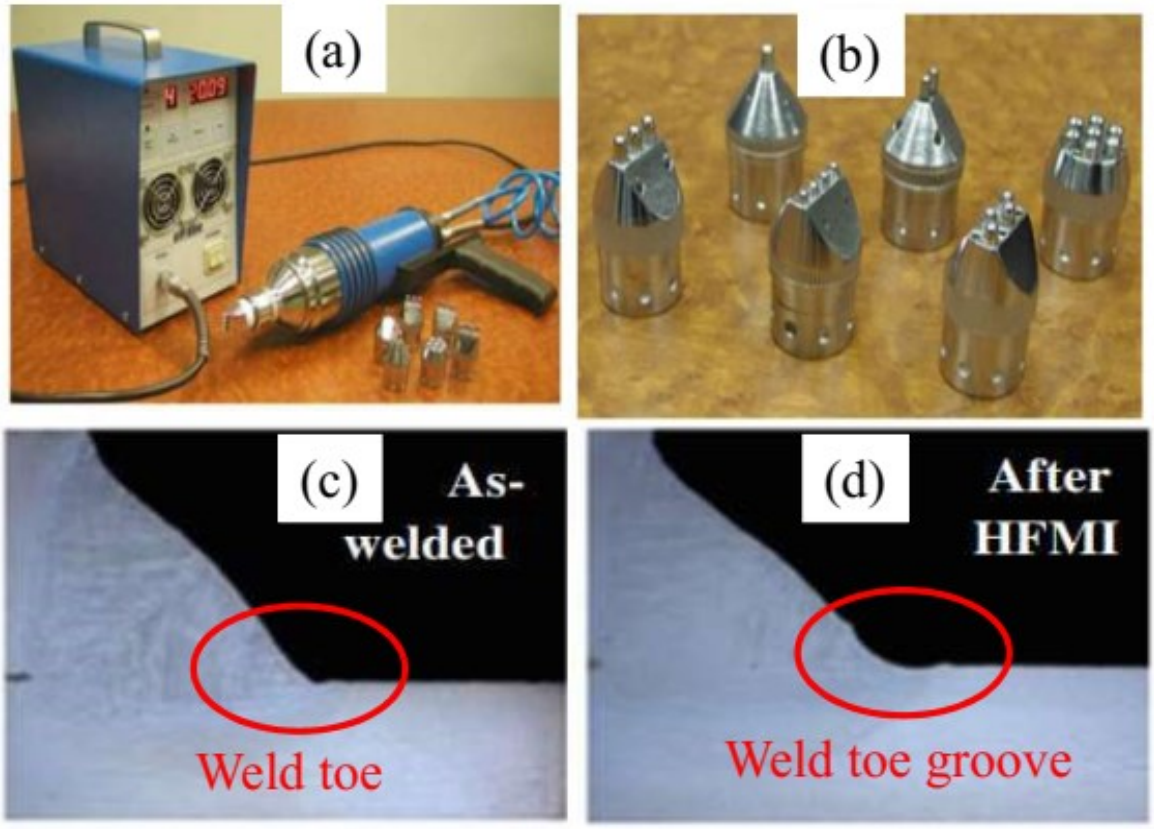

Figure 1.2: (a) HFMI tool ; (b) HFMI indenter; (c) Weld toe profile in as-welded condition; (d) Weld toe profile after HFMI treatment (Pedersen et al. 2010; SINTEC 2019)

The beneficial compressive residual stress introduced during HFMI treatment process is the primary mechanism through which the HFMI treatment improves the fatigue life of welded

joints. The improvement in fatigue life due to impact treatment has been found to be more significant in the high cycle fatigue (HCF) domain and at low-stress ratios, R (where R = minimum stress / maximum stress). It has been observed that post-weld treatment technologies (such as hammer or needle peening) are not suitable for loading conditions when load ratio is more than 0.5 or maximum stress level is more than 80% of the yield strength of the material (Haagensen and Maddox 2013). VA loading histories containing large compressive underload cycles have been found to be particularly detrimental for impact treated welds. Therefore, it is essential to carefully examine the effectiveness and limitations of the impact treatment under VA loading conditions in different material types in order to ensure their reliable fatigue performance. Most of the study on HFMI treatment to date has focussed on mild steel. Relatively less fatigue test has been performed to assess the improvement in fatigue life in joints made of high strength steels or softer materials like aluminum.

1.1.3 Models for fatigue life estimation

Testing and regular inspection of weldments can help in ensuring the safety and fatigue performance of cyclically loaded structures. However, as testing and inspection becomes increasingly expensive and time-consuming, one often has to depend on modelling and simulation for evaluating the structural performance of welded joints (Smallbone 2008). While modelling does not entirely replace the need for testing, fatigue life estimation models play an important role in designing new components, as well as maintaining existing components. Many fatigue life estimation models such as NASGROW, UNIGROW, FASTRAN, and SBFM have been developed over the years, and vary widely in their complexity, ease of implementation, and relative strengths. The current study focuses on improving and extending one such model, that is, the so-called strain-based fracture mechanics (SBFM) model, which was developed previously at the University of Waterloo (Ghahremani 2015; El Haddad, Topper, and Topper 1981; Khalil and Topper 2003; Lam, Topper, and Conle 1998; Walbridge 2008).

The SBFM model is thought to be well-suited for investigating the fatigue behaviour of new welding and post-weld treatment technologies, studying the reliability of these technologies, and performing studies to establish design guidelines for the following reasons:

1) It is self-contained (i.e. does not require interfacing with finite element analysis software), and relatively efficient from a computational perspective, which makes it well-suited for use in a probabilistic framework, where many repeated calculations are required.
2) It does not require the definition of a "crack initiation" phase and a "crack propagation" phase, as some comparable models do, since it was originally developed to model the growth of small fatigue cracks of the order of the grain size of the material.
3) It is well-suited for modelling non-linear material effects, which can be significant for certain welding and post-weld treatment technologies (e.g. HFMI treatment) and for soft materials such as aluminum, which may experience significant non-linear material behaviour at the weld toe under certain loading conditions.

Despite these advantages, several aspects of the previously-developed SBFM model have been identified as shortcomings or areas where focused improvements are warranted:

1) In previous implementations, the SBFM model only performs a 1D crack growth analysis, with the crack shape controlled by a crack shape function. This does not allow proper investigation of parameters that may affect the crack shape (such as the stress level, VA loading history type, and presence of the near-surface compressive residual stresses).
2) The model has been shown previously to be systematically conservative in predicting the fatigue performance of impact treated welds under VA loading (Ghahremani 2015).
3) Only superficial attempts (Raimbault 2016; Walbridge, Fernando, and Adey 2012) have been made to-date to implement the model in a probabilistic framework. This is a step that needs to be further investigated if the model is to be turned into a useful tool for the development of reliability-based design code provisions.

1.2 Objectives

Against this background, the objectives of this research are as follows:

1) To investigate opportunities for improving the existing SBFM modelling framework for application to notched or welded structural components, including: improvements to the failure criterion, and extension of the model to perform 2D crack growth analysis on surface defects (in non-uniform stress fields).
2) To extend the use of SBFM model to new applications, including fatigue analysis of HFMI treated aluminum and high-strength steel welds, and aluminum FSW joints.
3) To apply the SBFM model for studying the effects of geometric and welding defects on the fatigue performance of FSW joints.
4) To extend the SBFM modelling framework to enable a probabilistic analysis of HFMI treated joints for obtaining the probabilistic S-N curves equivalent to the design S-N curves available in various international design codes.

Major components of the work involved in this research are shown in Figure 1.3.

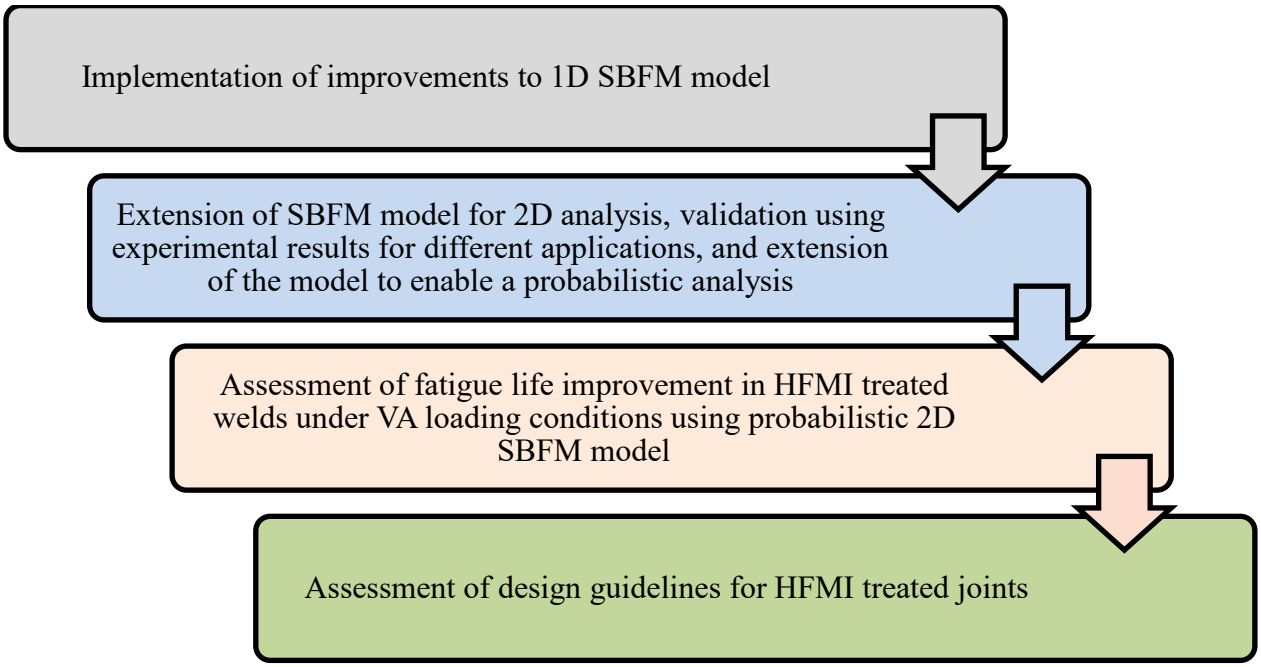

Figure 1.3: Major components of the work

1.3 Scope of work

This research is mainly focused on the development of a 2D SBFM model by extending and improving the existing 1D SBFM model for the fatigue study of structural steel and aluminum welded joints mostly used in heavy civil/structural applications, such as highway bridges. The study was limited to the analysis of the butt, lap, and cruciform welded joints under uniaxial loading conditions. In this study, a single crack was analyzed at one time, ignoring the possibility of multiple cracks, the coalescence of cracks, and the interaction of cracks. An assumed initial defect geometry and location were used to begin the fracture mechanics analysis for only surface defects. Subsurface defects were not investigated with the developed model. A crack closure model was adapted from the literature to consider load-interaction effects.

1.4 Overview of the thesis

This thesis is divided into six chapters including the current one. In Chapter 2, key concepts are introduced followed by a description of the methodology used for the fracture mechanics analysis. In Chapter 3, a study on the fatigue analysis of FSW butt and lap joints is presented. In Chapter 4, a study on the fatigue behaviour of HFMI treated welds is presented. In Chapter 5, a study on the probabilistic analysis of HFMI treated welds is presented. In Chapter 6, a summary, conclusions, and recommendations for future work are presented.

Chapter 2

Literature Review and Methodology Development

Welded joints are usually designed for fatigue using the so-called "detail category" approach, based on standard stress-life (S-N) curves available in design codes (see Figure 2.1). Each design S-N curve corresponds to a specific detail category, A, B, C, D, etc., which represents the severity of the stress concentration associated with the detail (connection geometry). The design S-N curves are generally obtained based on a statistical analysis of experimental fatigue test data. Fatigue test data is practically never enough to completely accommodate for scatter in the test data, therefore, a statistical analysis is performed to obtain design S-N curves, e.g. with a 97.7% survival probability (or "two standard deviations below the mean" used in North America).

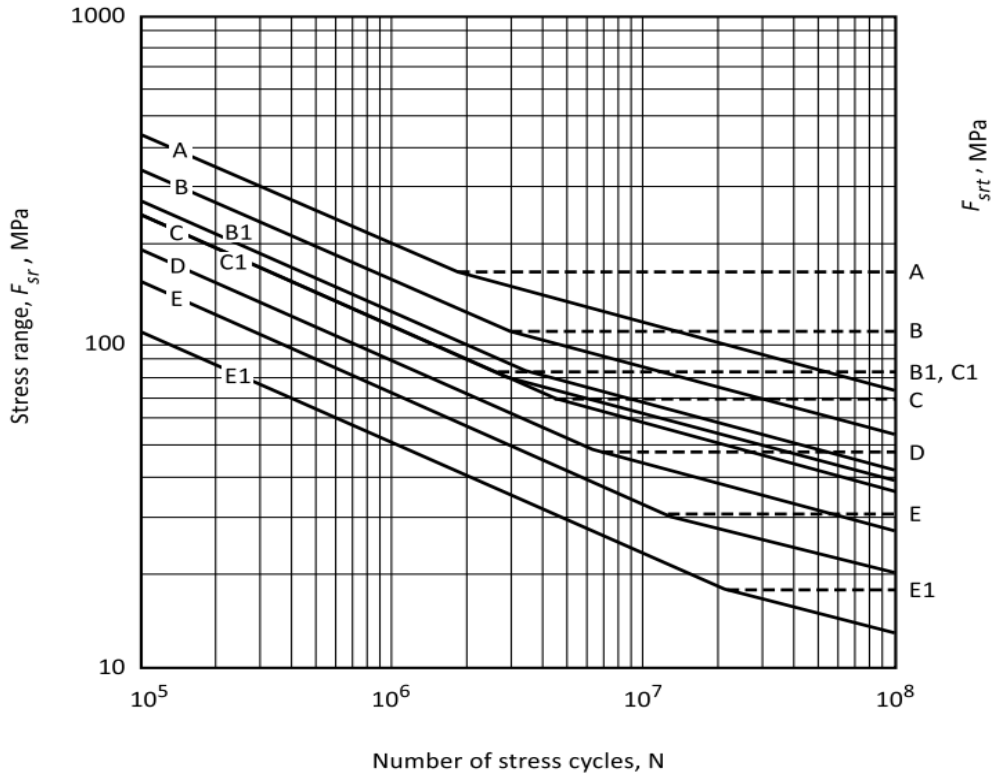

Figure 2.1: Design S-N curves from CSA S6 design code (Canadian Standards Association 2014)

New welding technologies like Friction Stir Welding (FSW) are evolving continuously and design code writers are struggling to establish design S-N curves at a rate that is sufficient to keep

up with the latest technological developments. It is challenging for the code writers to consider the wide range of metal alloys, connection geometries, and welding process parameters that might be used with these new welding processes, purely through a statistical analysis of fatigue test data. Similarly, it is difficult to have unified S-N curves in design codes, which quantifies improvements in fatigue life due to post-weld treatments such as high-frequency mechanical impact (HFMI) treatment for a wide range of materials and loading conditions. The magnitude of the improvement in fatigue life of welded joints due to HFMI treatments depends on several factors including the type of the HFMI indenter used, the frequency of vibration at which the indenter vibrates during the treatment process, the number of treatment passes, the angle at which an indenter is held while treating and the indent depth after the treatment. In summary, it is a challenging task to consider all of the uncertainties associated with new welding and post-weld treatment technologies during the development of design S-N curves.

To solve the aforementioned challenges, there is a need for suitable mechanistic models, which primarily employ inputs that can be either measured or estimated for a given welding or post-weld treatment process after the process is complete, including such things as residual stress distribution, local hardness variations, fatigue-related material properties, and local component geometry. The estimated S-N curve produced using the model should be equivalent to the standard S-N curves available in the design codes (i.e. they must correspond with a similar assumed survival probability). There are several models available in the existing literature, including NASGROW and UNIGROW, which have been commercialized and are being used for practical purposes. The current study entails further development of another model (SBFM) with a focus on its application to establish design provisions and quality control criteria for welded joints.

This so-called strain-based fracture mechanics (SBFM) model performs a crack propagation analysis at two locations (the deepest point and surface point of the crack), which represents an extension of a previously-developed 1D SBFM model described in (Walbridge 2008). This model was primarily developed to study fatigue in welded metal joints, which may be either in an “as-welded” or “HFMI treated” condition. In a previous study (Walbridge 2008) with the 1D SBFM model, variable amplitude loading conditions were identified for which ignoring nonlinear material behaviour may lead to an overestimation of the post-weld treatment benefit (measured as

in increase in the fatigue life of the weld). The key parameter of the SBFM model is the local inelastic strain history near the crack tip corresponding to a given nominal stress history. In order to describe the implementation of SBFM model, a particular specimen geometry is used, which is a cruciform welded joint, as shown in Figure 2.2. The cruciform welded joint has four similar weld toes, which are the most probable sites for crack initiation because of stress concentrations and the presence of welding defects. Along with the component geometry, a typical semi-elliptical crack initiated from the weld toe is also shown in Figure 2.2(right). Representative crack shapes are shown with crack depth denoted as a_i and full crack width denoted as $2c_i$ where, i is the current crack depth increment number.

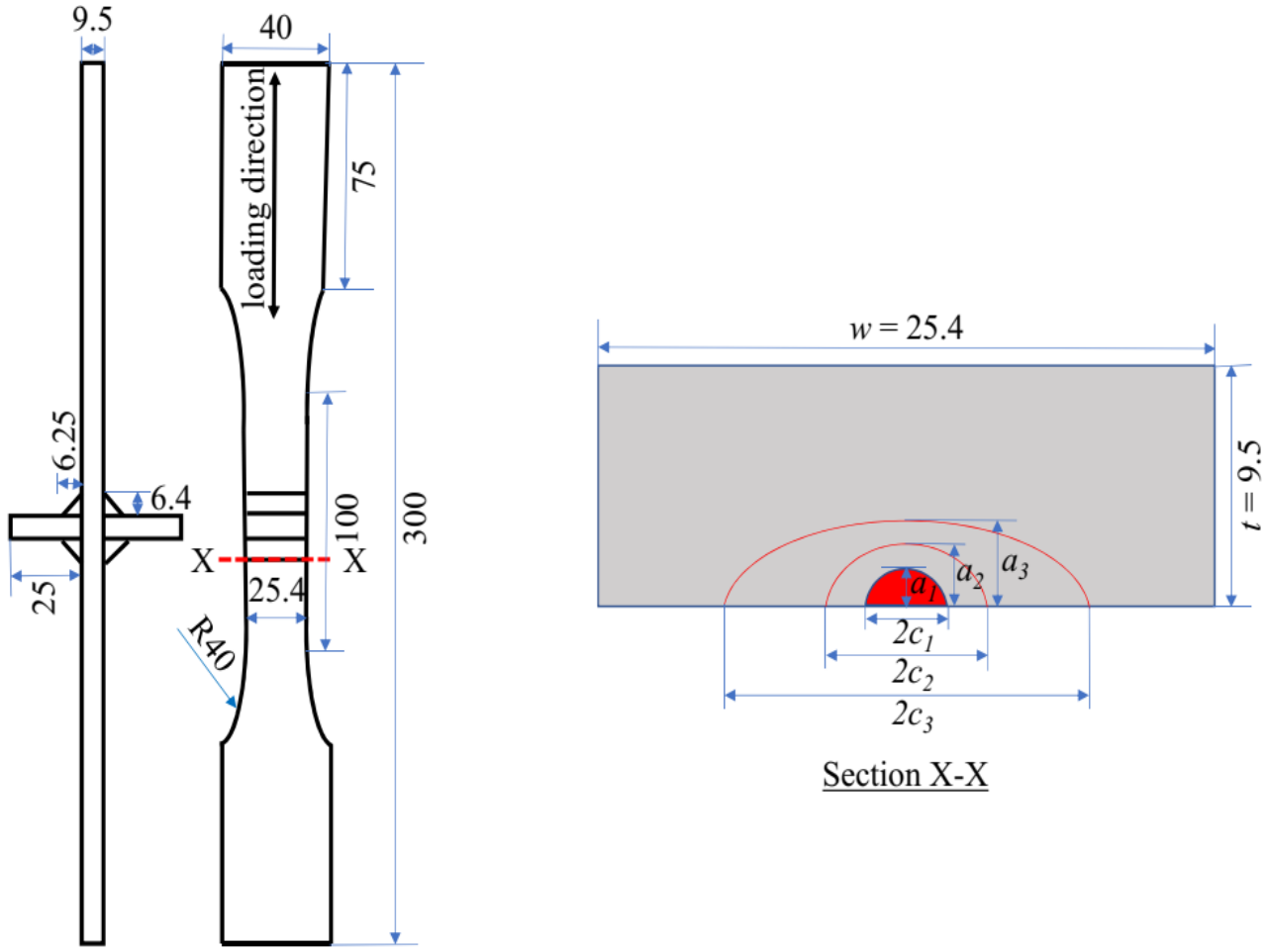

Figure 2.2: Component geometry (left) and cross-section with a typical semi-elliptical surface crack (right) (all dimensions in mm)

A description of the model implementation include the following elements:

1) Model assumptions, input parameters, and output format definition
2) Estimation of local inelastic strain
3) Estimation of crack opening strain
4) Estimation of effective stress intensity factor
5) Definition of a crack growth law
6) Integration of a crack growth law
7) Definition of a failure criterion

2.1 Model assumptions, input parameters, and output format definition

In this section, key assumptions made in the implementation of the SBFM modelling framework, input parameters required for the SBFM analysis, and output format are described.

2.1.1 Assumptions in the SBFM model

During the implementation of the SBFM model, several assumptions are made. A number of the key assumptions are listed in the following paragraphs:

- A single initial defect with a specific size and location is assumed to be known, from which a crack grows and the component fails eventually after the crack reaches a critical depth. However, under uniaxial loading, multiple cracks may initiate simultaneously, which can coalesce and interact with each other. Herein, the possibilities of interaction and coalescence of multiple cracks are ignored.
- The crack initiation period for weldments is assumed to be zero and hence all the fatigue life is assumed to be consumed in the crack propagation stage. This assumption is justified because of the high probability of defects being present in weldments. Also, this model considers small crack growth effects, and hence the deterministic or mean initial defect size can be as small as 0.1 mm, which is below the detectable limits of the non-destructive evaluation (NDE) methods commonly employed for detecting weld defects.
- Only a Mode 1 (opening mode) fracture under uniaxial loading is considered with this model. The non-uniform distribution of stress along the crack path because of the presence of a notch has been considered in this model using the weight function method.

- Transient effects on the non-linear material behaviour including cyclic hardening / softening or cyclic creep are not explicitly considered. These effects can be handled in an approximate sense by modifying the steady-state material parameters.
- The endurance limit and threshold stress intensity factor for a particular material is assumed to be constant throughout the service life of the component. However, these parameters may change due to corrosion or temperature variation.
- The variation of stress concentration factor (SCF) along the expected crack path in a component is estimated from an elastic finite element (FE) analysis of the uncracked component. It is assumed that the obtained SCF distribution is unaffected by the presence and growth of the crack. As the crack becomes large and the stresses in the vicinity of the weld are redistributed as a result, this assumption is questionable. However, in general, for the cases investigated in this thesis in particular, the vast majority of the fatigue life is spent at small crack sizes, where this assumption is thought to be reasonable.
- The cyclic Ramberg-Osgood (R-O) material model is used for modelling non-linear material behaviour. The parameters of the material model, K' and n', have been experimentally estimated by strain-controlled testing of smooth specimens under a uniaxial cyclic loading for a range of strain values of up to ± 1 %. However, in real life structural components, a complex local stress state exists, which is neither plane stress nor plane strain, and the value of strain may be higher than 1% locally, especially for thick components with complex notch geometries.

2.1.2 Input parameters

For the sake of systematic discussion, input parameters for the SBFM model have been categorized as (a) material properties, (b) component geometry and residual stresses, (c) information related to defect geometry and crack shape evolution, and (d) loading history.

2.1.2.1 Material properties

The material properties relevant for the fracture mechanics analysis and the corresponding sources are listed in Table 2.1, along with the symbols used in the relevant equation.

Table 2.1: SBFM model input parameters related to material properties

Material Properties	Symbol	Source
Elastic modulus	E	Static strength test / hardness data
Static and cyclic yield strength	σ_y, S_y	Static and cyclic strength tests / hardness data
Ultimate strength	σ_u	Static strength test / hardness data
Paris-Erdogan crack growth law constants	C, m	Crack growth rate test / existing literature
Threshold stress intensity factor range	ΔK_{th}	Crack growth rate test / existing literature
Cyclic Ramberg-Osgood material parameters	K', n'	Cyclic incremental strain test of material / hardness data
Crack closure build-up parameter	μ_{op}	Crack closure test / existing literature
Hardness vs. depth along the expected crack path	HVN	Vickers hardness test / existing literature

To obtain the input parameters, material testing is required on coupons or (in some cases) these parameters can be related to local hardness data when specific material test data is not available. Static tension tests of dog-bone shaped specimens have been performed for the materials investigated in the current study to obtain elastic modulus, yield strength, ultimate strength, and static Ramberg-Osgood material properties of the "as-received" parent metal as well as metal in the "heat affected zone" (HAZ) of the weld. For the current study, HAZ properties were obtained with specimens that were heat-treated simulating the welding heat cycle. Crack growth rate tests were performed as per (ASTM E647-13 2013) on compact tension (CT) specimen to estimate the Paris-Erdogan crack growth law constants, C and m. Threshold stress intensity factor range, ΔK_{th} was also estimated with the crack growth rate test or a suitable value of ΔK_{th} was assumed based on the data available in the existing literature. The CT specimens were pre-cracked under

compressive cyclic loading and then the test was performed under CA loading, at a high load ratio (R = 0.8), to obtain closure free crack growth data.

Incremental strain tests were performed on smooth specimens with strain ranges varying from -1% to +1 % to estimate the cyclic Ramberg-Osgood material model parameters K' and n'. The value of the crack closure build-up parameter, μ_{op}, was adapted from the existing literature. Vickers microhardness testing was performed in the region of the expected crack path to capture the spatial variability of material properties. The magnitude of hardness was related to σ_y, σ_u, K' and n' using fitted equations on two sets of hardness and material property test data.

2.1.2.2 Component geometry and residual stresses

The various input parameters related to component geometry and residual stresses are summarized in Table 2.2.

Table 2.2: SBFM model input parameters related to component geometry and residual stresses

Component geometry	**Symbol**	**Source**
Component-thickness	t	Measurement
Component-width	w	Measurement
Weld toe geometry	-	Silicon impression
SCF along the expected crack path	SCF vs. depth	FE analysis
Residual stress along the expected crack path	σ_r vs. depth	Fitted to measured data

Specimen width and thickness were measured using vernier calipers for each specimen tested in this study. The stress concentration factor (SCF) along the expected crack path was estimated by performing a linear elastic FE analysis in ABAQUS. Component thickness was discretized into several (n = ~300) levels to estimate the variation of SCF as a function of depth along the crack path.

The residual stress distribution for the as-welded and impact treated cruciform welded joints was obtained by manually fitting a curve through experimental data available in the existing literature. While fitting the curve it was made sure that the overall residual stress distribution is

self-equilibrating and the fitted curve passes through most of the experimental data points. Based on experimental data available in (Ghahremani 2015; Kuhlmann et al. 2005; Suzuki et al. 2014) for as-welded mild steel cruciform joints, the distribution of residual stress was fitted as shown in Figure 2.3. In this figure, the normalized residual stress is plotted on the vertical axis and the normalized depth is plotted along the horizontal axis. The normalized depth is the ratio of depth below the weld toe and thickness of the component. A significant amount of scatter can be observed in the experimental data. Most of the measurements were available for depths varying from the surface to 10% of the plate thickness. Peak values of residual stress near the weld toe for as-welded mild steel cruciform joints can be observed to vary in between $-0.2 \cdot \sigma_y$ to $+1.5 \cdot \sigma_y$, where σ_y is the nominal yield strength. Here, the "-" sign corresponds to a compressive nature of stress and "+" sign corresponds to a tensile nature of stress.

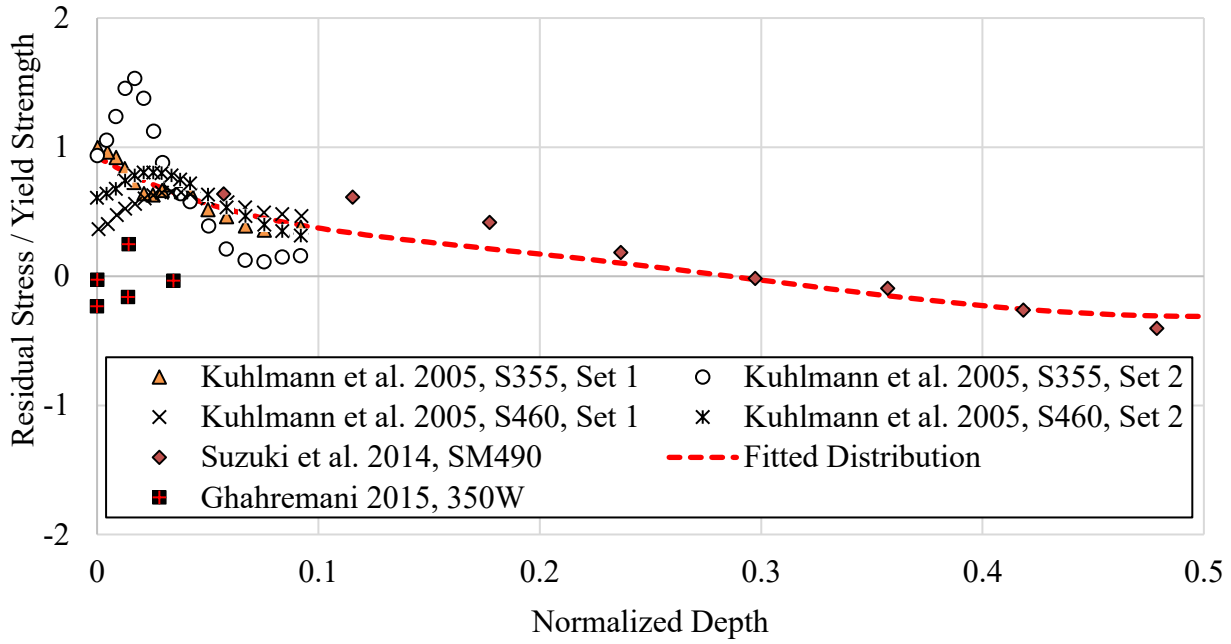

Figure 2.3: Residual stress distribution for as-welded mild steel cruciform joints

Similarly, based on experimental data available in the literature for residual stress in HFMI treated cruciform welded joints (Gerster, Schäfers, and Leitner 2013; Ghahremani 2015; Kuhlmann, Dürr, and Günther 2017; Leitner et al. 2015; Suzuki et al. 2014; Tehrani Yekta, Ghahremani, and Walbridge 2013; U. Kuhlmann, J. Bergmann, A. Dürr, R. Thumser, H.-P.

Günther 2005) for different metal alloys, a distribution of residual stress was fitted as shown in Figure 2.4. Again, a large degree of scatter in the experimental data can be observed. The peak value of the residual stress near the surface of the weld toe was observed to vary from -1.7·σ_y to -0.3·σ_y. For this study, residual stress measurements were obtained by an electropolishing and x-ray diffraction for each material type. Depending on the measured residual stress data for a specific material type (350W steel, A514 steel, 5083 aluminum) for the current study, the fitted distribution was scaled to estimate the residual stress distribution for the specimen and material type of interest.

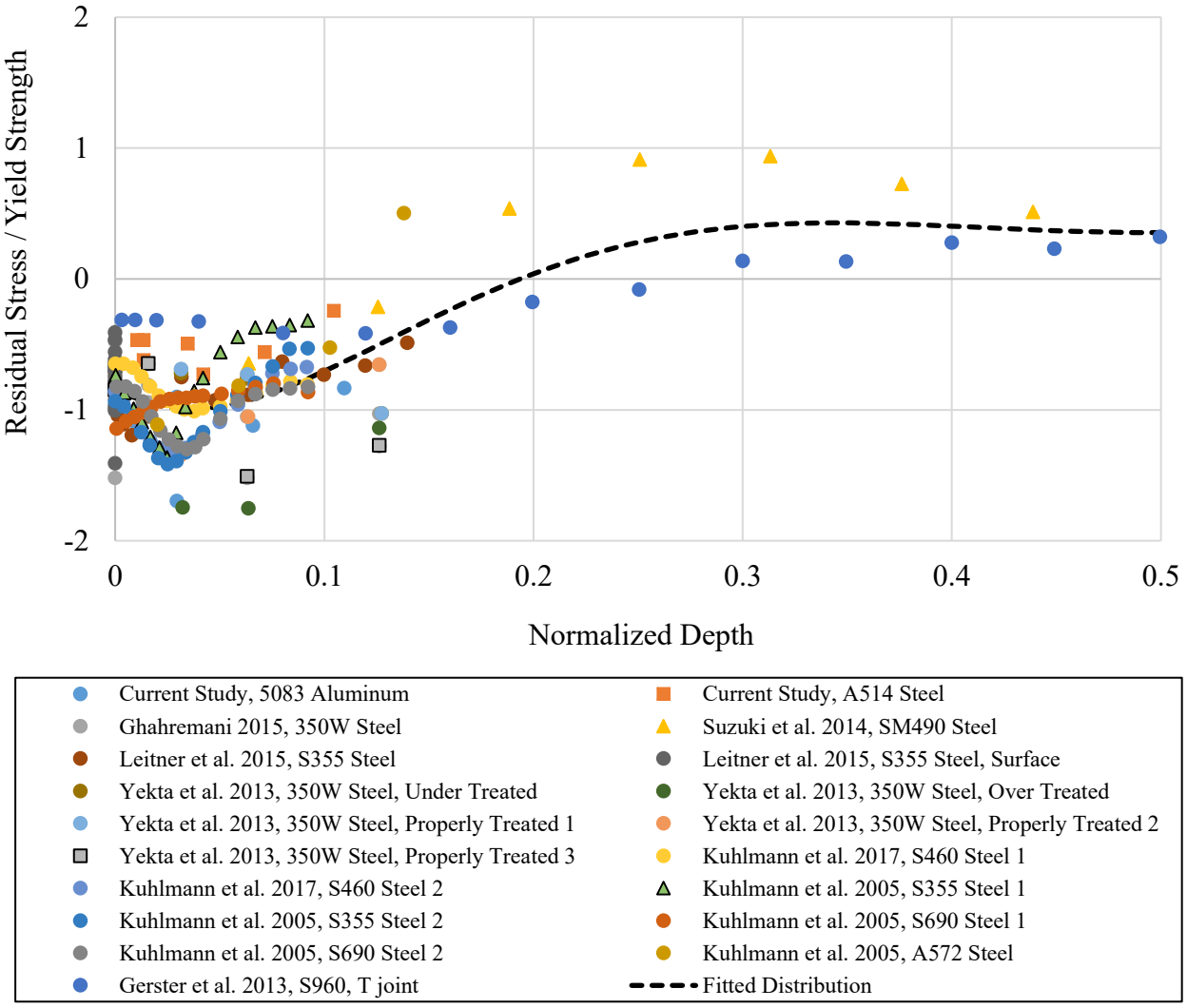

Figure 2.4: Residual stress distribution for impact treated cruciform welded joints

2.1.2.3 Information related to defect geometry and crack shape evolution

The input parameters needed for the SBFM model related to defect geometry and crack shape evolution are summarized in Table 2.3, which include defect (initial crack) depth, defect (initial crack) aspect ratio, and possible crack shape evolution.

Table 2.3: Initial defect geometry and possible crack shape evolution

Defect Geometry	**Symbol**	**Source**
Defect depth	a_i	NDE test / fracture surface observation
Defect aspect ratio	$(a/c)_{initial}$	NDE test / fracture surface observation
Crack shape evolution	Semi- or quarter-elliptical	Fracture surface / assumed

The defect geometry can be observed using non-destructive evaluation (NDE) techniques such as x-ray testing, or by destructive techniques such as sectioning and polishing similar untested samples. The defect geometry, defect (crack initiation) location, and crack shape evolution can also be observed from the fracture surface of the fatigue tested specimens. In the absence of experimental data, the initial defect depth was assumed to be 0.1 mm to 0.15 mm in most cases, which is below the detectable limits of generally used NDE equipment and consistent with measurements and initial defect depth assumptions reported by others (Lotsberg, Sigurdsson, and Wold 2002; Righiniotis and Chryssanthopoulos 2003) for structural welds. The initial aspect ratio of the crack-like defect is generally assumed to be ~0.5, based on measurements and modelling assumptions made previously by others (Brückner and Munz 1983; Righiniotis and Chryssanthopoulos 2003). To model a linear defect like a wormhole or long kissing bond defect running along the entire length of the weld, an initial aspect ratio of 0.1 is assumed. This number is established based on the limit on the aspect ratio of a crack for using weight function equations and coefficients available in (Glinka and Shen 1991; Zheng, Glinka, and Dubey 1996). Two types of crack shapes, namely: semi- or quarter-elliptical are considered for the 2D crack propagation analysis in a rectangular component (main plate of the cruciform joint) as shown in Figure 2.5. The three crack depths shown in Figure 2.5 are representative. In general, the thickness of the component is discretized into many (~300 for this study) depth levels and crack growth analysis is performed at that depth levels.

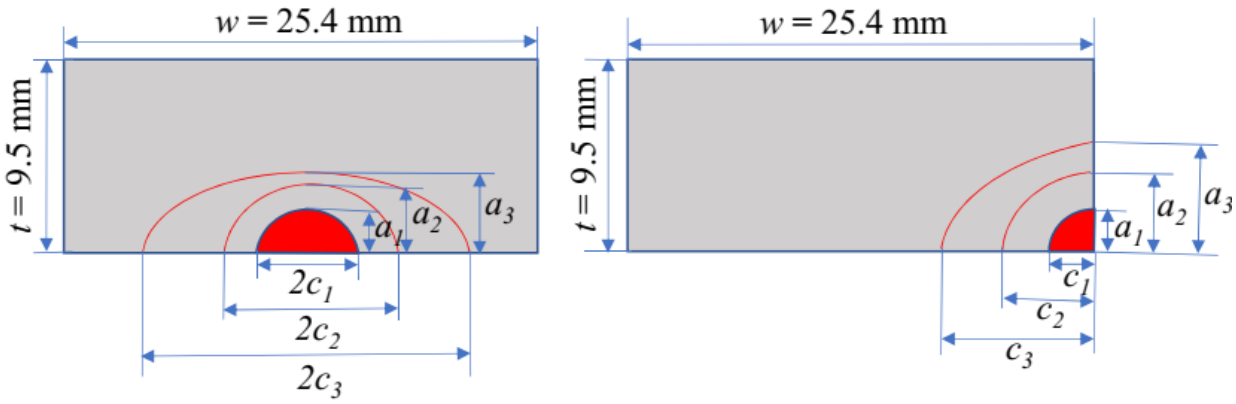

Figure 2.5: Semi-elliptical (left) and quarter-elliptical (right) crack shape evolution

2.1.2.4 Loading history

Four loading histories were used for fatigue testing and SBFM analysis of cruciform welded joints, namely constant amplitude (CA) loading with load ratio (R) of 0.1, CA loading with underloads (CA-UL), variable amplitude history #1 (VA1) and variable amplitude history #2 (VA2). The load histories consist of alternate peak and valley points corresponding to maximum and minimum nominal stress respectively. For a given loading history, a cycle is defined as going from one peak stress level to the next valley stress level and then coming back to the next peak stress level, which makes a closed hysteresis loop on stress-strain plot. A representative CA and CA-UL loading histories are shown in Figure 2.6. For the CA-UL loading history with 1000 cycles of load, there were 50 cycles (101 peaks) with a load ratio of 0.1 and 950 cycles with a load ratio of 0.5.

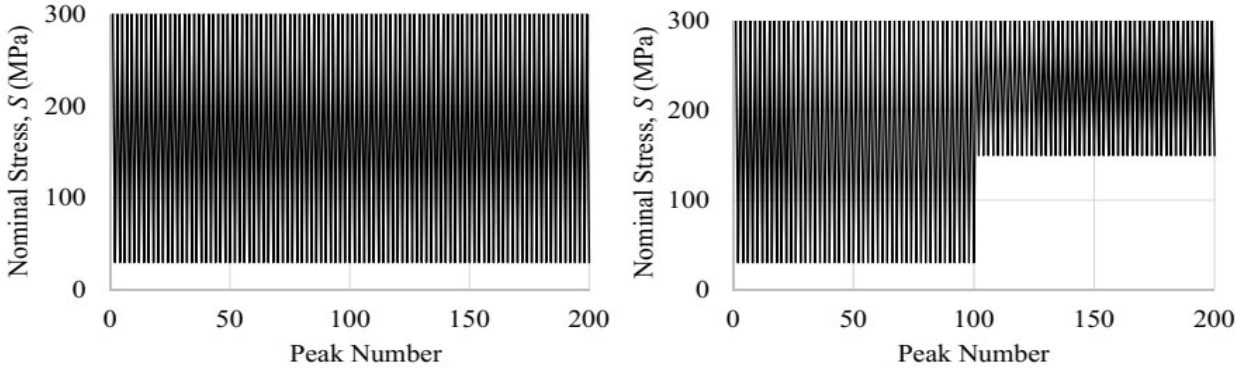

Figure 2.6: CA loading history with R = 0.1 (left) and CA-UL loading history (right)

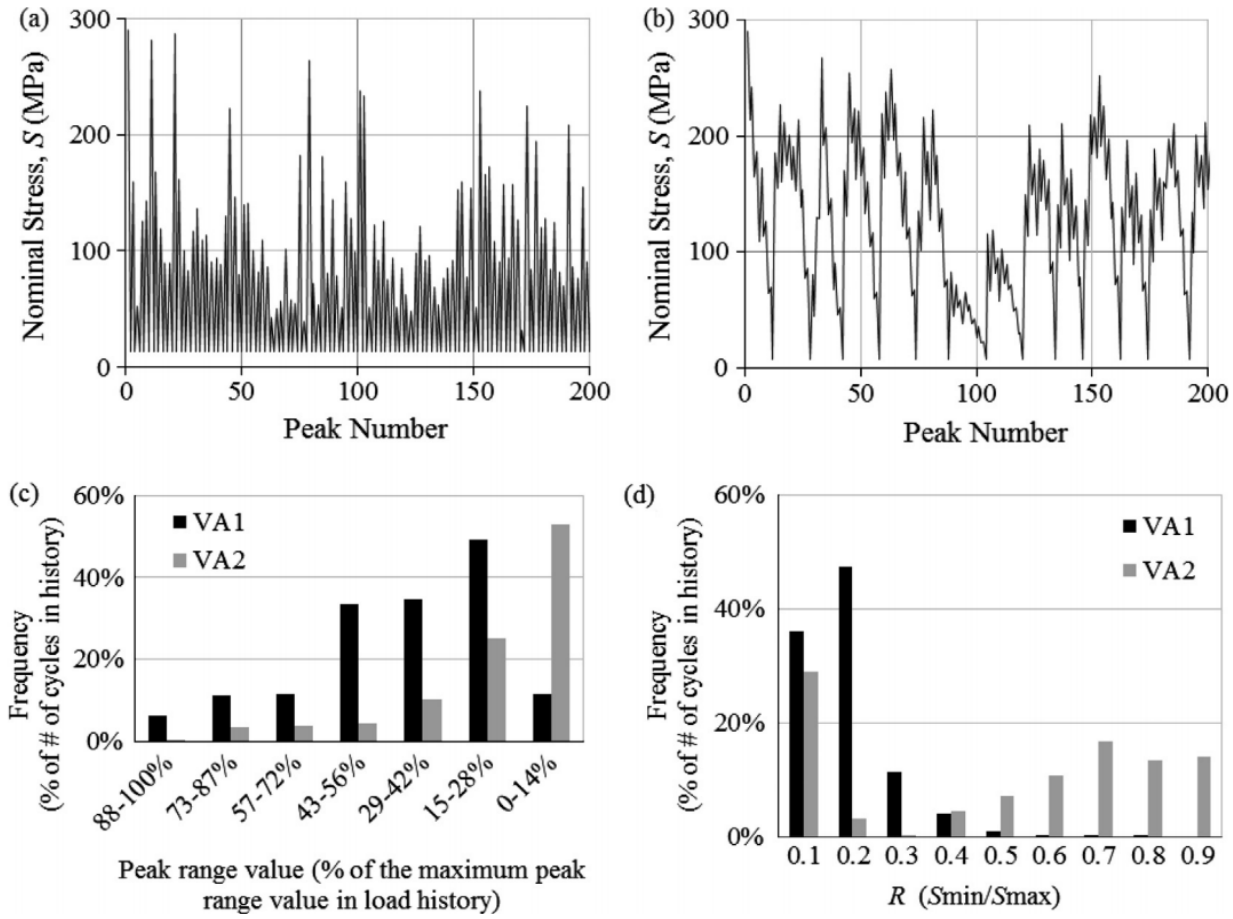

Figure 2.7: VA loading histories: (a) mid-span moment of a 40 m long girder (VA1); (b) support reaction of a 15 m long girder (VA2); (c) VA loading histograms; (d) load ratio (R) histograms [adapted from (Ghahremani, Walbridge, and Topper 2015)]

A representative VA1 and VA2 loading histories are shown in Figure 2.7, which were generated based on axle spacing and load survey data collected by the Ministry of Transportation of Ontario in 1995, which included data for 10198 trucks. As discussed in (Ghahremani and Walbridge 2011), the VA1 loading history was generated by passing 10198 trucks successively over the influence line for mid-span moment of a 40 m long simply supported bridge girder. The VA2 loading history was generated by passing 6470 trucks (after removing cycles with nominal stress range lower than one-third of the constant amplitude fatigue limit) successively over the influence line for support reaction of a 15 m long simply supported bridge girder. The generated VA loading histories were scaled to obtain nominal stress histories corresponding to different CA

equivalent stress ranges. Rainflow analysis results for the VA loading history from (Ghahremani, Walbridge, et al. 2015) are shown in Figure 2.7(c) and Figure 2.7(d). It can be observed in Figure 2.7(c) and Figure 2.7(d) that the VA2 history consists of stress cycles with lower stress ranges but generally higher *R* values than the VA1 history. The relatively larger number of cycles with higher load ratios makes the VA2 history more detrimental from a fatigue perspective compared to the VA1 history. The first cycle for the VA loading histories is set to be the one starting with the highest stress peak, which corresponds to the maximum stress range value of the loading history. Equivalent stress ranges (ΔS_{eq}), for the VA loading histories, were calculated using a method of Miner sum:

$$\Delta S_{eq} = \left(\frac{\sum_{i=1}^{N} \Delta S_i^{m'}}{N} \right)^{\frac{1}{m'}} \tag{2.1}$$

Here, ΔS_i is the nominal stress range for each cycle of load, N is the total number of cycles and m' is the assumed slope of the S-N curve. For the present research, when calculating ΔS_{eq} using Equation (2.1), $m' = 3$ is used for as-welded steel specimens and $m' = 5$ is used for HFMI treated steel specimens, considering the theoretical Palmgren-Miner damage sum of 1.0, and not including mean stress and load interaction effects.

2.1.3 Output format

The results generated by the SBFM model are presented as nominal stress range (S) vs. fatigue life (N) as shown in Figure 2.8. On the S-N plot, a logarithmic value of fatigue life, N (number of cycles) is plotted along the X-axis and a logarithmic value of ΔS (nominal stress range) is plotted along the Y-axis. Here, the nominal stress range means the applied load range divided by the nominal cross-sectional area of the component. The nominal cross-sectional area is perpendicular to the direction of the applied load. The fatigue life is expressed in terms of the number of cycles of load needed to cause the failure of a component, when a crack propagates from an initial crack depth to a critical crack depth. In addition to the S-N curve, the 2D SBFM model also provides crack shape evolution curves, which are shown in Figure 2.9. The starting

point of the crack shape evolution curve is located at an a/t of about 0.015 and an a/c of 0.5, which shows that the assumed defect depth (initial crack depth) was $0.015t$ and assumes that the aspect ratio of the defect (initial crack) was 0.5.

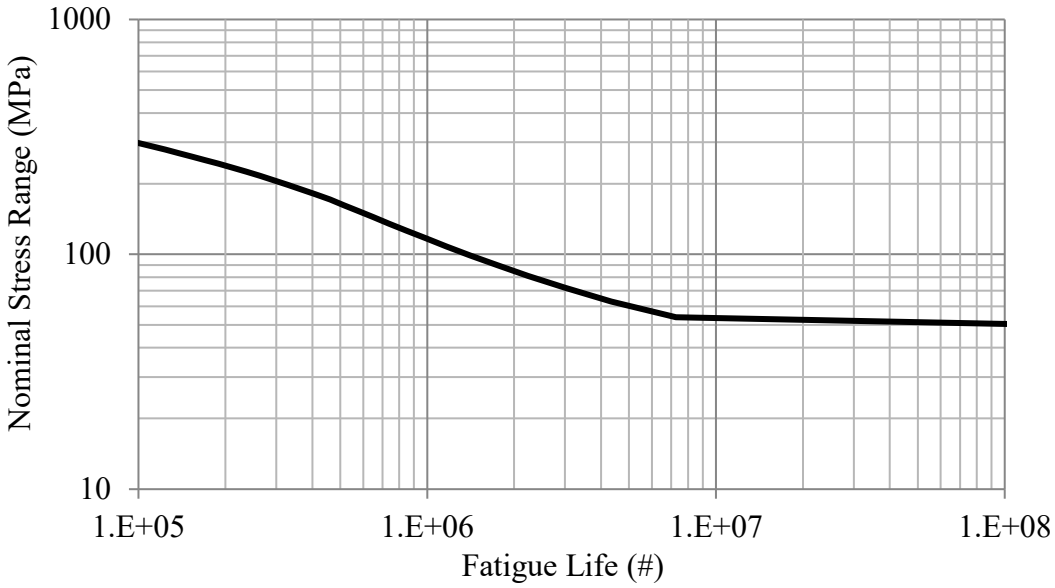

Figure 2.8: Typical output from the SBFM model in the form of an S-N curve

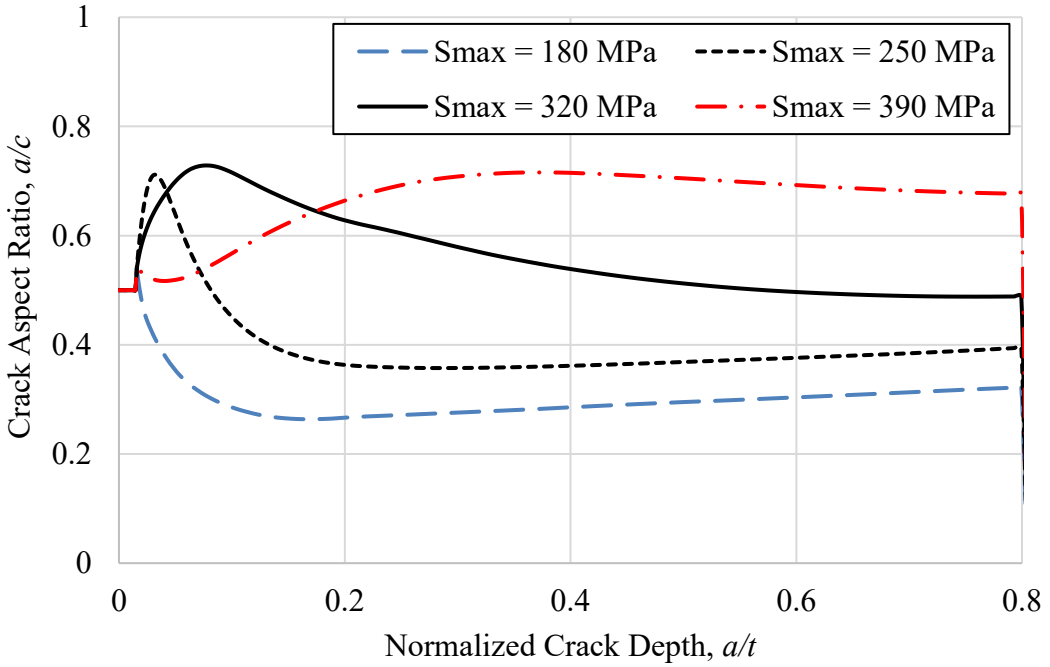

Figure 2.9: Typical crack shape evolution curves as predicted by the 2D SBFM model

The general pattern of the crack shape evolution curve is such that it starts with an a/c of 0.5 (assumed), then the a/c increases with crack depth, approaching $a/c = 1$ (semi-circular crack). It may then decrease followed by another increase at higher crack depths depending on the nature of loading history. The sudden drop at the normalized crack depth of 0.8 in Figure 2.9 indicates that failure happened or failure was assumed to happen at that value of a/t.

2.2 Estimation of local inelastic strain

The local inelastic strains corresponding to each peak and valley point of the cyclic loading history is estimated near the deepest and surface point of the assumed semi- or quarter-elliptical crack, which work as inputs for the calculation of the stress intensity factor (K). In the SBFM model, these local inelastic strains depend on the applied loading history, the material properties, the component geometry, the residual stress distribution, and the crack shape at each crack depth. Steps to estimate local inelastic strains near the deepest and surface points of a crack are described in this section.

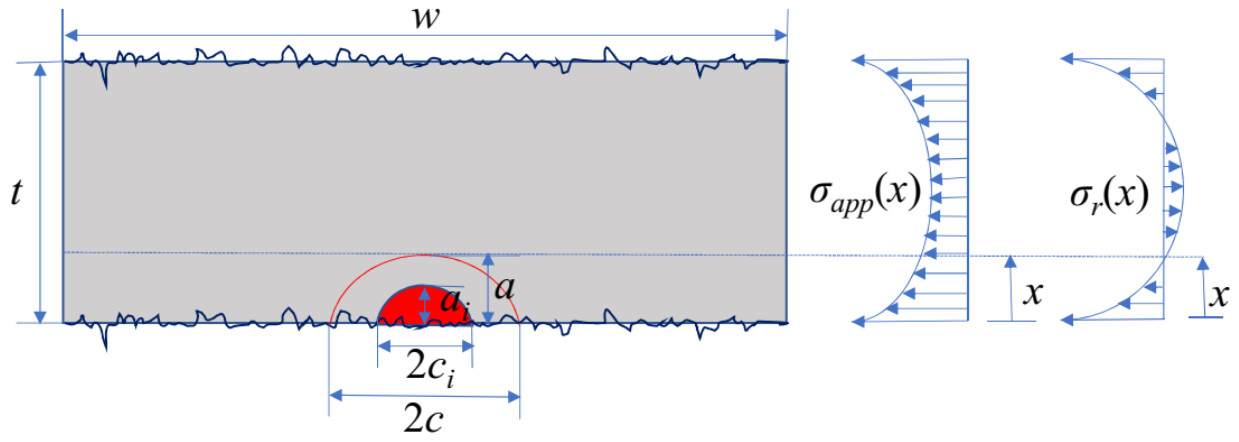

Figure 2.10: Component cross-section and non-uniform applied elastic and residual stress distribution

Figure 2.10 shows a cross-section of a cruciform welded joint with a semi-elliptical surface crack. Here, the top and bottom edges of the cross-section represent the two symmetric weld toes of a cruciform welded joint from where a crack is expected to initiate. The squiggly lines at the top and bottom edges are used to represent the weld toe line and roughness at the weld toe. The left and right edges represent the machined edges of the plate. The non-uniform local elastic stress

distributions, $\sigma_{app}(x)$ due to the applied load (including stress concentration), and the non-uniform residual stress distributions, $\sigma_r(x)$ due to welding or post-weld treatment are shown on the right side of Figure 2.10.

Because of the presence of the stress-concentration, $\sigma_{app}(x)$ is non-uniform. This distribution is determined by multiplying the $SCF(x)$ at each depth (x), with the nominal stress (S), as shown in Equation (2.2). In this equation, S is the known nominal stress corresponding to a given load (P) history as calculated from Equation (2.3). In Equation (2.3), w is the width of the main plate and t is the thickness of the main plate of the cruciform welded joint. The non-uniform residual stress distribution, $\sigma_r(x)$, is known in this study and modelled using a fitted distribution based on residual stress measurement data.

$$\sigma_{app}(x) = SCF(x) \cdot S \tag{2.2}$$

$$S = \frac{P}{w \cdot t} \tag{2.3}$$

The stress intensity factor is a key parameter that characterizes the stress state near the tip of a crack or notch caused by a remote load and/or residual stress in a cracked component. The classical equation for estimating the stress intensity factor (K) at each crack depth "a" is shown in Equation (2.4). In this equation, $Y(a)$ is a combined correction factor to account for the crack shape (if it is not a through-crack), the free surface on one side of the crack, the finite thickness of the cracked plate and the presence of a non-uniform stress distribution along the anticipated crack path. In Equation (2.4), there is no scope to consider material non-linearity directly, and this equation does not consider small crack growth behaviour.

$$K(a) = Y(a) \cdot \sigma \cdot \sqrt{\pi \cdot a} \tag{2.4}$$

In the SBFM model, K, which is also known as the strain-based stress intensity factor, is estimated at each crack depth following Equation (2.5), adapted from (El Haddad, Topper, and Smith 1979). In Equation (2.5), a_o is a material constant, which is added to the crack depth (a) for considering small crack growth behaviour. It can be calculated using Equation (2.6), where ΔK_{th} is threshold stress intensity factor range and $\Delta\sigma_e$ ($\approx 0.5 \cdot \sigma_u$) is the fatigue limit at the load ratio, R =

-1. The term $\varepsilon(a)$ in Equation (2.5) is the local inelastic strain near the crack tip, which is calculated considering non-linear material behaviour and the presence of a non-uniform stress distribution.

$$K(a) = Y(a) \cdot E \cdot \varepsilon(a) \cdot \sqrt{\pi \cdot (a + a_0)} \tag{2.5}$$

$$a_0 = \left(\frac{\Delta K_{th}}{\Delta \sigma_e} \right)^2 \cdot \frac{1}{\pi} \tag{2.6}$$

The correction factor $Y(a)$ in the SBFM model is calculated using the weight function method according to Equation (2.7) rather than using empirical or analytical equations available in the existing literature (Albrecht, Yamada 1977). In Equation (2.7), the term $m(x,t)$ is the weight function coefficient, which is a function of crack shape (semi-elliptical or quarter-elliptical), crack depth, crack width and the component thickness. The correction factor Y(a) in Equation (2.5) is calculated from Equation (2.7) and it is used to account for the crack shape, the free surface on one side of the crack, and the finite thickness of the cracked plate but not the presence of a non-uniform stress distribution along the anticipated crack path.

$$Y(a) = \frac{\int_0^a 1 \cdot m(x,t) \mathrm{d}x}{\sqrt{\pi \cdot a}} \tag{2.7}$$

The non-uniform stress distribution is modelled by modifying the local elastic applied stress distribution $\sigma_{app}(x)$ and the residual stress distribution, $\sigma_r(x)$, using the weight function method according to equations (2.8) and (2.9) respectively.

$$\sigma'_{app}(a) = \frac{\int_0^a \sigma_{app}(x) \cdot m(x,t) \mathrm{d}x}{\int_0^a m(x,t) \mathrm{d}x} \tag{2.8}$$

$$\sigma'_{r}(a) = \frac{\int_0^a \sigma_{r}(x) \cdot m(x,t) \mathrm{d}x}{\int_0^a m(x,t) \mathrm{d}x} \tag{2.9}$$

The modification is performed to obtain a uniform stress distribution that is equivalent to the actual, non-uniform stress distribution, so that K can be estimated from Equation (2.5) without using a separate correction factor to consider the presence of non-uniform stress distribution. The equivalence of the stress distributions calculated from Equations (2.8) and (2.9) is in terms of the K, which means that the K calculated at a specific crack depth using the actual non-uniform stress distribution and using the equivalent uniform stress distribution will be equal in magnitude. The numerator on the right-hand side of Equation (2.8) is the stress intensity factor (K) based on the non-uniform elastic stress distribution, $\sigma_{app}(x)$, which does not include the effect of material non-linearity.

The weight function method is generally used to estimate K under a non-uniform "elastic" stress distribution. However, in the SBFM model, the weight function method is used for two different purposes: 1) to modify the non-uniform stress distributions ($\sigma_{app}(x)$, $\sigma_r(x)$) to obtain equivalent uniform stress distributions ($\sigma'_{app}(x)$, $\sigma'_r(x)$) according to Equations (2.8) and (2.9), and 2) to obtain the correction factor $Y(a)$ according to Equation (2.7). Since the K obtained by directly using the weight function method does not consider the effect of material non-linearity, this K (such as numerator in Equation (2.8)) is not used directly to perform crack growth analysis. The strength of the weight function method is that it allows the computation of K under a non-uniform stress distribution for any shape of semi- or quarter-elliptical crack without using an FE analysis after each crack depth increment. For calculation of weight function coefficients for a specific component geometry, FE analysis results are needed for only two reference stress distribution. This strength has been utilized in the SBFM model to modify the non-uniform stress distribution to obtain an equivalent uniform stress distribution and to compute the correction factor for each crack geometry during the propagation of a crack. The obtained parameters ($\sigma'_{app}(x)$, $\sigma'_r(x)$) are further used to estimate the local inelastic strain $\varepsilon(x)$ at each crack depth "a", which includes the effect of applied stress, the presence of a residual stress, and material non-linearity. The obtained $\varepsilon(a)$ and $Y(a)$ is used to obtain K at the deepest and surface point of a crack according to Equation (2.5), which is then used for a crack growth analysis. The process to estimate $\varepsilon(x)$ at the deepest and surface points of a crack after each crack depth increment is presented in the following subsections.

2.2.1 Estimation of combined local elastic stress (S_{cl}) at the deepest point

Figure 2.11 shows semi- and quarter-elliptical cracks with the deepest point "A", surface point "B", crack depth "*a"*, crack width "2*c"* for a semi-elliptical crack, and crack width "*c*" for a quarter-elliptical crack in a rectangular component of finite thickness "*t*". Weight function coefficients are available in the existing literature to estimate elastic stress based SIF (K_{el}) for the crack shapes shown in Figure 2.11 under a non-uniform stress distribution. (Glinka and Shen 1991) provide weight function coefficients to estimate K_{el} at the deepest and surface points of a semi-elliptical surface crack under non-uniform applied stress distribution. (Zheng et al. 1996) provide weight function coefficients to estimate K_{el} at the deepest and surface points of a quarter-elliptical crack. Weight function for the surface point can be considered only as an average quantity associated at the boundary layer near the surface point "B". The reason behind this is $r^{-0.5}$ singularity of the near crack tip stress field, which vanishes at the intersection of three free surfaces such as point "B".

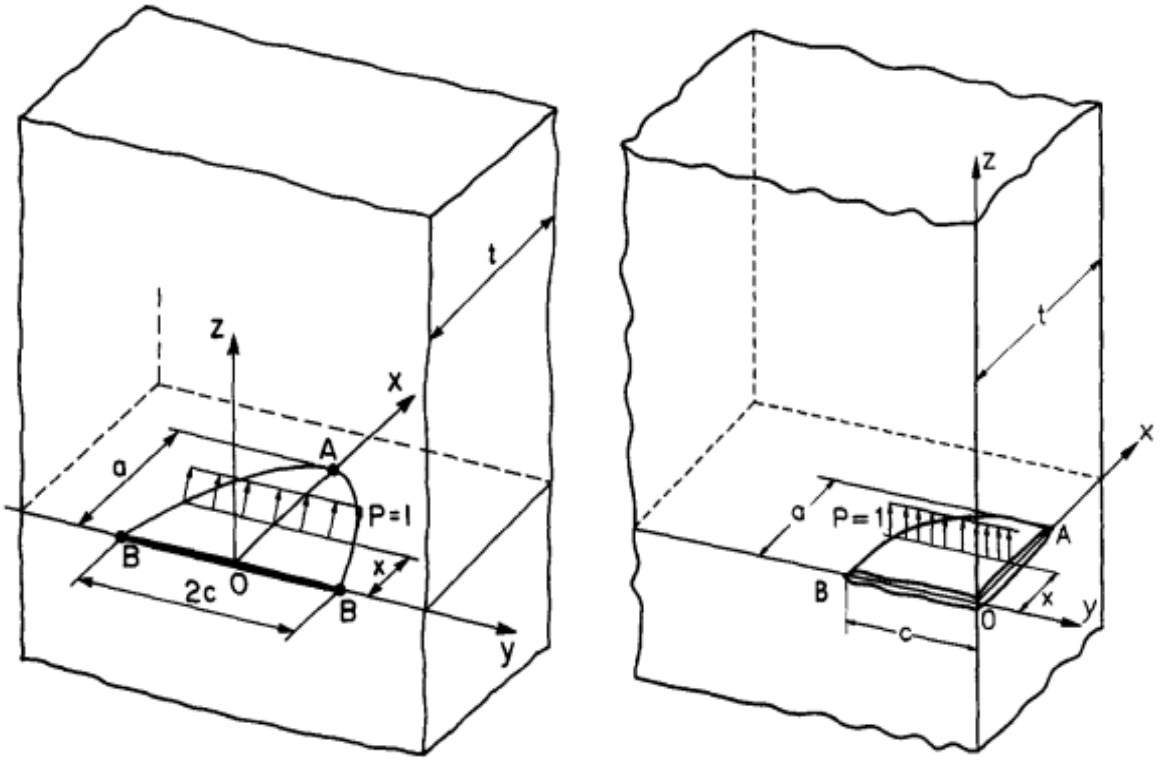

Figure 2.11: Semi and quarter elliptical crack in a component (Zheng et al. 1996)

Using these weight function coefficients, the equivalent uniform stress can be calculated at each crack depth using Equation (2.8) for a non-uniform applied stress distribution and using Equation (2.9) for a non-uniform residual stress distribution. (Anderson and Glinka 2006) provide a closed-form numerical method for integrating the weight functions involved in Equations (2.8) and (2.9). The piecewise linear method mentioned in (Anderson and Glinka 2006) was followed to the perform numerical integration involved in Equations (2.8) and (2.9).

The combined local elastic stress (S_{cl}), including the effect of applied load, stress concentration and the residual stress, near the deepest point of a crack is calculated following Equation (2.10) corresponding to each peak and valley point of the nominal stress(S) history.

$$S_{cl}(x=a, y=0) = \sigma'_{app}(x=a, y=0) + \sigma'_{r}(x=a, y=0) \tag{2.10}$$

2.2.2 Estimation of combined local elastic stress (S_{cl}) at the surface point

The local uniform elastic stress $\sigma'_{app}(x=a, y=c)$ at the surface point "B" is estimated using Equation (2.11).

$$\sigma'_{app}(x=a, y=-c) = \frac{\int_0^a \sigma_{app}(x) \cdot m(x,t)\mathrm{d}x}{\int_0^a m(x,t)\mathrm{d}x} \tag{2.11}$$

It should be noted that in Equation (2.11), the weight function coefficient $m(x,t)$ is for estimating K_{el} at the surface point of a given semi- or quarter-elliptical crack. Relevant weight function coefficients were used corresponding to the surface point "B" following (Glinka and Shen 1991) for semi-elliptical cracks and (Zheng et al. 1996) for quarter-elliptical cracks. The residual stress distribution $\sigma_r'(x=a, y=-c)$ at the surface point was also estimated using an equation similar to Equation (2.11). The combined local elastic stress (S_{cl}) at the surface point of a crack was then calculated using Equation (2.12) for each peak and valley point of the nominal stress (S) history.

$$S_{cl}(x=0, y=-c) = \sigma'_{app}(x=0, y=-c) + \sigma'_{r}(x=0, y=-c) \tag{2.12}$$

2.2.3 Calculation of local inelastic strain from combined local elastic stress

To characterize the non-linear stress-strain behaviour of a material, the Ramberg-Osgood material model is used in the SBFM model, which requires the cyclic material model parameters: *K'* and *n*'. Given the combined local elastic stress history (S_{cl}), the local inelastic stress-strain history is determined by simultaneously solving the Neuber and Ramberg-Osgood equations, as indicated in Figure 2.12 and Figure 2.13 for the case of a monotonic loading and for the case of a cyclic loading respectively. The Ramberg Osgood material model is represented in these figures by a red curve and the Neuber equation is represented by a green curve. In these figures, S_{cl} is the combined local elastic stress, calculated according to Equation (2.10) for the deepest point and according to Equation (2.12) for the surface point of a crack, corresponding to each peak and valley point of the given nominal stress (S) history. The term e_{cl} is the combined local elastic strain, which is related to S_{cl} through an elastic stress-strain relationship (Hooke's law) as shown with a blue line in Figure 2.12 and Figure 2.13. The symbols σ and ε represent local inelastic stress and strain, which includes the effect of the *SCF*, the applied stress and the residual stress. The local inelastic stress and strain are calculated at the deepest and surface points of a crack corresponding to each peak and valley point of the nominal stress history. This step provides the key parameters ε_{max}, ε_{min}, σ_{max}, and σ_{min} to estimate the crack growth rate at a particular crack depth along the depth and width directions of a crack for a given load cycle.

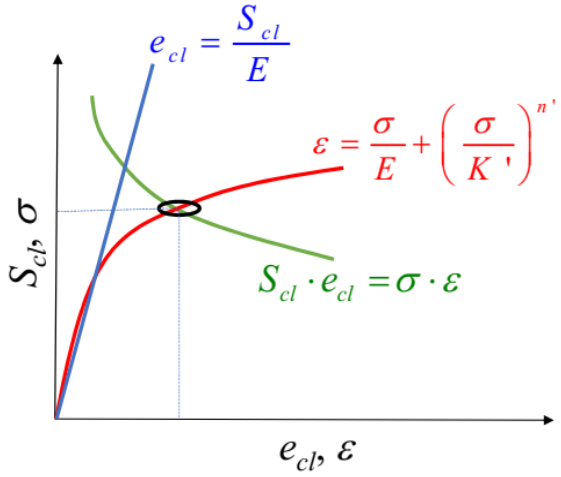

Figure 2.12: Ramberg-Osgood material model and Neuber rule under monotonic loading

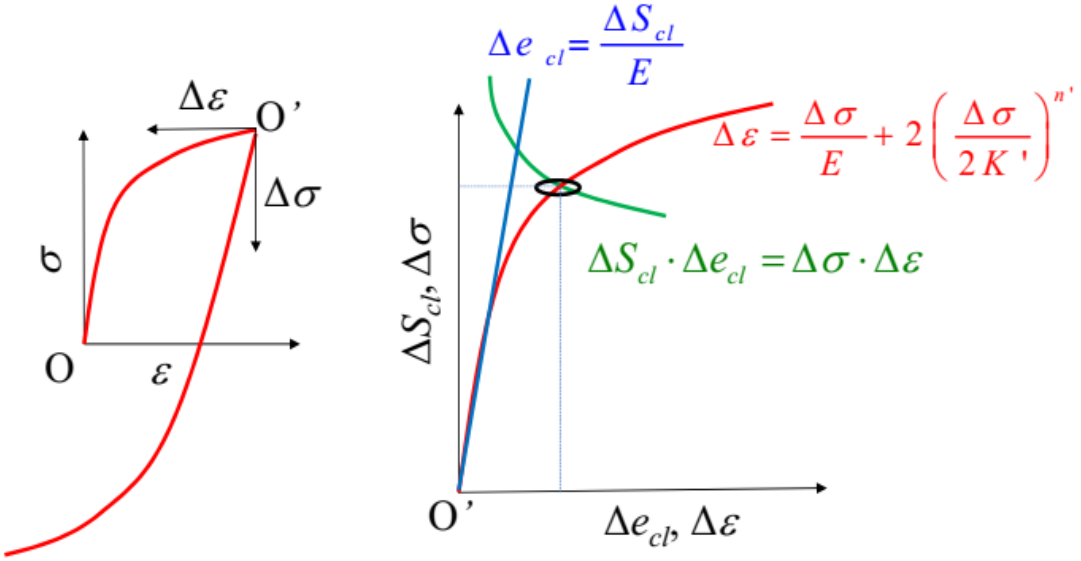

Figure 2.13: Ramberg-Osgood material model and Neuber rule under cyclic loading

After performing the same process of solving the Neuber equation and R-O equation simultaneously, corresponding to each nominal stress of a given loading history, local inelastic stress-strain behaviour is estimated at the weld toe or notch root of a component subjected to an arbitrary nominal stress history, and then simulated strain ranges of the closed hysteresis loops are used to calculate the crack growth rate at each crack depth. A push-down list counting method mentioned in (Conle, A., Oxland, T.R., and Topper 1988) has been used to count the number of cycles under a variable amplitude loading condition. An algorithm for implementing the push-down list counting method was adapted from (Conle, A., Oxland, T.R., and Topper 1988), which simulates the material memory events. The material memory events were subdivided into two types: 1) memory of a previously interrupted monotonic curve and 2) memory of a previously interrupted hysteresis loop curve. The following general rules were hypothesized while modelling memory events, as mentioned in (Conle, A., Oxland, T.R., and Topper 1988):

1. In any deformation history the maximum point of excursion on the monotonic or skeleton curve will represent an absolute limit or bound which will exist on both sides of the strain or stress axis, irrespective of whether the actual reversal occurred on the tension or compression side.

2. All deformation between these absolute bounds will utilize the cyclic hysteresis loop shape.

3. Whenever deformation exceeds these absolute bounds, the locus will again follow the shape of the monotonic curve and, after another reversal, will set a new absolute bound.

2.3 Estimation of crack opening strain

Fatigue cracks in metals under cyclic loading remain closed until a high enough magnitude of the load is applied to open the crack. The stress corresponding to the magnitude of load that opens the crack is known as the crack opening stress. It is assumed that only the portion of the applied load cycle which is more than crack opening load contributes to driving the crack further. It has been shown by experiment (Elber 2009) and analysis (Newman 2009) that this tendency can be used to explain load interaction effects on crack growth rates. Most of the previous analytical models for finding crack opening stress (S_0) were based on the Dugdale strip-yield model (Dugdale 1960) but were modified to leave plastically-deformed material as a result of the advancing crack. In the SBFM model, crack closure is modelled using Newman's equations. To consider the VA loading effect on crack closure, a crack closure build-up equation is used from (Vormwald and Seeger 1991).

2.3.1 Estimation of crack opening stress under constant amplitude (CA) loading

In the SBFM model, crack closure is modelled through the crack opening stress equation proposed by (Newman 1984). A general crack opening stress equation is provided in equations (2.13) and (2.14) as a function of load ratio (R), stress level (S_{max}) and plastic constraint factor (α), which is applicable for middle-crack tension specimens under CA loading. For non-negative load ratios, Equation (2.13) is used and for negative load ratios Equation (2.14) is used to calculate the crack opening stress.

$$S_0 = S_{\max}(A_0 + A_1 R + A_2 R^2 + A_3 R^3) \tag{2.13}$$

$$S_0 = S_{\max}(A_0 + A_1 R) \tag{2.14}$$

The parameters A_0, A_1, A_2, and A_3 are a function of α, S_{max} and flow stress (σ_0). These parameters are calculated from Equations (2.15), (2.16), (2.17), and (2.18).

$$A_0 = (0.825 - 0.34\alpha + 0.05\alpha^2)\left[\cos\left(\frac{\pi S_{\max}}{2\sigma_0}\right)\right]^{\frac{1}{\alpha}} \tag{2.15}$$

$$A_1 = (0.415 - 0.071\alpha)\frac{S_{\max}}{\sigma_0} \tag{2.16}$$

$$A_2 = 1 - A_0 - A_1 - A_3 \tag{2.17}$$

$$A_3 = 2A_0 + A_1 - 1 \tag{2.18}$$

Equations (2.13) and (2.14) provide steady-state crack opening stress values under CA loading for different values of load ratio. A steady-state condition of crack closure is reached when the residual plastic deformations and crack closure along the crack surfaces are fully developed and stabilized under CA loading. The equations for crack opening stress are valid only when the magnitude of crack opening stress is higher than the minimum stress level of the stress cycle. In the crack opening stress equation, the effects of three-dimensional constraint were simulated in a two-dimensional closure model (Newman 1984) by using a plastic constraint factor α on tensile yielding. That is, the material yields when the maximum stress reaches $\alpha \cdot \sigma_0$. The material is assumed to yield in compression when the stress reaches $-\sigma_0$. Here, σ_0 is flow stress which is taken to be the average of the yield and ultimate strength of the material obtained from a static uniaxial tension test. A plastic constraint factor α of 1.0 corresponds to a plane stress condition and an α of 3.0 corresponds to a plane strain condition.

The precise effect of three-dimensional constraint on the crack opening stress is not known for a given loading condition and component geometry. McClung (McClung 1994) performed a finite element analysis to compute component geometry effects on fatigue crack closure and recommended that the term S_{max} / σ_0 in Equation (2.15) and (2.16) should be replaced with $Y \cdot S_{max} / \sigma_0$ to consider the component geometry effects on crack closure. Here, Y is the geometry correction factor, which is the same as the one used in the calculation process of K in Equation (2.5). In the SBFM model, while estimating crack opening stress, the McClung recommendation has been applied at the deepest and surface point of the crack. (Wang, Rose, and Newman 2002) modelled closure of plane-strain cracks under large scale yielding conditions and recommended that the magnitude of α should be estimated from Equation (2.19). In the SBFM model, the value

of α is calculated from Equation (2.19) at the deepest point of a semi-elliptical crack where an approximate plane strain condition exists. For the surface point of the semi-elliptical crack, and surface and deepest points of the quarter elliptical crack, the value of α is assumed to be 1.2 to simulate an approximate plane stress condition at the free surface of the component.

$$\alpha = 1.78 - 0.628\frac{\sigma_{\max}}{\sigma_y} \tag{2.19}$$

2.3.2 Estimation of crack opening stress under variable amplitude (VA) loading

Vormwald et al. (Vormwald and Seeger 1991) proposed a simple equation, which relates the change in the crack opening stress in a given cycle to the difference between the current crack opening stress (S_{cu}) and the steady-state crack opening stress (S_{opss}):

$$\Delta S_{op} = \mu_{op}\left(S_{opss} - S_{cu}\right) \tag{2.20}$$

Here, ΔS_{op} is the change in the crack opening stress and "μ_{op}" is a crack closure build-up parameter, which is a material constant obtained through a series of damage tests. The step by step calculation of crack opening stress in the SBFM model under VA loading is similar to that described in (El-Zeghayar 2010) and can be summarized as follows:

1. For the first stress cycle, the value of S_{op} is calculated using Newman's equation.
2. For all stress cycles following the first, the crack opening stress (S_{op}) used in the crack growth analysis is calculated based on the following assumptions:
   a) If $S_{cu} \geq S_{opss}$, then the crack opening stress level is assumed to be instantaneously decreased to the constant amplitude steady-state level for that cycle.
   b) If $S_{cu} < S_{opss,}$ then the crack opening stress level is assumed to follow the exponential build-up according to Equation (2.20) unless the range of stress in that cycle is below the intrinsic stress range or the maximum stress in that cycle is below zero.

Once the crack opening stress is known, the corresponding crack opening strain is calculated using cyclic Ramberg-Osgood equation. A sample of a stress-strain history corresponding to a VA loading history is shown in Figure 2.14. This history and the identified stress-strain points in this figure have been calculated using the assumptions and procedure defined in the preceding paragraphs.

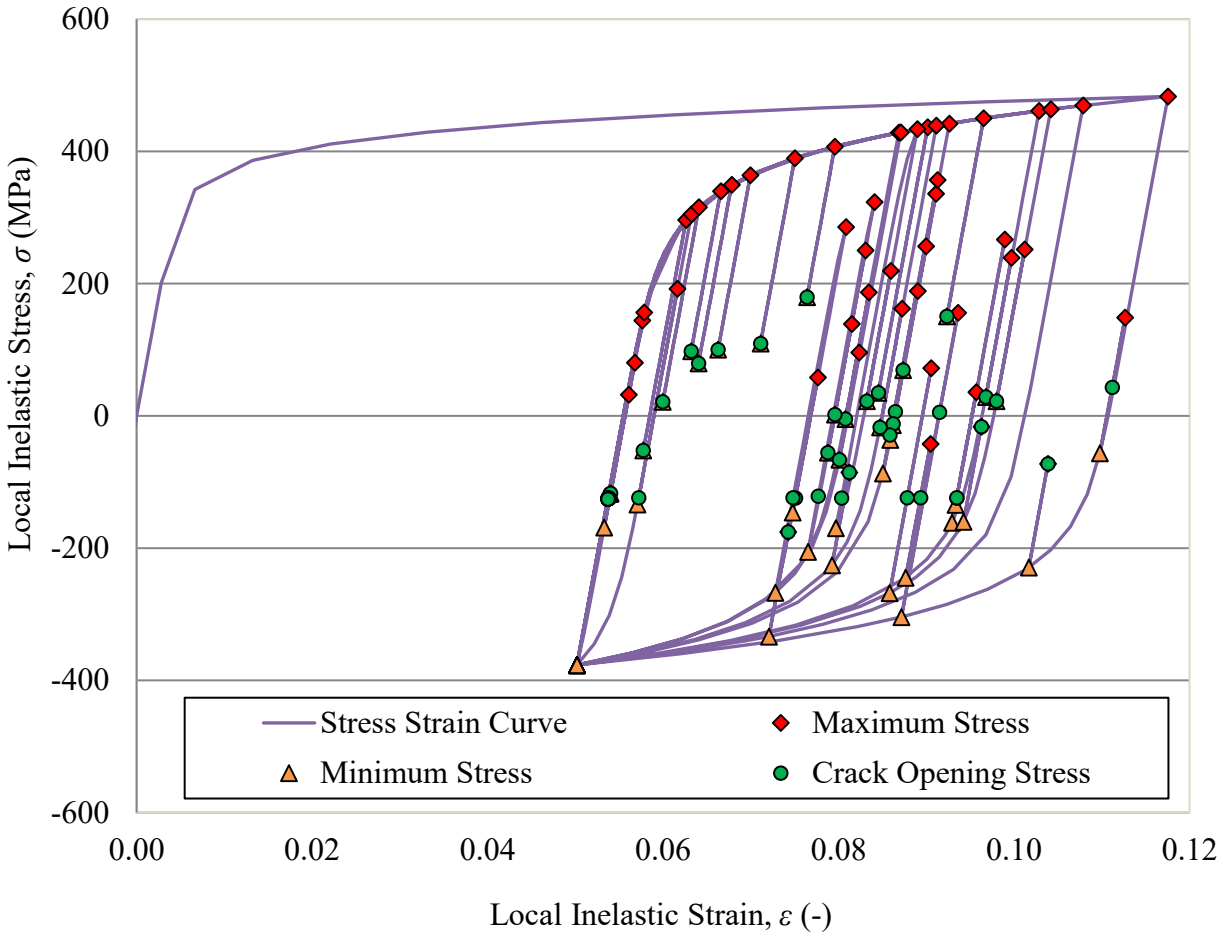

Figure 2.14: A sample stress-strain history under variable amplitude (VA) loading

For each closed stress-strain hysteresis loop, the local inelastic maximum, minimum, and crack opening stress-strain points are shown in Figure 2.14. It can be noted that for some cycles, the minimum and crack opening stress-strain points are one and the same. Also, the value of ε in the figure is in between 5% to 12%, which is very high but it was intentionally obtained with an arbitrary value of material model parameters to show large stress-strain loops.

2.4 Estimation of effective stress intensity factor range

The effective SIF range, ΔK_{eff}, considering crack closure, is determined as follows:

$$\Delta K_{eff} = K_{max} - \max\left(K_{op}, K_{min}\right) \tag{2.21}$$

where K_{max} and K_{min} are the SIFs due to the maximum and minimum local inelastic strain levels

(ε) for a particular stress cycle and K_{op} is the SIF corresponding to the crack opening strain level for a given load cycle, which is calculated according to Equation (2.5). This step provides ΔK_{eff} at each crack depth for the deepest and surface point of the crack corresponding to each stress cycle of given nominal stress history.

2.5 Definition of crack growth law

The Paris-Erdogan crack growth law is used to relate the crack growth rate with the SIF, which is commonly done in linear elastic fracture mechanics. It is modified to consider crack closure effects and a threshold stress intensity factor range, ΔK_{th}. Given ΔK_{eff} from Equation (2.21) and ΔK_{th} from the materials test, the crack growth rate at each crack depth is calculated following Equation (2.22) corresponding to each stress cycle of a given nominal stress history.

$$\frac{da}{dN} = C \cdot \max\left[\left(\Delta K_{eff} - \Delta K_{th}\right)^{m}, 0\right] \tag{2.22}$$

Here, C and m are the Paris-Erdogan crack growth law constants estimated from a closure-free crack growth rate test (e.g., at a high load ratio, such as R = 0.8) on a compact tension specimen. This step provides the crack growth rate at the deepest and surface points of the crack when the crack is propagating from one crack depth to another.

2.6 Integration of crack growth law

Given the crack growth rates at the deepest point and at the surface point of a crack, the fatigue life (number of cycles) is calculated for successive specific crack depth increases from $d(k,1)$ to $(k+1,1)$, until a critical crack depth is reached, as shown in Figure 2.15.

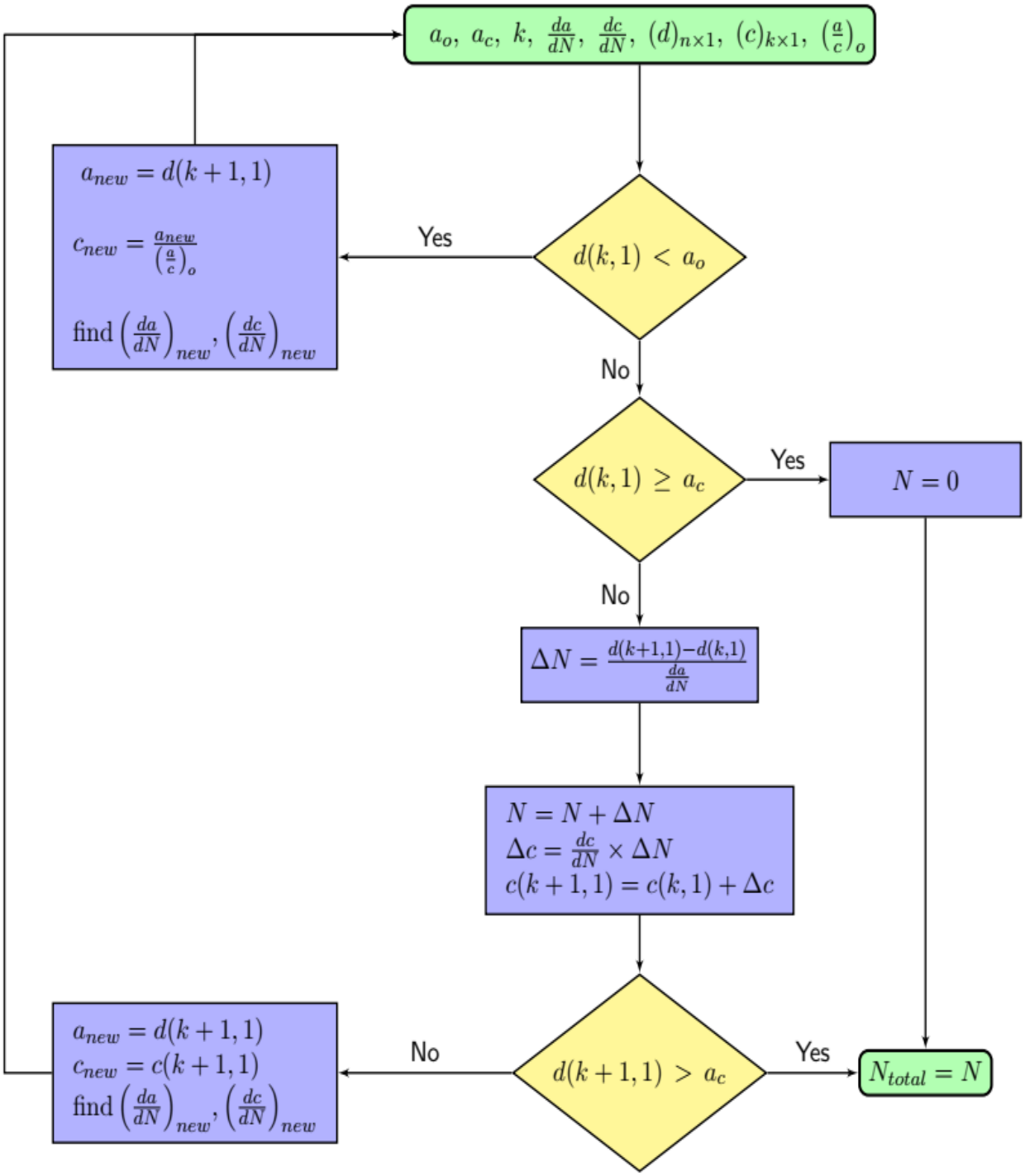

Figure 2.15: Steps to estimate fatigue life in 2D SBFM model

The symbol d represents discrete depths at which fracture mechanics analyses are performed, which is a vector of size $n \times 1$. The variable k takes values from 1 to n (~300). As outlined in Figure 2.15, it is first checked that the depth, $d(k,1)$ is in between the initial and the critical crack depth. If this check is passed, then a crack growth analysis is performed, otherwise, the same check is performed for the next higher depth. At each depth, first, the number of cycles (ΔN) is calculated for the deepest point of the crack corresponding to the change in crack depth from $d(k,1)$ to $d(k+1, 1)$ with a known crack growth rate da/dN at the depth $d(k,1)$. Now, for the calculated number of cycles (ΔN), crack depth increment (Δc) is calculated along the surface direction, this step provides an updated crack width for further calculation at the next crack depth. From the crack growth analysis, for depth range $d(k,1)$ to $d(k+1,1)$, the updated crack depth a and half crack width c is obtained, which provides an updated aspect ratio (a/c) of the crack. This is used subsequently to calculate the number of cycles corresponding with the next crack depth increment from $d(k+1,1)$ to $d(k+2,1)$ and so on. These steps are repeated until a critical crack depth is reached.

2.7 Definition of failure criterion

There are several conditions that can be used as failure criteria during crack propagation such as exceedance of the material fracture toughness limit or, exceedance of the material yield or ultimate strength. The existing ASTM standards (ASTM E399, ASTM E1820) recommend guidelines to perform fracture toughness test to estimate plane strain fracture toughness, which provides a conservative estimate of fracture toughness for real-life components. Depending on the specific application (component size and notch geometry), a suitable fracture toughness test (adequate thickness of test coupon) should be devised to get fracture toughness data which represent stress state of the specific component geometry which is usually in between plane stress and plane strain condition. For the current work, no fracture toughness test was performed simulating the stress state in the tested specimen, therefore, fracture toughness was not used while defining the failure criteria. In this study, the critical crack depth has been calculated based on net section failure depending on half crack width c, component width w, component thickness t, the ultimate strength of the material σ_u and maximum nominal applied stress $\sigma_{nom,max}$. The four cases

of crack shapes, considered for the estimation of critical crack depths are shown in Figure 2.16 and Figure 2.17. The equations to estimate the critical crack depth for all four cases are derived in the next subsections.

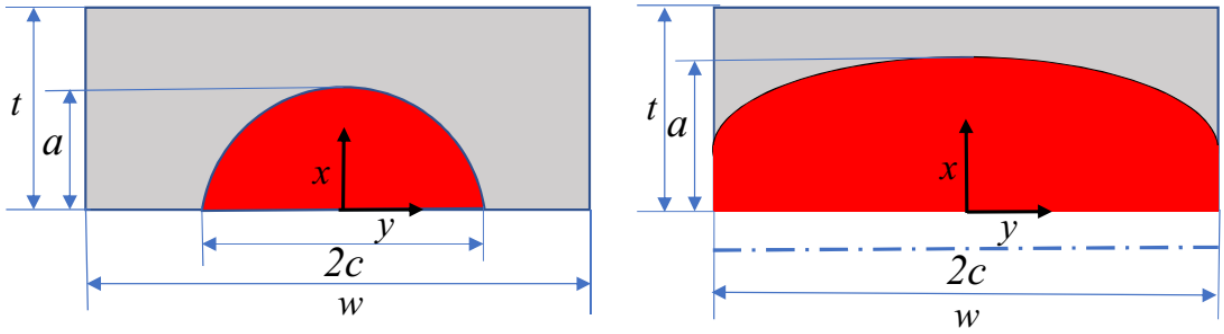

Figure 2.16: Semi-elliptical crack shapes with dimension $2 \cdot c < w$ (left) and $2 \cdot c > w$ (right)

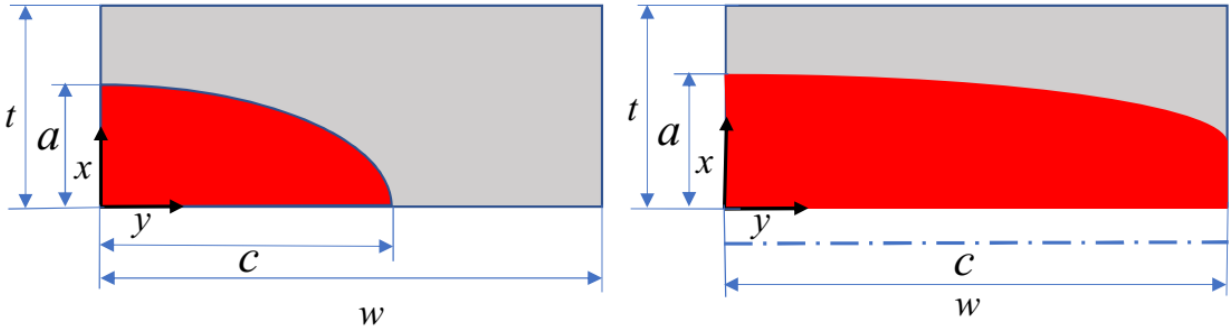

Figure 2.17: Quarter elliptical crack shapes with dimension $c < w$ (left) and $c > w$ (right)

Case 1: Semi-elliptical crack shape with $2 \cdot c < w$ (see Figure 2.16 (left))

The formula for calculation of the area of the semi-elliptical crack (A_{se}) is presented in Equation (2.23). In this equation, a and c are the ellipse dimensions, as shown in Figure 2.16 (left). The net area (A_{net}) is calculated by subtracting the area of crack from the total cross-sectional area (A) according to Equation (2.24). Then, the net stress is calculated by dividing the peak load (of the loading history) with the net cross-sectional area as shown in Equation (2.25). For failure, the net stress in the cracked component should be equal to or greater than the ultimate strength of the material. After equating the net stress to the ultimate strength of the material, Equation (2.26) is obtained. After rearranging the Equation (2.26) and equating a with a_{crit}, the expression for critical crack depth (a_{crit}) is obtained, which is shown in Equation (2.27).

$$A_{se} = \frac{\pi \cdot c \cdot a}{2} \tag{2.23}$$

$$A_{net} = A - A_{se} = w \cdot t - \frac{\pi \cdot c \cdot a}{2} \tag{2.24}$$

$$\sigma_{net} = \frac{P_{\max}}{A_{net}} = \frac{\sigma_{nom,\max} \cdot w \cdot t}{w \cdot t - \frac{\pi \cdot c \cdot a}{2}} \tag{2.25}$$

$$\sigma_u = \frac{\sigma_{nom,\max} \cdot w \cdot t}{w \cdot t - \frac{\pi \cdot c \cdot a}{2}} \tag{2.26}$$

$$a_{crit} = \frac{2 \cdot w \cdot t}{\pi \cdot c}\left(1 - \frac{\sigma_{nom,\max}}{\sigma_u}\right) \tag{2.27}$$

Case 2: Quarter elliptical crack shape with *c* < *w* as shown in Figure 2.17 (left)

The process to calculate the critical crack depth for this case is similar to Case 1, except that the formula for the area of the crack, which should be one half of the area of a semi-elliptical crack (for the case of the quarter-elliptical crack) as shown in Equation (2.28). The calculated critical crack depth is shown in Equation (2.29), which is just double in the magnitude of the critical crack depth calculated for a semi-elliptical crack.

$$A_{qe} = \frac{\pi \cdot c \cdot a}{4} \tag{2.28}$$

$$a_{crit} = \frac{4 \cdot w \cdot t}{\pi \cdot c}\left(1 - \frac{\sigma_{nom,\max}}{\sigma_u}\right) \tag{2.29}$$

Case 3: Semi-elliptical crack with 2*c* > *w* as shown in Figure 2.16 (right)

The area of the semi-elliptical crack with 2c > *w* is calculated from Equation (2.30). The net area (A_{net}) is calculated by subtracting the area of crack from the total cross-sectional area (A) according to equation (2.31). Then, the net stress is calculated by dividing the maximum load by the net cross-sectional area as shown in equation (2.32). For failure, the net stress should be equal to or greater than the ultimate strength of the material, σ_u, which is described in Equation (2.33). After rearranging Equation (2.33) and equating a with a_{crit}, the critical crack depth (a_{crit}) is calculated as shown in Equation (2.34).

$$A_{se} = \int_{-\frac{w}{2}}^{\frac{w}{2}} a\sqrt{1-\frac{y^2}{c^2}}dy \;=\; a\cdot c\left\{\sin^{-1}\left(\frac{w}{2c}\right)+\frac{w}{4c^2}\sqrt{4c^2-w^2}\right\} \tag{2.30}$$

$$A_{net} = A - A_{se} = w\cdot t - a\cdot c\left\{\sin^{-1}\left(\frac{w}{2c}\right)+\frac{w}{4c^2}\sqrt{4c^2-w^2}\right\} \tag{2.31}$$

$$\sigma_{net} = \frac{P_{\max}}{A_{net}} = \frac{\sigma_{nom,\max}\cdot w\cdot t}{w\cdot t - a\cdot c\left\{\sin^{-1}\left(\frac{w}{2c}\right)+\frac{w}{4c^2}\sqrt{4c^2-w^2}\right\}} \tag{2.32}$$

$$\sigma_u = \frac{\sigma_{nom,\max}\cdot w\cdot t}{w\cdot t - a\cdot c\left\{\sin^{-1}\left(\frac{w}{2c}\right)+\frac{w}{4c^2}\sqrt{4c^2-w^2}\right\}} \tag{2.33}$$

$$a_{crit} = \frac{\left(\frac{w\cdot t}{c}\right)\left(1-\frac{\sigma_{nom,\max}}{\sigma_u}\right)}{\left\{\sin^{-1}\left(\frac{w}{2c}\right)+\frac{w}{4c^2}\sqrt{4c^2-w^2}\right\}} \tag{2.34}$$

Case 4: Quarter elliptical crack with *c* > *w* as shown in Figure 2.17 (right)

The process to calculate critical crack depth for this case is similar to Case 3, except that the formula used for the area of the crack, which should be for the area of quarter-elliptical crack front rather than the area of the semi-elliptical crack front as described in Equation (2.35). The expression for critical crack depth is presented in Equation (2.36).

$$A_{qe} = \int_{0}^{w} a\sqrt{1-\frac{y^2}{c^2}}dy \;=\; \frac{a\cdot c}{2}\left\{\sin^{-1}\left(\frac{w}{c}\right)+\frac{w}{c^2}\sqrt{c^2-w^2}\right\} \tag{2.35}$$

$$a_{crit} = \frac{\left(\frac{2w\cdot t}{c}\right)\left(1-\frac{\sigma_{nom,\max}}{\sigma_u}\right)}{\left\{\sin^{-1}\left(\frac{w}{c}\right)+\frac{w}{c^2}\sqrt{c^2-w^2}\right\}} \tag{2.36}$$

The critical crack depth calculated based on abovementioned equations was limited to a maximum value of 80 % of the thickness of the component because the weight function method used in the SBFM model is not applicable when $a > 0.8\cdot t$. At each crack depth during crack

propagation stages, the critical crack depth is calculated based on failure at the net section. If the calculated critical crack depth exceeds $0.8 \cdot t$, then failure is assumed to be immanent or to have occurred from a practical standpoint. The abovementioned equations to calculated critical crack depth will not work for a very wide component ($w \sim \infty$), which means the criteria with net stress exceeding ultimate strength may not be applicable. In that case, the use of fracture toughness in failure criteria may be a better choice. However, it is assumed herein that the effect of the failure criterion choice will be relatively minor for the studied component geometry.

This completes the description of the SBFM model used for the two-dimensional fracture mechanics analysis of welded joints. In Chapter 3, the one-dimensional version of the described model is applied to study the fatigue behaviour of FSW joints. In Chapter 4, the described 2D model is applied to study the fatigue life improvement in HFMI treated welds. In Chapter 5, the described 2D model is extended to enable probabilistic SBFM analysis.

Chapter 3

Effects of Geometric Misalignment and Welding Defects on the Fatigue Performance of Friction Stir Welded Joints

In this chapter, a study on the effects of geometric misalignment and welding defects on the fatigue performance of FSW butt and lap joints is presented. FSW is a solid-state joining process, which has rapidly gained attention for a wide range of structural applications. Most experimental fatigue studies on FSW have focused on fatigue tests under uniaxial tensile cyclic loading, without considering the presence of a significant geometric misalignment or welding defects. Also, very few studies have been performed to assess the fatigue performance of aluminum FSW joints under bending loads. In the current study, two separate projects were carried out. The purpose of the first project was to study the effect of angular misalignment on the fatigue performance of FSW butt joints under a tension loading and to assess the relative fatigue performance of the top side vs. the bottom side of the weld through fatigue study under bending load. The purpose of the second project was to study the effects of intentionally introduced welding defects on the fatigue performance of FSW joints with dimensions and loading conditions typical for structural applications. For the second project, defects including a wormhole, a lack of penetration (kissing bond), and toe flash were investigated experimentally as well as using the 1D SBFM model.

In the next sections of this chapter, a background of previous research in this subject area is presented, followed by a description of the experimental plan and fatigue test results for the first project (investigation of the angular misalignment effects). An analysis of the weld cross-section and comparison of the fatigue test results with fatigue test data available in the existing literature is then presented. Following this, probabilistic survival probability curves are established using a procedure recommended by the International Institute of Welding (IIW). The test results are then compared with S-N curves derived using a 1D SBFM model. Based on this work, conclusions are drawn and recommended areas for further study are identified. Following this, the experimental program, SBFM analysis, conclusions and recommendations for the second project (investigation of the effects of welding defects) are presented.

3.1 Background

Friction stir welding (FSW) was invented in 1991(Thomas 1991). Since then, this welding technique has seen continuous improvement, resulting in welds with better fatigue performance in comparison with fusion welds. Lomolino et al. (Lomolino, Tovo, and Dos Santos 2005) studied the fatigue behaviour of aluminum FSW butt joints and concluded that a better fatigue performance can be achieved for aluminum welded structures with FSW. Dalle Donne et al. (Dalle Donne et al. 2000) studied the fatigue and fracture performance of 2024-T3 FSW joints and concluded that the fatigue crack propagation behaviour and fracture toughness of 2024-T3 FSW joints is comparable or even superior to that of the base material. Given the better fatigue performance of components joined by FSW, its use for the fabrication of aluminum structures is rapidly increasing. However, there remains a lack of design guidelines and quality control criteria, which hinders the use of FSW components in civil engineering applications.

New improvements to FSW techniques and processes have been occurring continuously, since the invention of this welding technology. The pace of development of design code provisions and quality control criteria for FSW joints has lagged considerably and struggled to keep up with these improvements. Considering the lack of contemporary test data, it is a challenge to develop design provisions and quality control criteria based on the few available fatigue test results obtained from a limited range of specimen sizes and geometries, tested under a restricted set of cyclic loading conditions. Due to the lack of existing design provisions, many design codes and standards assume that the fatigue strength of FSW joints is no better than conventional arc welded joints, which may be a very conservative assumption.

The first edition of American National Standard, “Specification for friction stir welding of aluminum alloys for aerospace applications” (AWS-D17.3/D17.3M:200X 2010) was published in 2010. Subsequently, the rapidly increasing use of FSW created the need for an International Organization for Standardization (ISO) standard, which was published in 2011 and included five parts (ISO 25239 2011). Additionally, (AWS D1.2/D1.2M 2014) has recently introduced an entire section on FSW, wherein inspection acceptance criteria for FSW is broadly discussed. The Canadian code for welded aluminum construction (CAN/CSA W59.2 2018) has also recently added a chapter on FSW wherein inspection acceptance criteria for FSW is discussed. Generally

absent in these welding standards are details concerning fatigue design, specifically for FSW joined components. The common practice is to use the available fusion weld design curves for similar joint geometries (e.g. butt joints) in structural aluminum standards such as Eurocode 9, the Aluminum Design Manual (ADM), and CAN/CSA S157.

Several studies have suggested that the approach of following fusion weld design curves may actually be overly conservative due to the improved properties of FSW joints as compared to fusion joints (Dickerson and Przydatek 2003; Miranda et al. 2015). For example, it has been reported that 5xxx and 6xxx FSW samples that contained "kissing bond" defects up to 0.35 mm, cause no measurable degradation in mechanical performance compared to defect-free welds (Dickerson and Przydatek 2003). In addition, samples with kissing bond defects up to 1 mm in depth could still meet the fatigue requirements of the Eurocode 9 design curve (Svensson, L.-E., Karlsson, L., Larsson, H., Fazzini, M., & Karlsson 2000). Based on a statistical analysis of the test data, the conservativism of the Eurocode and ADM design curves for fusion-welded butt joints is highlighted in a recent study (Miranda et al. 2015), and a FAT62 design curve has been recommended with a slope of $m' = 7.0$ for the design S-N curve for aluminum FSW butt joints.

The fatigue life of FSW specimens can vary significantly depending on the welding process parameters. (Aydin et al. 2010) studied the influence of welding process parameters on the fatigue behaviour of 3003-O aluminum alloy FSW joints. It was observed that the fatigue lives of the FSW joints made with a welding speed of 40 mm/min were about 2 – 3 times longer than those of joints made with welding speeds of 80 mm/min and 112 mm/min, at different rotating speeds and under a fixed stress amplitude and a stress ratio, $R = -1.0$.

Few researchers have studied the effects of geometric and welding defects on the fatigue performance of FSW aluminum joints. Fowler et al. (Fowler, Toumpis, and Galloway 2016) studied the fatigue and bending behaviour of friction stir welded DH36 steel. Fowler et al. observed in his study that the bottom of a weld under direct tension load was subjected to secondary bending stress of compressive nature, because of misalignment, which increased the fatigue life of the tested specimen artificially. This secondary bending stress was measured with the help of strain gauges, and a correction was made to estimate the applied nominal stress range. (Dickerson and Przydatek 2003) studied the fatigue of FSW joints in aluminum alloys containing root flaws. It

was found that flaws are often present at the weld root of FSW joints when unsuitable welding parameters are used during fabrication. The vertical length of the flaws studied in (Dickerson and Przydatek 2003) was 0.31–0.33 mm for the 4 mm thick FSW butt joints. The fatigue lives of the flawed welds were found to be 33–80 times shorter than that of flaw-free welds, and the fatigue strength was found to decrease from 120.6 MPa for flaw-free welds to 54.7 MPa for flawed welds at two million cycles of fatigue life.

Despite this recent progress, a number of gaps in the current state-of-the-knowledge appear to remain unaddressed. In addition to the conservative fatigue performance assumptions made in the structural design codes, the tolerance limits for the various defect types in the welding codes do not appear to have been related to fatigue performance, but seem to have been established based on "best practice" in the industry. A lack of a fatigue test database under variable amplitude loading conditions simulating an in-service loading is also apparent.

Against this background, this study was undertaken with the following objectives:

Angular misalignment project

1) to assess the fatigue performance of the top vs. the bottom side of FSW butt joints; and
2) to assess the effect of angular misalignment on the fatigue performance of FSW butt joints.

Weld defect project

1) to fabricate FSW joint specimens with different weld defect types and degrees of severity by varying the welding process parameters, and to characterize the metallurgical properties of the joints using various destructive and non-destructive evaluation (NDE) methods;
2) to perform fatigue tests and an SBFM analysis of the fabricated FSW specimens under a range of loading conditions, including a constant amplitude (CA) loading and a variable amplitude (VA) loading simulating service conditions typical for vehicular bridge decks; and
3) to relate the weld quality and fatigue performance with the goal of providing recommendations for the future development of "performance-based" quality control (QC) criteria and improved fatigue design provisions for structural aluminum FSW joints.

So far, this research has focused on two common aluminum alloys: 6061-T651 and 5083-H321 and two joint geometries (butt joints and a lap joint detail) in ~10 mm thick plate. It has also focused on a limited subset of geometric and welding defects, including: angular misalignment, kissing bond, toe flash, and wormhole defects.

3.2 Angular misalignment project

In this section, experiment details and fatigue test results are first presented, followed by a statistical analysis and a comparison of the fatigue test results with standard design curves. Following this, fracture mechanics analysis results are presented and compared with the experimental S-N data. Lastly, the results are summarized and conclusions are drawn.

3.2.1 Experiment details

The weld specimens tested for this study were fabricated from 6061-T651 aluminum alloy plates. Two 175 x 420 x 9.5 mm plates were joined by FSW process along the long (420 mm) edge. The welded plates were subsequently cut into strips perpendicular to the welding direction to fabricate the specimens (see Figure 3.1) for fatigue test. Specimens with 30 mm and 12.75 mm width (w) were cut along the 175 mm long edge and the specimen length was then reduced from 175 mm to 163 mm, so that the specimen size is compatible with the four-point bending test frame available at Waterloo. The relation between the applied load and bending stress for the four-point bending test frame is provided in Appendix A.

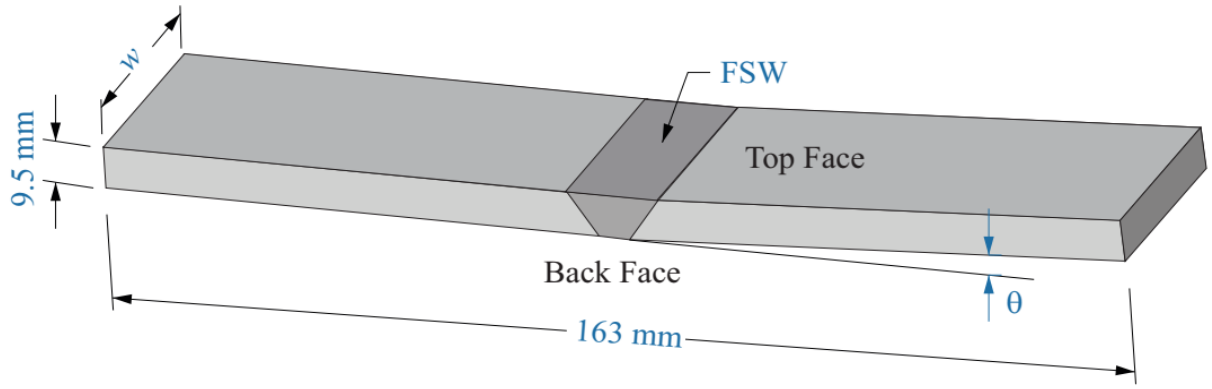

Figure 3.1: Specimen geometry

The employed FSW process parameters for fabrication of specimens are provided in Table 3.1. The plate used for the specimen fabrication conformed to (ASTM B209M 2014). The equipment used for the specimen fabrication was a Jafo FWR40J milling machine with displacement control via digital readout accurate to within 0.005 mm.

Table 3.1: Friction stir welding process parameters

Variable type	**Variable**	**Values**
Tool design variables	Shoulder and pin material	H13 Tool steel
	Shoulder diameter	15 mm
	Pin diameter	5 mm with 10° conical shape
	Pin length	~ 9.3 mm
	Thread pitch	M6 thread
	Feature geometry	Three flats 10° conical M6 threaded
Machine variables	Welding speed (traverse)	63 mm / minute
	Spindle speed (rotational)	1120 rpm
	Plunge depth	~ 9.3 mm
	Tool tilt angle	2.5°
Other variables	Anvil material	Hardened steel
	Anvil size	380 x 420 mm
	Work piece size	175 x 420 x 9.5 mm

The plan for the experimental testing is summarized in Table 3.2 and included tests on 37 specimens in total. In Table 3.2, specimen orientation, “Top” means that under bending load, the specimen is placed in the four-point bending test frame in such an orientation that tension is imposed on the top side of the weld, and specimen orientation “Bottom” means that under bending load, tension is imposed on the bottom or root side of the weld. Testing of specimens with width, w = 30 mm was performed at the University of Brasília. Specimens with a narrower width, w = 12.57 mm were tested on a four-point bending test apparatus (see Figure 3.2) at the University of

Waterloo. The fatigue testing at Waterloo was performed under load control at a testing frequency of 3 Hz or under displacement control at a test frequency of 30 Hz. The testing at Brasilia was performed under load control at a test frequency of 40 Hz.

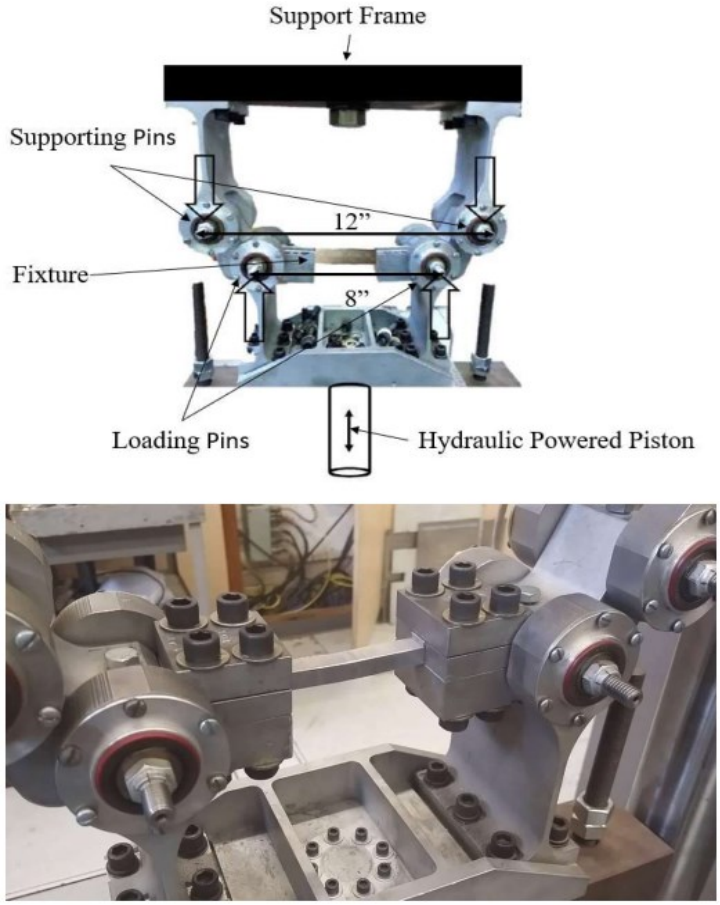

Figure 3.2: Four-point bending test apparatus at Waterloo (Top) and close view of the fixture (Bottom)

Table 3.2: Test matrix for fatigue test under bending and tension load

Loading Type	**Specimen Orientation**	**Number of Specimen**	**Specimen Width, *w* (mm)**	**Test Location**
Bending	Top	5	12.57	Waterloo
Bending	Top	9	30.00	Brasilia
Bending	Bottom	14	12.57	Waterloo
Bending	Bottom	2	30.00	Brasilia
Tension	-	7	30.00	Waterloo

After the fabrication process, the specimens were observed to have an angular misalignment defect with an angle θ (see Figure 3.3) of approximately 0.5° for all the specimens as measured with a protractor. Fatigue tests under a tension load were performed first followed by fatigue tests under a bending load. The misalignment was such that, when the specimen was gripped in the axial load testing frame with no external load in the axial direction, the grip-pressure produced tensile stress on the "top" surface and compressive stress on the "bottom" surface of the weld as shown in Figure 3.3. It was observed that crack always initiated from the weld root during fatigue test under uni-axial tension load even if there was presence of compressive stress at the weld root. Therefore, the effective stress under which the crack was propagating at the bottom of the weld was less than the stress due to the applied axial load on its own. In order to confirm the effect of the angular misalignment, strain gauges were placed on three out of the seven specimens tested under a uniaxial tension loading, and the strains were measured during the clamping operation in the axial load testing frame at Brasilia. After gripping, stress magnitudes of -35, -55, and -25 MPa were obtained, based on strain measurements on the compression face (weld root) with an average of -38.3 MPa.

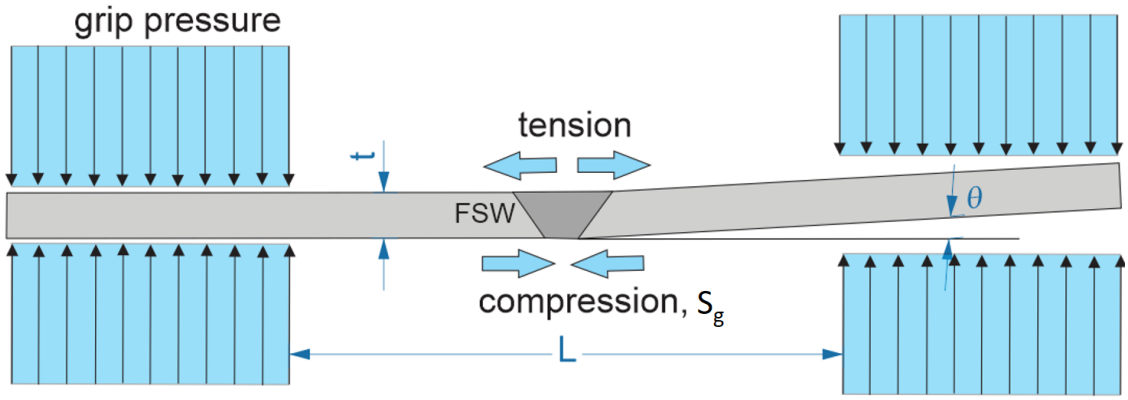

Figure 3.3: Nature of stress after gripping the misaligned specimen in an axial tension test frame

The IIW(Hobbacher 2009) provides a factor to compute the magnitude of secondary stress because of angular misalignment. However, it is also possible to estimate the misalignment stress level (S_g) using the following simple equation:

$$S_g = -\frac{\theta E t}{2L} \tag{3.1}$$

where θ is the angle representing the extent of misalignment, E is the elastic modulus, t is the thickness, and L is the length of the specimen in between the two gripped ends, as shown in Figure 3.3. The equation (3.1) can be derived by considering the specimen as a cantilever beam with span L and fixed support near the left grip (with the specimen oriented horizontally, as it is in Figure 3.3), and the beam is subjected to a constant moment at the free end (right grip in Figure 3.3). It can be noted that the initial secondary stress because of misalignment as calculated from Equation (3.1) can have an effect on many of the fatigue test results already published in the existing literature, where, even a minor misalignment may have been present in the tested specimens.

3.2.2 Fatigue test results

After the fatigue tests under tension loading, it was observed from the fracture surface that the crack initiated from the weld root (WR), despite the presence of a compressive secondary stress at the WR. The likely reason behind this cracking from the bottom of the weld is thought to be the presence of a more severe initial defect at the bottom side of the weld as compared to defect size at the top side of the weld. When an FSW joint with the angular misalignment discussed here fails from the bottom surface having a secondary compressive stress, when fatigue tested under a uniaxial tension load, then the observed number of cycles will provide non-conservative estimates for the fatigue life of a properly aligned specimen. The observed number of cycles will correspond to a lower effective nominal mean stress because of the compressive secondary stress generated as a consequence of misalignment. If the same number of cycles is assumed for the applied stress range ignoring the presence of misalignment, then this would result in a non-conservative fatigue life estimate for a properly aligned specimen. A measured misalignment of approximately 0.5° generates stress of about -38.3 MPa at the bottom of the weld, which can have a significant effect on fatigue life.

The experimental fatigue test results performed under CA loading with a load ratio, R = 0.1 are shown in Figure 3.4. Raw fatigue test data is available in Appendix B. Fatigue tests were stopped if the specimen did not fail after 10^7 cycles of load and the corresponding S-N test data point was marked as a “run-out”, which is shown in the figure with a marker and an arrow. The experimental S-N dataset was superimposed on a cloud created using S-N data available in the

existing literature for FSW specimens tested under a uniaxial tension loading with a load ratio of 0.1 for different aluminum alloys and plate thicknesses (Cavaliere et al. 2006, 2009; Cavaliere, Squillace, and Panella 2008; Das, Chakraborty, and Kumar Pal 2014; Ericsson, Jin, and Sandström 2007; Grujicic et al. 2011; HAGISAWA and OKURA 2009; Kainuma et al. 2008; Kobayashi et al. 2007; Mahdavi Shahri, Höglund, and Sandström 2012; Moreira, de Figueiredo, and de Castro 2007; Okura et al. 2005; Uzun et al. 2005; Vidal, Infante, and Vilaça 2014; Vigh and Okura 2013; Zhou, Yang, and Luan 2005, 2006b, 2006a). In Figure 3.4, the bending test results are located near the top region of the cloud and the tension test results are located closer to the bottom region of the cloud. This result is what would typically be expected when comparing a set of otherwise identical direct tension and bending test results, since there is a larger volume of material experiencing the highest stress level in the direct tension test and – as the crack propagates – a more severe stress intensity factor associated with a uniform stress field in comparison with a stress field due to bending.

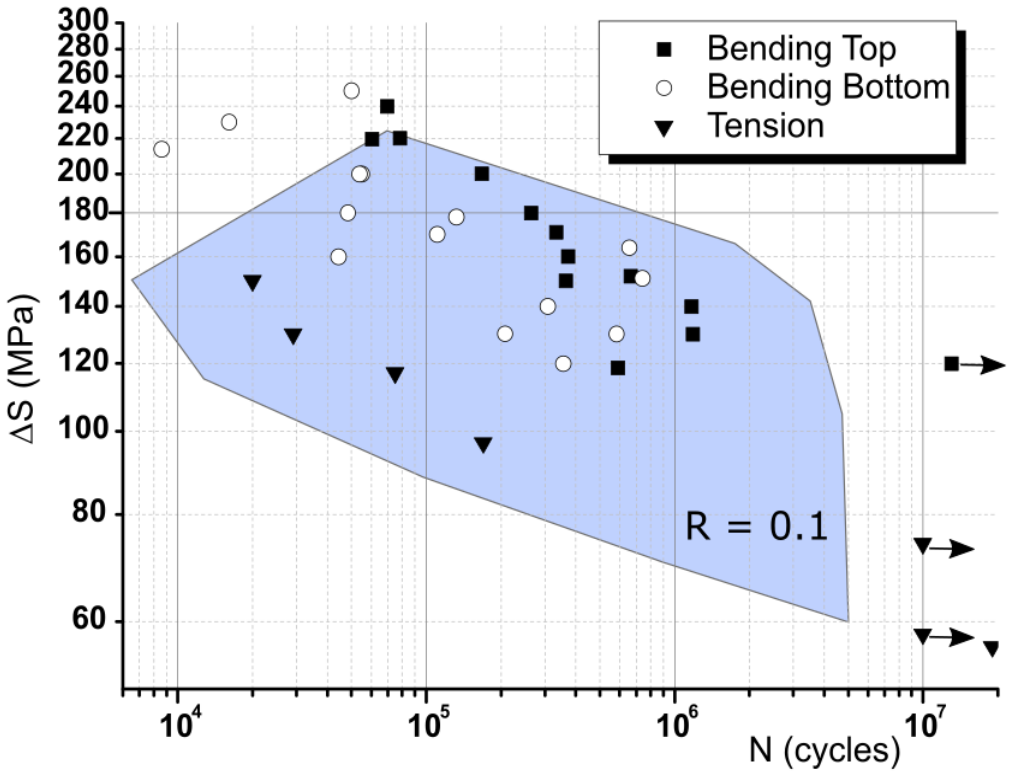

Figure 3.4: Fatigue test results under bending and tension load

In Figure 3.4, the plotted stress range for the tension tests is the stress range with the correction for the angular misalignment, based on Equation (3.1), where the misalignment stress and applied cyclic stress were summed (i.e. the compressive misalignment stress was subtracted from the applied stress near the weld root). There was no effect of angular misalignment on the fatigue life of specimens tested under bending load, because, after placing the specimen in four-point bending test frame, the load was made zero at the beginning of the test, which removed the bending stress because of misalignment. It can be observed in Figure 3.4 that the circular markers are to the left of the rectangular markers at the same stress level, which indicates that the specimens tested in bending with tension on the root side of the weld have a lower fatigue life than the specimens subjected to tension at top side of the weld, which shows that the weld root (WR) is more critical from a fatigue perspective than the weld top. This is thought to be because there is a more severe defect at the WR rather than on the top side of the weld in these tested specimens. The material at the top side of the weld is relatively homogenous, because of the high degree of material stirring at the top. On the other hand, incomplete joint penetration or "kissing bond" defects are known to be commonly present at the WR. It can also be observed in Figure 3.4 that the scatter in the test data is greater for the "Bending Bottom" case than for the "Bending Top" case, which indicates more uncertainty at the WR, possibly because of a variation in defect geometry. It can also be observed that the triangular markers are below the circular and rectangular markers, which indicates that fatigue strength under cyclic tension load is less than under cyclic bending load.

After the fatigue test under bending load, the specimens were cut into two pieces to observe the weld cross-section under a microscope. Figure 3.5 shows the cross-sections of FSW specimens tested in two different orientations. For the specimens tested in bending with tension at the bottom of the weld, the crack initiated at the joint line (see Figure 3.5 (left)). The joint line in the weld region is shown with a dashed line and weld stir zone edge is shown with a dotted line. For the specimens tested in bending with tension at the top of the weld, the specimens failed at the interface of the stir zone and the parent material on the advancing side (AS) of the weld (Figure 3.5(right)). Near the AS, there is a slight change in thickness, resulting in a small stress concentration (toe flash), which is usually the crack initiation site for "Bending Top" test configuration. It can be

noted from Figure 3.5 that during bending tests, the specimens did not break into two pieces. For the bending tests, failure was assumed to happen when the visually observed final crack depth reached around 35% - 45% of the thickness of the specimen. Under tension loading, failure was assumed when the specimen fractured into two pieces or the final crack depth reached more than half of the specimen thickness. Given the high crack growth rates at these crack depths, it is not expected that these distinctions in final crack depths influenced the reported fatigue life by more than a few cycles.

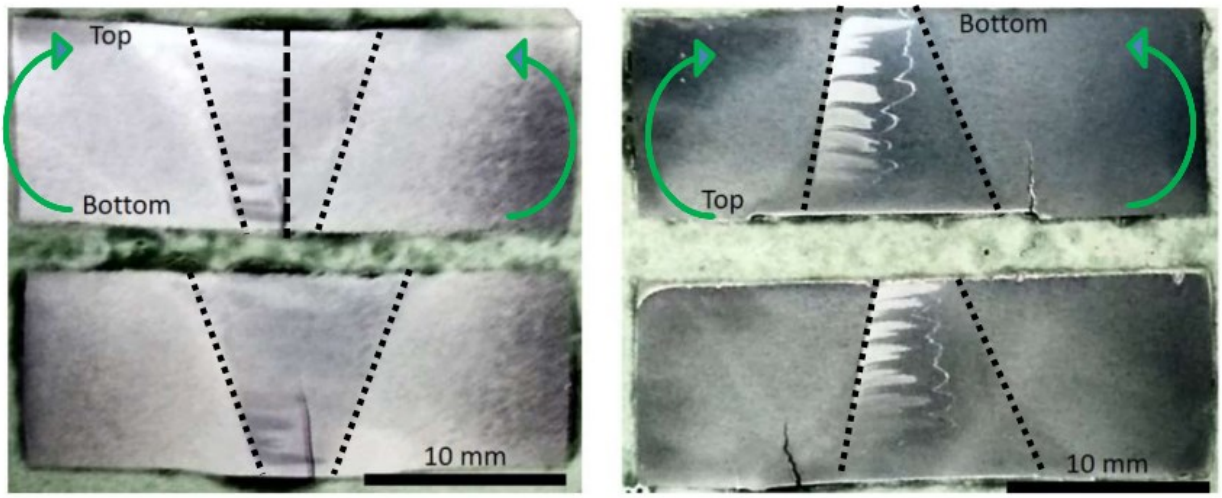

Figure 3.5: Cross-section of welds after bending tests for specimens tested in "Bending Bottom" test configuration (left) and in "Bending Top" test configuration (right)

3.2.3 Statistical analysis and comparison with standard design curves

In order to better understand the fatigue performance of the tested FSW specimens, a statistical analysis was performed, following a procedure recommended by the International Institute of Welding (Hobbacher 2009). As per this approach, the fatigue life, N, is treated as the dependent variable, which varies depending on the nominal stress range, ΔS. The S-N curve is defined as follows:

$$\log(N) = \log(C') - m' \cdot \log(\Delta S) \tag{3.2}$$

where C' and m' are constants which determine the vertical position and slope of the S-N curve respectively.

Table 3.3: S-N curve parameters based on IIW statistical analysis (units: MPa)

Test configuration \ Parameter	*m'*	$\log(C')_{\mu}$	Std. Dev. of $\log(C')$	$\log(C')_{d}$
Tension	7.46	20.3655	0.2970	19.4745
Bending Top	5.70	18.2532	0.2983	17.3583
Bending Bottom	5.83	18.0891	0.4113	16.8552

Given the test results and the number of data points, slope of the S-N curve, *m'*, is established, along with the intercept, $\log(C')$, for a given survival probability which is provided in Table 3.3. In this table, the terms μ (mean curve) and *d* (design curve) correspond to 50% and 95% survival probability with a 75 % confidence level on the mean respectively, which is in accordance with the IIW recommendation (Hobbacher 2009). Figure 3.6 shows the mean and design S-N curve for the "Bending Top" and "Bending Bottom" test configurations.

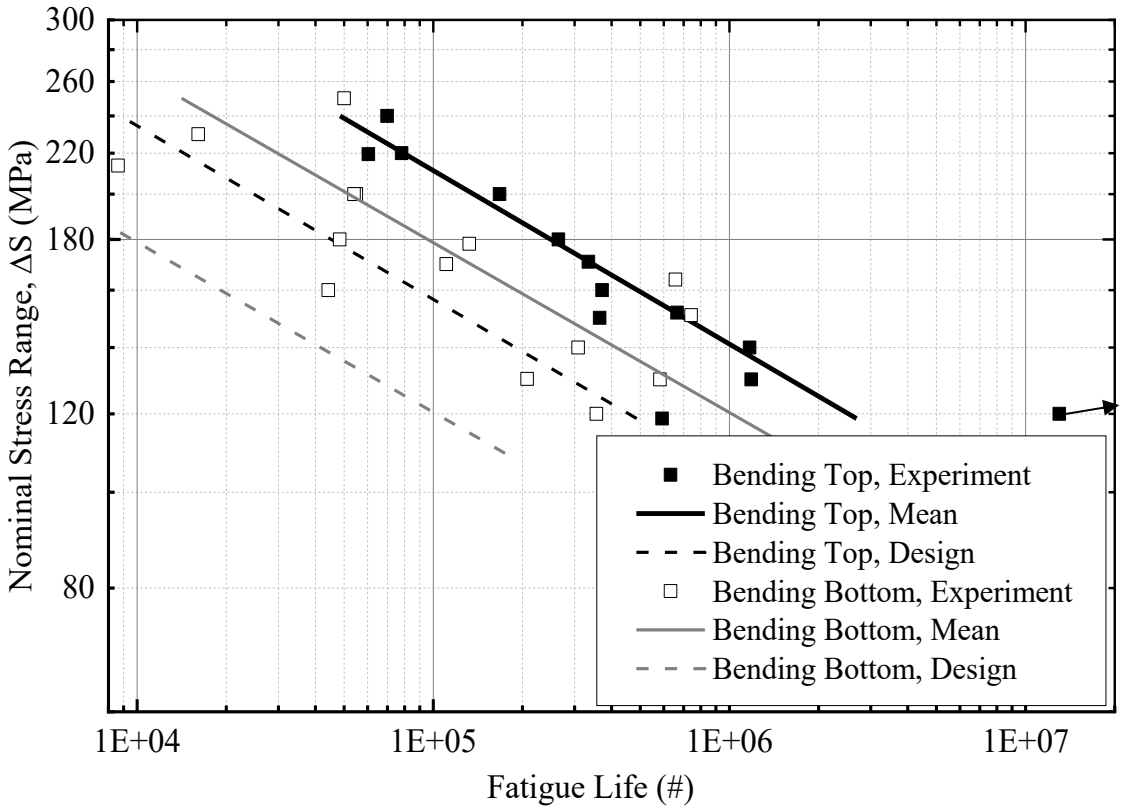

Figure 3.6: IIW Probabilistic S-N curves for specimens tested under bending load

Figure 3.7 shows the mean and design S-N curves for specimens tested under axial tension loading. It can be observed from Figure 3.6 and Figure 3.7 that there is a bigger gap between the mean and design S-N curves for the "Bending-Bottom" case as compared to "Bending-Top" and "Tension" cases, which indicates more scatter in the experimental test results for the Bending-Bottom case.

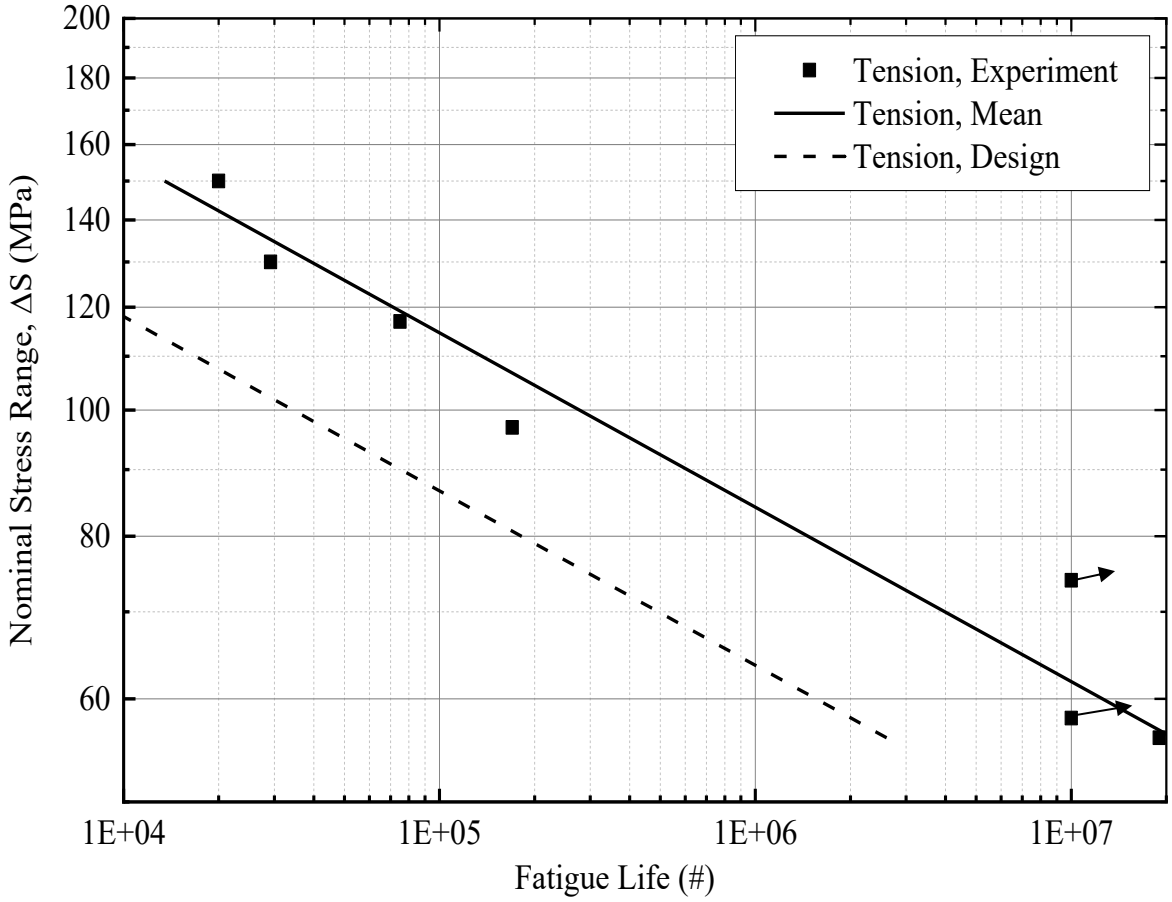

Figure 3.7: IIW Probabilistic S-N curves for specimen tested under tension load

Figure 3.8 shows a comparison of the obtained design S-N curves with the standard Eurocode design curves applicable for conventional arc welded aluminum butt joints under a tension loading. It can be observed from this figure that the fatigue strength of the FSW joints under a tension loading is very close to that of a double-sided, full penetration conventional arc welded joint. The design curve for tested specimens has a flatter slope than the ones for the single-

sided arc welded joints, with a much higher fatigue strength at longer fatigue lives. The statistically-derived S-N curves based on the bending test data are on or above all of the Eurocode curves for $N > 5 \cdot 10^3$ cycles.

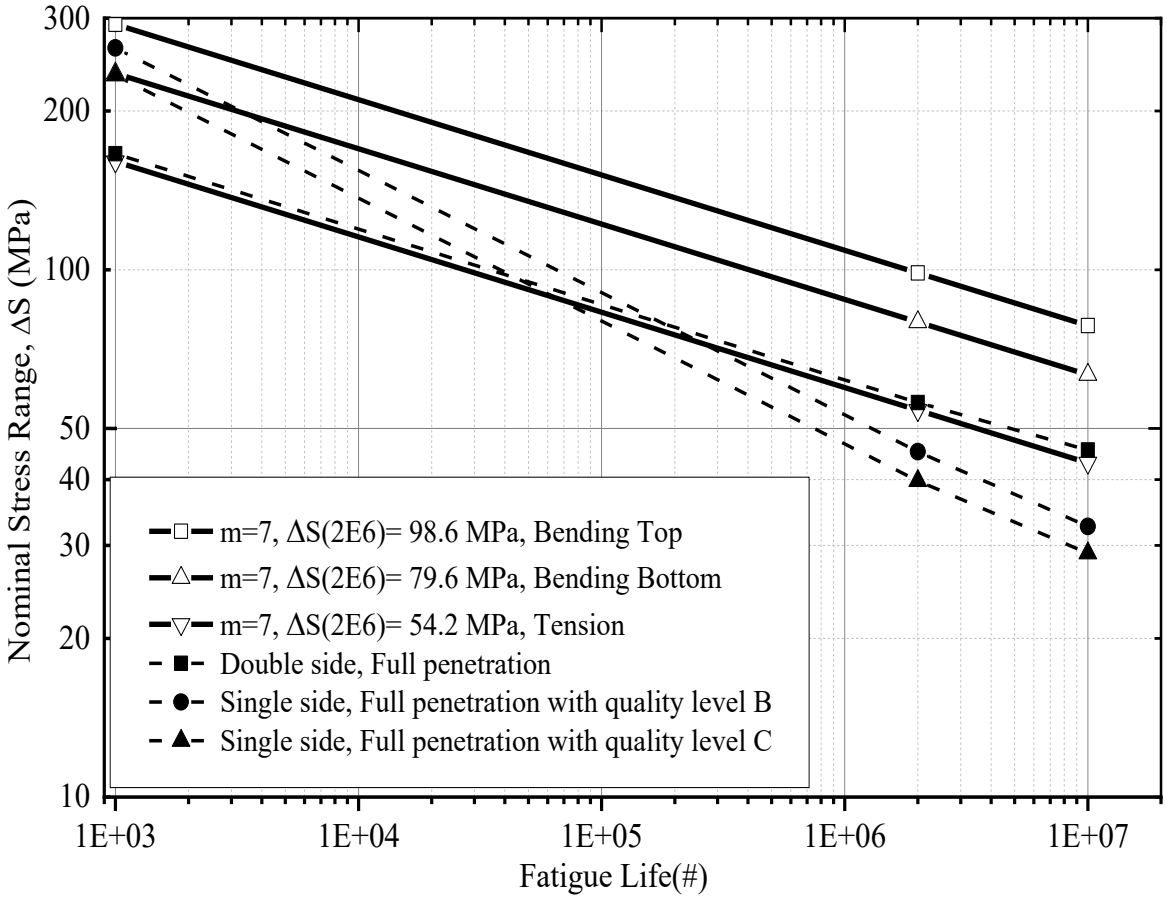

Figure 3.8: Design stress-life curves from EN 1999-1-3 and from analysis of fatigue test data

Figure 3.9 shows a comparison of the obtained stress-life curves for tested specimens with standard IIW curves applicable to conventional arc welded aluminum joints under tension loading. It can be observed that the fatigue strength of the FSW joints is above the FAT 45 curve in the high cycle fatigue (HCF) regime (> 10^6 cycles). It can be noted that the slope, *m'*, of the IIW FAT curves is 3.0, while the slopes of S-N curves for the tested FSW joints are around 7.0 (5.83-7.46), which is also mentioned in Table 3.3.

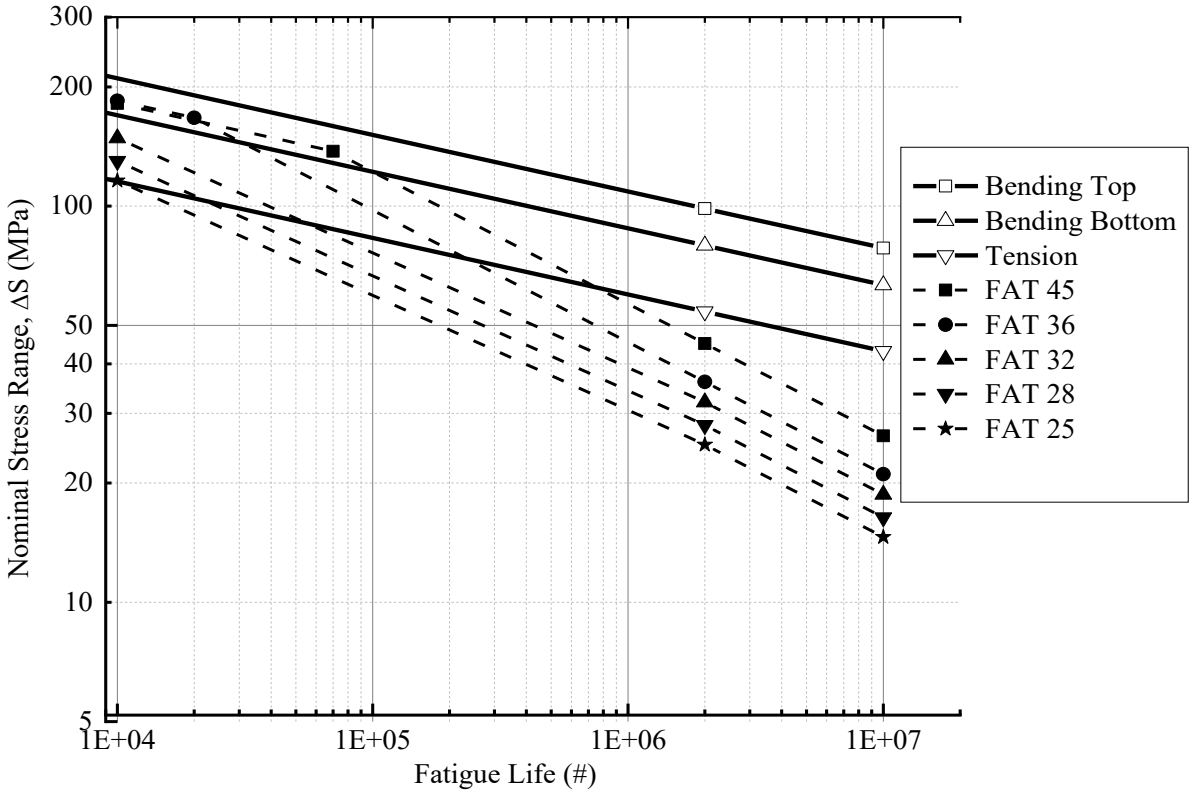

Figure 3.9: Design stress-life curves from IIW and from analysis of fatigue test data

It must be acknowledged here that due to the very small size of the specimens, care should be taken in drawing conclusions from these comparisons with the design curves (available in the various standards). While it would be concerning to see the test data falling below these curves, small specimens tend to benefit from "scale effects" such as those due to the reduced probability of large defects being present, as a result of their size. Thus, it would not be advisable to use this fatigue test data to adjust the design curves without careful further experimental study using larger specimens.

3.2.4 Fracture mechanics analysis

For the fracture mechanics analysis of FSW joints, a 1D version of SBFM model was used, where a constant crack aspect ratio (*a/c*) was assumed at all crack depths, as a simplification. It was observed from the fracture surfaces of the fatigue tested FSW joints that failures from cracks initiating at the weld root always resulted in through-width cracks, which could be easily simulated

with a 1D SBFM model. The 1D SBFM model was therefore sufficient to estimate the fatigue test results for small-scale FSW joints where mostly through-width cracks were observed. In this subsection, the input parameters used for a 1D SBFM analysis and the corresponding analysis results are described. Table 3.4 provides values for the input parameters used for the SBFM analysis. Several assumptions have been made while deciding on the input parameters for the fracture mechanics analysis, which are explained or justified here. It should be noted that E, σ_y, σ_u, K', and n' were estimated based on hardness measurements reported in prior work (Guo et al. 2019), and interpolating between the measured properties for 6061 alloy T651 and O tempers from (Coughlin and Walbridge 2012). The initial crack depths assumed in the analysis were: 0.05 mm for the "Bending Top" case and 0.1 mm for the "Bending Bottom" and "Tension" cases. The assumed initial crack depth is the same for the "Bending Bottom" and "Tension" cases because for these two cases, the crack initiated at the weld root. This assumption was based on the belief that the incomplete joint penetration (kissing bond) defects at the weld root will typically be bigger than the defects at the top side of the weld (Guo et al. 2019). During crack propagation, a constant crack aspect ratio of 0.1 was assumed for the "Bending Bottom" and "Tension" cases, representing an essentially linear defect or "through-width crack", while an aspect ratio of 0.55 was assumed for the "Bending Top" case, based on crack shape measurements reported in (Guo 2018).

To estimate the Paris-Erdogan crack growth law constants, C and m, crack growth rate tests were performed on four compact tension (CT) specimens as per (ASTM E647 2016). The CT specimens were prepared from the same FSW plate (including weld) from which the specimens were fabricated for fatigue testing. During the preparation of CT specimens, polishing was done, which caused removal of the top ~1 mm layer of material from both sides. This polishing might have reduced the effect of residual stresses introduced during the FSW process. The test on CT specimens was performed at a high load ratio, $R = 0.8$, to avoid crack closure effects. The measured crack growth rate data and fitted Paris law is shown in Figure 3.10. The constant m was assumed to be 4 and the value of the constant LN(C) was estimated to be -30.6 (units of MPa and mm) by manually (by varying the value of LN(C) till a good fit is observed visually) fitting the data on a Log-Log plot. The value of the threshold stress intensity factor range, ΔK_{th} was assumed to be 45 MPa$\sqrt{}$mm.

Table 3.4: Input parameters used for the SBFM analysis

	Variable	Value	Source
1	Specimen thickness, t	9.5 mm	Measured
2	Elastic modulus, E	70.5 GPa	(Coughlin and Walbridge 2012)
3	Yield strength, σ_y	134.1 MPa	(Guo et al. 2019)
4	Ultimate strength, σ_u	181.5 MPa	(Guo et al. 2019)
5	Paris constant, $LN(C)$	-30.6	Figure 3.10
6	Threshold stress intensity factor range, ΔK_{th}	45 MPa√mm	Assumed
7	Ramberg-Osgood cyclic material model parameter, K'	304.5 MPa	(Guo et al. 2019)
8	Ramberg-Osgood cyclic material model parameter, n'	0.13	(Guo et al. 2019)
9	Initial crack depth, a_i, and crack initiation location	0.1 mm at the weld root for Bending Bottom & Tension case, 0.05 mm at the weld top for Bending Top case	Initial crack depth: assumed, Crack initiation location: observed from the fracture surface
10	Final crack depth, a_f	4.75 mm	Assumed
10	Crack closure parameter (μ_{op})	0.003	(Guo et al. 2019)
11	Paris law constant, m	4.0	Assumed
12	Specimen width, w	30 mm /12.57 mm	Measured
13	Initial crack aspect ratio, $(a/c)_0$	0.55	Assumed
14	Crack aspect ratio at all other depth, (a/c)	0.1 for Bending Bottom & Tension case, 0.55 for Bending Top case	Observed from the fracture surface of the tested specimens

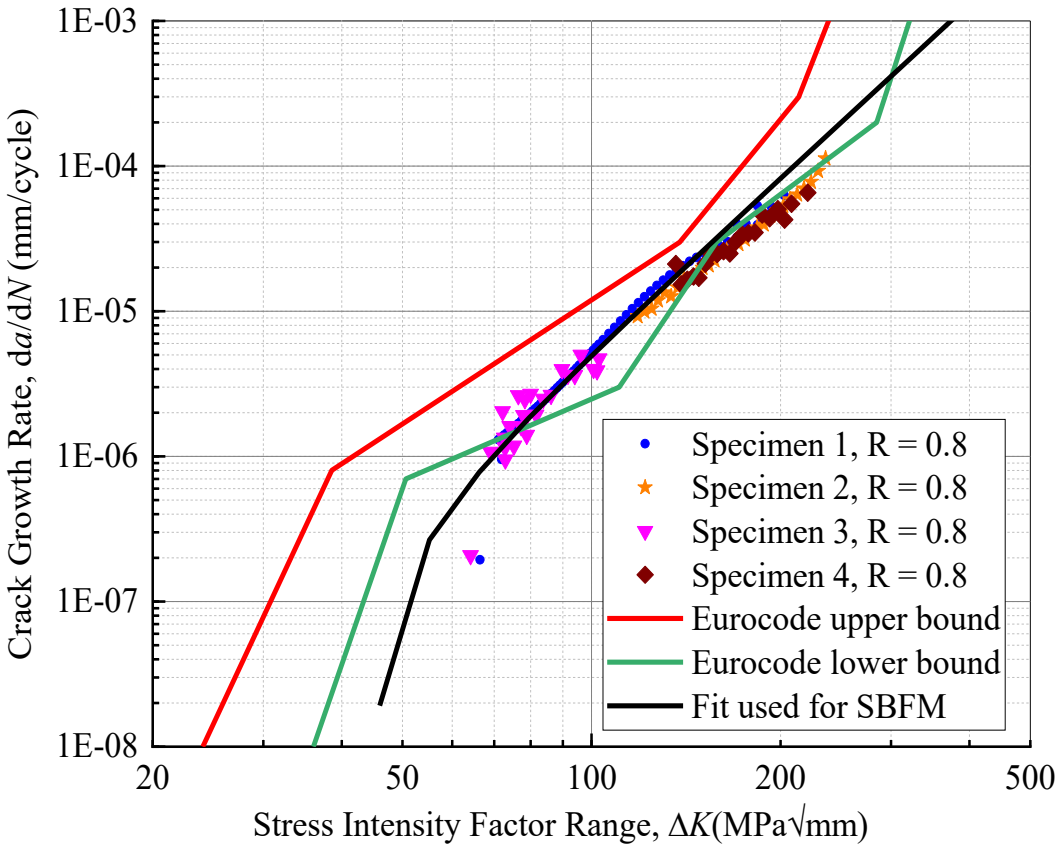

Figure 3.10: Crack growth rate test results and comparison with Eurocode curves

It can be observed in Figure 3.10 that the manually fitted crack growth curve represents a conservative upper bound of the measured test data at higher SIF ranges and best fit at lower stress ranges. For slower crack growth rates ($<10^{-6}$), the fitted curve is below the lower bound of crack growth rate for aluminum alloys available in the Eurocode (Development 2000). Since, there was only one parameter, LN(C), which was varied while fitting the curve and significant number of experimental data was available, the fit was made manually to get the crack growth rate curve which represents upper bound of test data at higher stress ranges and best fit at lower stress ranges (where scatter is high).

There are two variants of the crack growth law, which can be used in fracture mechanics analysis as shown in Equation (3.3) and Equation (3.4). For estimating the constants C and m for

this project, the Equation (3.4) was used. The same equation was used for the SBFM analysis as well.

$$\frac{da}{dN} = C \cdot \max\left[\left(\Delta K_{eff} - \Delta K_{th}\right)^{m}, 0\right] \tag{3.3}$$

$$\frac{da}{dN} = C \cdot \max\left[\left(\Delta K_{eff}^{m} - \Delta K_{th}^{m}\right), 0\right] \tag{3.4}$$

The secondary stress distribution because of misalignment along the crack path was assumed to vary linearly with the magnitude of 38.3 MPa on the top surface of the weld to -38.3 MPa at the bottom surface of the weld for the specimens tested under tension load. The applied stress distribution along the crack path was uniform for the case of "Tension". In the "Bending Top" case, the applied stress is tensile at the top face of the weld and compressive at the bottom face of the weld. For the "Bending Bottom" case, the applied stress is tensile at the weld root and compressive at the weld top. Residual stresses induced by the FSW process have been found to be low in magnitude due to the low welding temperatures (Miranda et al. 2015), and are thus ignored for the present SBFM analysis.

Figure 3.11 shows the results of the performed SBFM analyses for the case of specimens tested under a uniaxial tension load. In Figure 3.11, it can be observed that at two million cycles, the fatigue strength of a specimen without misalignment is 71.04 MPa while the fatigue strength of the specimen with misalignment is 97.91 MPa. Here, the increase in strength from 71.04 MPa to 97.91 MPa occurred because of a beneficial compressive stress at the weld root due to the angular misalignment. It should be clear from Figure 3.11 that if the misalignment effect is ignored then the S-N curve for a properly aligned specimen (dashed S-N curve) underestimates the test results by a considerable margin. If such a model (with alignment effects ignored) were calibrated to the tension loading test results and then used for prediction purposes (e.g. to predict the fatigue life of welds under bending), then this could lead to unconservative predictions. It can be understood from this figure that if test data obtained from specimens with favorable misalignments, such as the ones tested in the current study, are used to establish design curves, then these curves will be unconservative for welds fabricated without misalignment.

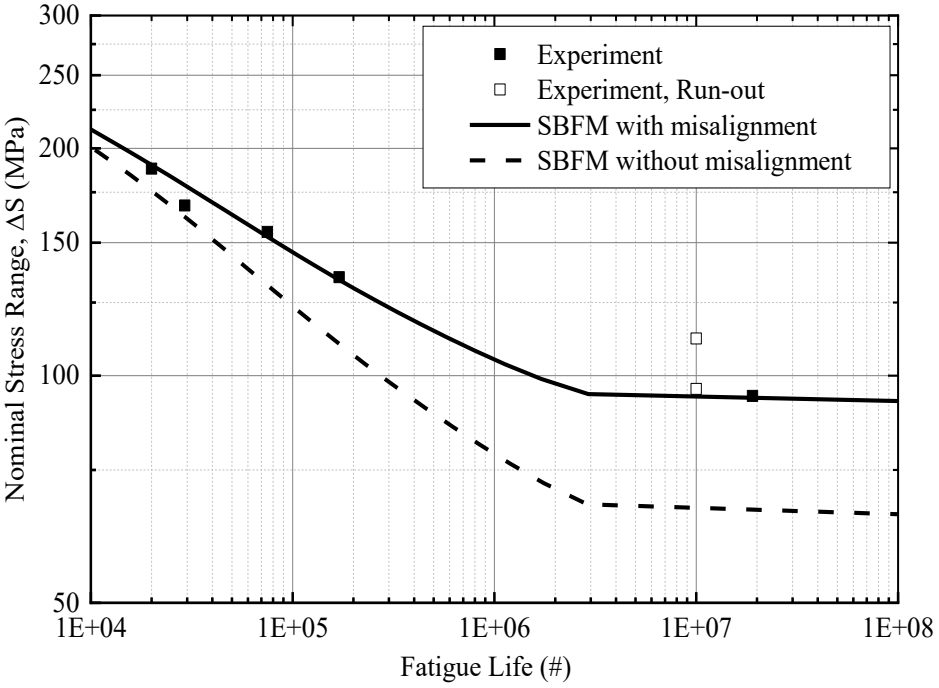

Figure 3.11: Test data and S-N curves for specimens tested under a uni-axial tension load

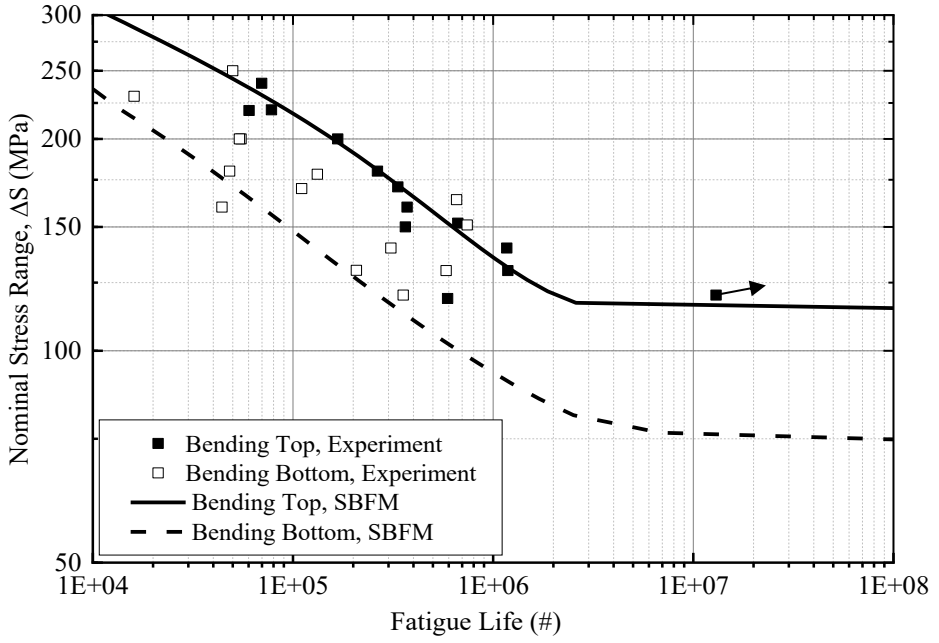

Figure 3.12: Test data and S-N curves for specimens tested under bending load

Figure 3.12 shows S-N curves for the case of bending tests under two specimen orientations. It can be observed that the fatigue performance for the case of tension at the top of the weld (Bending Top) is better than for the case of tension at the weld root (Bending Bottom). Here, the marker with an arrow represents run-out test data. At two million cycles of fatigue life, the fatigue strength for the "Bending Bottom" case is 83.83 MPa while for the "Bending Top" case it is 120.71 MPa.

Looking at Figure 3.11 and Figure 3.12, it can be seen that, with the assumed initial defect geometries on the top and bottom sides of the weld and by considering the presence of secondary stress because of angular misalignment for the tension tests, the experimental test results are estimated reasonably well using the 1D SBFM model. It is believed that these predictions might have been better if the angular misalignment defect was measured more precisely prior to testing for each specimen. However, given the high degree of scatter in the test data – for the "Bending Bottom" tests in particular – it is believed that these results have value in showing that the fatigue performance of FSW joints can be predicted by the SBFM model and that the effect of angular misalignment on the tension tests is significant.

3.2.5 Summary and conclusions for the angular misalignment project

In this project, new fatigue tests under four-point bending and tension load were performed to investigate the fatigue behaviour of FSW aluminum butt joints. The test results were analyzed statistically using an approach recommended by the IIW. Also, the test results were estimated using 1D SBFM with a reasonable accuracy. An angular misalignment defect due to inadequate clamping during the welding process was seen to have a significant effect on the results of the tests conducted under an axial (tensile) loading. The significance of the angular misalignment defect observed in the specimens fabricated for the current study was assessed using a simple equation and strain gauges and was confirmed by the fracture mechanics analysis.

The fatigue strengths of different specimen configurations tested in this study are summarized in Figure 3.13. It can be observed that the favorable misalignment increased the fatigue performance of specimens tested under tension loading from 71.0 MPa to 97.9 MPa. This fatigue performance of misaligned specimens was even better than that of the "Bending Bottom"

case. It was also observed that under a bending load, the fatigue performance of the top side of the weld is better than that of the bottom side of the weld as evident from Figure 3.13.

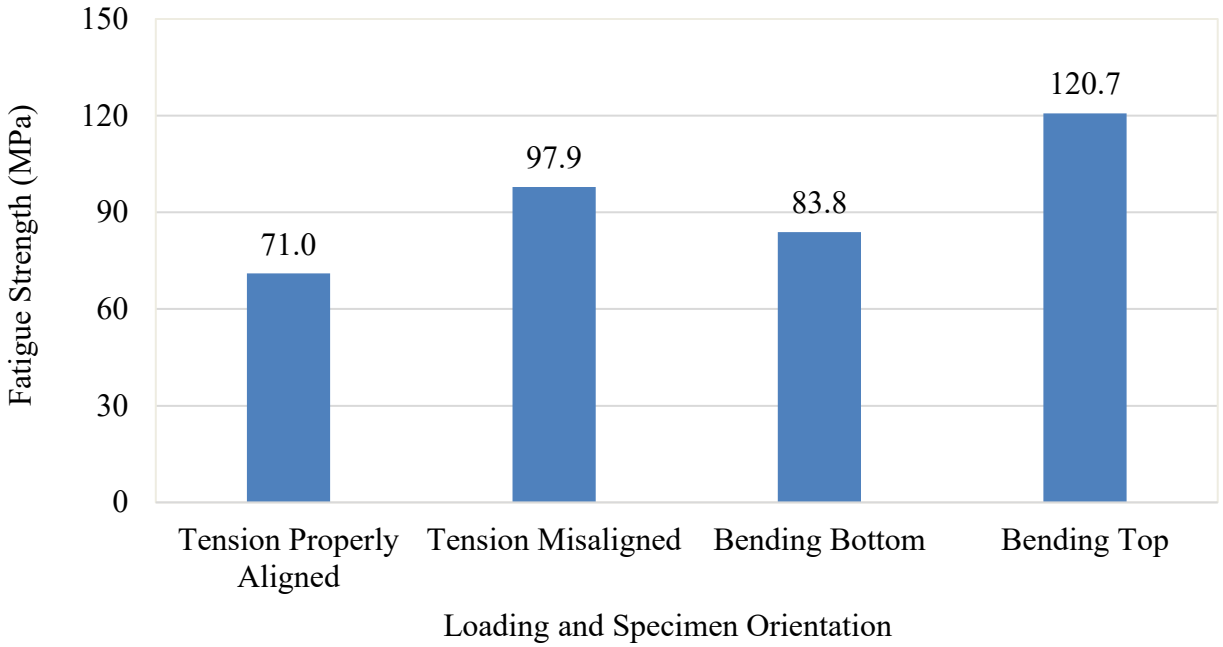

Figure 3.13: Fatigue Strength of different specimen types at two million cycles of fatigue life

Most of the fatigue test results available in the literature do not consider the possibility of an angular misalignment defect. In this project, the influence of such a defect on the fatigue strength of an FSW joint specimen was assessed and it was observed that even a slight angular misalignment of the order of 0.5° can create secondary stresses of ±38 MPa or more. Ignoring these favourable secondary stresses can result in non-conservative estimates of fatigue life for properly welded specimens.

Based on this work, further research is recommended to investigate other kinds of misalignment (e.g. linear misalignment) that can result from the FSW process and relate the extent of misalignment defect with fatigue performance. This work would contribute towards the necessary future development of limits on the severity of these defect types that should be respected in order to ensure a certain fatigue performance for design purposes.

3.3 Weld defect project

In this section, experimental details and fatigue test results for the project investigating the effects of weld defects in FSW joints are presented first. Fracture mechanics analysis results are then presented, along with a summary and conclusions.

3.3.1 Fatigue test description

The specimens tested in this study were fabricated from 6061-T651 and 5083-H321 aluminum alloy plate with nominal thicknesses of 9.5 mm and 9.1 mm, respectively. The variation in nominal plate thickness between the specimens fabricated with these two alloys was the result of local material availability. The alloy compositions were verified based on (ASTM E1097 - 12 2017) and (ASTM E1479 – 99 2011) by an external laboratory (see Table 3.5).

Table 3.5: Compositions of base materials in weight percentage (wt%)

Alloy\Elements	Al	Mn	Mg	Si	Cr	Cu	Zn	Fe
6061-T651	Balance	0.08	0.81	0.53	0.06	0.18	0.01	0.19
5083-H321	Balance	0.79	4.74	0.05	0.06	0.07	0.14	0.21

To fabricate the specimens, pairs of 175 mm by 420 mm plates were prepared and welded along the long edge, which was oriented parallel to the rolling direction of the plate. The welding edges were cleaned before welding to avoid contamination potentially leading to voids and unexpected defects. The plates were held in place using clamps mounted on a backing plate with both vertical and horizontal restraints (see Figure 3.14(A)). Each of the welded plates was then cut into four “dog-bone” shaped fatigue specimens using a CNC machine. The specimens had a 90 mm width in the end regions (see Figure 3.14(B)), a 70 mm minimum width in the narrow region between the ends, and a curved transition with a radius of 85 mm. The tool used for the welding process is shown in Figure 3.14 (C). The employed FSW tool was made from H13 steel, quenched and tempered to 46-48 HRC. The pin geometry was 10° tapered and M6-threaded with three flats. The VA loading history used in the fatigue testing program is shown in Figure 3.14 (D).

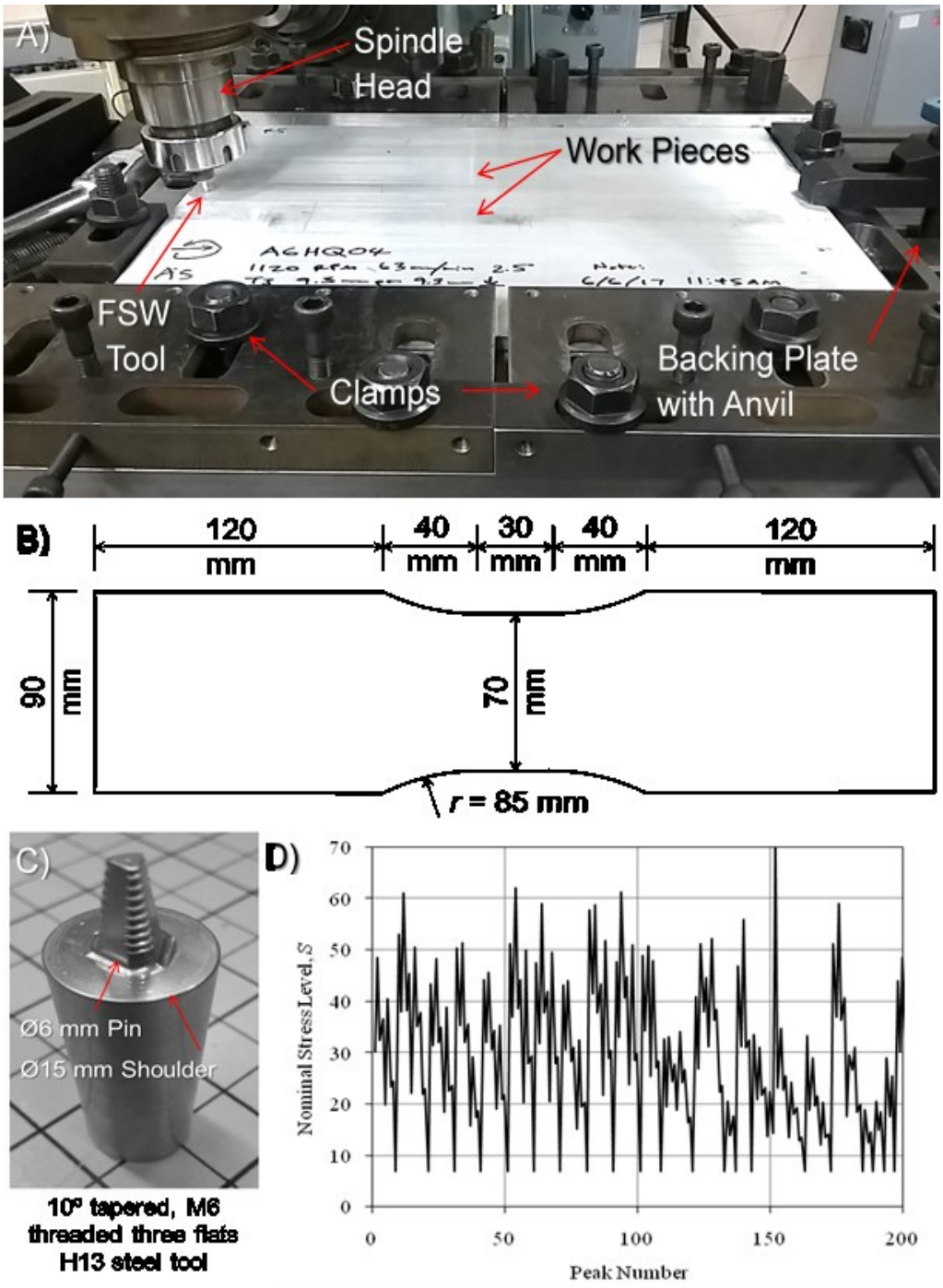

Figure 3.14: Specimen fabrication and loading details: (A) welding process setup, (B) specimen layout, (C) FSW tool, and (D) VA loading history

A typical profile of a properly-welded (PW) butt joint is shown in Figure 3.15 (A). A specimen with significant toe flash (TF) can be seen in Figure 3.15 (B), which was intentionally created in the butt joint through excessive penetration of a slightly shorter welding tool. In addition to the butt joint specimens, a special lap joint (LJ) detail shown in Figure 3.15(C) was also investigated, which was designed to simulate a lap joint between extrusions in a multi-extrusion vehicular bridge deck panel (for example). The lap joint is a convenient way to provide built-in backing material for a one-sided weld. On the other hand, it results in a crack-like gap, which runs parallel to the loading direction as shown in Figure 3.15(D). One of the objectives of testing this detail was to assess the fatigue performance of this complex joint type. The lap joint specimens were fabricated by milling 19.05 mm (3/4") 6061-T651 aluminum plates to half of their thickness at one end with a filleted transition in the weld region.

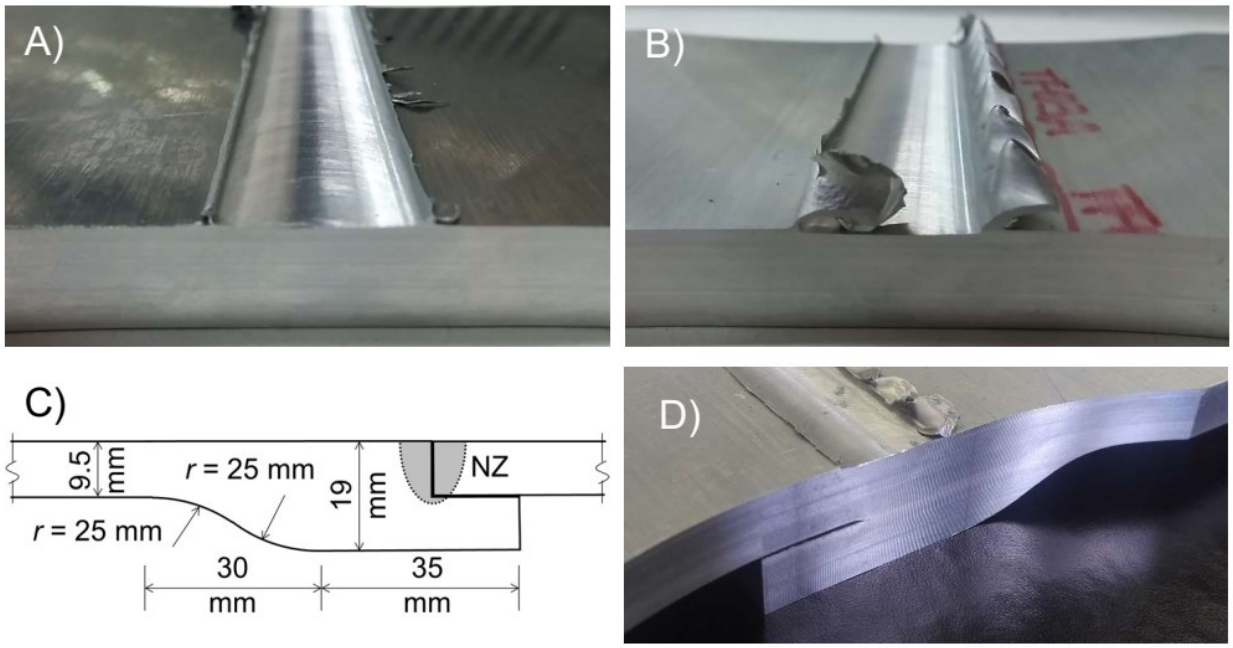

Figure 3.15: Specimen profiles: (A) 6061 proper weld profile, (B) 6061 toe flash weld profile, (C) lap joint detail, and (D) lap joint weld profile

In total, seven types of specimen were fabricated: 1) A6PW: "properly-welded" 6061 aluminum butt joints, 2) A6PO: "polished" 6061 aluminum butt joints, 3) A6KB: 6061 aluminum butt joints with a kissing bond defect, 4) A6TF: 6061 aluminum butt joints with a toe flash defect,

5) A6LJ: 6061 aluminum lap joints, 6) A5PW: "properly-welded" 5083 aluminum butt joints and 7) A5WH: 5083 aluminum butt joints with a wormhole defect. Polished specimens are properly welded specimens, which were polished at the weld toe to remove any stress concentration because of a possible toe flash. The idea of testing intentionally introduced defects in this manner is similar to the one employed in (Kadlec, Růžek, and Nováková 2015) to study the effects of kissing bond defects on the fatigue behaviour of 7475 alloy FSW specimens, and conceptually similar to the approach used by (Tehrani Yekta, Ghahremani, and Walbridge 2013) to study under- and over-treatment in HFMI treated welds.

Welding process parameters used during the fabrication of all specimen types are summarized in Table 3.6. For the 6061 aluminum butt joints, the tool plunge depth was set at 9.3 mm for the 9.5 mm thick aluminum plates. Similarly, for the 5083 aluminum butt joints, the plunge depth was set at 8.9 mm for the 9.1 mm thick aluminum plates. For the specimens with kissing bond and toe flash defects, the pin length was reduced to 8.4 mm and 8.5 mm respectively. The plunge depth was then varied as needed to create each defect type. A plunge depth of 10.7 mm was used for the lap joint detail in order to ensure that the weld penetrated through the entire 9.5 mm plate thickness to create a horizontal initial crack-like defect.

Table 3.6: Welding process parameters used for the fabrication of specimens

Specimen type	**Aluminum alloy**	**Plate thickness**	**Tool pin length (mm)**	**Tilt angle (°)**	**Rotation speed (rpm)**	**Travel speed (mm/min)**	**Plunge depth (mm)**
A6PW	6061	9.5	9.3	2.5	1120	63	9.3
A6PO			9.3				9.3
A6KB			8.4				8.4
A6TF			8.5				9.3
A6LJ			10.7				10.7
A5PW	5083	9.1	8.9	2.5	1120	63	8.9
A5WH						90	

71 fatigue tests were performed in total for this study. The raw data from the experimental fatigue test is available in Appendix C. For each specimen type, at least four tests were completed under tension-only constant amplitude (CA) loading conditions at different stress ranges, ΔS (= $S_{max} - S_{min}$), and at a stress ratio, R (= S_{min} / S_{max}), of 0.1. Tests that exceeded 3 million or so applied cycles without failure were identified as "run-out". It should be noted here that the term "run-out" simply refers to a test that was stopped before failure – not a test for which an "infinite" fatigue life is necessarily expected. Following the CA loading tests, specimens were tested under a variable amplitude (VA) loading history, which corresponds to the support reaction on a 15 m long simply-supported girder subjected to measured highway traffic loading in the Province of Ontario (see Figure 3.14(D)). This history was found to be relatively severe for aluminum welds in bridges (Coughlin and Walbridge 2012). Figure 3.16 shows typical weld root defect depths measured for the A6KB, A6PW, and A6LJ specimen types.

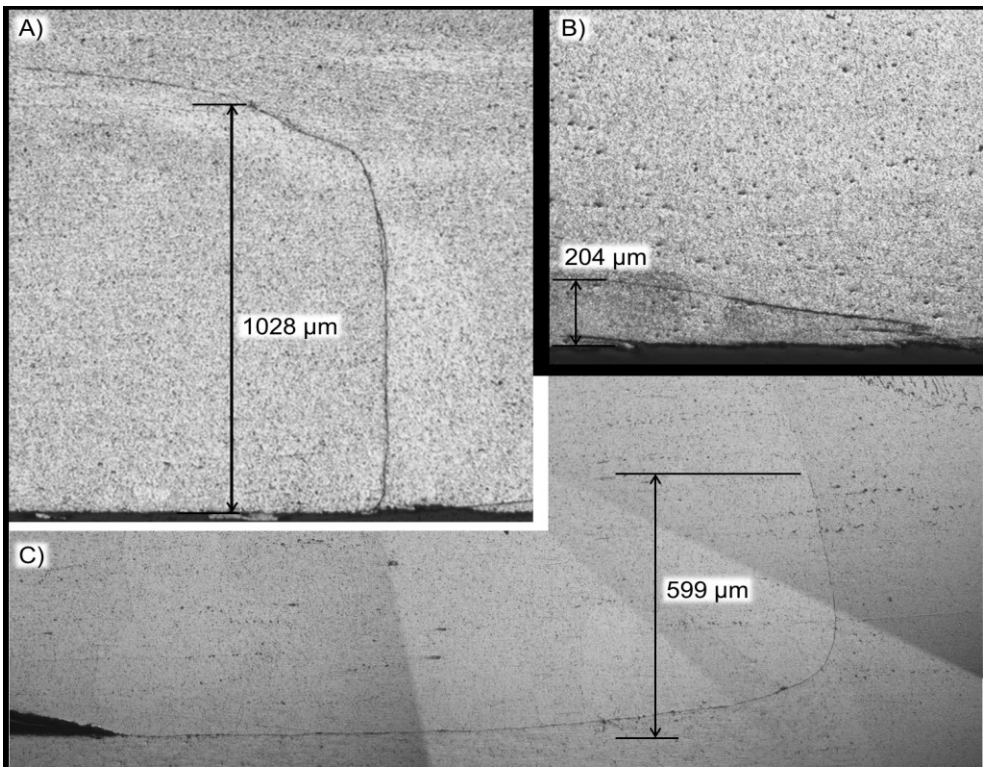

Figure 3.16: Weld root defect size measurements in (A) A6KB, (B) A6PW, and (C) A6LJ specimens

For the A6KB specimens, the WR defect was on the order of 1 mm in depth and was initially straight and perpendicular to the bottom edge of the specimen as shown in Figure 3.16(A).

Within the thickness of the plate, the kissing bond defect turns towards the AS of the weld and approaches an orientation parallel to the transverse direction of the weld at its visible tip. The minor WR defects observed in the A6PW specimens tended to appear as a straight fold aligned at a shallow angle with respect to the specimen bottom edge as shown in Figure 3.16(B). The crack-like defects observed in the A6LJ specimens, were hook-shaped as shown in Figure 3.16(C), which resulted in failures from the weld root. In the lap joint, the defect started out in a horizontal direction, parallel to the specimen bottom edge, and then turned upwards near the nugget zone (NZ) edge, possibly due to the upward flow of the plasticized material in this region.

Figure 3.17 shows an example of the cross-sectional weld profile for one of the specimens with a toe flash. While the toe flash generated during fabrication of these specimens was readily apparent, it is the loss of cross-section and the sharp stress concentration resulting from the excess tool penetration that is thought to be detrimental from a fatigue perspective. In general, the thickness reduction for these specimens was on the order of 0.5 mm at the NZ.

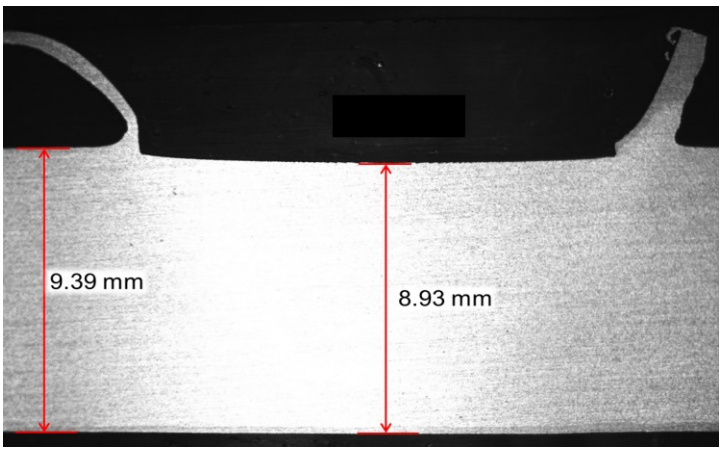

Figure 3.17: Weld profile of A6TF specimens with a significantly large toe flash defect

The fatigue tests were performed on a 500 kN MTS structural testing frame at a frequency of 10-15 Hz. The formation of fatigue cracks was detected by a visual inspection and the use of displacement limits, which stopped the test when there was displacement beyond a predetermined limit. When a visible crack was detected, the crack surface was stained with dye penetrant, to enable measurement of the crack size and shape after specimen fracture.

3.3.2 Fatigue test results

In this section, fatigue test results are presented for all seven specimen types. The fatigue test results are compared with design S-N curves from an aluminum design manual (ADM) for conventional arc welded butt joints. Detailed S-N data including failure location and initial defect size is available in Appendix C. Figure 3.18 shows fatigue test results for the 6061 properly welded specimens under CA and VA loading conditions. An equivalent stress range for the case of a VA loading has been calculated using a Palmgren-Miner's sum. The slope, *m'*, for calculating ΔS_{eq} was taken as 4.84, which is the slope of Cat. B design S-N curve for butt joints in the ADM (The Aluminum Association 2015). In the ADM, the Cat. B detail represents a single-sided full penetration arc welded butt joint, while Cat. A represents a double-sided full penetration arc welded butt joint which is as good as base metal (BM).

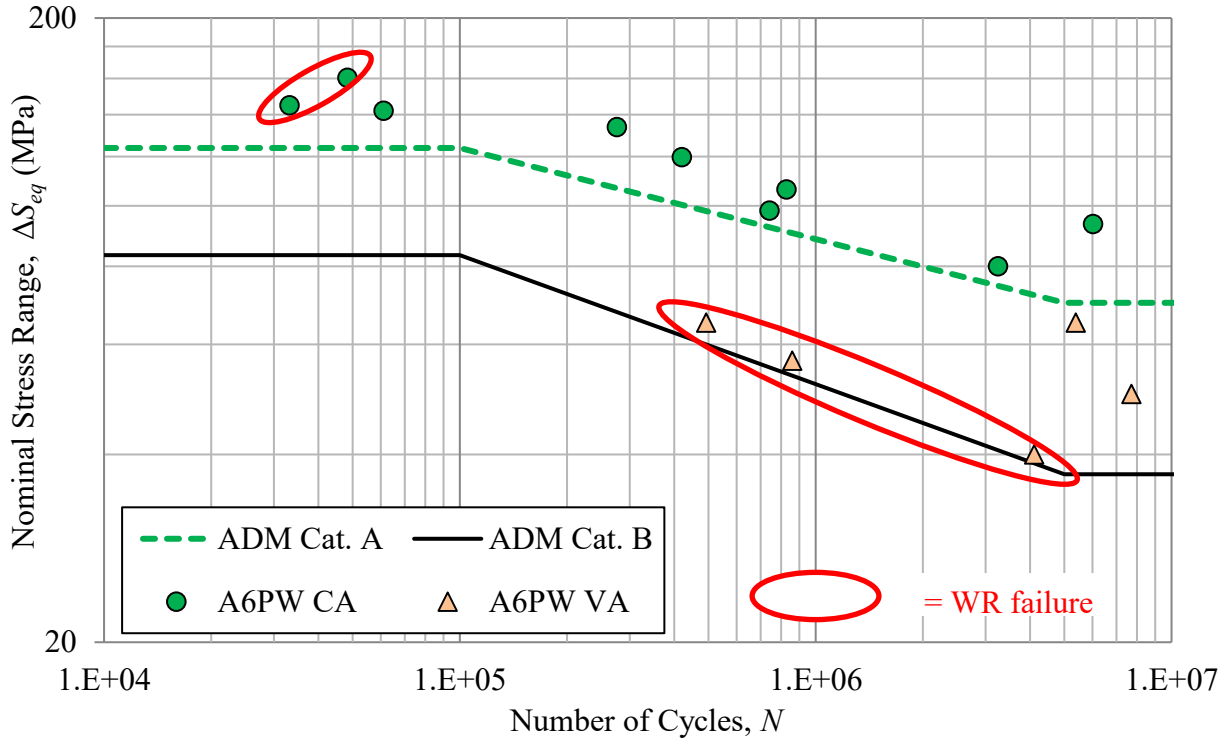

Figure 3.18: Fatigue test results for A6PW specimens and comparison with the ADM design curves

It can be observed in Figure 3.18 that the fatigue performance of A6PW specimens is close to that of a double-sided full penetration arc welded butt joint unless the failure is due to crack

propagation from the weld root (WR) under VA loading. In the case of WR cracking, all of the experimental S-N data points fall above detail Cat. B. While, it was intended to fabricate the A6PW specimens without any defect, after fabrication, it was found that some of the PW specimens had an unintentional kissing bond defect on the order of 204 μm as shown in Figure 3.16(B). Practically, detecting/preventing a defect of this size is difficult. Therefore, these specimens are still categorized as "properly welded" specimens.

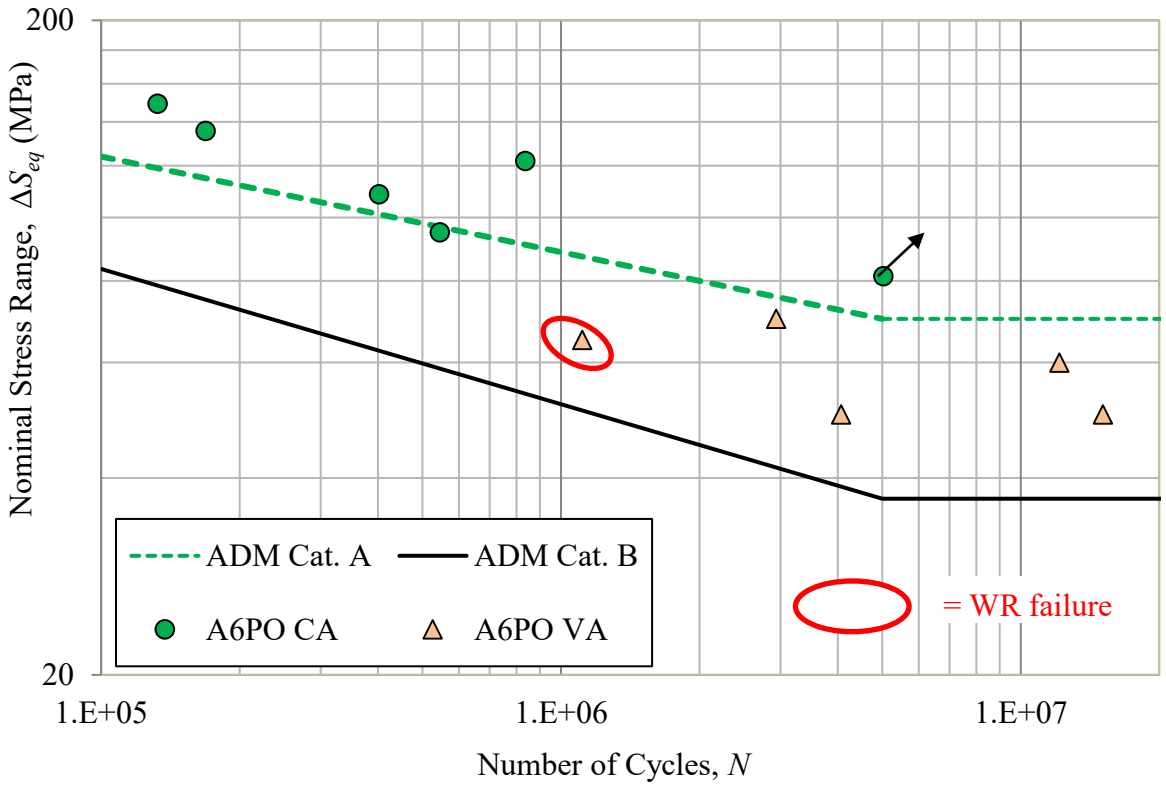

Figure 3.19: Fatigue test results for A6PO specimens and comparison with the ADM design curves

Figure 3.19 shows the fatigue test results for the A6PO specimens. The fatigue performance of the A6PO specimens is close to that of the base metal (Cat. A). Again, the poorest VA test result was the result of a premature failure from the WR due to an unintentional KB defect. Beyond 5 million cycles, VA test results falling below the ADM Cat. A design curve is expected, as VA design in this domain is done by extrapolating the sloped S-N curve beyond the (horizontal) fatigue limit.

The fatigue test results for specimens with kissing bond defects are shown in Figure 3.20. It can be observed from this figure that the fatigue performance of the A6KB specimens is worse than the fatigue performance of similar single-sided arc welded joints (ADM Cat. B).

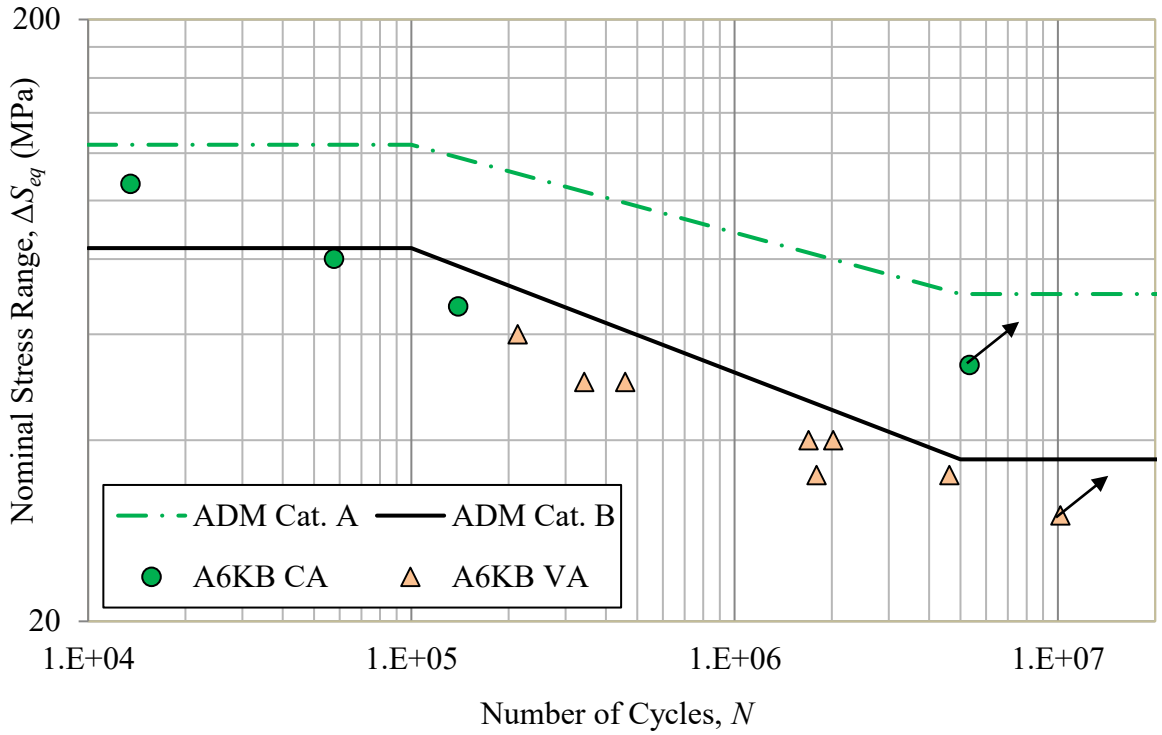

Figure 3.20: Fatigue test results for A6KB specimens and comparison with the ADM design curves

Figure 3.21 shows the experimental S-N data for the A6LJ specimens along with the ADM Cat. A, ADM Cat. B and ADM Cat. D design curves. It can be observed from this figure that the fatigue performance of the LJ specimen is also lower than the ADM Cat. B design curve under both loading conditions. Therefore, the S-N data for the A6LJ specimens is also compared to the design S-N curve for ADM Cat. D (m = 3.73). It can be observed that the fatigue performance of the LJ detail can be said to be as good as an ADM Cat. D detail. Another aspect, which can be noted in Figure 3.20 and Figure 3.21, is that there is less scatter in the S-N data for the A6KB and A6LJ specimens, which is because of the consistency in the failure mode (from the WR) and the defect size for these specimens. Also, the CA and VA loading test results fall along a straight line for these specimens.

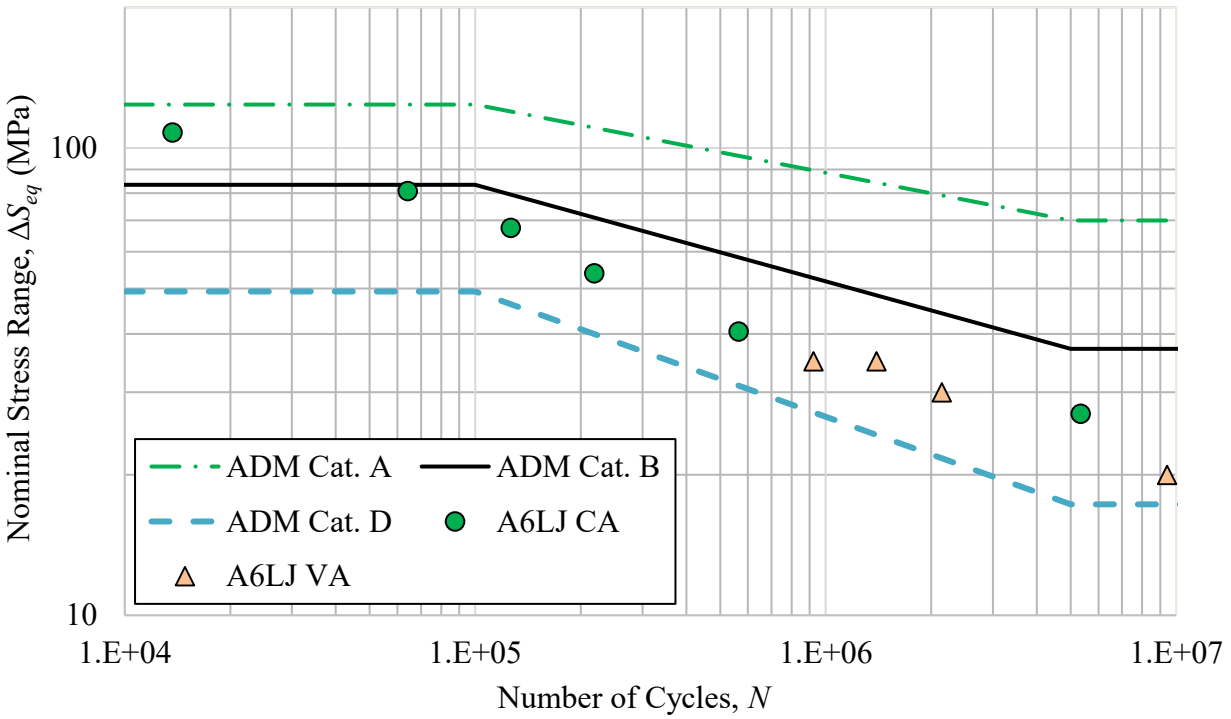

Figure 3.21: Fatigue test results for A6LJ specimens and comparison with the ADM design curves

Figure 3.22 shows experimental S-N data for A6TF specimens along with the ADM design curves. Most of the S-N test data is above the ADM Cat. B curve except for two VA test results, which correspond to cracking from the WR. Based on this observation, it can be said that the toe flash defect is not as detrimental as the kissing bond defect and is not a big concern in FSW joints.

Figure 3.23 shows the experimental test results for the A5PW and A5WH specimens. Fatigue tests for 5083 aluminum specimens were carried out only under CA loading with a load ratio, R, of 0.1. All A5PW test results but one fall above the ADM Cat. A design curve, which shows the superior fatigue performance of the A5PW specimens than the typical aluminum base metal. The A5WH results are shown with a triangle symbol in Figure 3.23. It can be observed that these markers are below the circular ones, but are still above the ADM Cat. B design curve in all cases but one. This shows that small wormhole defects of the observed geometry have only a minor effect on the fatigue performance.

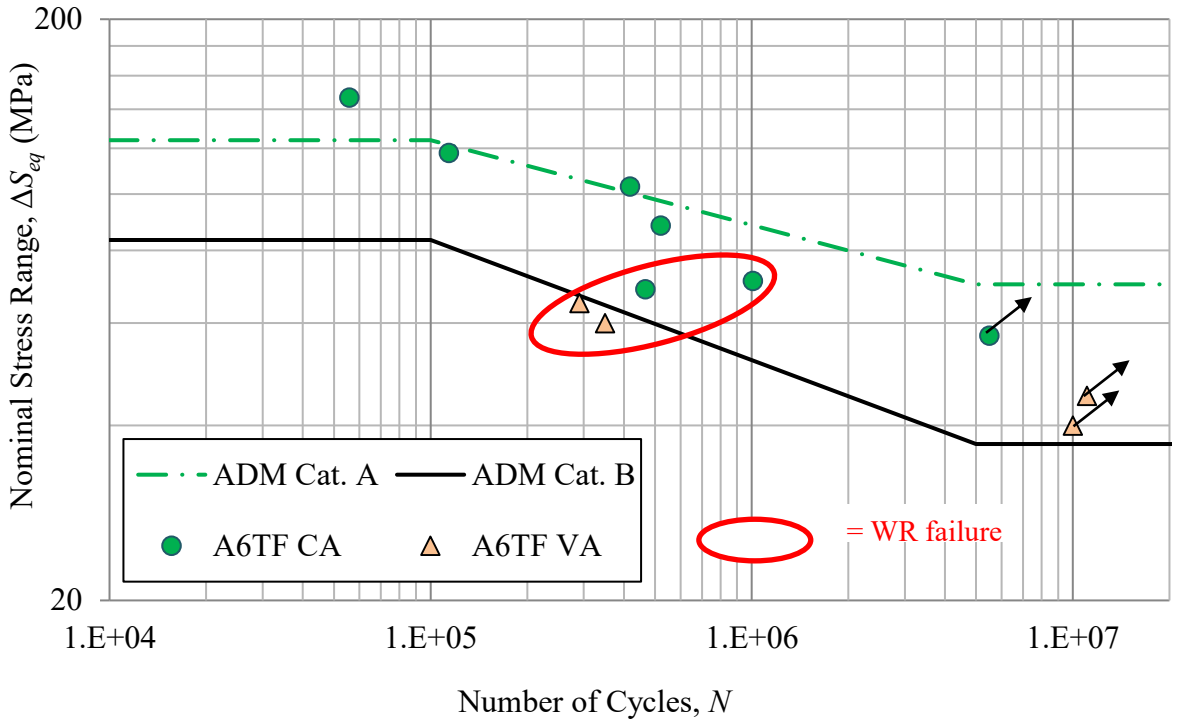

Figure 3.22: Fatigue test results for A6TF specimens and comparison with the ADM design curves

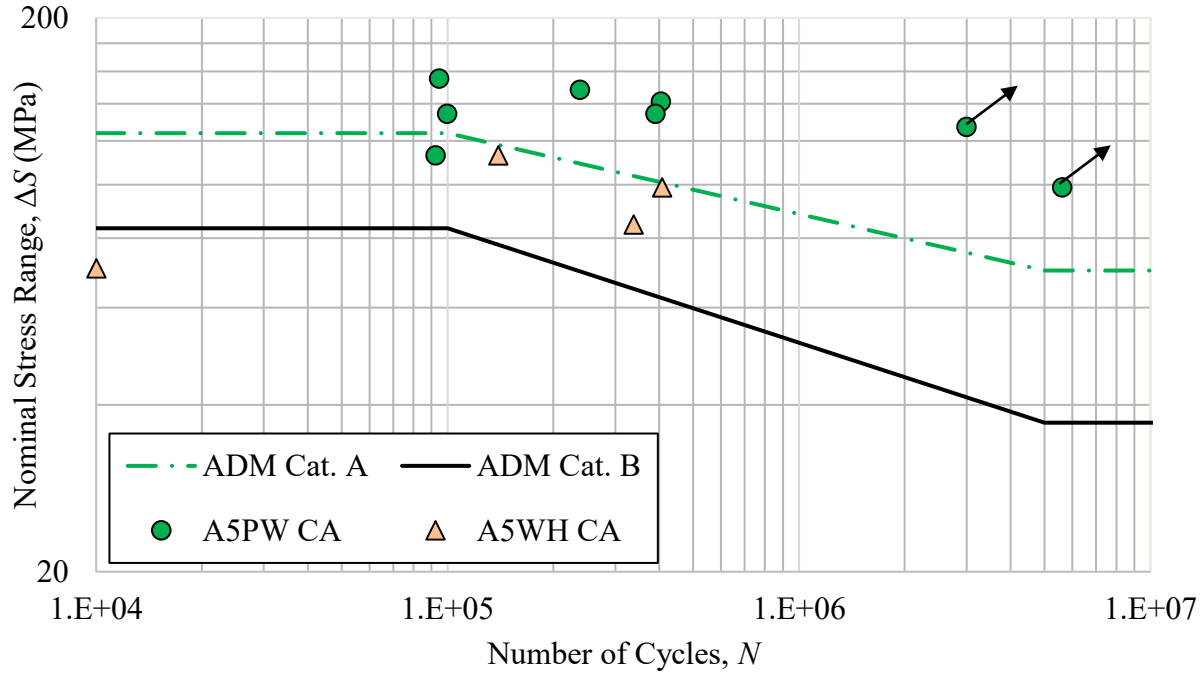

Figure 3.23: Fatigue test results for A5PW and A5WH specimens with ADM design curves

Several attempts were made to create a wormhole defect in 6061 aluminum plate, but they were unsuccessful. After several trials, the wormhole defect was created in the 5083 aluminum plate with a different welding tool (a circular end rather than the usual conical end). However, the wormhole depth was not consistent along the length of the weld. This may be considered to be a good thing: if it is so difficult to intentionally create the wormhole defect by varying the welding process parameters, then in practice, wormhole defects should rarely happen in the 5083 and 6061 aluminum FSW joints fabricated with a tool of similar profile.

3.3.3 Fracture mechanics analysis

Following the fatigue testing, fracture surface observations and a fracture mechanics analysis were conducted to facilitate further understanding of the effects of all of the investigated defect types and demonstrate that the experimental results could be predicted with a reasonable accuracy using the 1D SBFM model. Table 3.7 provides values for the input parameters used in the fracture mechanics analysis for the two investigated aluminum alloys.

Table 3.7: Input parameters used for the fracture mechanics analysis

Parameter	6061 Aluminum	5083 Aluminum	Units
t	9.5	9.1	mm
E	64011	71389	MPa
σ_y	134.1	243.33	MPa
σ_u	181.5	365.5	MPa
LN(C)	-30.6	-26.3	MPa, mm
m	4.0	3.2	MPa, mm
ΔK_{th}	45.0	35	MPa·√mm
K'	304.5	643	MPa
n'	0.13	0.1	-
μ_{op}	0.003	0.003	-

Regarding these input parameters, the following comments provide more insight:

- E, σ_y, σ_u, K', and n' were estimated based on the hardness measurements reported in (Guo et al. 2019) and by interpolating between the measured properties for 6061 alloy T651 and O tempers from (Coughlin and Walbridge 2012).

- LN(C), m, ΔK_{th}, and μ_{op} values were similar to the values used in (Coughlin and Walbridge 2012; Miranda et al. 2015), which are intended to represent averages of measured data for 5xxx and 6xxx series alloys.
- Tabulated material properties for 5083 aluminum alloy was obtained from base metal coupons test results available in (Ranjan et al. 2016).

In addition to these input parameters, implementation of the fracture mechanics model requires a knowledge of the local elastic stress distribution along the anticipated crack path due to the stress concentration. The elastic stress distribution was assumed to be uniform for the A6PW and A6KB specimens. For the A6TF and A6LJ specimens, the stress distributions were taken from (Guo et al. 2019), who obtained these distributions by using FE analysis software ABAQUS. 2D plane strain models were used to obtain stress concentration factors (SCFs) relating the nominal stress in the plate to the local elastic stress along the crack path. The resulting SCF distributions along the crack paths for these specimen types are shown in Figure 3.24.

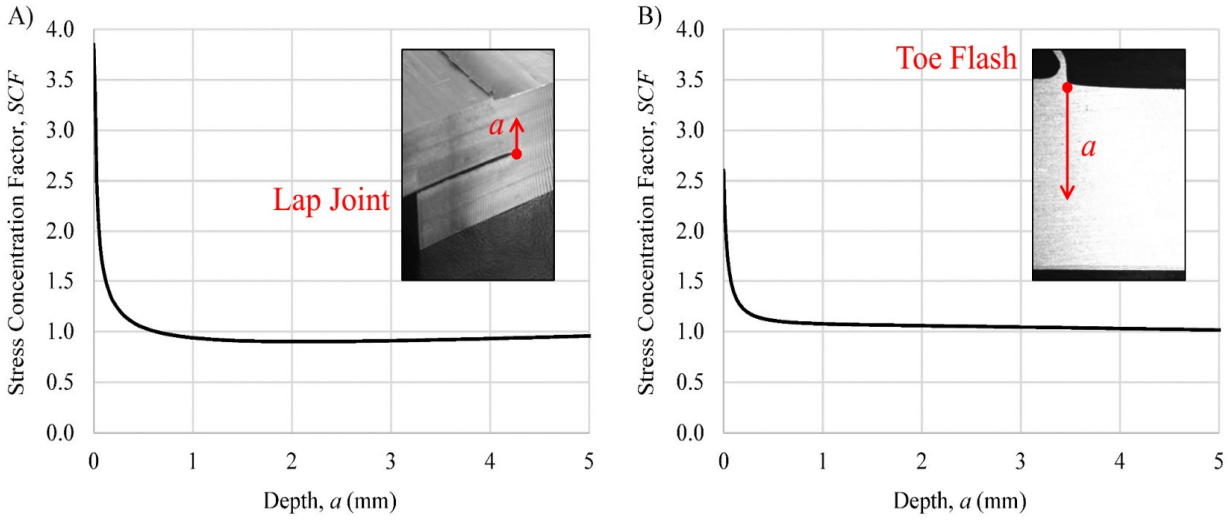

Figure 3.24: SCF distributions for (A) lap joint, and (B) toe flash specimens

During the SBFM analysis, a uniform, tensile residual stress of 8.45 MPa was assumed, as recommended in prior work (Miranda et al. 2015). Analyses were performed under a CA loading as well as under a VA loading history (see Figure 3.14(D)) used in the experimental study. In the

next subsections, observations concerning the fracture surface of each specimen type are presented first, followed by S-N curves obtained from a deterministic 1D SBFM analysis.

3.3.3.1 Case 1: 6061 Aluminum, Properly Welded (PW) butt joints

Fracture surfaces of the A6PW specimens are presented in Figure 3.25. The specimen name, nominal stress range, failure location (FL), and final crack aspect ratio (a/c) are stated above each fracture surface. Nominal stress range (ΔS) is stated for the case of CA loading and an equivalent nominal stress range (ΔS_{eq}) is stated for the case of a VA loading. The top edge of the fracture surface represents the weld top and the bottom edge represents the bottom of the weld or weld root (WR). The A6PW specimens failed from four different crack initiation sites: base metal (BM), advancing side (AS) of the weld top, retreating side (RS) of the weld top, and WR. It can be observed from Figure 3.25 that whenever the crack initiated from the weld top (AS/RS), the crack shape is round ($0.38 < a/c < 0.58$). However, when crack initiated from the WR, the crack shape is flat (a through-width crack). Cracks initiating from the BM were mostly bullet-shaped as visible for specimen A6PW01D.

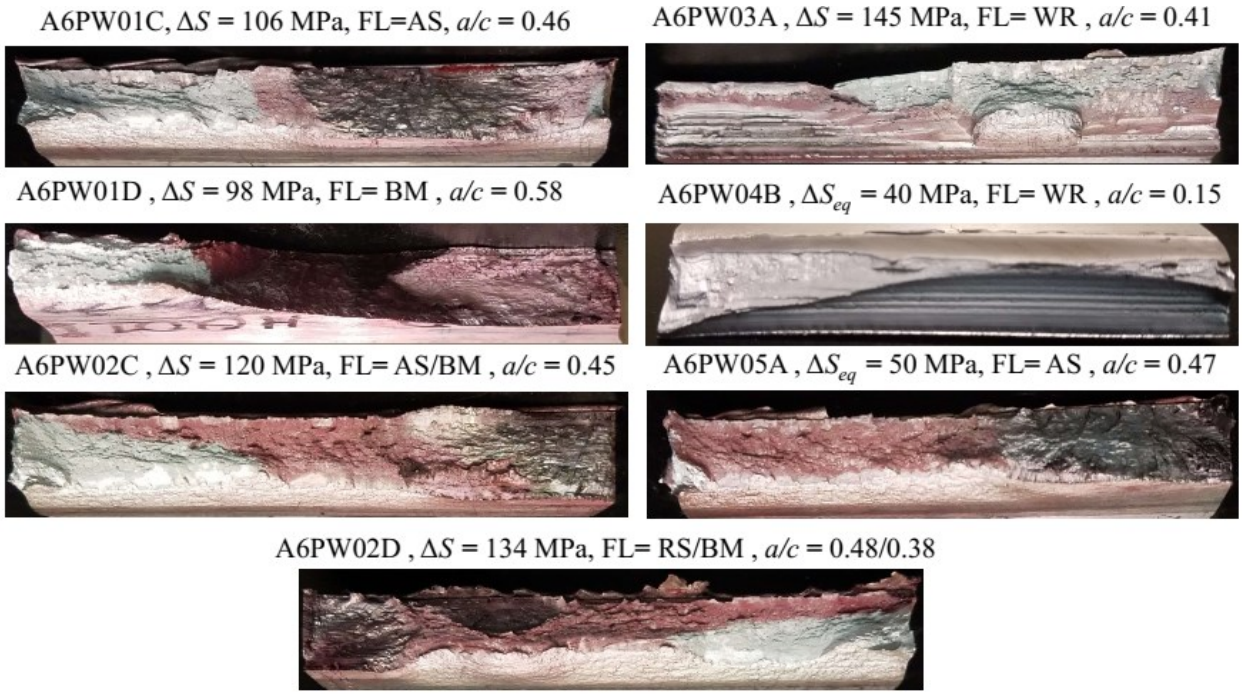

Figure 3.25: Fracture surfaces of properly welded specimens

Figure 3.26 shows the SBFM analysis results along with experimental S-N data for the A6PW specimens under a CA loading. Two S-N curves are presented: one with a/c = 0.1, which represents cracking from the weld root (i.e. a through-width crack, essentially), and other with a/c = 0.55, which simulates a semi-elliptical crack propagating from the weld top (AS/RS). The observed defect depth under a microscope at the WR was about 0.33 mm for A6PW specimens, therefore a defect depth of 0.3 mm at the WR was used as input while performing SBFM analysis. Defect geometry measurements were not available at the weld top; therefore, a defect depth of 0.15 mm was assumed while performing SBFM analysis. It can be observed that with an assumed defect size of 0.3 mm at weld root (for failure scenario from weld root) and an assumed defect size of 0.15 mm at weld top (for failure scenario from weld top), the obtained S-N curves from the SBFM model provided a reasonable estimation for fatigue test results.

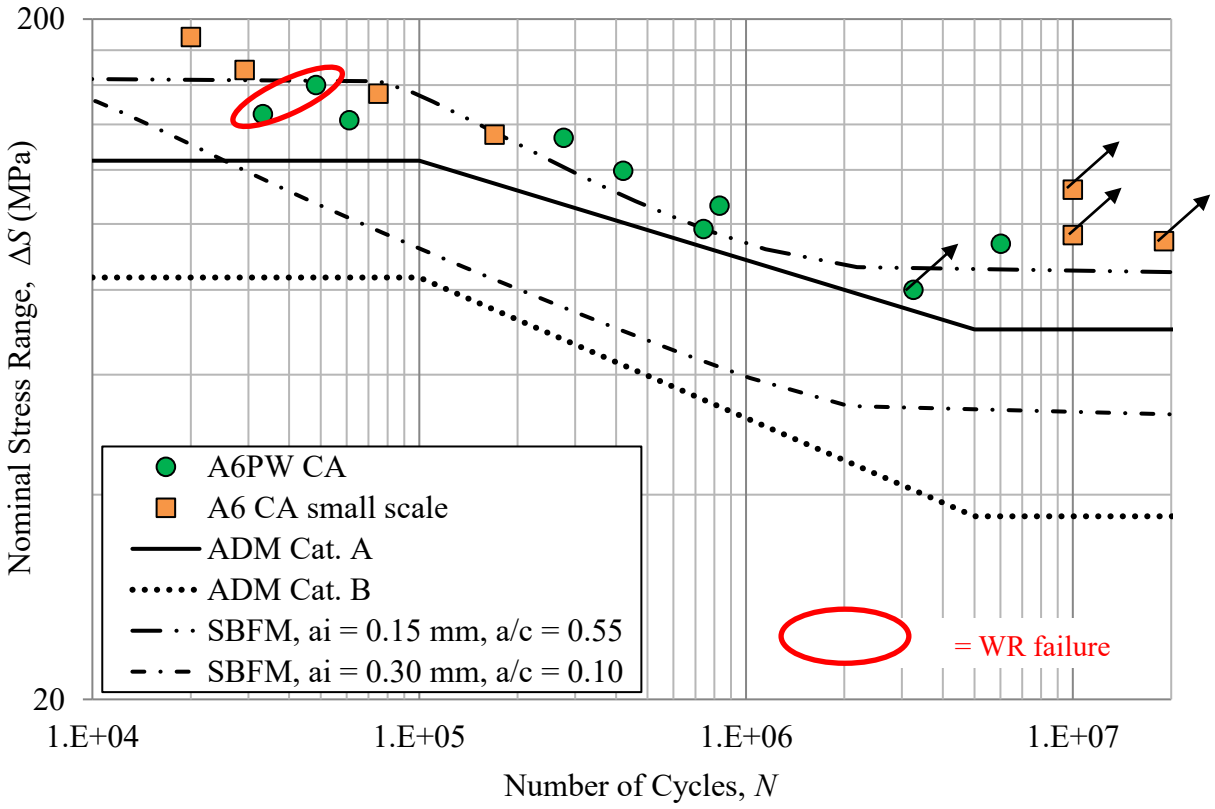

Figure 3.26: SBFM analysis results for A6PW specimens under CA loading

Figure 3.27 presents SBFM analysis results along with experimental S-N data for A6PW specimens under a VA loading. Here, two S-N curves have been obtained from an SBFM analysis with the same two sets of assumed defect geometry as those used to analyze for the A6PW specimens under CA loading. Here again, the chosen initial crack defects depths and shapes are seen to result in a close prediction of the fatigue test results.

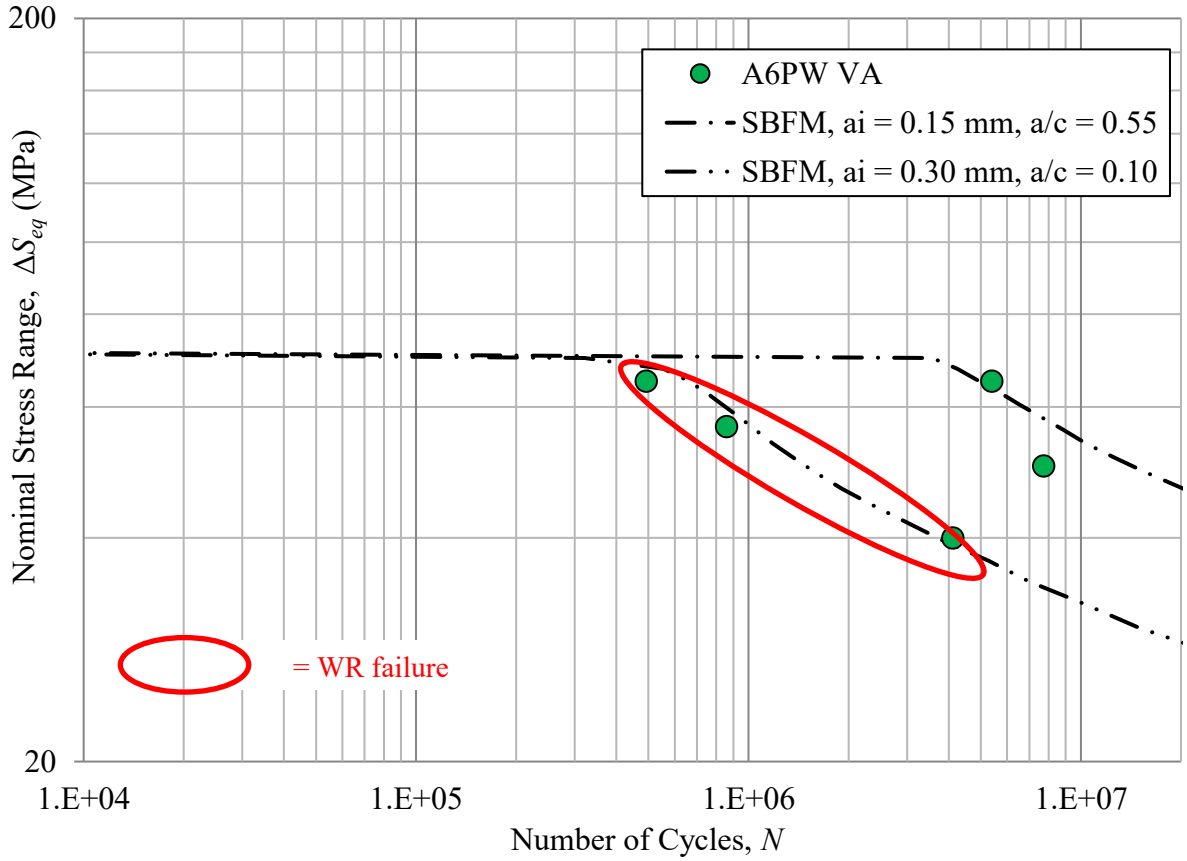

Figure 3.27: SBFM analysis results for A6PW specimens under VA loading

3.3.3.2 Case 2: 6061 Aluminum, Polished butt joints

The fracture surfaces of A6PO specimens are shown in Figure 3.28. It can be observed that A6PO specimens failed from all four possible crack initiation sites (AS/RS/BM/WR) but a majority of the failures initiated in the BM (away from the weld). This confirms that with polishing, it is possible to achieve a fatigue performance in FSW joints equal to or better than that of the base metal. It can be observed from the fracture surfaces that when failure happens from the top of the

weld, the crack shape is round and the final crack aspect ratio was measured to vary in between 0.38 and 0.72. When the crack initiated from the BM, the crack is bullet-shaped, which can be seen for A6PO03D specimen.

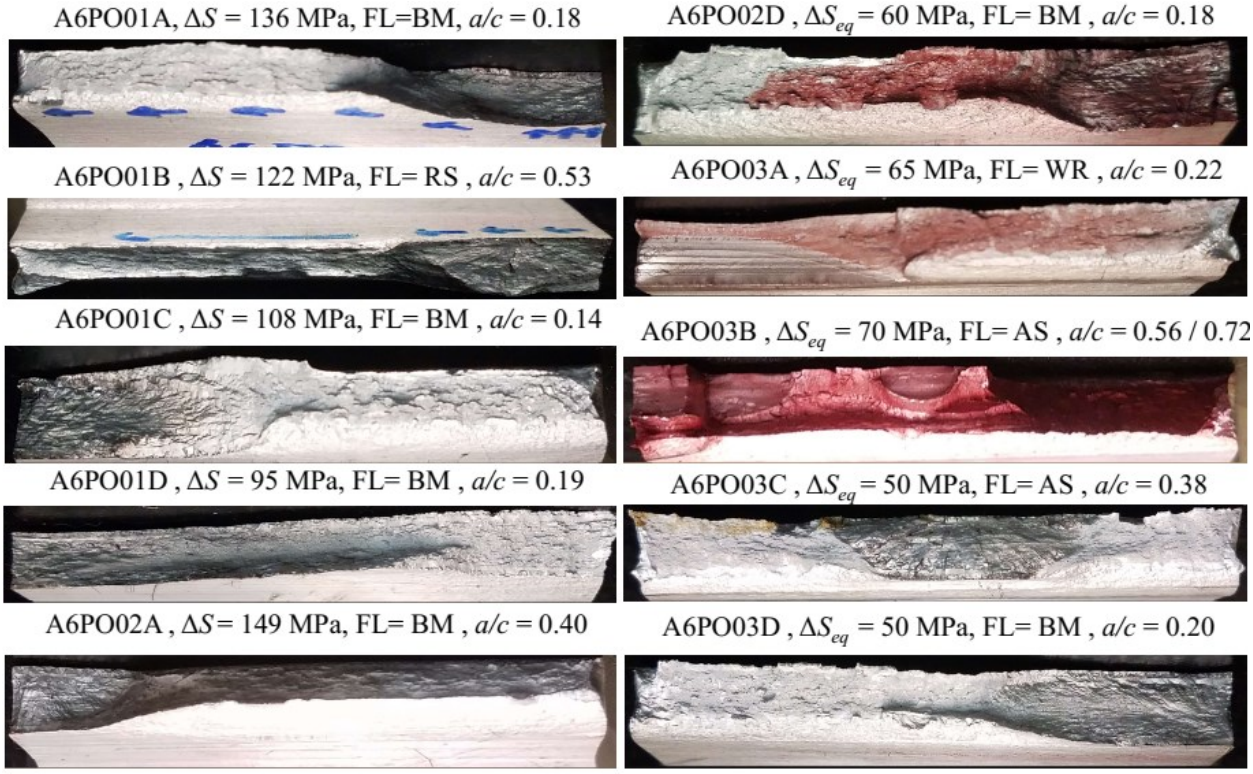

Figure 3.28: Fracture surfaces of polished specimens

Figure 3.29 shows SBFM analysis results for A6PO specimens under a CA loading. There was only one A6PO specimen which failed from the WR location (under VA loading), while others failed from the AS/RS of the weld or from the BM. Therefore, during the fracture mechanics analysis, two cracking scenarios are simulated, cracking from AS/RS with an a/c of 0.55 and cracking from the WR with an a/c of 0.10. Reasonably good agreement between test results and S-N curves can be seen for five test data points in Figure 3.29. Figure 3.30 shows SBFM analysis results for A6PO specimens under a VA loading. The two SBFM-derived S-N curves provide a reasonably accurate estimation of the fatigue test results under VA loading condition.

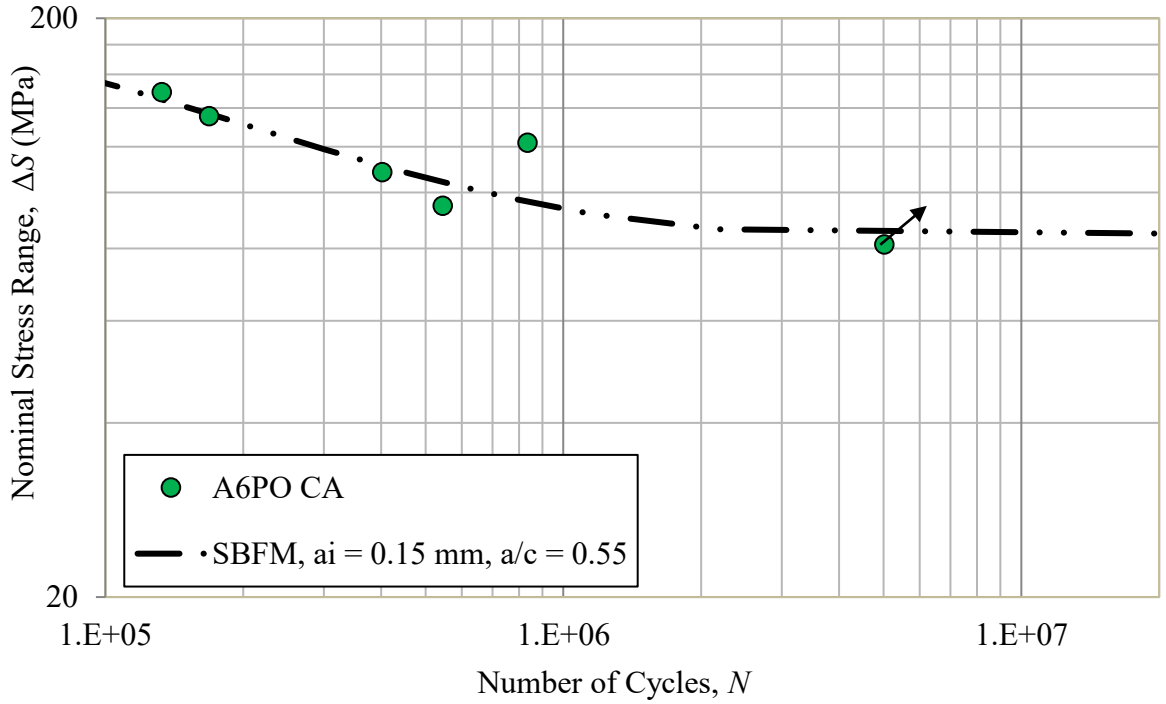

Figure 3.29: SBFM analysis results for A6PO specimens under CA loading

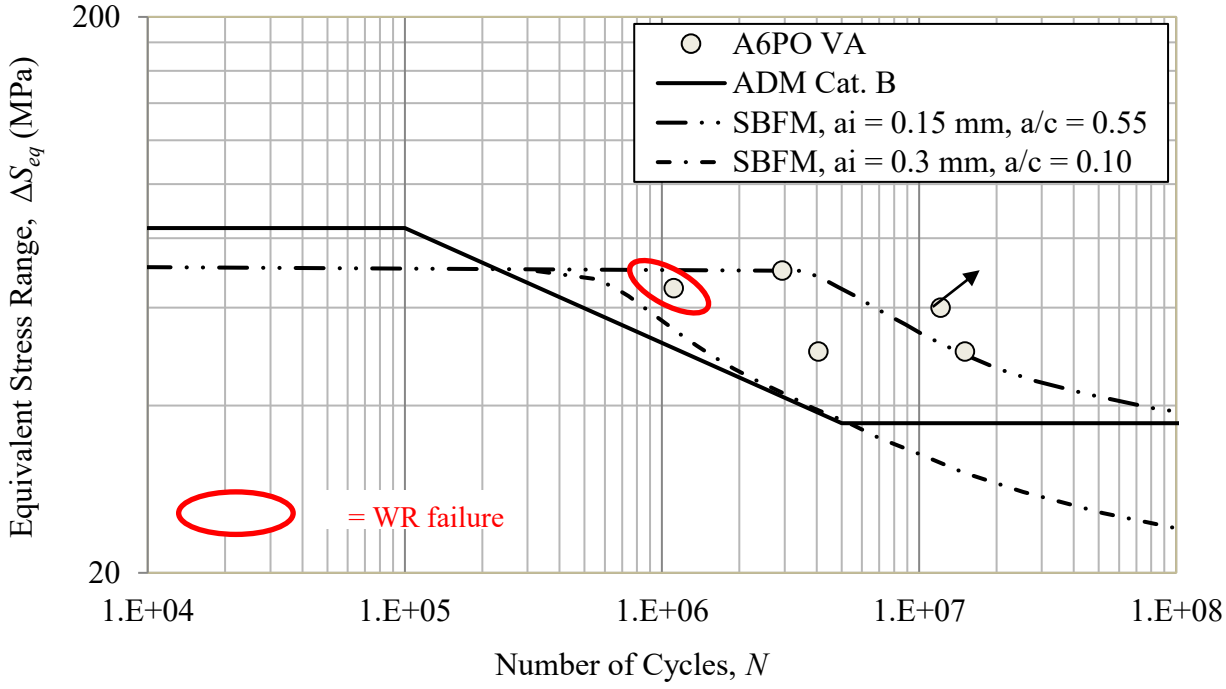

Figure 3.30: SBFM analysis results for A6PO specimens under VA loading

3.3.3.3 Case 3: 6061 Aluminum, Butt Joints with a kissing bond defect

Figure 3.31 shows the fracture surfaces of A6KB specimens. For all of the A6KB specimens, cracks initiated from the WR, where the defect was intentionally introduced during fabrication of specimens. The defect size was measured under a microscope and it was found that a kissing bond defect of about 0.8 – 1.0 mm in depth was present in A6KB specimens. The crack shape was observed to be that of a through-width crack essentially, with a low crack aspect ratio of about 0.1.

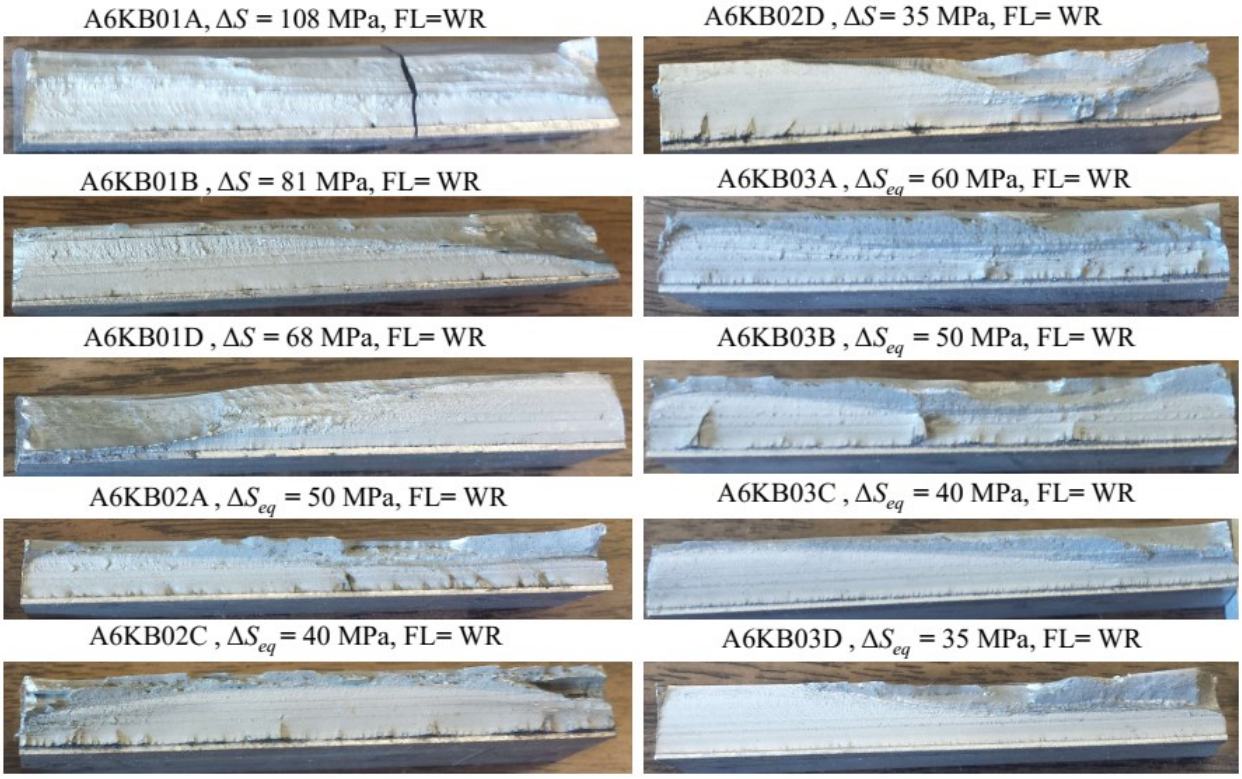

Figure 3.31: Fracture surfaces of the specimens with kissing bond defect

Figure 3.32 shows the SBFM analysis results as well as experimental S-N data for the A6KB specimens under CA and VA loading conditions. Since the failure always happened from the WR, only one cracking scenario was simulated, consisting of a through-width crack (with a/c = 0.1) initiating from the WR. An initial defect depth of 0.8 mm was used to obtain two S-N curves from the SBFM model for the two loading conditions. An excellent match between the fatigue test results and S-N curves can be seen in Figure 3.32 under both loading conditions.

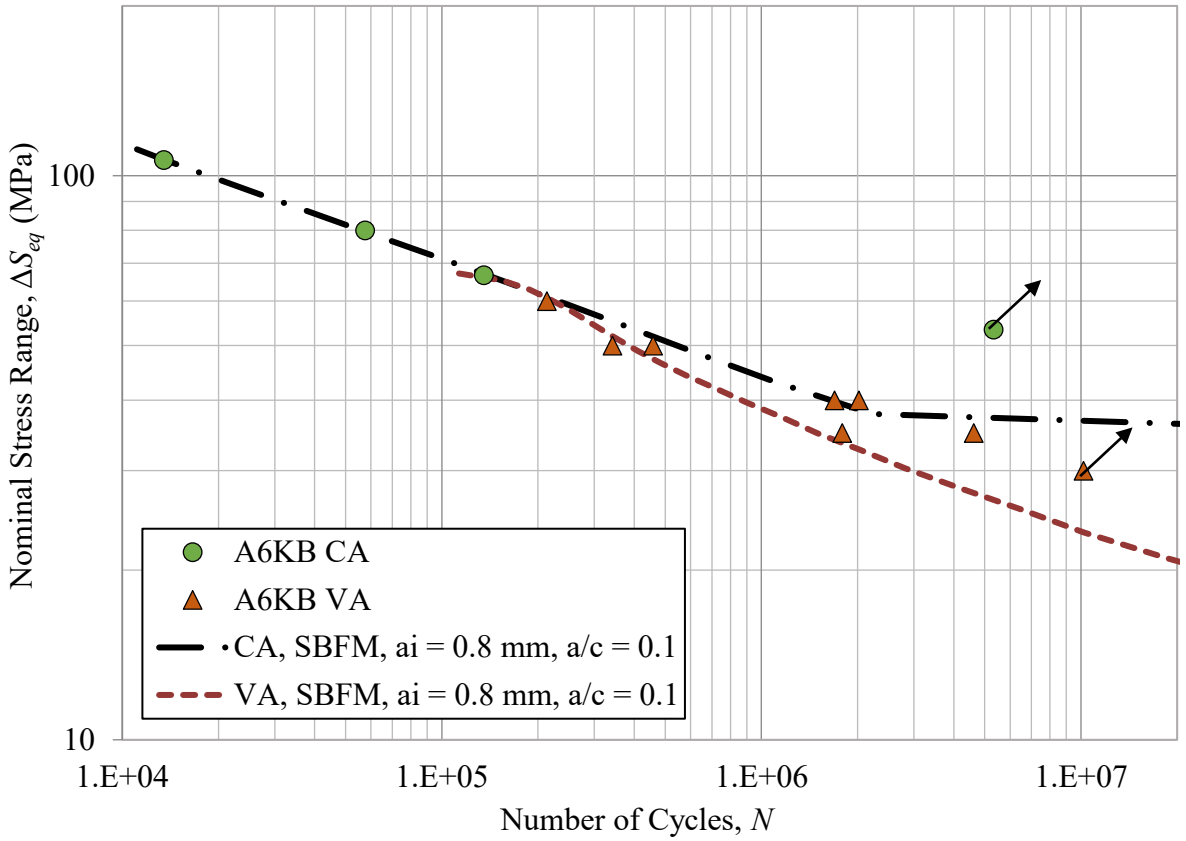

Figure 3.32: SBFM analysis results for A6KB specimens under CA and VA loading

3.3.3.4 Case 4: 6061 Aluminum, butt joints with a significant toe flash

Fracture surfaces of the A6TF specimens are shown in Figure 3.33. It can clearly be seen from the fracture surfaces that there were two cracking scenarios in which A6TF specimens failed, one with a crack initiating from the AS of the weld and other with a crack initiating from the WR. Because of the two cracking scenarios, a significant scatter in the experimental S-N data was observed. For the last specimen (A6TF02D), there was a kissing bond defect in addition to a toe flash defect, which caused failure from the weld root. The kissing bond defect was big enough to shift the crack initiation site from weld top to the weld root.

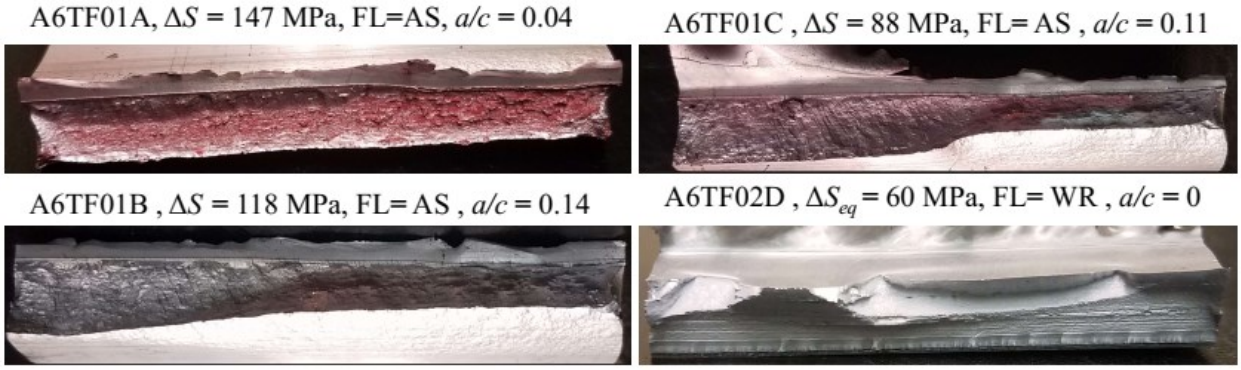

Figure 3.33: Fracture surfaces of specimens with significant toe flash

Figure 3.34 shows SBFM analysis results for A6TF specimens under CA loading. Two cracking scenarios were simulated using the SBFM model, one with a crack initiating from weld top (a/c = 0.55) and other with a crack initiating from the WR (a/c = 0.1). Two crack depths were assumed to model the defect geometry, one with a depth of 0.15 mm at the weld top and the other with a depth of 0.6 mm at the WR. The defect depth at the weld root was about 0.6 mm as measured from the fracture surface and cross-section, which is tabulated in Appendix C for each specimen. The SCF distribution (as shown in Figure 3.24) along the crack path because of toe flash was considered during the SBFM analysis. With the assumed defect depth and the estimated SCF distribution, the predicted S-N curves provide a reasonably good estimation of the fatigue test results. SBFM analysis results for the A6TF specimens under VA loading are shown in Figure 3.35. With the same cracking scenarios and initial defect depths as considered for CA loading, the two SBFM-derived S-N curves provided a reasonably good estimation of the fatigue test results under VA loading condition as well.

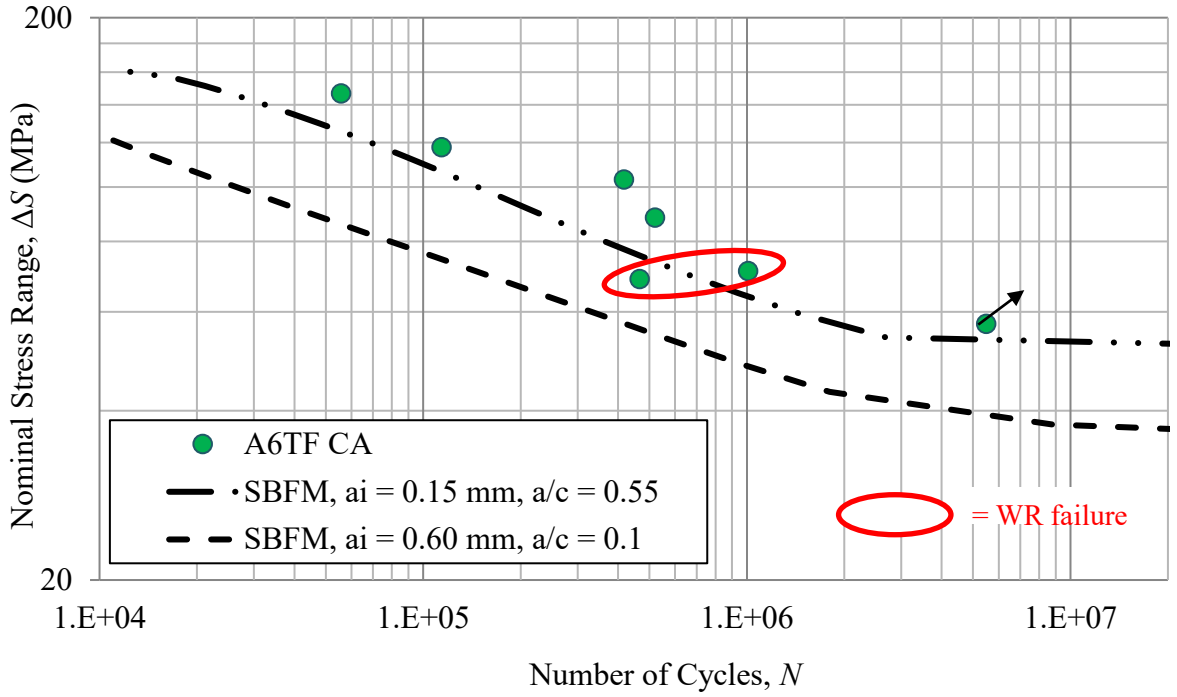

Figure 3.34: SBFM analysis results for A6TF specimens under CA loading

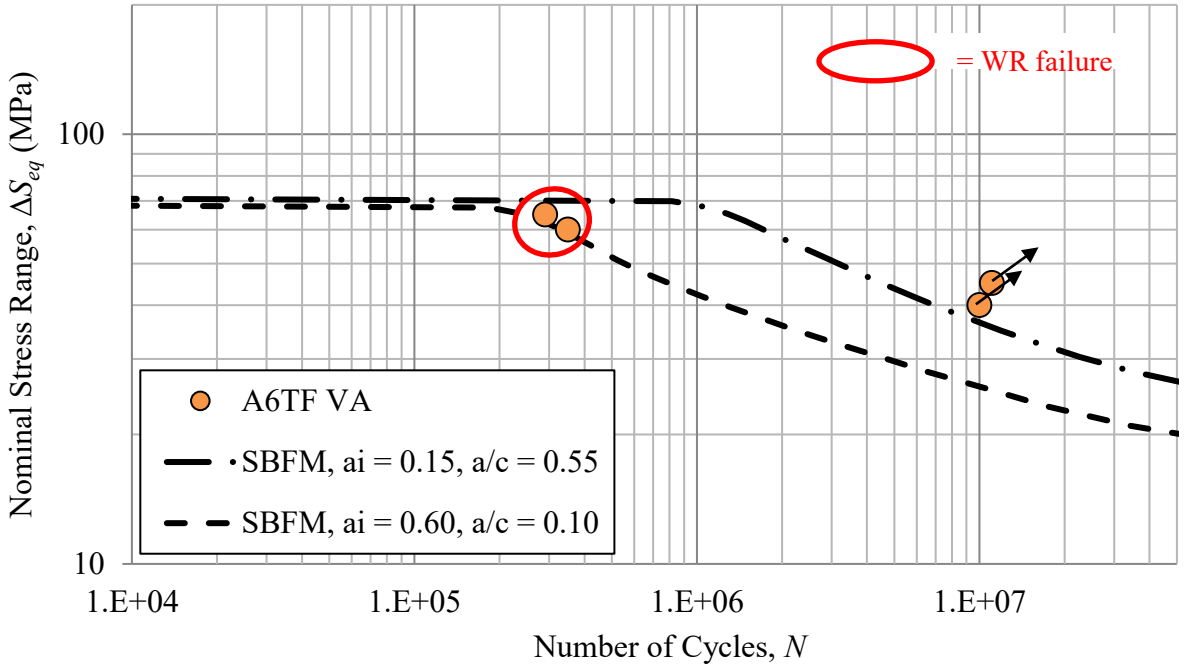

Figure 3.35: SBFM analysis results for A6TF specimens under VA loading

3.3.3.5 Case 5: 6061 Aluminum, Lap Joints

Figure 3.36 shows fracture surfaces of the A6LJ specimens. It can be observed that all of the specimens failed from the WR. Vertical striations near the WR can be seen on the fracture surface indicating hook-shaped crack, which is typical in lap joints.

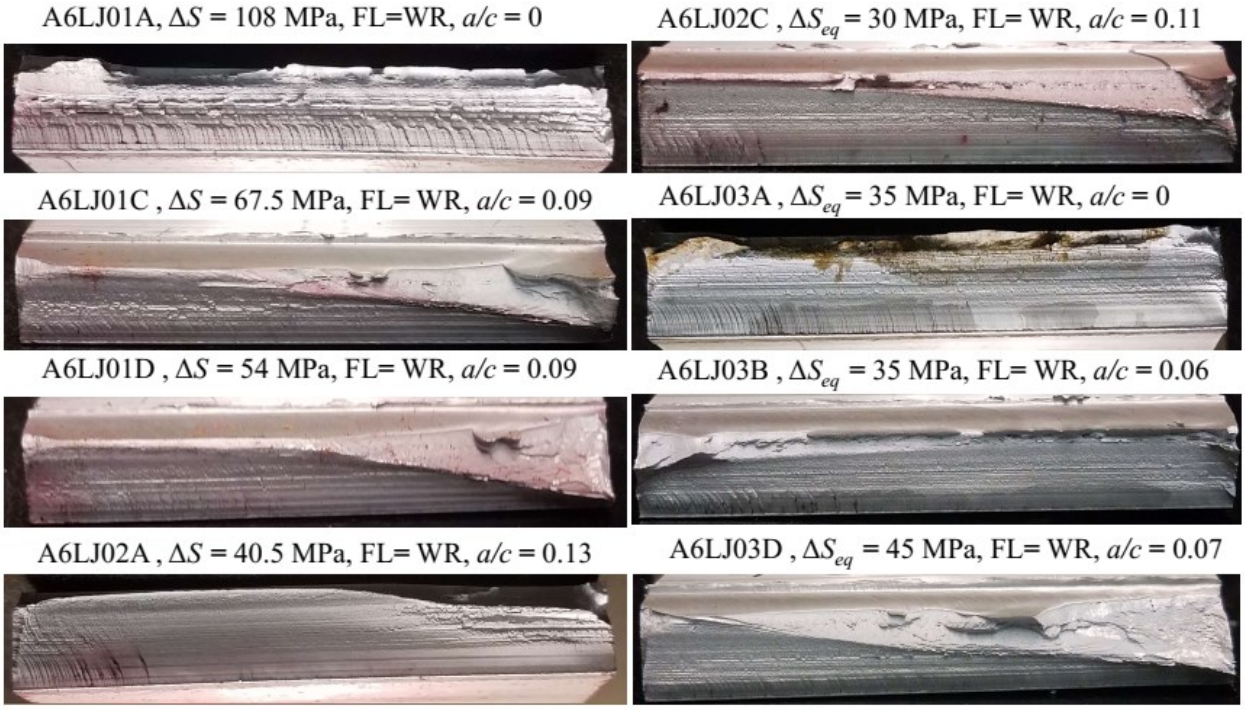

Figure 3.36: Fracture surfaces of lap joint specimens

Figure 3.37 shows SBFM analysis results for the A6LJ specimens under CA loading. Defect depths in the A6LJ specimens were measured under a microscope and found to vary in between 0.26 mm and 0.60 mm. Therefore, two defect depths of 0.3 mm and 0.6 mm were used to obtain the two S-N curves from the SBFM model. It can be observed that these S-N curves provide a good estimation of the fatigue test results. The SBFM analysis results for the A6LJ specimens under VA loading are shown in Figure 3.38. With the same defect geometry as used under CA loading, the predicted S-N curves under VA loading provide a reasonably good estimate for the fatigue test results.

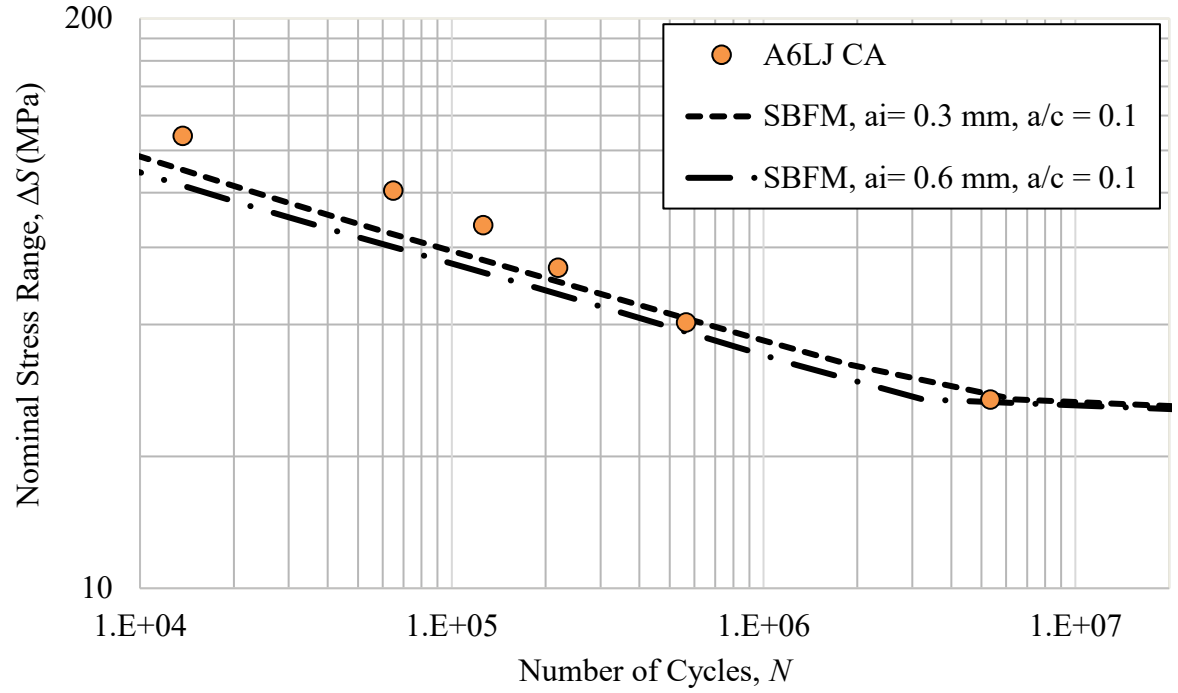

Figure 3.37: SBFM analysis results for A6LJ specimens under CA loading

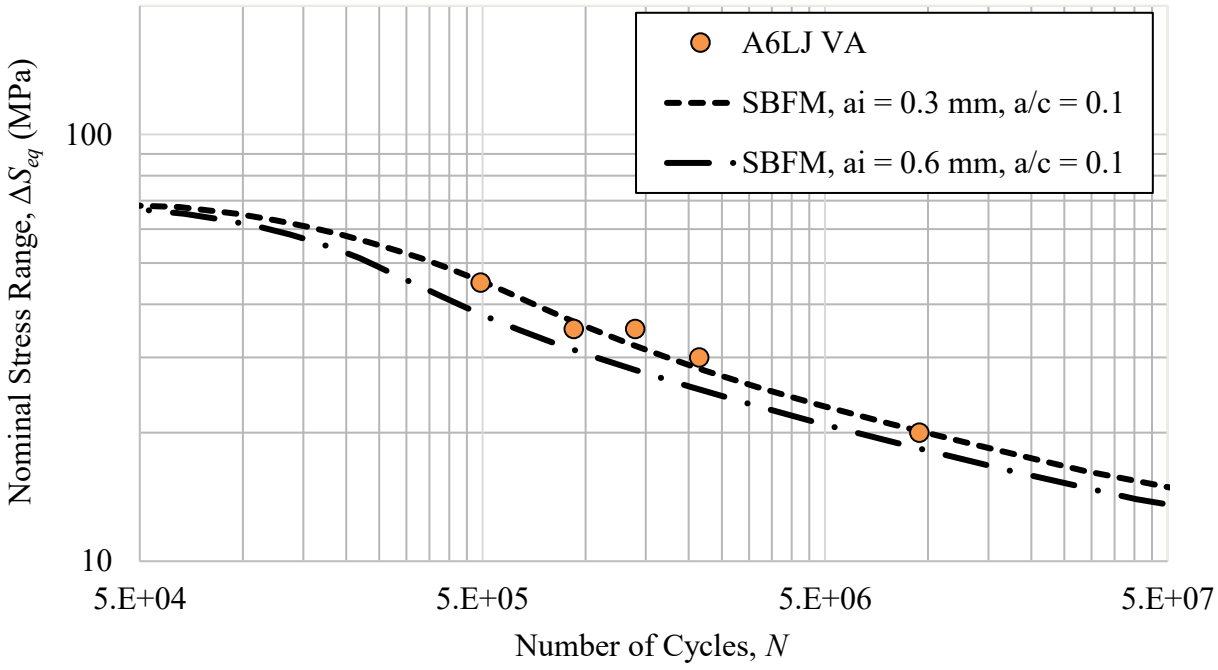

Figure 3.38: SBFM analysis results for A6LJ specimens under VA loading

3.3.3.6 Case 6: 5083 Aluminum, Properly welded butt joints

Fracture surfaces for A5PW specimens are shown in Figure 3.39. It can be observed in this figure that the first specimen (A5PWO2A) failed from the BM with a bullet shape crack and the other four specimens failed from the WR with semi-elliptical cracks. Since there is no significant softened region prone to localized straining for this heat treatable alloy (5083) at the weld top (AS/RS), the crack did not initiate from weld top, which is different from the case of A6PW specimens. One difference between the fracture surfaces of the A5PW and A6PW specimens is that rounder crack shapes were observed in the case of failure from the WR for the A5PW specimens ($a/c \sim 0.45$) compared to relatively flatter cracks ($a/c \sim 0.1$) in the case of the A6PW specimens.

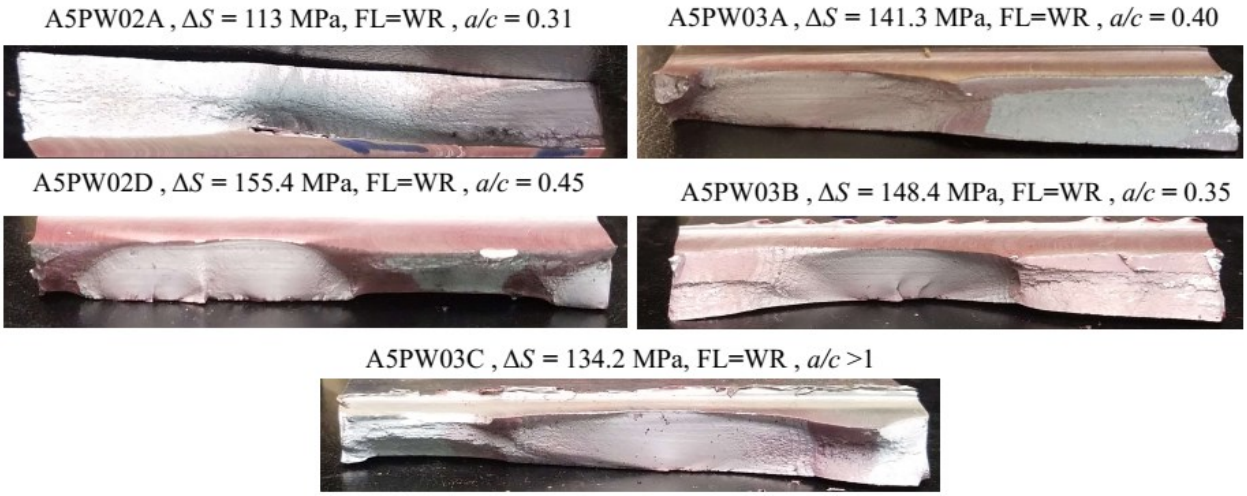

Figure 3.39: Fracture surfaces of polished specimens

Figure 3.40 shows the SBFM analysis results and experimental S-N data for the A5PW specimens under CA loading. One cracking scenario was simulated during the SBFM analysis for A5PW specimens, which is crack initiating from the WR with a/c of 0.45. The defect (JLR) depths for A5PW specimens were found to vary in between 0.033 mm to 0.365 mm based on weld cross-section observation under a microscope. Therefore, the two defects depths of 0.05 mm and 0.40 mm were selected to perform SBFM analysis. The two S-N curves in Figure 3.40, corresponding to two defect depths of a 0.05 mm and 0.40 mm, provide a reasonably good estimation for the fatigue test results.

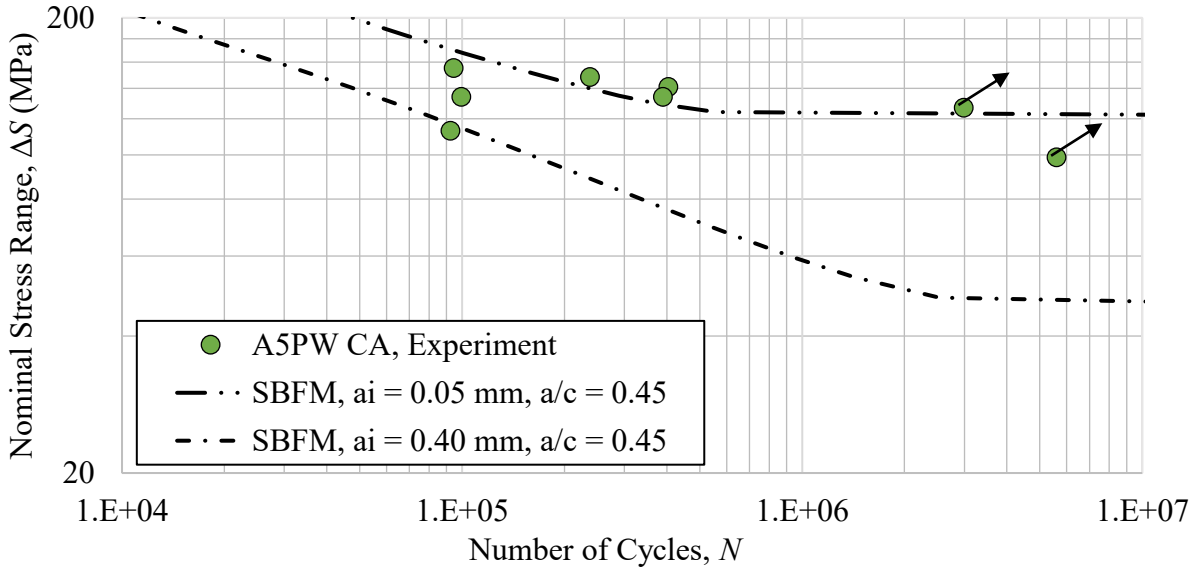

Figure 3.40: SBFM analysis results for A5PW specimens under CA loading

3.3.3.7 Case 7: 5083 Aluminum, Butt joints with wormhole defect

Figure 3.41 shows fracture surfaces of the A5WH specimens under CA loading. All A5WH specimens failed from the bottom of the weld. It can clearly be observed that only one specimen (A5WH01D) had a consistent depth of WH defect. The other specimens had partial WH defects and it failed from that location. Because of the inconsistent WH depths, the final crack aspect ratio varied significantly from almost zero for the last specimen to 0.39 for the first specimen.

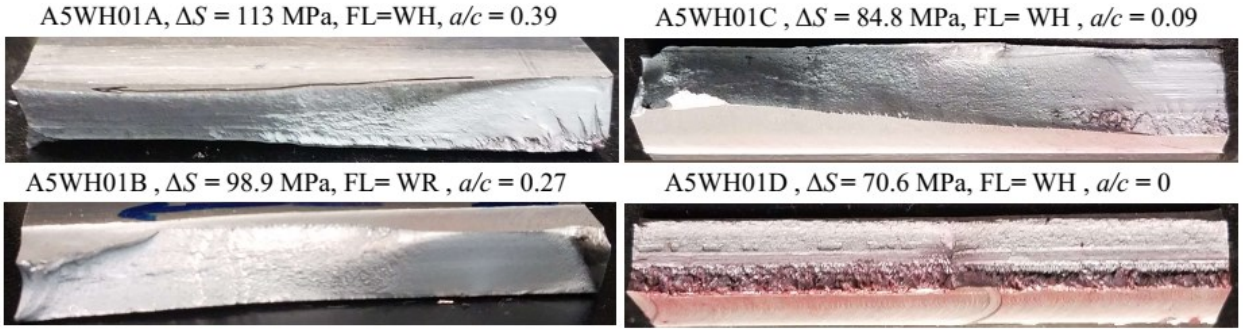

Figure 3.41: Fracture surfaces of specimens with wormhole defect

In Appendix C, WH depth is reported for each specimen, based on microscopic images of the fracture surfaces. The wormhole depths were observed to vary from 0 to 3.18 mm. The last

specimen (A5WH01D) had a consistent wormhole defect and failed after the application of just 2951 cycles.

3.3.4 Summary and conclusions

In this project, the fatigue performance of FSW joint specimens with intentionally introduced welding defects was studied. Welding defects including toe flash, wormhole, and kissing bond defects were studied. It is shown that the toe flash defect in FSW butt joints is not a big concern from a fatigue perspective compared to the wormhole and kissing bond defects. For specimens with wormhole and kissing bond defects, it was found that the fatigue performance was reduced to the level of fatigue performance of an ADM Cat. D detail. Apart from the butt joint specimens, a lap joint detail was also studied and it was found that the fatigue performance of this detail is as good as the fatigue performance of an ADM Cat. D detail. The fatigue performances for all seven types of the specimen are summarized in Table 3.8.

Table 3.8: Fatigue performance of various types of specimens under CA and VA loading

Specimen Type	**Fatigue performance under CA loading (ADM)**	**Fatigue performance under VA loading (ADM)**
A6PW, (a_i < 0.3 mm)	> Cat. A	~ Cat. B
A6PO, (a_i < 0.15 mm)	~ Cat. A	> Cat. B, when ($2 \cdot 10^5 < N < 1 \cdot 10^7$)
A6KB, (a_i < 0.8 mm)	> Cat. D	> Cat. D
A6TF, (a_i < 0.5 mm)	~ Cat. B	~ Cat. B, when (a_i < 0.5 mm)
A6LJ, (a_i < 0.6 mm)	> Cat. D	> Cat. D
A5PW, (a_i < 0.4 mm)	> Cat. B	-
A5WH, (a_i ~3.3 mm)	< Cat. D	-

Based on the fatigue tests, metallurgical analysis, and nonlinear fracture mechanics (1D SBFM) analysis completed for this project, the following conclusions are drawn:

- Properly welded FSW butt joints were generally seen to achieve fatigue performance above the ADM Cat. B. design curve.
- Kissing bond defects on the order of 0.3-1.0 mm in depth in the 6061-T651 alloy specimens generally resulted in a significant fatigue life reduction and a shift in the failure mode from crack initiation on the weld top to the weld root.
- The investigated toe-flash defect had a less significant effect on fatigue performance compared to the kissing bond and wormhole defects.
- The tested lap joint detail resulted in a lower fatigue life than that of the butt joint detail, which can be safely estimated using the ADM Cat. D design curve.
- It is shown that the fatigue test results can be predicted reasonably well, using a nonlinear fracture mechanics (SBFM) model with typically assumed input parameters for 5xxx and 6xxx series alloys and a knowledge of the initial defect geometry.

Further work is recommended to quantify the effects of uncertainty related to defect geometry and material properties on the fatigue performance of FSW joints. Combinations of two or more defect types can also be modelled using SBFM to identify worst-case scenarios from a fatigue perspective. Apart from the studied defects, linear misalignment (i.e. offset) defects should also be studied and a probabilistic analysis should be performed to consider the various sources of uncertainty and quantify their effect on the fatigue performance of FSW joints.

Chapter 4

Testing and Fracture Mechanics Analysis of HFMI Treated Weldments

In this chapter, new fatigue tests conducted on cruciform welded specimens are described. The specimens were fabricated with metal intert gas (MIG) welding process and then subjected to high-frequency mechanical impact (HFMI) treatment. Further, the geometry measurements and metallurgical analyses of the tested specimens are presented, and fatigue life estimation using the 2D SBFM model is discussed. The specimens were fabricated from 9.5 mm (3/8") thick aluminum (5083-H321) and high strength steel (ASTM A514) plate. The specimen geometry and preparation followed procedures used in another study (Ghahremani 2015) on mild steel (CSA 350W) cruciform welded joints. Fatigue tests were performed on the as-welded (AW) and HFMI treated specimens under two loading histories (constant amplitude with and without periodic underloads) at several equivalent stress ranges. Residual stress distributions were estimated based on experimental data obtained using the x-ray diffraction technique. In addition, weld toe geometry measurements were obtained using silicon impressions and micro-hardness distributions were obtained on polished weld samples for each material type. Hardness measurements and silicon impressions were used to establish input parameters needed for the SBFM model. The effectiveness of the 2D SBFM model in estimating the fatigue test results for the three materials, including the CSA 350W steel, is assessed.

4.1 Background

The potential of the HFMI treatments for fatigue retrofitting of existing structures or weight reduction in new fatigue critical components is considerable. Various studies have been undertaken to quantify the resulting fatigue life increase and investigate: the significance of scale effects (Roy, Fisher, and Yen 2003), the treatment effectiveness for high strength steels (Roy et al. 2003; U. Kuhlmann, J. Bergmann, A. Dürr, R. Thumser, H.-P. Günther 2005; Weich et al. 2009), the treatment effectiveness under variable amplitude loading (Yildirim and Marquis 2013), and, the effects of treatment quality control (Ghahremani, Safa, et al. 2015; Tehrani Yekta et al. 2013). Estimation of the HFMI treatment benefit has been limited to comparison using nominal stress-life (S-N) curves (Marquis et al. 2013) and local stress approaches (Ghahremani 2015). Only a few

studies have used fracture mechanics models to estimate the fatigue life increase due to HFMI treatment either alone or in two-stage (initiation-propagation) models (G. Josi 2010; Ghahremani 2015; Tehrani Yekta et al. 2013; V.-M. Lihavainen 2006). Considering these previous studies, this study presents new fatigue tests on HFMI treated welds, aimed at extending the current database of test results, and providing a means for validating a 2D SBFM model over a broader range of material properties and loading conditions.

In the following sections of this chapter, the fatigue test program is first described. Following a presentation and statistical analysis of the fatigue test results, the results of residual stress measurements, weld toe geometry measurements, and, metallurgical analyses of the HFMI treated weld toes are presented. Input parameters used for the fracture mechanics model are then presented and the benefits of the model as a tool for modelling the effects of impact treatments on fatigue performance are discussed. Following this, the effectiveness of the model in estimating the fatigue life of specimens fabricated with A514 steel, 5083 aluminum, and 350W steel is critically assessed.

4.2 Description of the fatigue test program

Welded joint specimens were fabricated from 9.5 mm (3/8") thick aluminum (5083-H321) plate (nominal HAZ properties: σ_y = 115 MPa, σ_u = 270 MPa) and high strength steel (ASTM A514) plate (nominal base metal properties: σ_y = 690 MPa, σ_u = 760-895 MPa). 5083 aluminum (chemical designation: Al Mg4.5Mn0.7) is a common alloy for structural sheet applications. Nominally, it contains 4.0-4.9 wt. % Mg, 0.05-0.25 wt. % Cr, and 0.4-1.0 wt. % Mn. The H321 temper indicates that it has been strain-hardened and partially annealed (quarter hard). A514 steel is a weldable, high yield strength, quenched and tempered alloy steel. According to the mill test, the steel used in the current study contained: 0.18 wt. % C, 1.22 wt. % Mn, 0.014 wt. % P, 0.004 wt. % S, 0.24 wt. % Si, 0.02 wt. % Ni, 0.12 wt. % Cr, 0.14 wt. % Mo, and 0.02 wt. % Cu.

The stiffener welds were fabricated by the MIG welding process. The welds have a nominal size of 6.4 mm and were performed in a single pass. Following the fabrication of the 300 mm wide welded plate samples, HFMI treatment was applied to a number of the samples (see Figure 4.1).

Figure 4.1: HFMI treatment of 12 ” long high strength steel weld

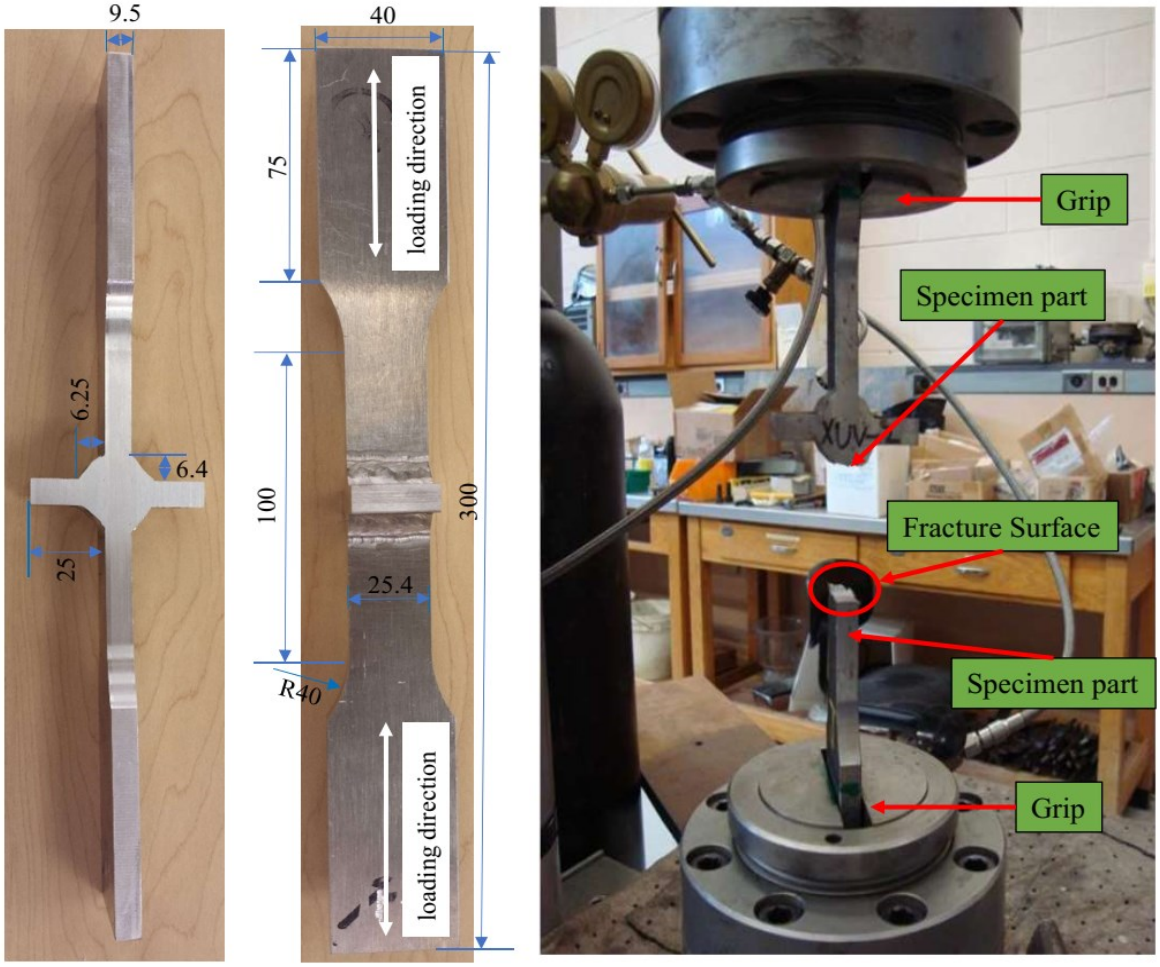

Figure 4.2: Component geometry (left), fatigue test frame (right), all dimensions in mm

The HFMI tool was set to an amplitude of 50-60 μm for the steel specimens and 40 μm for the aluminum specimens, which resulted in a similar indent depth for both materials. According to the tool supplier, the tool operates at a vibration frequency of 20 kHz with an impact frequency of about 220 Hz (depending on the contact pressure). The treatment was performed using a single 3 mm ϕ pin. After treatment, the 300 mm wide samples were cut with a saw into 50 mm wide strips, which were machined to their final "dog bone" shape using a CNC machine (see Figure 4.2, left).

Fatigue tests were performed under uni-axial loading in an MTS test frame shown in Figure 4.2 (right). Table 4.1 shows the test matrix for the fatigue test program, which includes the details of the welding process and the wire used. The test program consisted of 48 fatigue tests on welded specimens. Of these, 24 specimens were fabricated of aluminum and 24 of high strength steel. Half of the specimens were tested in the "as-welded" (AW) condition and half were tested in an "HFMI treated" (HFMI) condition. Two loading histories were investigated: constant amplitude (CA) loading at a stress ratio, R (= S_{min} / S_{max}), of 0.1 and constant amplitude loading with periodic under-loads (CA-UL) as shown in Figure 2.6. The fatigue tests were carried out using a 100 kN MTS test frame at test frequencies that varied with the loading level and ranged between 10 and 50 Hz. The tests were monitored and run until complete specimen fracture. In general, tests were halted if cracking was not observed after ~4 million cycles, in this case, the test was labelled as a "run-out".

Table 4.1: Test matrix for the experimental fatigue test program

Material	**Welds**	**Loading**	**Treatment**		**Number of Specimens**
A514 Steel	MIG, ER70S-6 wire 0.9 mm ϕ	CA	AW	-	6
			HFMI	50-60 μm	6
		CA-UL	AW	-	6
			HFMI	50-60 μm	6
5083-H321 Aluminum	MIG, 5356 wire 1.2 mm ϕ	CA	AW	-	6
			HFMI	40 μm	6
		CA-UL	AW	-	6
			HFMI	40 μm	6

4.3 Fatigue test results

The results of the fatigue tests under CA loading on 5083 aluminum and A514 steel specimens are summarized in Figure 4.3. For comparison purposes, fatigue test results on mild steel (CSA 350W) under CA loading from (Ghahremani 2010, 2015; Tehrani Yekta et al. 2013) are shown in Figure 4.4. The 350W steel specimens were treated using two different HFMI tools and slightly different treatment parameters. These figures show the beneficial effect of the HFMI treatment on the fatigue lives of the welded specimens. In Figure 4.3 and Figure 4.4, the "as-welded" specimens are indicated with red/pink symbols and the HFMI treated specimens are indicated in blue symbols. A filled symbol indicates that the specimen failed, whereas a hollow symbol indicates a "run-out".

In all cases, the blue symbols are shifted to the right in comparison to the red/pink symbols at the same level of stress range, indicating that an increase in fatigue life has resulted from the HFMI treatment. In general, this fatigue life increase is more pronounced for the mild and high strength steel specimens than for the aluminum specimens.

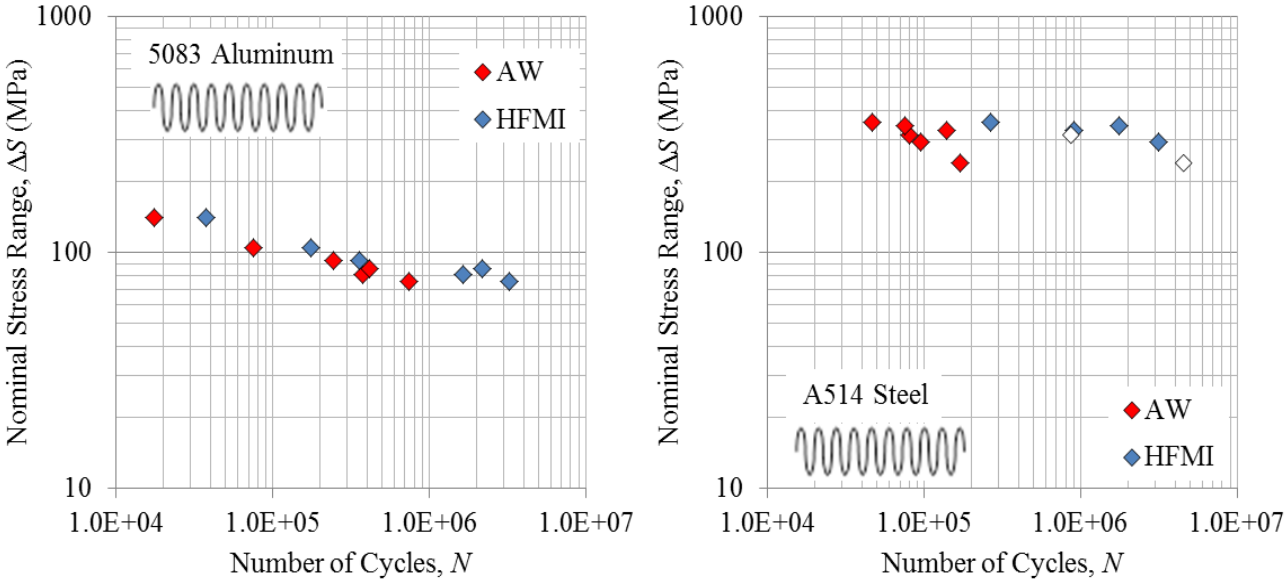

Figure 4.3: Fatigue test results for 5083 aluminum and A514 steel specimens under CA loading

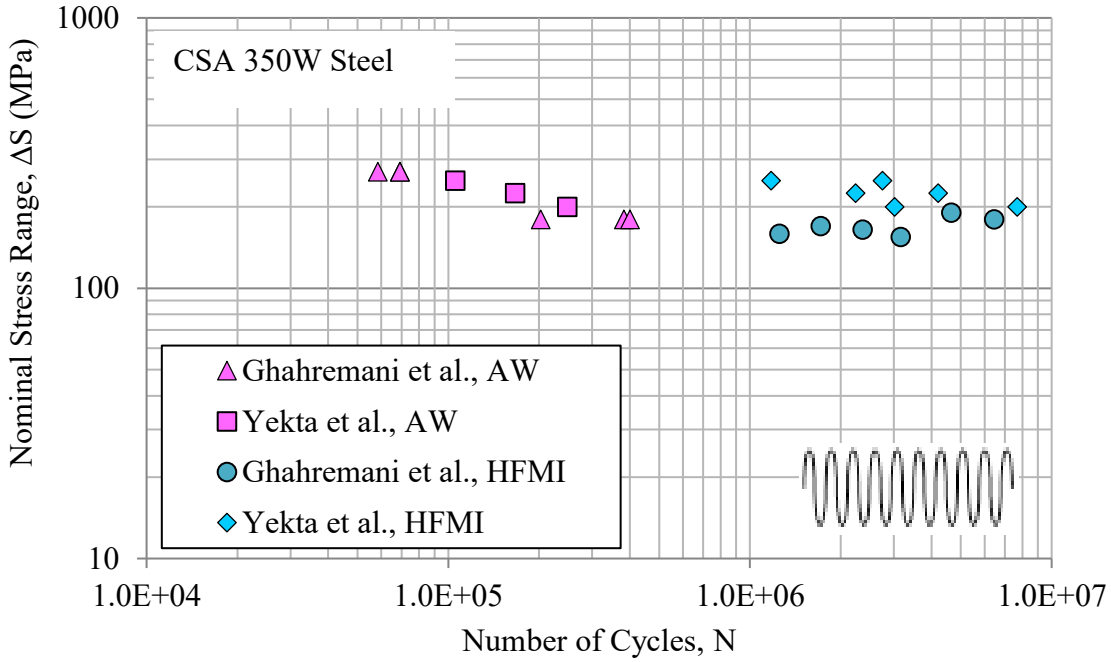

Figure 4.4: Fatigue test results for 350W steel specimens under CA loading

Fatigue test results under CA-UL loading condition are shown in Figure 4.5 and Figure 4.6 for 5083 aluminum and A514 steel specimens respectively. Fatigue life improvement was observed under CA-UL loading condition for both the materials. The extent of the fatigue life improvement is lower under CA-UL loading compared to the fatigue life improvement under CA loading. In fact, there is a load level for the aluminum (under CA-UL loading) for which the as-welded and treated data points overlap (see Figure 4.5). This result can be explained by the natural scatter of the test data and the minimal benefit of HFMI treatment for the aluminum due to the low magnitude of the beneficial compressive residual stress for this material as observed from residual stress measurement data.

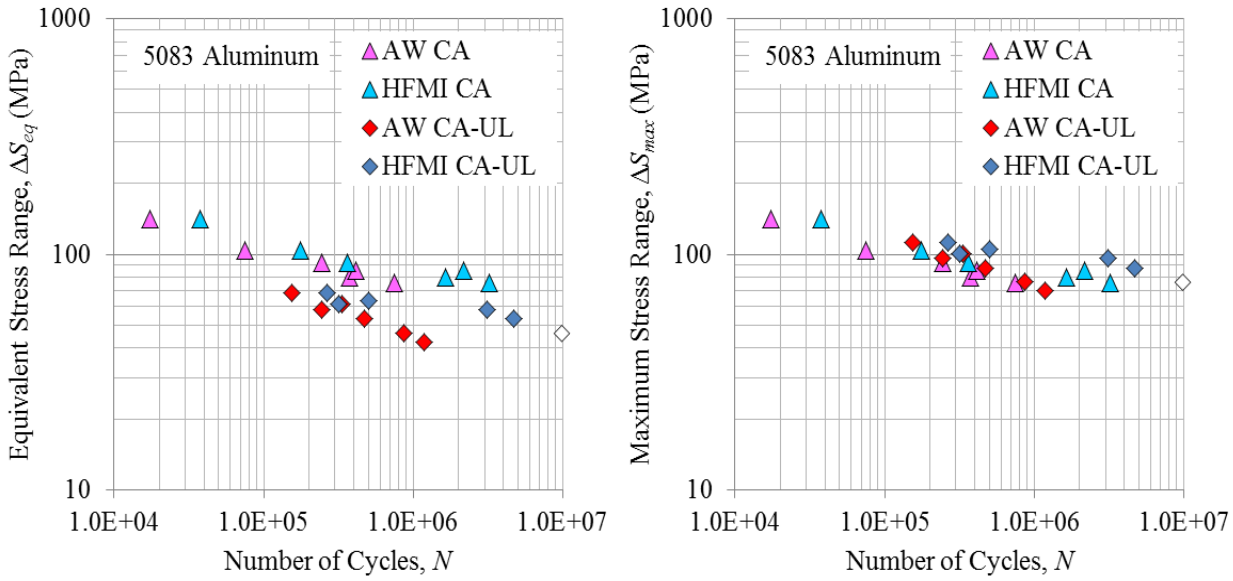

Figure 4.5: Fatigue test results for 5083 aluminum specimens under CA and CA-UL loading

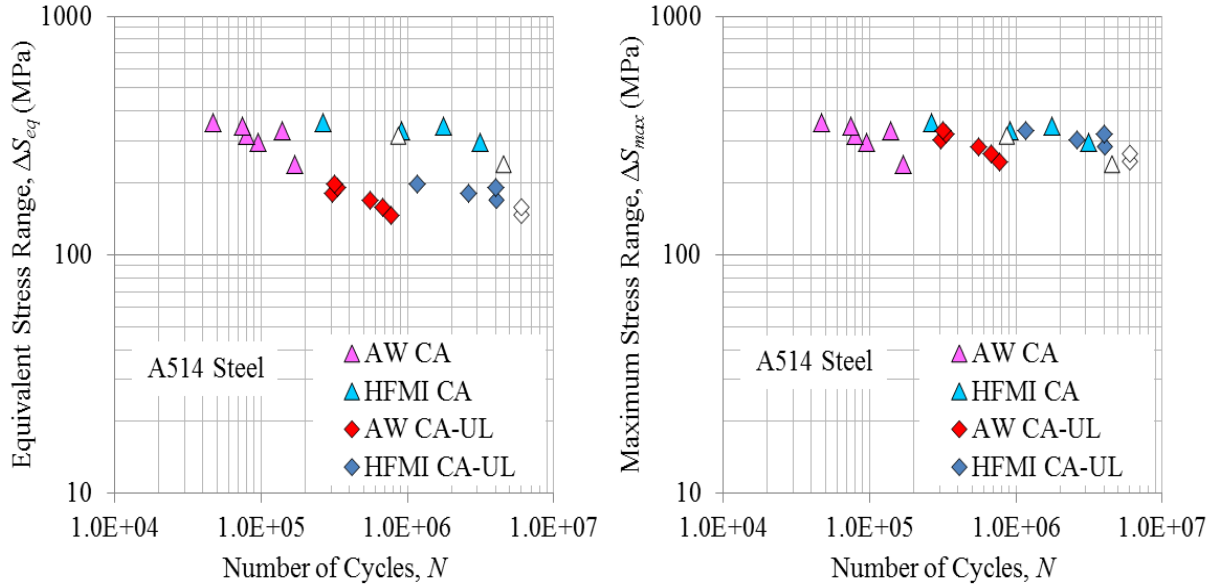

Figure 4.6: Fatigue test results for A514 steel specimens under CA and CA-UL loading

For the constant amplitude (CA) test results, the plotted stress range, ΔS, is simply $S_{max} - S_{min}$. The stress is simply the nominal stress or the load divided by the nominal cross-sectional area. For the variable amplitude (CA-UL) tests, there are both large and small stress blocks. It was,

therefore, necessary to calculate an equivalent stress range based on the Palmgren-Miner summation method, i.e.:

$$\Delta S_{eq} = \left(\frac{\Delta S_1^{m'} \cdot N_1}{N_{tot}} + \frac{\Delta S_2^{m'} \cdot N_2}{N_{tot}} \right)^{1/m'} \tag{4.1}$$

where ΔS_1 is one stress range and ΔS_2 is the other. For the CA-UL loading history, N_1 = 50 large cycles, N_2 = 950 small cycles and N_{tot} = 1000 cycles. The parameter *m'* in Equation (4.1) is the assumed slope of the constant amplitude S-N curve. In accordance with North American structural design codes for steel and the IIW recommendation (Anon 2006; Marquis and Barsoum 2016), *m'* was taken as 3.0 for the as-welded specimens and 5.0 for the HFMI treated specimens respectively. In accordance with the aluminum design manual (Anon 2010), for aluminum, the value of *m'* was taken as 3.64 for the tested transverse stiffener detail, which is classified as "Detail Category C". The use of Equation (4.1) along with the assumed S-N curve slopes are applicable when: 1) there is no "knee" in the S-N curve, and 2) failure will occur when the Palmgren-Miner sum reaches a value of exactly 1.0. Some researchers have suggested that a damage sum other than 1.0 should be associated with failure (e.g.: (Sonsino 2008; Yıldırım, Marquis, and Sonsino 2016)), and it can be argued that different S-N curve slopes could be used in Equation (4.1). For these reasons, the CA-UL results are plotted in Figure 4.5 and Figure 4.6 using two stress range measures: 1) the equivalent stress range, ΔS_{eq}, based on Equation (4.1) with the design S-N curve slopes for as-welded steel and aluminum, and 2) the maximum stress range, ΔS_{max}.

The equivalent stress range for VA1 and VA2 loading history, which was used for fatigue testing of 350W mid steel specimens, were calculated using the Palmgren-Miner summation method. The first cycle of the VA loading history was the biggest cycle which corresponded to peak (maximum) stress range of the loading history and was used as a reference stress range. For a peak stress range of 1, the factor used to evaluate the equivalent stress range for different VA loading histories is provided in Table 4.2, where it is labelled as "VA loading factor" (= ΔS_{eq} / ΔS_{max}). The VA loading history was scaled to obtain loading histories corresponding to different equivalent stress ranges. The peak (maximum) stress range of the scaled loading history was multiplied with the tabulated VA loading factor to obtain the equivalent stress range.

Table 4.2: VA loading factor calculated based on the Palmgren-Miner summation method

Material and Loading Type	VA Loading Factor
Steel / Aluminum: CA	1.00
Steel AW: CA-UL (m' = 3.0)	0.597
Steel HFMI: CA-UL (m' = 5.0)	0.631
Steel AW: VA1 (m' = 3.0)	0.479
Steel HFMI: VA1 (m' = 5.0)	0.555
Steel AW: VA2 (m' = 3.0)	0.361
Steel HFMI: VA2 (m' = 5.0)	0.469
Aluminum AW/HFMI: CA-UL (m' = 3.64)	0.606

The purpose of the CA-UL loading tests was to investigate the effectiveness of the HFMI treatment under a loading history that is known to be particularly severe for HFMI treated welds. Specifically, loading histories with periodic "underload" cycles, where the minimum stress level is significantly lower than the other cycles tend to result in lower fatigue lives for HFMI treated welds, since the underload cycles can have two negative effects (Walbridge 2008): 1) reducing the crack opening stress level, and thus increasing the portion of each cycle that causes fatigue damage, and 2) relaxing the residual stresses, due to the cyclic plasticity that occurs at the weld toe. Looking at the results under CA-UL loading in Figure 4.5 and Figure 4.6, it can be seen that a significant fatigue life increase still resulted due to HFMI treatment, even under this loading history.

4.4 Statistical analysis of fatigue test results

In order to better understand the fatigue performance increase resulting from HFMI treatment, a statistical analysis of the fatigue test data obtained under CA loading was performed, using the procedure recommended by the International Institute of Welding (IIW) (Hobbacher 2011). According to this approach, the fatigue life, N, is treated as the dependent variable, which varies depending on the nominal stress range, ΔS. Given the test results and the number of data points, the S-N curve slope and intercept on the y-axis can be established for a given survival probability. In Table 4.3 and Figure 4.7, results are summarized for the mean curve (50% survival

probability) and a "design" curve. The IIW normally assumes a survival probability of 95% for the design curve. The S-N curve is defined as follows:

$$\log(N) = \log(C') - m' \cdot \log(\Delta S) \tag{4.2}$$

where C' and m' are constants representing the vertical position and slope of the S-N curve respectively. In Table 4.3, the values for C' and m' are given for the mean (μ) and design (d) S-N curves.

Table 4.3: S-N curve parameters based on IIW statistical analysis (units: MPa)

Material	Treatment	m'	$\log(C')_\mu$	Std. Dev. of $\log(C')$	$\log(C')_d$
5083 Aluminum	AW	6.07	17.2391	0.0903	16.9451
	HFMI	7.35	20.2544	0.1944	19.6216
350W Steel (Ghahremani, Walbridge, et al. 2015)	AW	3.84	14.1902	0.0954	13.9233
	HFMI	4.41	16.8303	0.1945	16.1972
A514 Steel	AW	2.39	10.9215	0.1323	10.4907
	HFMI	5.61	20.1075	0.2702	19.2281

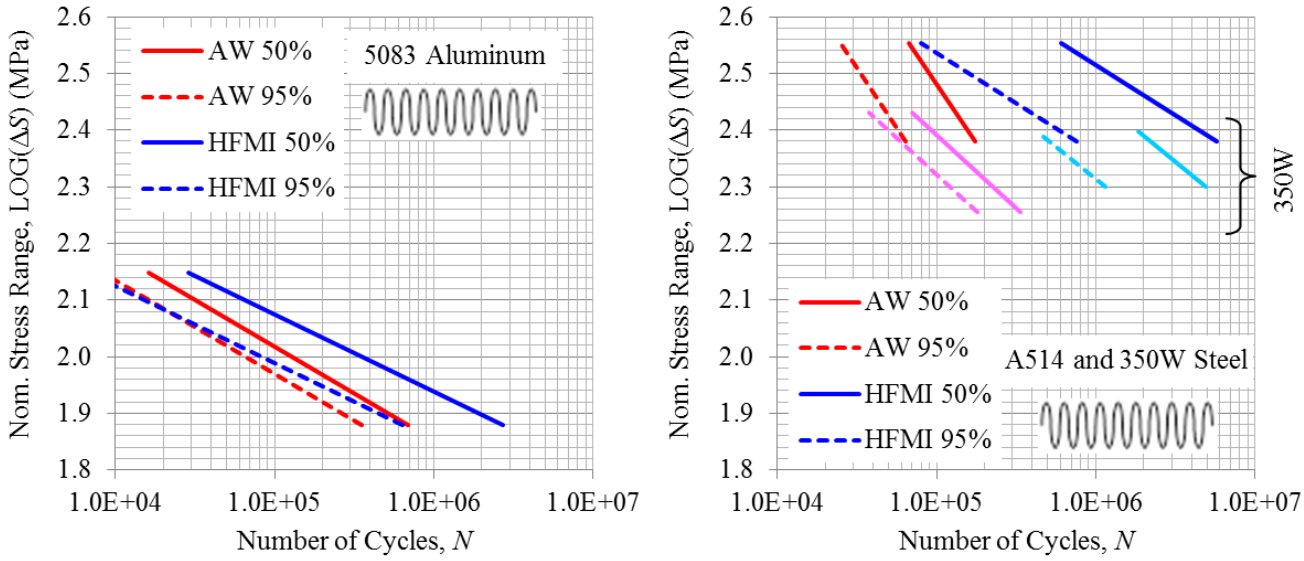

Figure 4.7: Mean and design S-N curves for aluminum and steel specimens

It can clearly be observed from Table 4.3 and Figure 4.7 that a significant increase in the fatigue performance (increase in fatigue strength or fatigue life) resulted for both materials,

regardless of whether the mean or design S-N curves are compared. In general, the fatigue performance increase due to HFMI treatment increases as the nominal stress range decreases, due to the shallower slope of the S-N curves for the treated specimens.

4.5 Static and cyclic materials tests

Static tension tests were performed in accordance with (ASTM E8 2010) on three base metal coupons and three HAZ simulated coupons of each material type. The test coupons made of aluminum were heat-treated in accordance with (ASTM B918/B918M-17a 2017). The heat-treated coupons were prepared by subjecting the base metal coupons to a heating cycle which the heat-affected zone (HAZ) adjacent to the welds is subjected during arc welding of metal joints. Specifically, the coupons were subjected to the temperature history shown in Figure 4.8 for A514 steel and Figure 4.9 for 5083 Aluminum followed by "mass quenching" to room temperature using a procedure developed in (Ghahremani 2015). The A514 steel coupons were kept at a temperature of 990°C for 30 minutes and 5083 aluminum coupons were kept inside the oven at a temperature 342°C for 67 minutes.

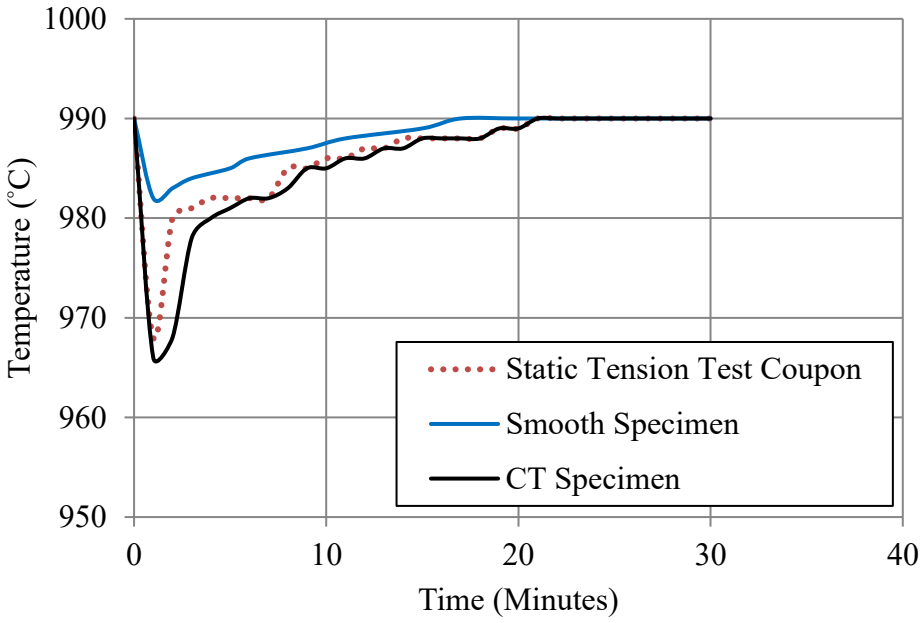

Figure 4.8: Oven temperature during heat treatment of A514 steel coupons

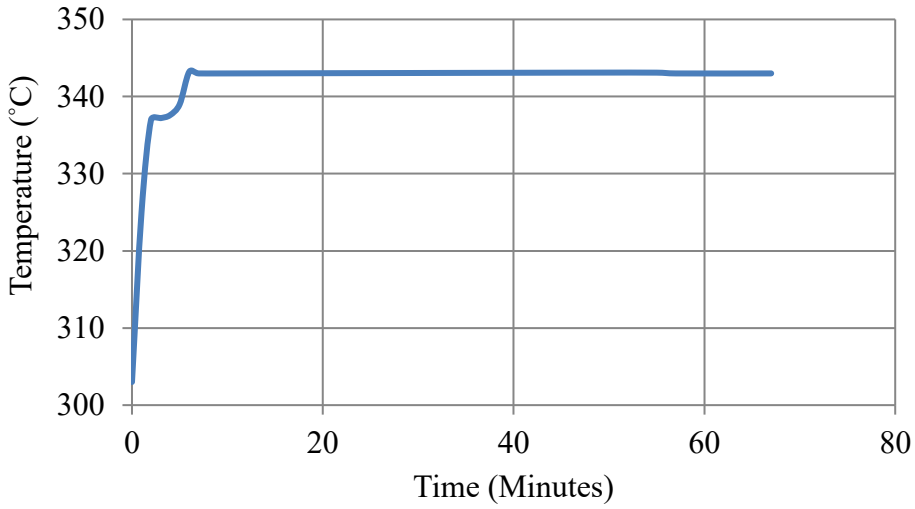

Figure 4.9: Oven temperature during heat treatment of 5083 Aluminum coupons

Rockwell hardness tests were performed before and after heat treatment to assess the effect of heat treatment. The change in hardness for different types of the coupon is summarized in Table 4.4. The hardness data shows that both materials softened after heat treatment.

Table 4.4: Hardness test results before and after heat treatment

Test Coupon Type	**Hardness (Rockwell C Scale)**	
A514 Steel	**Before Heat Treatment**	**After Heat Treatment**
Tension Test (dog-boned)	26	19
Smooth Specimen	24	23
CT Specimen	23	19
5083 Aluminum	**Hardness (Rockwell B Scale)**	
Tension Test (dog-boned)	54	33
Smooth Specimen	55	34
CT Specimen	56	35

4.5.1 Static tension tests of material

Three coupons of base metal and three coupons of simulated HAZ material were tested under static tension load to estimate the value of elastic modulus, yield strength, ultimate strength, and monotonic Ramberg-Osgood material model parameters K_m' and n_m'. Engineering stress-strain plots for the A514 steel are provided in Figure 4.10 and Figure 4.11. Tests with a clip gauge

on the coupons were used to estimate elastic modulus and yield strength of the material, while tests without clip gauge were used to estimate the ultimate strength of the material.

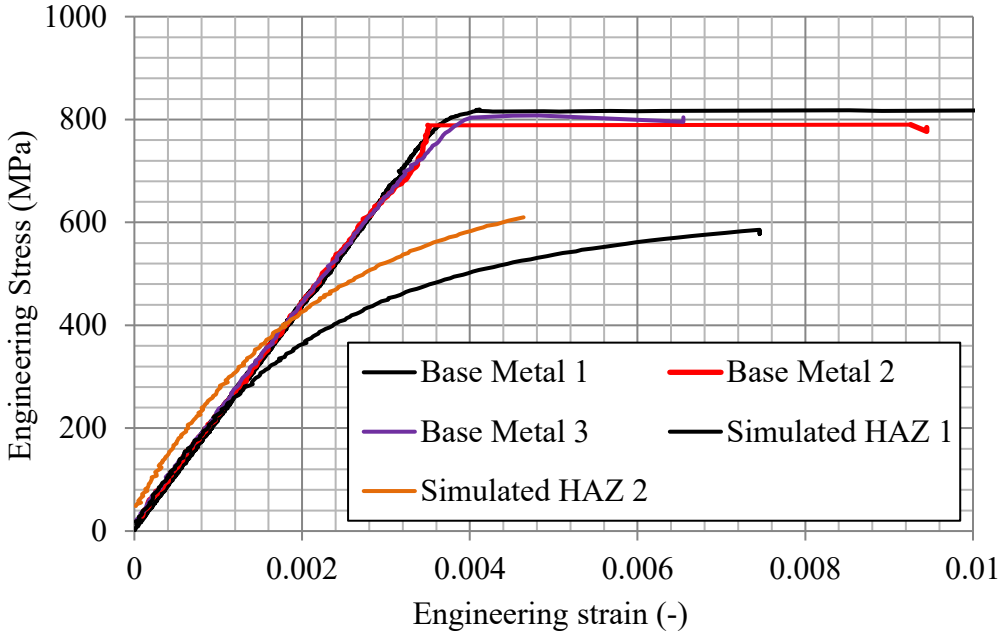

Figure 4.10: Static tension test results for A514 steel coupons with clip gauge

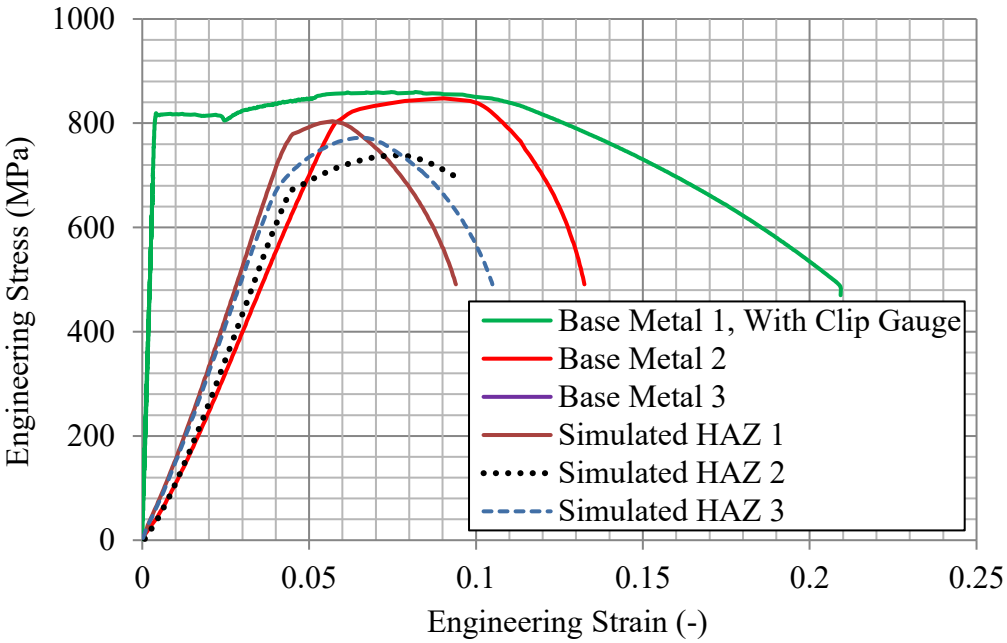

Figure 4.11: Static tension test results for A514 steel without clip gauge

The monotonic Ramberg-Osgood material model parameters were estimated from data obtained during a static tension test with a clip gauge. The resulting elastic modulus (E), yield strength (σ_y), ultimate strength (σ_u), monotonic (K_m') and monotonic (n_m') values are summarized in Table 4.5. Engineering stress-strain plots for 5083 aluminum are provided in Figure 4.12.

Table 4.5: Summary of static tension test results for 5083 aluminum and A514 steel coupons

Treatment Condition and Material Type	**Elastic Modulus (MPa)**	**Yield Strength (MPa)**	**Ultimate Strength (MPa)**	**Monotonic K_m' (MPa)**	**Monotonic n_m'**
Base Metal, 5083 aluminum	71389	243.33	365.50	440.56	0.086
Simulated HAZ, 5083 aluminum	71978	124.00	324.22	369.75	0.142
Base Metal, A514 steel	211724	814.67	849	1088.67	0.043
Simulated HAZ, A514 steel	210361	566.5	771.33	818	0.055

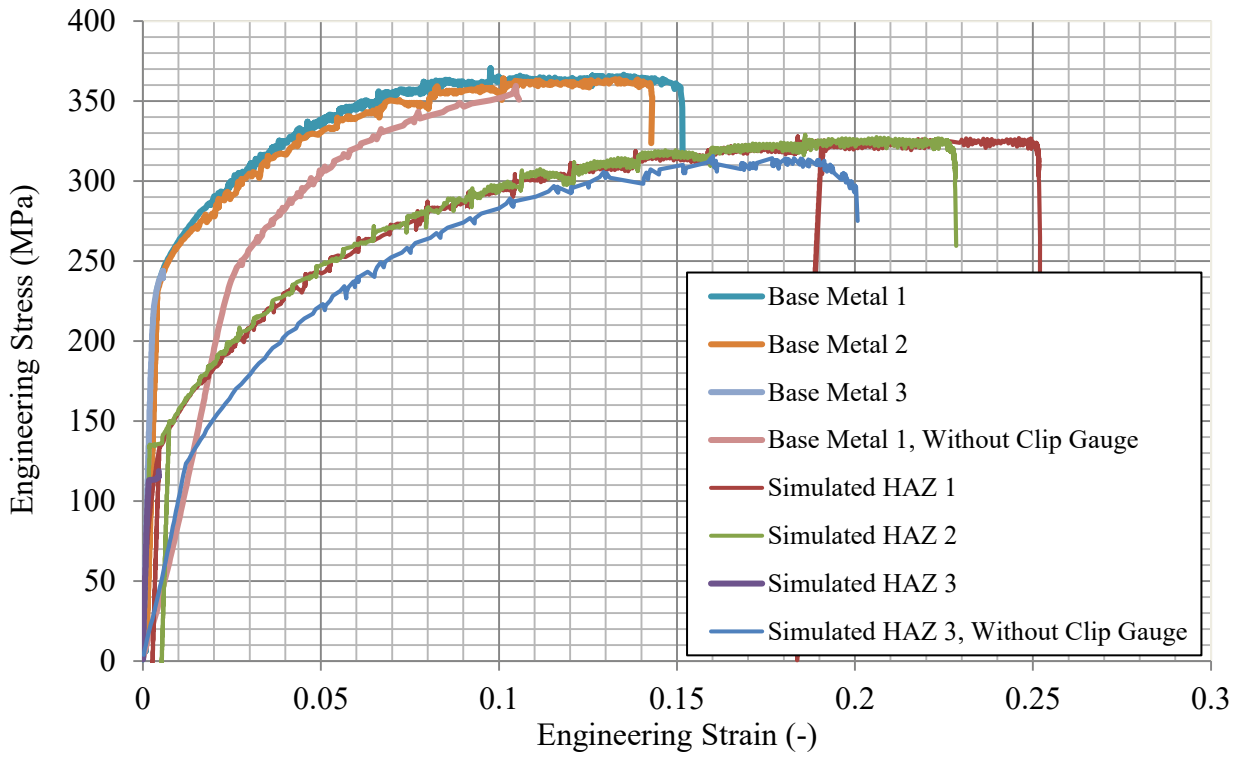

Figure 4.12: Static tension test results for 5083 aluminum specimens

4.5.2 Cyclic material tests on smooth specimens

Cyclic materials tests were conducted on three base metal and three HAZ simulated smooth specimens to determine the cyclic Ramberg-Osgood material constants (*K'* and *n'*). These tests were performed on polished smooth cylindrical, variable width specimens having a 5.0 mm diameter within the 7.6 mm (0.3") gauge length as shown in Figure 4.13 (left). The tests were conducted by imposing strain cycles (10 per strain level) at load ratio, R = -1.0 in increments of 0.1% up to ±1.0% strain and then back down to ±0.1% strain, and repeating until the load stabilized for each strain level as shown in Figure 4.13 (right).

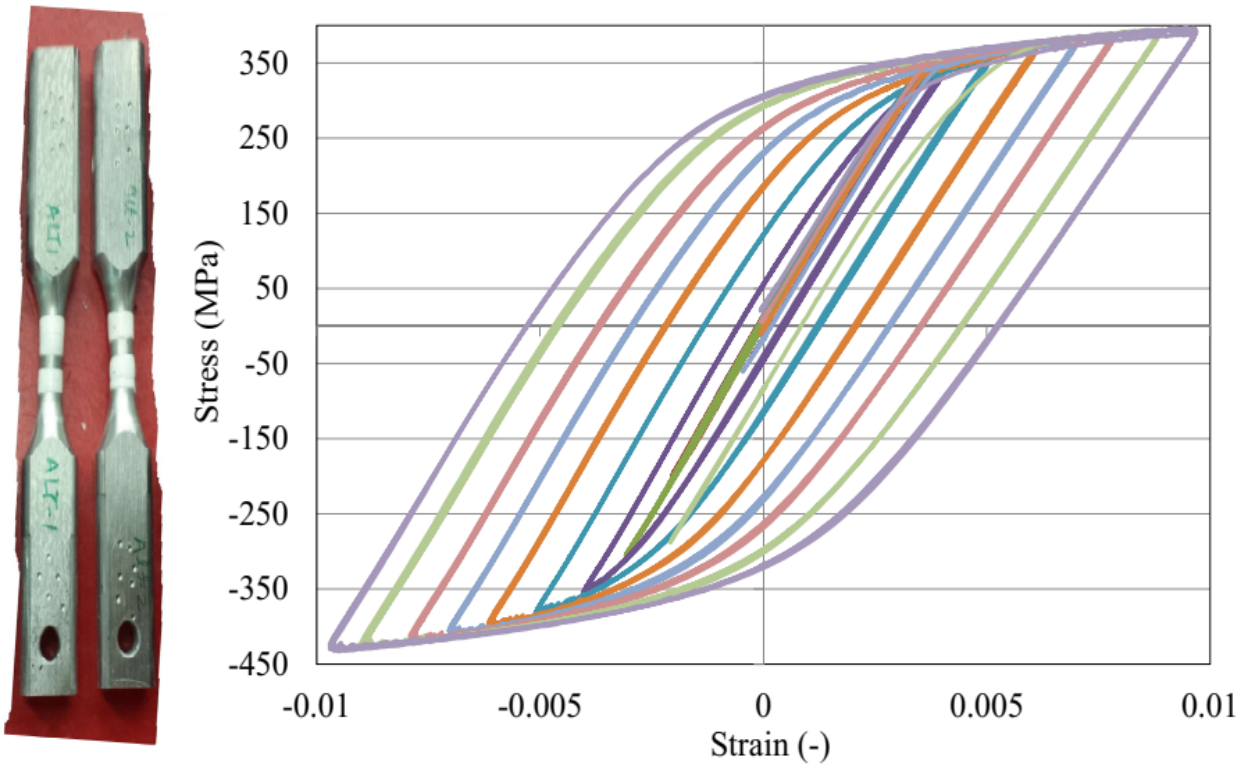

Figure 4.13: Smooth specimen used in the cyclic materials tests (left) and stress-strain response (right) for simulated HAZ aluminum specimen

The constants *K'* and *n'* were determined by fitting the cyclic Ramberg-Osgood model to the stabilized stress-strain data as shown in Figure 4.14. The cyclic material test results are summarized in Table 4.6.

Table 4.6: Cyclic material test results performed on aluminum and high strength steel specimen

Parameter	5083 Aluminum		A514 Steel		Units
	Base Metal	Simulated HAZ	Base Metal	Simulated HAZ	
K' (cyclic)	643.0	475.0	2033.7	1251.3	MPa
n' (cyclic)	0.1000	0.0567	0.2110	0.1480	-

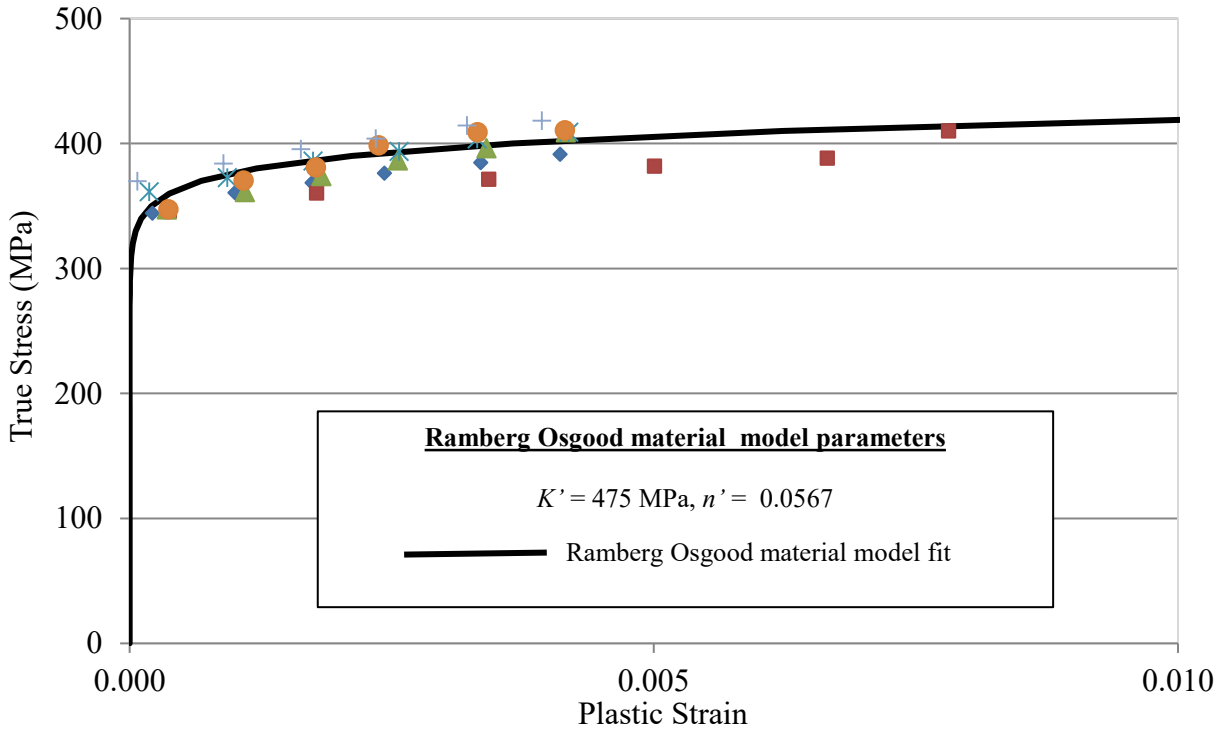

Figure 4.14: Fitted cyclic Ramberg-Osgood material model parameters for simulated HAZ aluminum samples

4.6 Residual stresses, geometry measurements, and metallurgical analysis

Residual stress measurements on untested HFMI treated specimens were performed using a procedure of electropolishing and x-ray diffraction (XRD) by an external laboratory (Proto Manufacturing Ltd., Canada). The residual stress measurement results are shown in Figure 4.15. A significant scatter in the residual stress measurement data can be seen in this figure. In general, the HFMI treatment introduced compressive residual stress near the surface of the treated weld toe in the range of 75-200 MPa for the aluminum specimens and 300-600 MPa for the A514 steel

specimens. The scatter in the measured residual stress is significant – for one of the aluminum welds (at two depths) - the near-surface residual stress after HFMI treatment was seen to be almost zero.

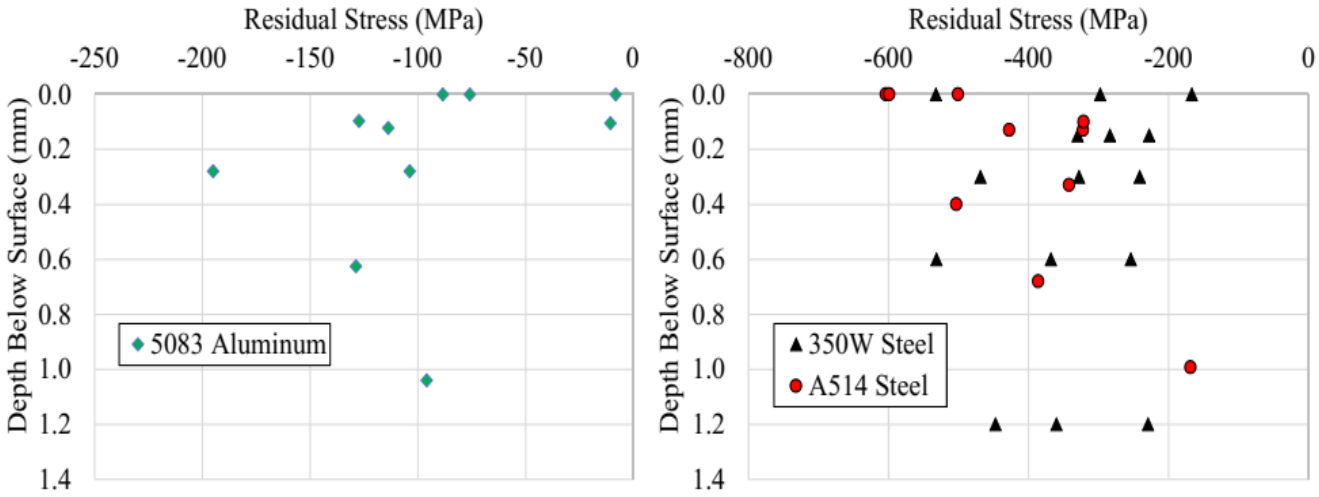

Figure 4.15: Residual stress measurements on aluminum (left) and steel (right) weld samples

Comparing the results for the two steel grades, it can be seen that the residual stresses for the A514 steel are at the higher end of the range of the results for 350W steel specimens tested in (Tehrani Yekta et al. 2013). A larger difference was expected. However, it should be noted that the 350W steel specimen was treated at a different time, by a different operator, with a different tool and treatment settings, so quantitative conclusions regarding the effect of material strength on these results cannot be easily made.

Weld toe geometry measurements were also performed using a method of silicon impressions and photographs previously used in (Tehrani Yekta et al. 2013). Figure 4.16 shows an impression being taken and the definitions of the dimensions measured. Figure 4.17 shows an impression slice photograph and the dimensions after treatment being measured.

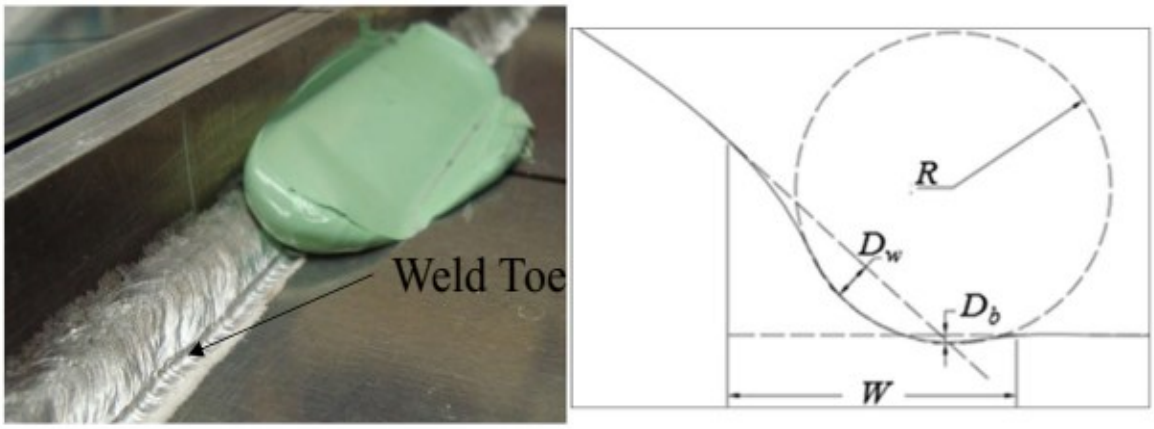

Figure 4.16: Silicon impression of the 5083-H321 aluminum specimen after HFMI treatment (left) and definition of indent depth (on the weld side and base metal side) and radius

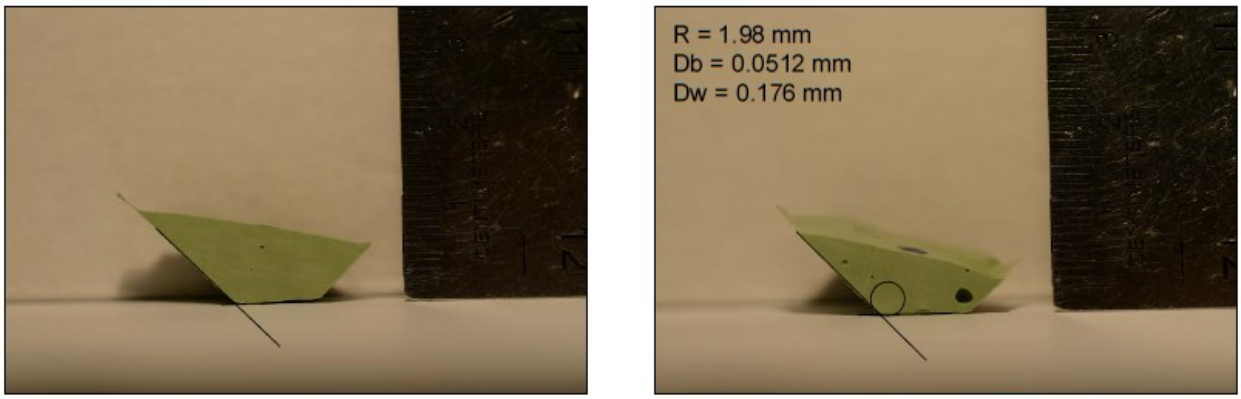

Figure 4.17 Silicon impression of A514 steel specimen before (left) and after (right) treatment.

The HFMI indent geometry measurement results are summarized in Table 4.7. To gain an understanding of the scatter in the weld toe geometry dimensions, impressions from four aluminum and four steel specimens were taken before and after HFMI treatment. The impressions taken before treatment mainly served to confirm that the notch before treatment was sharp ($R_w \leq 0.5$ mm) and to establish the angle, θ, between the weld surface and the base metal surface (see Figure 4.16). The impressions taken after treatment at the same location were then used to measure the weld toe radius, R_w, and the indent depths on the weld and base metal sides of the weld toe, D_w and D_b. To perform the geometry measurements, the images were imported into AutoCAD (see Figure 4.17).

Each of the four impressions was sliced at three locations to see the parameter variations along the same weld toe.

Table 4.7: HFMI indent geometry measurements

Material		D_b (mm)	D_w (mm)	D_{avg} (mm)	R (mm)
5083 Aluminum	Average	0.161	0.136	0.149	2.21
	Std. Dev.	0.058	0.044	0.044	0.24
350W Steel (Tehrani Yekta et al. 2013)	Average	0.312	0.390	0.351	2.03
	Std. Dev.	0.278	0.305	0.126	0.29
A514 Steel	Average	0.177	0.162	0.170	1.93
	Std. Dev.	0.086	0.056	0.052	0.26

In general, the HFMI treatment of the 5083 aluminum and A514 steel specimens resulted in an indent with a radius of ~2 mm and a depth (average of depth on weld side, D_w, and base metal side, D_b) of ~0.15 mm. An effort was made during the treatment of these specimens to achieve the same indent depth in both materials, by varying the needle displacement range on the treatment tool. This was essentially achieved, as seen in Table 4.7. Comparing the measurements for these materials with the indent geometry measurements from (Tehrani Yekta et al. 2013), it can be seen that the treatment of the mild steel (CSA 350W) specimens in (Tehrani Yekta et al. 2013) resulted in an average indent depth (D_{avg}) with more scatter, but also a much higher mean of 0.351 mm. In both studies, the treatment was performed until visual evidence of the weld toe was removed, and an indent was achieved, which could be measured with a welder's undercut gauge.

One parameter that has a significant impact on fracture mechanics based fatigue life calculations is the crack shape, normally described by the depth-to-width ratio, a/c. Although this parameter was not monitored during the fatigue testing, the fractured specimen ends were photographed after the test program was completed, and the images were used to determine the final crack shape. The average results for all of the aluminum and high strength steel specimens tested in this study are summarized in Table 4.8. These results were obtained by fitting an ellipse through the digital image of the final crack shape and then measuring the dimensions of the ellipse. Looking at this table, it can be observed that the final crack aspect ratio is systematically larger for the HFMI treated samples. The suspected reason for this trend is that the impact treatment slows

down the crack growth in the transverse (*c*) direction along the treated surface more than in the depth (*a*) direction. No clear trend can be seen between loading type and crack shape. A similar trend has been reported in other studies (Yuan and Sumi 2015).

Table 4.8: Measured average value of final crack aspect ratio (*a/c*) from observation of fracture surfaces

Material:	**5083 Aluminum**		**A514 Steel**	
Loading:	**CA**	**CA-UL**	**CA**	**CA-UL**
AW	0.34	0.33	0.20	0.24
HFMI	0.50	0.48	0.58	0.60

In addition to the residual stress, weld toe geometry, and crack shape measurements, samples of the weld toes were sectioned and polished for metallurgical analysis, including micro-hardness measurements. Figure 4.18 shows typical results of the Vicker's micro-hardness measurement study along the expected crack path for the 5083 aluminum welds (two as-welded and two HFMI treated samples). For the as-welded specimen, the Vickers hardness near the weld toe was about 85, while for the treated specimen hardness varied to a maximum value of about 120 as shown in Figure 4.18. In a subsequent study, 2D hardness "maps" were also generated in a region near the weld toes of representative samples for each material type and treatment condition. The hardness test results for the as-welded and HFMI treated 5083 aluminum welds are shown in Figure 4.19 and Figure 4.20 respectively.

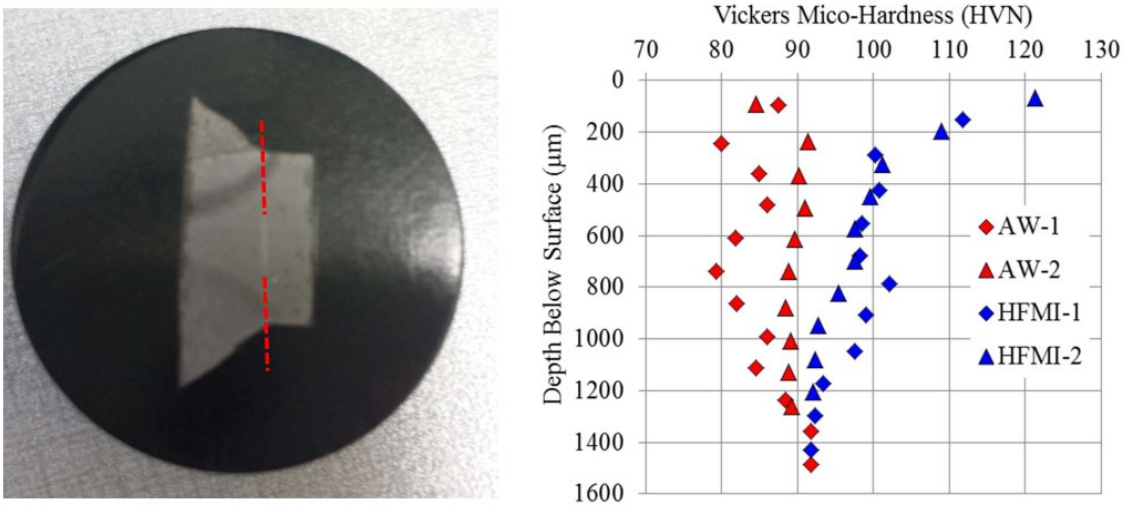

Figure 4.18: Micro-hardness measurements for 5083 aluminum welds

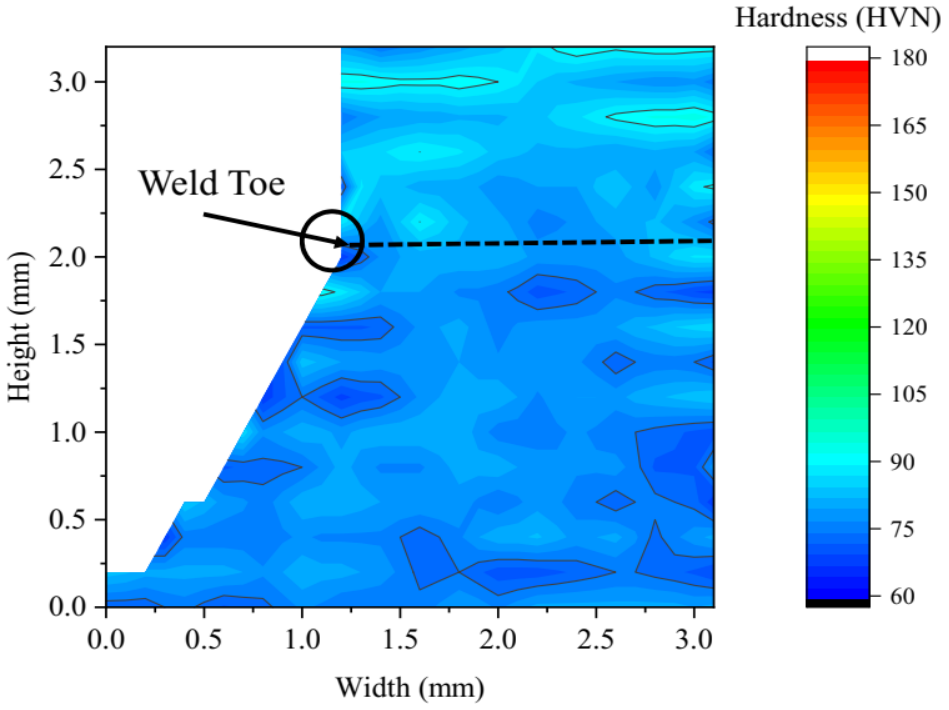

Figure 4.19: Hardness map for as-welded 5083 aluminum specimen near weld toe

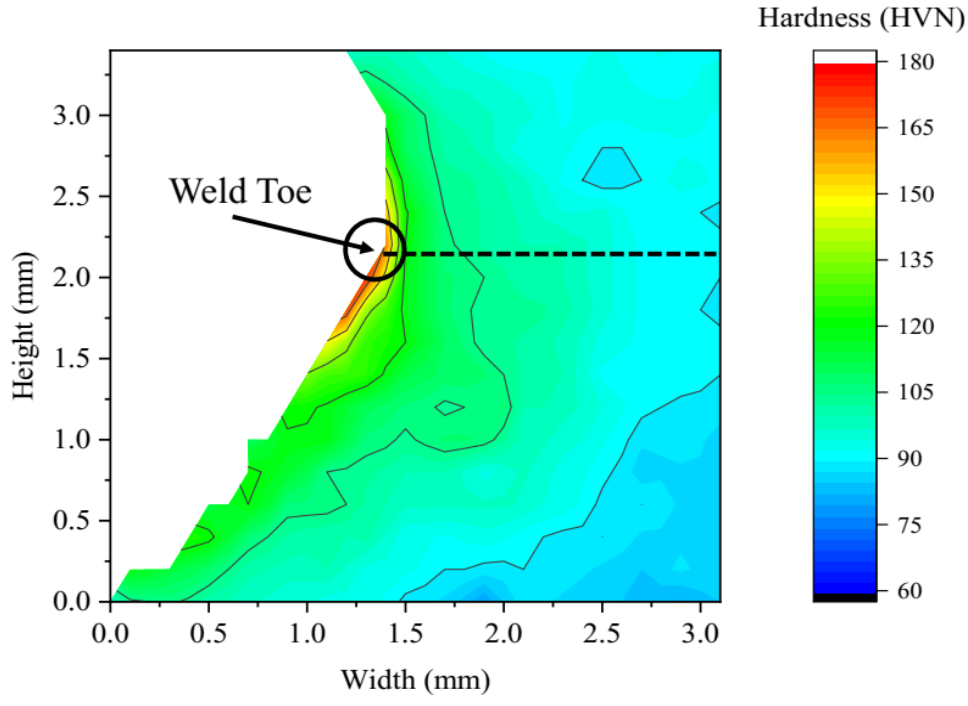

Figure 4.20: Hardness map for HFMI treated 5083 aluminum specimen near weld toe

Figure 4.21 shows hardness test results for all three materials in two conditions, namely: as-welded (AW), and HFMI treated. In general, impact treatment results in plastic deformation near the surface, which leads to localized work hardening and an increase in hardness. The affected depth is similar to the depth of the compressive residual stress introduced by the treatment (~1.0 mm). The increase in hardness for the aluminum due to the treatment was from ~92 HVN in the untreated weld to a maximum of ~124 HVN at the surface of the treated weld (see Figure 4.21). Similarly, the increase for the A514 steel was from ~320 HVN to ~420 HVN as shown in Figure 4.21.

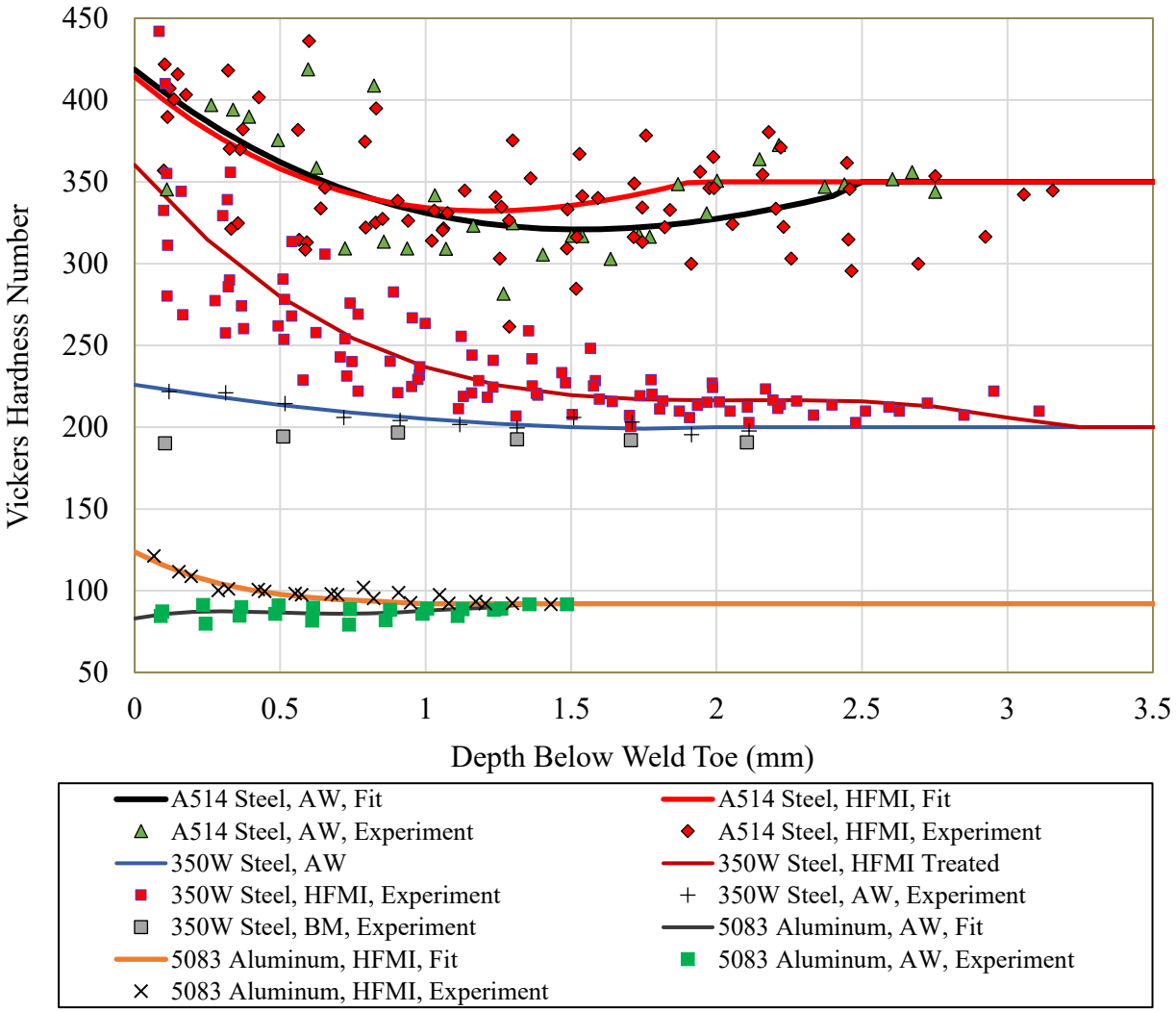

Figure 4.21: Hardness test results on polished specimens

As reported in (Tehrani Yekta et al. 2013), the hardness increase for the CSA 350W steel due to HFMI treatment was seen to be from ~230 HVN to ~325 HVN for properly executed treatment. In (Ghahremani 2015), the hardness increase for the CSA 350W steel due to HFMI treatment was from ~230 HVN to ~350 HVN as shown in Figure 4.21. A three-degree polynomial to represent hardness variation was fitted for all three materials, as shown in Figure 4.21. It can be observed that for the aluminum welds, in the as-welded condition, hardness is lower than the hardness of the base metal, while for the steel specimens, the hardness is higher in the as-welded condition, compared to the base metal. The hardness number for base metal is taken to be equal to the hardness number observed at depths more than 3 mm below the weld toe.

Given this hardness information for steel, the effect of welding on the material property gradient was conservatively ignored in the subsequent analysis for the 350W steel and A514 steel. On the other hand, the fitted hardness distribution was used to consider material property variations along the crack path for the 5083 aluminum welds, according to the fitted variation, shown in Figure 4.22. Empirical relationships similar to the one used in (Ghahremani 2015) were used to correlate hardness with yield strength, ultimate strength, and material model parameters *K'* and *n'*. The following linear relations were used to correlate hardness and material properties for the 5083 aluminum specimens, based on the data for base metal and simulated HAZ aluminum:

$$\sigma_y = 6.28\,HVN - 334.48 \tag{4.3}$$

$$\sigma_u = 2.17\,HVN - 165.62 \tag{4.4}$$

$$K' = 8.84\,HVN - 170.47 \tag{4.5}$$

$$n' = 0.0023\,HVN - 0.1097 \tag{4.6}$$

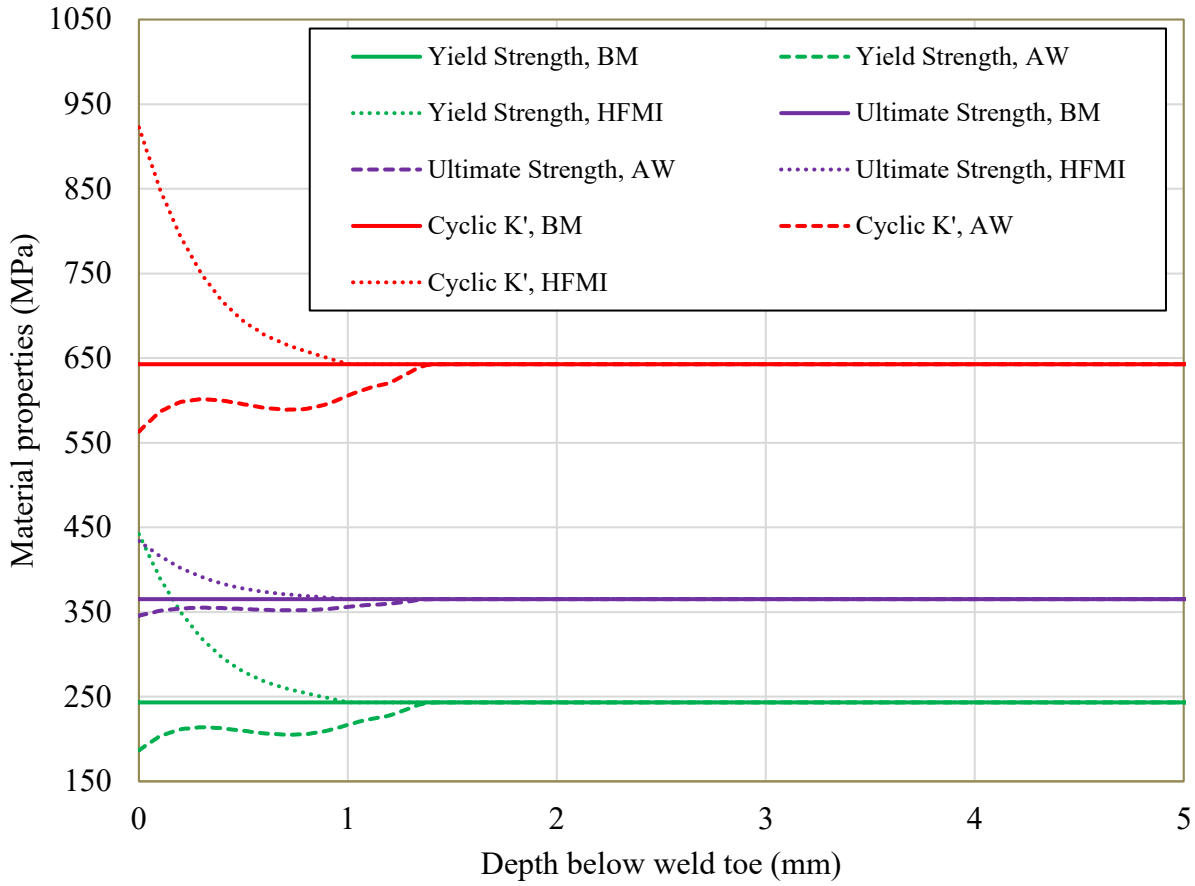

Figure 4.22: Material property gradient along the crack path for 5083 aluminum

4.7 Crack growth rate tests on compact tension specimens

Crack growth rate tests were performed to estimate the Paris-Erdogan crack growth law constants, which are one of the most important parameters for fracture mechanics analysis. Results of such tests for "base metal" and "simulated HAZ" 350W steel from (Ghahremani 2015) are presented in Figure 4.23 along with a fitted crack growth curve (labelled "SBFM Input") used for the subsequent fracture mechanics analysis. The tests were performed using compact tension (CT) specimens fabricated in accordance with (ASTM E647-13 2013) and precracked under cyclic compression loading. It was assumed that "closure free" crack growth rates were obtained under a high R-ratio (0.8). The constants C, m, and ΔK_{th}, were determined for 350W steel specimens based on the crack growth rate test data collected from (Ghahremani 2015) and data available in (Maddox 1975). The crack growth rate data points for the simulated HAZ specimens were in between those

for the two base metal 350W steel specimens. Note that the manually (by varying the value of C for the fitted curve and observing the fit visually) fitted crack growth rate curve is an upper bound of the test data at higher stress ranges and best fit at the lower stress ranges, which is assumed to represent the "closure free" crack growth rate curve.

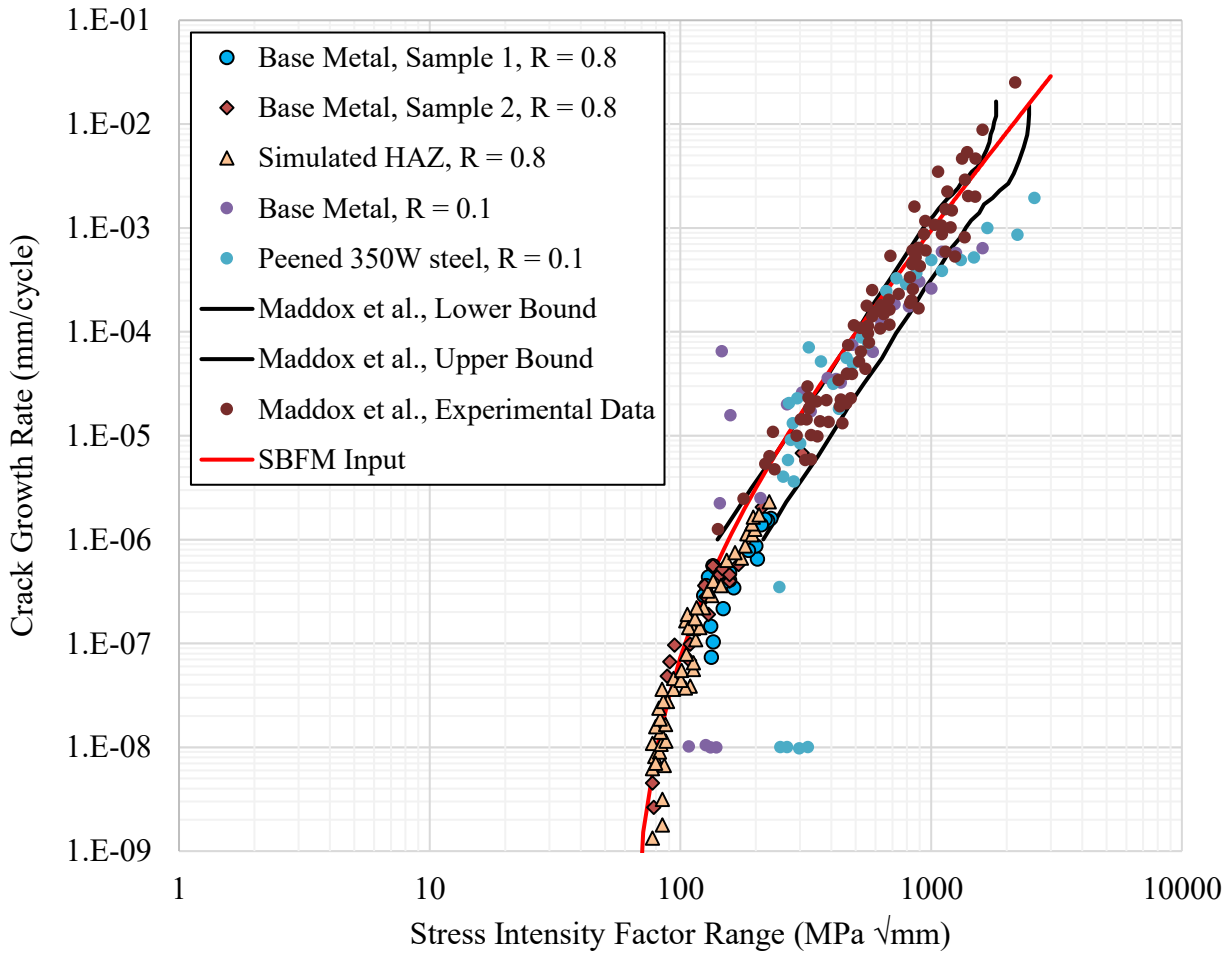

Figure 4.23: Crack growth rate measurements and fitted curve for 350W steel

Crack growth rate test results for A514 steel from the experiment performed for the current study are presented in Figure 4.24 along with the fitted curve used in the subsequent fracture mechanics analysis. For A514 steel, crack growth rate tests were performed on one base metal CT specimen and two simulated HAZ CT specimens. Crack growth rate data was also obtained from other sources (Barsom, J. M., & Novak 1977; Parry, M., Nordberg, H., & Hertzberg 1972) to

complement the test data. The fitted crack growth rate curve and experimental data for A514 steel are shown in Figure 4.24.

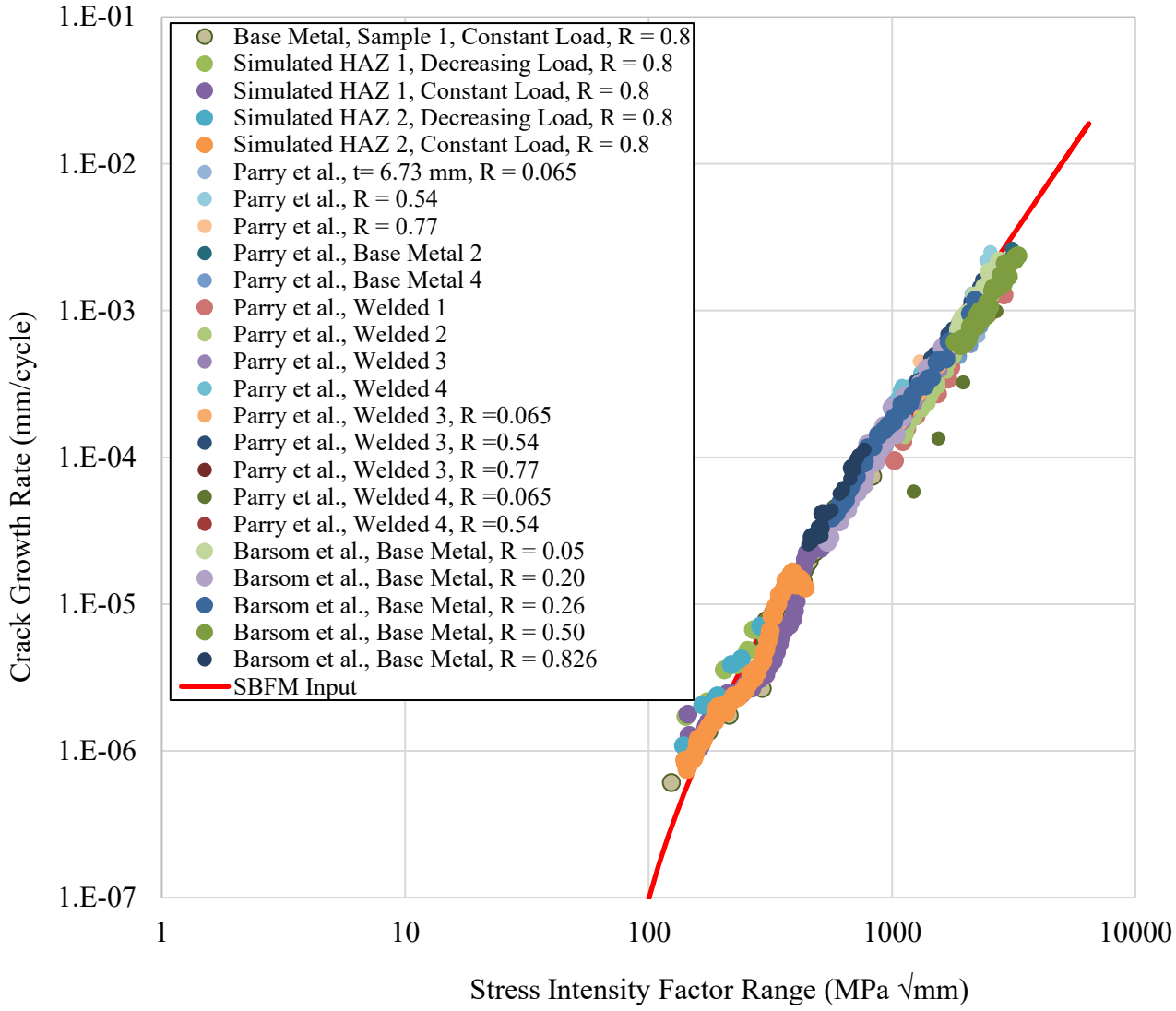

Figure 4.24: Crack growth rate measurements and fitted curve for A514 steel

Crack growth rate test results for 5083 aluminum from the experiment performed for the current study are presented in Figure 4.25 along with the fitted curve used in the subsequent fracture mechanics analysis. For the 5083 aluminum material, the crack growth rate data obtained for the base metal specimen was higher than that of the simulated HAZ specimens as shown in Figure 4.25. However, at higher stress intensity factor (SIF) ranges (> 150 MPa√mm), the crack

growth rates were the same for both tempers. Data from the existing literature (Tobler and Reed 2010) complemented the test data obtained for this project, especially at the higher SIF ranges. An upper bound of the test data is assumed to provide the "closure free" crack growth rate curve.

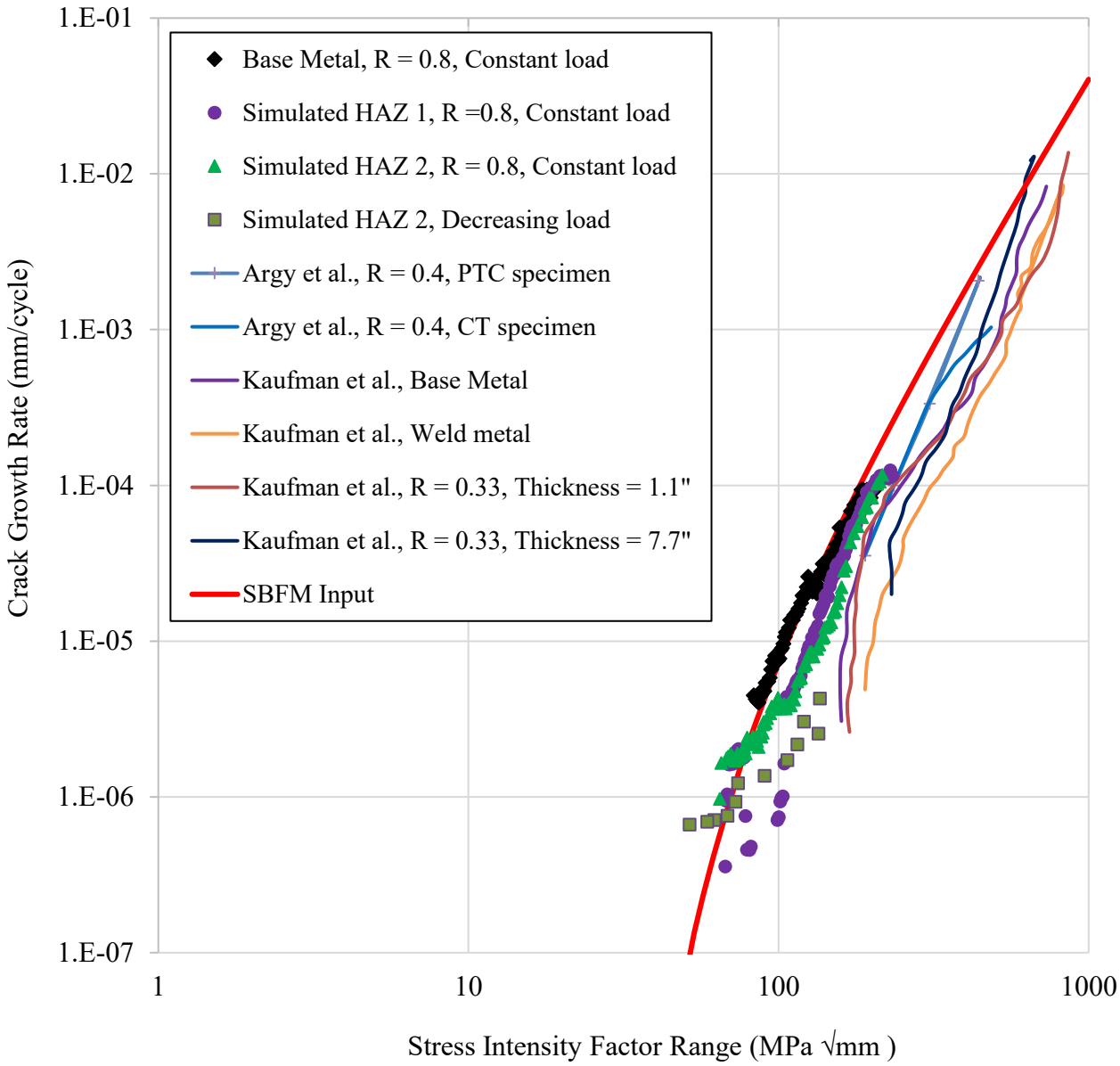

Figure 4.25: Crack growth rate measurements and fitted curve for 5083 aluminum

The following crack growth equations were established based on the crack growth rate test results for different material types:

For 350W steel (mm/cycle, MPa√mm):

$$\frac{da}{dN} = 1.14\times10^{-12}(\Delta K - 60)^{3.0} \tag{4.7}$$

For A514 steel (mm/cycle, MPa√mm):

$$\frac{da}{dN} = 1.39\times10^{-12}(\Delta K - 60)^{2.4} \tag{4.8}$$

For 5083 aluminum (mm/cycle, MPa√mm):

$$\frac{da}{dN} = 1.14\times10^{-11}(\Delta K - 35)^{3.2} \tag{4.9}$$

4.8 Fracture mechanics analysis

A detailed description of the strain-based fracture mechanics (SBFM) model used in the analysis conducted for the current study is provided in Chapter 2. The input parameters used for the three different materials are summarized in Table 4.9.

Table 4.9: Input parameters used in fracture mechanics analysis

Parameter	350W Steel	A514 Steel	5083 Aluminum	Units	Source
t	9.5	9.5	9.5	mm	Measured
E	208083*	211724	71389	MPa	Material Tests
σ_y	356*	814.67	*f*(HVN)	MPa	Material Tests
σ_u	616*	849	*f*(HVN)	MPa	Material Tests
LN(C)	-27.5	-25.0	-25.2	MPa, mm	Material Tests
m	3.0*	2.4	3.2	MPa, mm	Material Tests
ΔK_{th}	60*	60	35	MPa·√mm	Assumed
K'	812.0*	2033.7	*f*(HVN)	MPa	Material Tests
n'	0.108*	0.211	*f*(HVN)	-	Material Tests
a_i	0.15*	0.15	0.10	mm	(Coughlin and Walbridge 2012; Ghahremani 2015)
μ	0.018*	0.002	0.003	-	(Coughlin and Walbridge 2012; Khalil and Topper 2003; Tehrani Yekta et al. 2013)

Note: *taken from (Ghahremani 2015)

The following comments provide more insight into the input parameters used in the SBFM analysis:

- Material properties obtained from the base metal coupons were used for the SBFM analysis of the steel specimens, since this represented a conservative simplification, given that welding and impact treatment had either no effect or a positive effect on the material properties of the two tested steel alloys. For the 5083 aluminum specimens, hardness-based material property gradient was considered during the SBFM analysis, since the aluminum softened in the weld region compared to the base metal.
- Non-Uniform residual stress distributions for as-welded and HFMI treated specimens were obtained based on extensive data available in existing literature as described in Figure 2.3 and Figure 2.4 of Chapter 2. The distributions obtained in Chapter 2 were scaled to pass through the measured residual stress data points (obtained by x-ray diffraction method) for each material type. For 350W steel in the as-welded condition, the residual stress data had a range from $-0.18 \cdot \sigma_y$ to $+ 0.28 \cdot \sigma_y$ at the weld toe, as shown in Figure 4.26. Therefore two bounds were considered, as shown in Figure 4.26, for each specimen type (AW & HFMI) representing the lower and upper bound of the residual stress distribution. It should be noted that the experimental residual stress data were obtained at one weld toe but it is plotted in the figure at both sides of the weld to show a symmetric residual stress distribution. It is suspected that the actual distribution varies considerably, based on measurements obtained for the studies in (Ghahremani 2015; Tehrani Yekta et al. 2013). However, the overall distribution must be self-equilibrating and pass through the measurement data. They are more-or-less bounds of the measured values, with a distribution shape that agrees well with the measured distributions from other studies. For the HFMI treated specimens, peak residual stresses near the weld toe were assumed to be $-0.80 \cdot \sigma_y$ and $-0.35 \cdot \sigma_y$ for the lower and upper bound of residual stress distributions respectively.

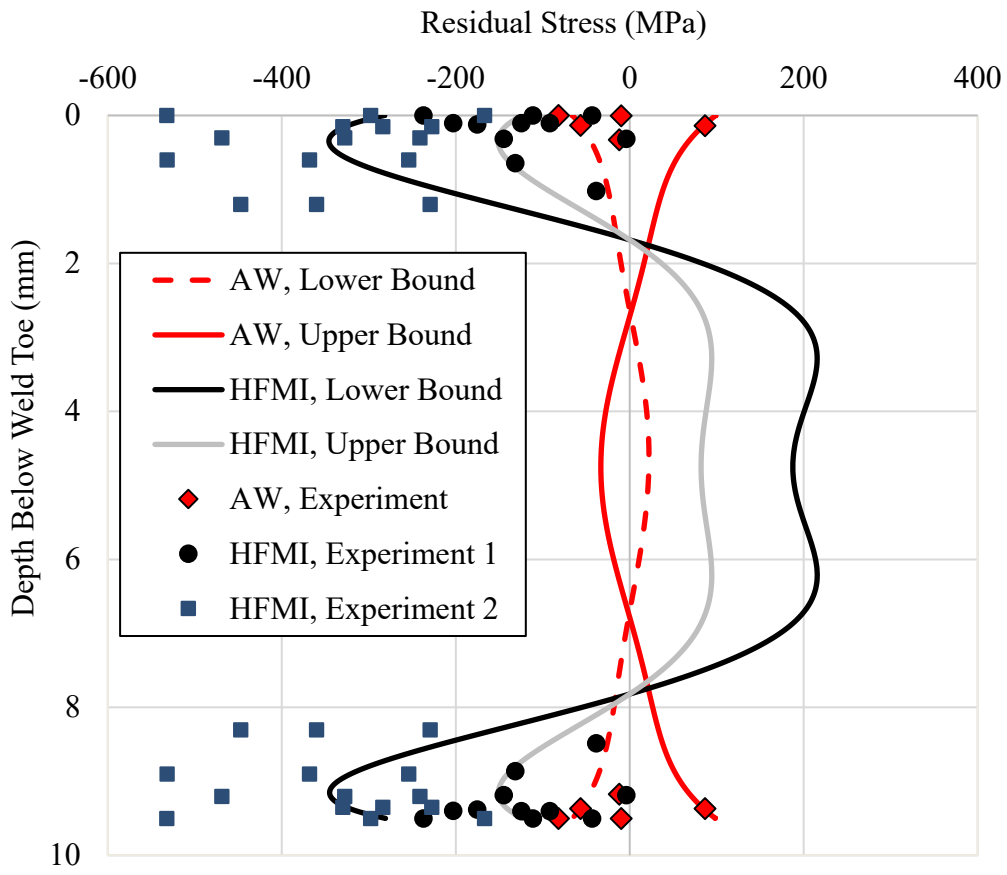

Figure 4.26: Assumed residual stress distributions for 350W steel specimens

- While fabricating the cruciform welded joints, welds were performed on four sides of the cruciform joint sequentially – not simultaneously. Therefore, in some regions, the residual stress at the surface after welding was small but compressive, rather than tensile. It is suspected that the first weld toe in the welding sequence will have compressive residual stress and the last weld toe in the welding sequence will have tensile residual stress. There are many competing factors that will decide the criticality of the four similar weld toes from which a crack will initiate. These include the presence of defects from the welding process, defect geometry, magnitude of residual stress, softening or hardening of material during the welding process, and magnitude of stress concentration at the weld toe. Due to these factors, it is possible that a crack may initiate from the weld toe where a small compressive residual stress

is present near the weld toe region. Therefore, a range of residual stress at the weld toe was considered by using bounds of residual stress distribution for fracture mechanics analysis.

- Residual stress measurement results and fitted lower and upper bound for treated A514 steel specimens are shown in Figure 4.27. Residual stress measurements were not obtained for A514 steel in the as-welded condition. Therefore, a distribution similar to the one for 350W steel was assumed. For the A514 treated steel specimens, residual stress distribution inputs were assumed to vary from -0.50·σ_y to -0.35·σ_y at the weld toe for SBFM analysis.
- For the treated 5083 aluminum specimens, the residual stress distribution inputs were assumed to vary from -0.30·σ_y to -0.05·σ_y at the weld toe, based on the residual stress measurement data, which is shown in Figure 4.28.

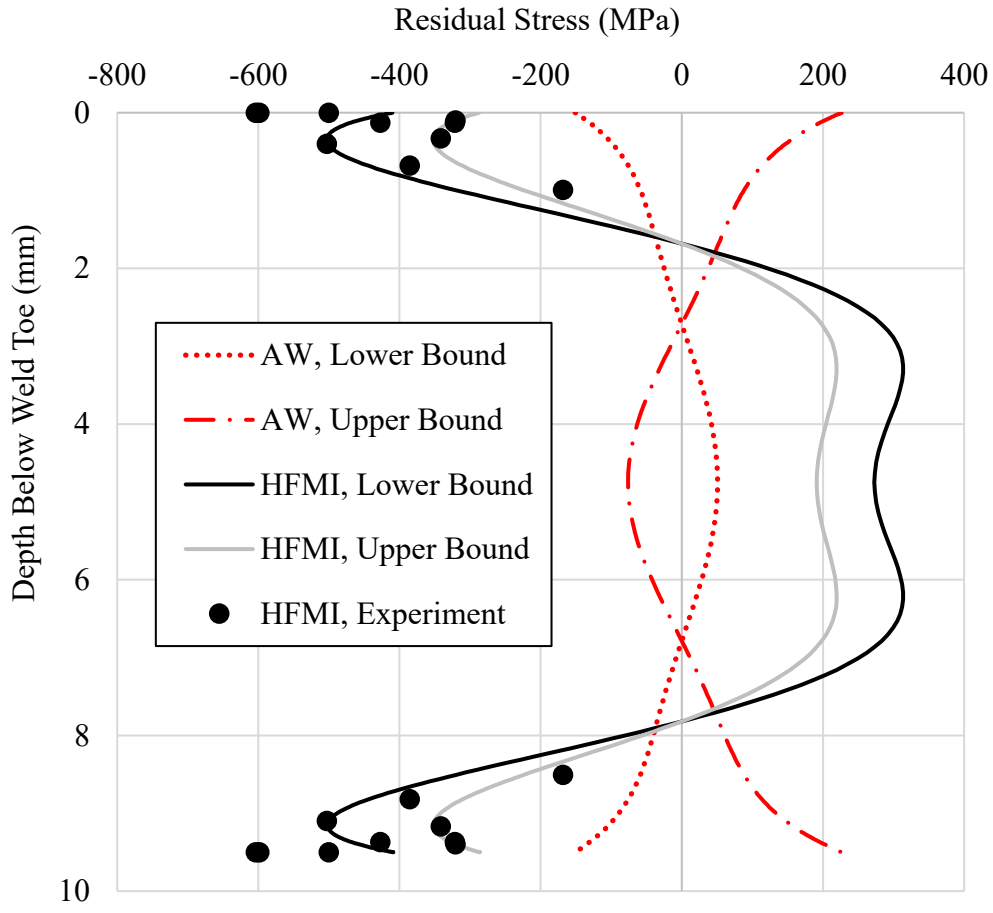

Figure 4.27: Assumed residual stress distributions for A514 steel specimens

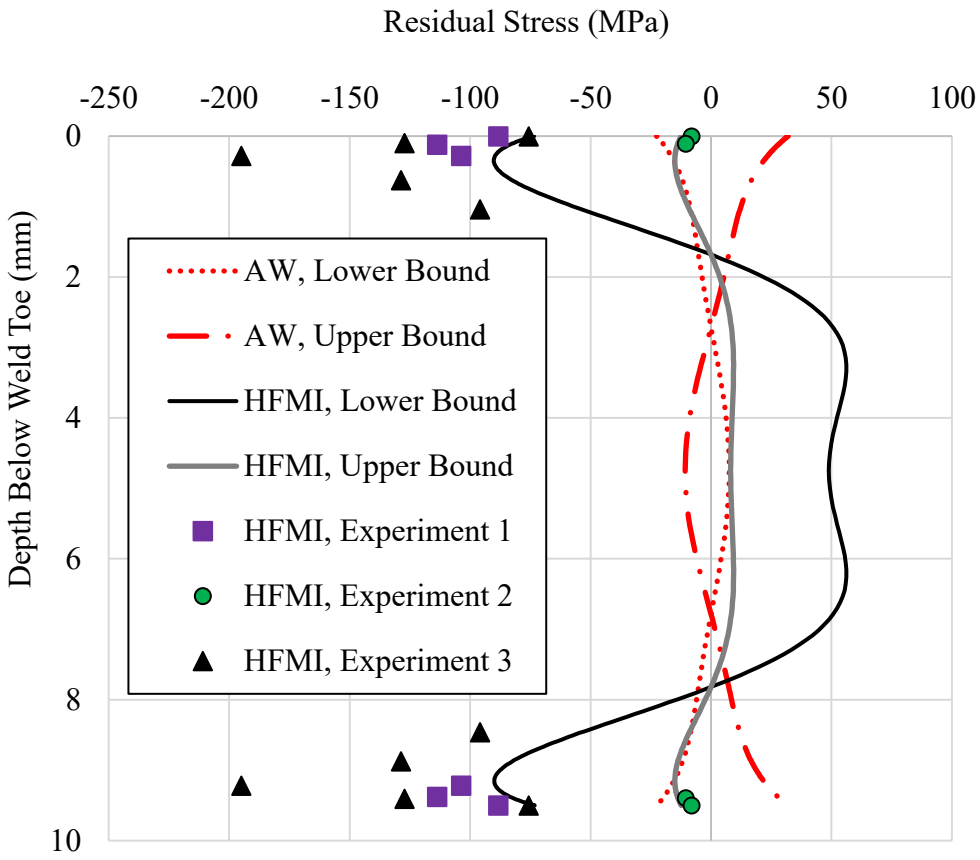

Figure 4.28: Assumed residual stress distributions for 5083 aluminum specimens

- The initial defect depth, a_i, was set to 0.15 mm for the steel welds and 0.10 mm for the aluminum welds. Importantly, impact treatment was assumed to have no effect on a_i. The value of a_i for steel specimens is a typically assumed value, as discussed in (Tehrani Yekta et al. 2013). A lower value for a_i is appropriate for aluminum, as discussed in (Coughlin and Walbridge 2012). An initial crack aspect ratio, $(a/c)_i$, of 0.5 was assumed for all three material types.
- The critical crack depth, a_c, is taken as the crack depth that will result in ductile fracture due to lack of sufficient remaining cross-section to carry the load as discussed in Chapter 2. The critical crack depth was limited to 80 % of the component thickness. This limit was imposed because of the validity range for the weight function method used in the SBFM model.

- A linear elastic finite element (FE) analysis was performed to estimate the stress concentration factor (*SCF*) along the crack path, with the weld toe geometry modelled by tracing silicon impression image shown in Figure 4.29. The symmetric component geometry along both axes (X and Y) meant that only a quarter of the specimen needed to be modelled. A four-node bilinear plane strain quadrilateral (CPE4R) element was used. A global mesh size of 0.5 mm and a local mesh size of 0.01 mm was employed to create the mesh. A unit pressure was applied at the end of the specimen to estimate the *SCF* along the crack path.

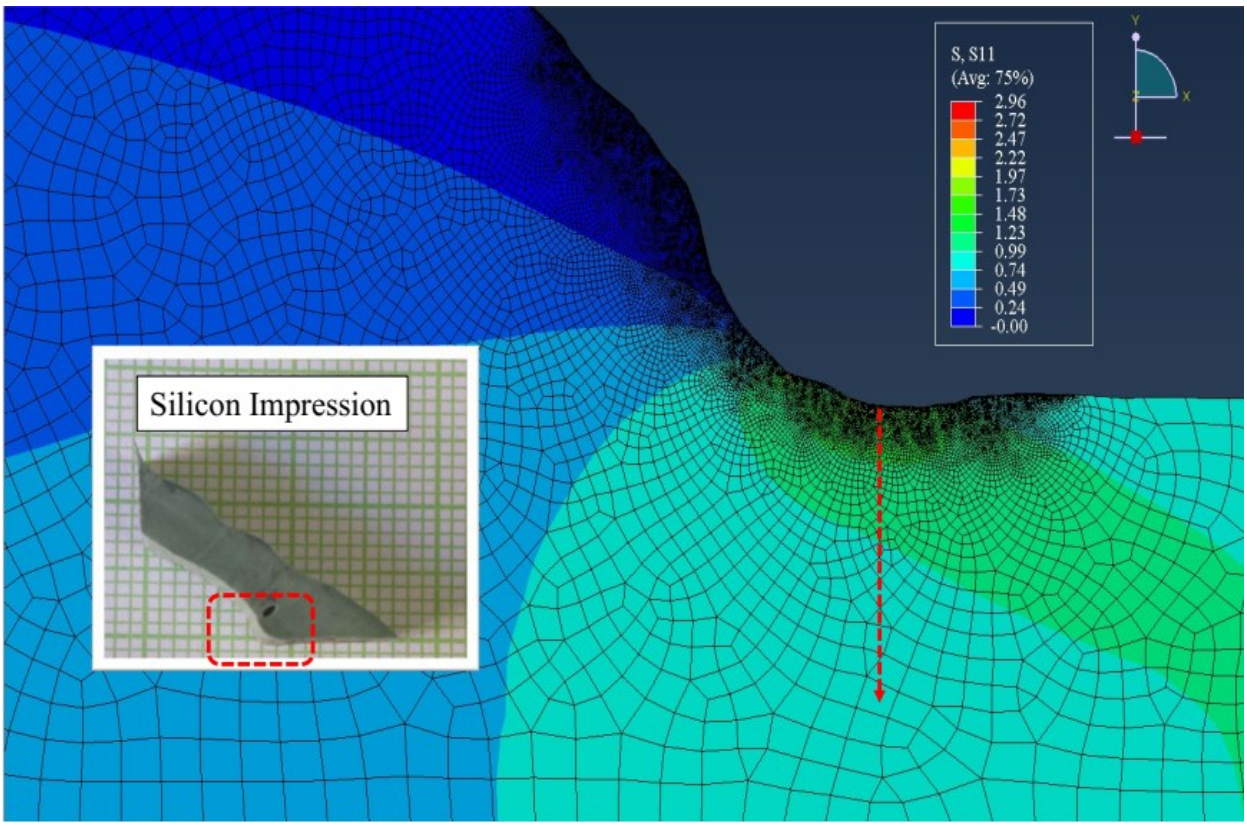

Figure 4.29: Notch geometry of a treated specimen used for finite element analysis

The resulting *SCFs* along the crack path are shown in Figure 4.30. Looking at Figure 4.30, it can be observed that the *SCF* at the weld toe reduces from 3.7 at the surface for the as-welded specimen to 2.8 for the treated specimen due to the change in weld toe radius.

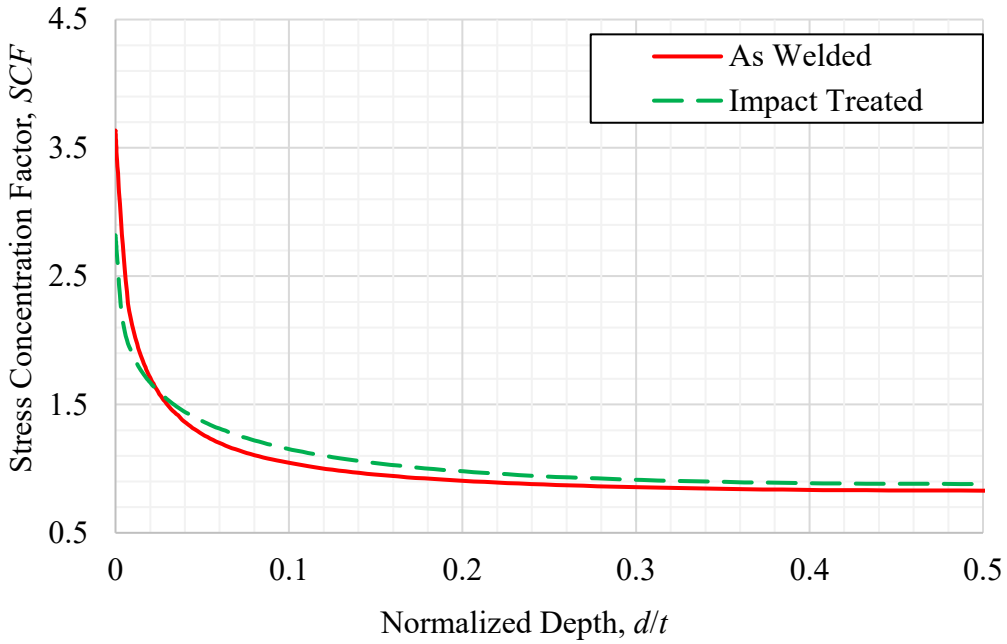

Figure 4.30: Linear elastic finite element analysis results

The results of the fracture mechanics analysis performed for this study are summarized in the next section. Results are first presented for 350W steel followed by A514 steel and 5083 aluminum specimens. For a particular material, stress-life (S-N) curves are first presented and compared with experimental stress-life data. Then, the crack shape evolution curves estimated by the 2D SBFM model are presented along with fracture surfaces of the fatigue tested specimens.

4.8.1 SBFM analysis results for 350W steel specimens

The analysis performed in this section for the 350W steel specimens is aimed at validating the 2D SBFM model with the experimental results from (Ghahremani 2015; Tehrani Yekta et al. 2013). The component geometries for the A514 steel and 5083 aluminum specimens were similar to the geometry used in (Ghahremani 2015) and the same testing frame was used to perform the experiments for the A514 steel and 5083 aluminum specimens. Three loading conditions, namely: CA, VA1, and VA2 loading were used for the fatigue test of 350W steel specimens. Figure 4.31 shows S-N curves for the as-welded 350W specimens, which were tested under CA loading (R = 0.1). For all S-N curves, fatigue life has been plotted along the x-axis on a logarithmic scale varying

from 10^4 to 10^7 or 10^8 cycles. Nominal stress range has been plotted on the y-axis on a logarithmic scale varying from 10 MPa to 1000 MPa.

Four S-N curves obtained by SBFM analysis are shown in Figure 4.31 where two S-N curves are based on the assumption of a semi-elliptical (SE) crack and two are based on the assumption of a quarter-elliptical (QE) crack. Two different magnitudes of residual stress distribution along the crack path have been considered. Here, the σ_r symbol stands for peak residual stress at the weld toe, which has been assumed to vary from $-0.18 \cdot \sigma_y$ to $+0.28 \cdot \sigma_y$ representing lower and upper bound of the residual stress for as-welded specimens. With the assumed defect geometry and residual stresses, the S-N curves provide an envelope, which contains most of the fatigue test results. Fatigue test results have been taken from two sources: triangular and circular markers from (Ghahremani 2010, 2015) and rectangular markers from (Tehrani Yekta et al. 2013) for the validation of SBFM results. It is observed that the higher the magnitude of the stress range, the lower is the effect of residual stress on the fatigue life since all the S-N curves converge at higher stress ranges. Raw fatigue test data for HFMI treatment study is available in Appendix D.

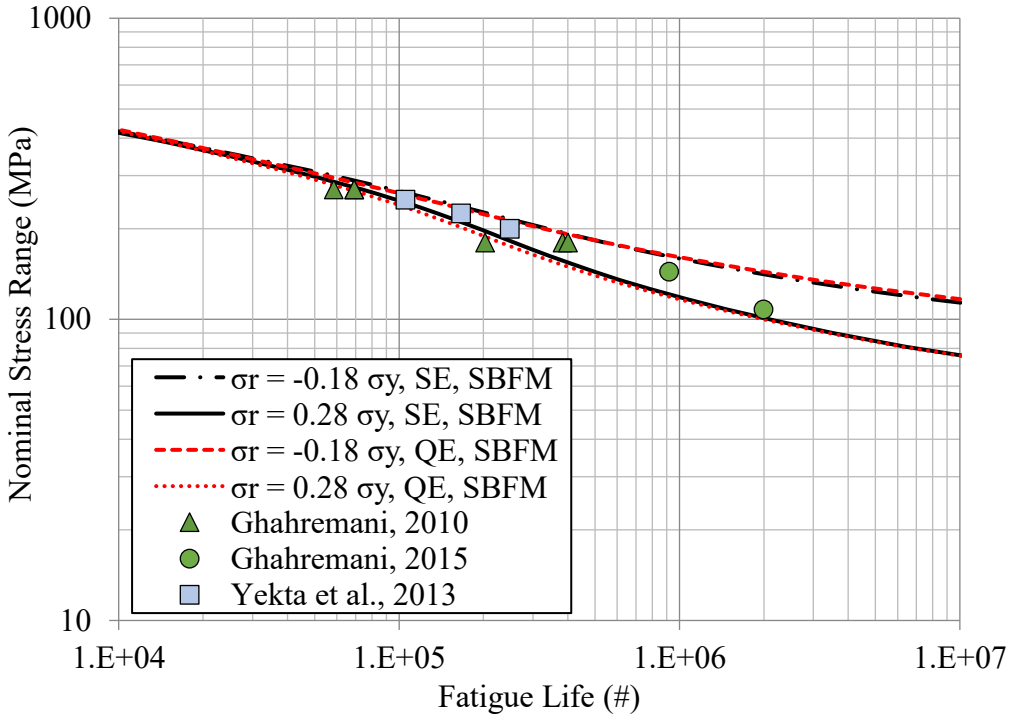

Figure 4.31: S-N curves for as-welded 350W steel specimens under CA loading

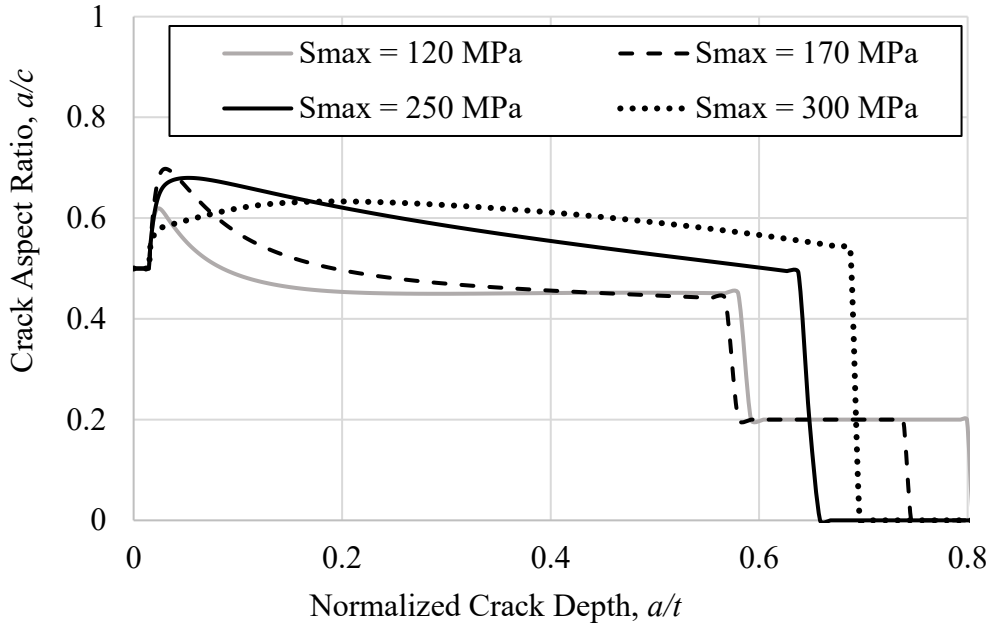

Figure 4.32: Crack shape evolution for SE crack under CA loading for as-welded 350W steel specimens, with $(\sigma_r)_{toe} = 0.28 \cdot \sigma_y$

Figure 4.32 shows crack shape evolution curves predicted by the SBFM model at different maximum stress levels. Normalized crack depth has been plotted on the x-axis and crack aspect ratio has been plotted on the y-axis. The normalized crack depth varied from 0 to 0.8. The normalized crack depth was limited to 0.8 because the weight function method is only applicable up to this range. The crack aspect ratio was constrained to vary from 0.2 to 1.0, this is also because the weight function method is applicable within this range of crack aspect ratio. Looking at Figure 4.32, it can be seen that once the crack propagates to a size that is sufficient for it to reach the far side of the specimen, a through-width crack is assumed for the subsequent analysis, with an aspect ratio of 0.2. Efforts to further refine this assumption and transition to a through crack were not pursued on the basis that at this stage ($a/t > 0.6$), the crack is growing so fast the effect on the fatigue life prediction is negligible.

It was observed from the fracture surface of the fatigue tested specimen that a semi-elliptical crack shape appeared in the as-welded specimens and quarter elliptical or corner crack appeared in the HFMI treated specimens for most of the cases. According to the SBFM model, there was no drastic difference in crack shape evolution due to a variation in the magnitude of the

residual stress from -0.18·σ_y to +0.28·σ_y. The lower (more compressive) the residual stress, the rounder was the crack shape because of slower crack growth along the surface point compared to the deepest point of the crack. Looking at the Figure 4.32, it can be observed that at a lower stress level of 120 MPa to 170 MPa, the aspect ratio of a SE crack initially increased from 0.5 to about 0.62 and then continued to decrease to about 0.44 at a normalized crack depth of 0.58. At a normalized crack depth, a/t = 0.58, a SE crack becomes a through-width crack, which is indicated by the sudden drop in the crack shape evolution curve as seen in Figure 4.32. The specimen at a lower stress range of 170 MPa failed at a normalized depth, a/t = 0.78, as shown by the dashed line. As observed in Figure 4.32, at lower stress ranges (< 170 MPa), a through-width crack happens, otherwise, the higher the stress level, the higher is the final crack aspect ratio just before failure. As discussed previously, a sudden drop in the aspect ratio in crack shape evolution curve shown in Figure 4.32 shows that either the specimen failed at that aspect ratio or it became a through-width crack with three free faces.

Figure 4.33 shows the S-N curve for HFMI treated 350W steel specimens under CA loading. Again, four S-N curves have been presented: two with a SE crack shape assumption and two with a QE crack shape assumption. For each crack shape, the peak residual stress because of impact treatment at the weld toe was assumed to vary between -0.80·σ_y and -0.35·σ_y. The S-N curves with a -0.35·σ_y peak residual stress provide a good estimation of the fatigue test results taken from (Ghahremani 2015), which was as expected since the specimens were believed to be slightly under-treated in that study. The S-N curve with a -0.80·σ_y as peak residual stress provided a good estimation of the fatigue test results taken from (Tehrani Yekta et al. 2013), in Yekta's study, the specimens were properly treated.

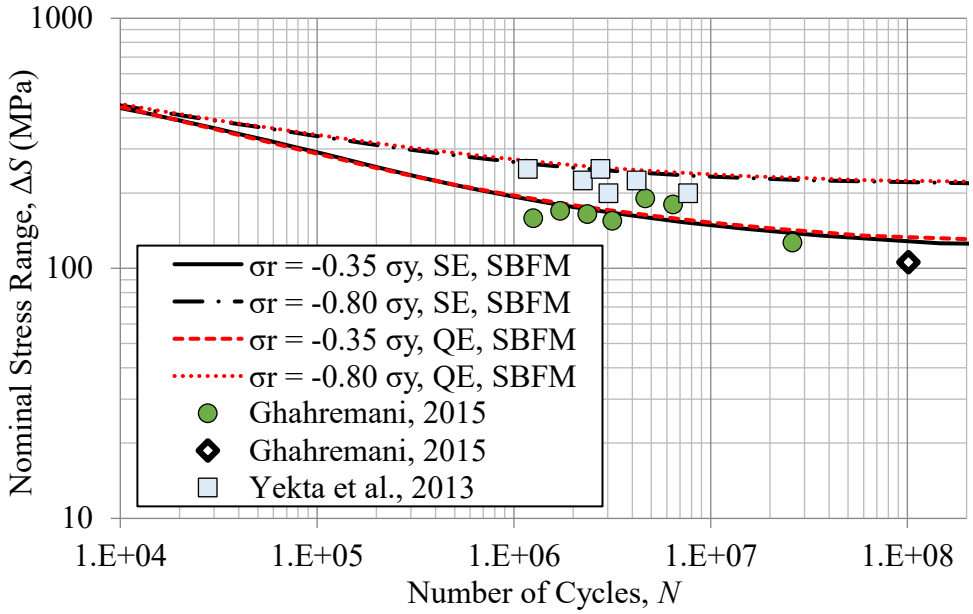

Figure 4.33: S-N curves for HFMI treated 350W steel specimens under CA loading

Figure 4.34 shows fracture surfaces of the fatigue tested HFMI treated 350W steel specimens under CA loading. The fracture surfaces of 350W steel cruciform joints were available at the University of Waterloo from previous research work (Ghahremani 2015). For the validation of the 2D SBFM model, the fracture surface was digitized and crack shape was measured for each specimen by the author for the current study. Nominal stress range (ΔS), maximum stress (S_{max}), and the number of cycles to failure (N) have been reported for each fracture surface. The top and bottom edge of each fracture surface are the two weld toes of the cruciform welded joint. The left and right edge of each fracture surface is a side of the cruciform joint which is base metal (untreated side). It can be observed from the figure that at lower S_{max} and higher S_{max} (1st and 3rd row), crack initiation location shifted from the treated edge of the specimen to the untreated side. For a moderate stress range (2nd row), a quarter elliptical crack was observed, which was common in most of the treated specimens. The final aspect ratio of the QE crack varied from 0.35 to 0.39 for treated 350W specimens, which is also predicted by the SBFM model, through the crack shape evolution curves as seen in Figure 4.35. For CA loading (R = 0.1) with a maximum stress level in between 150 to 280 MPa, the final crack aspect ratio was predicted to be in between 0.34 to 0.42, which matches with the observed final a/c (0.35, 0.39) on the fracture surface. The crack shape

evolution curves as shown in Figure 4.35 was obtained with assumed value of residual stress near the weld toe, $(\sigma_r)_{toe}$, of $-0.35 \cdot \sigma_y$.

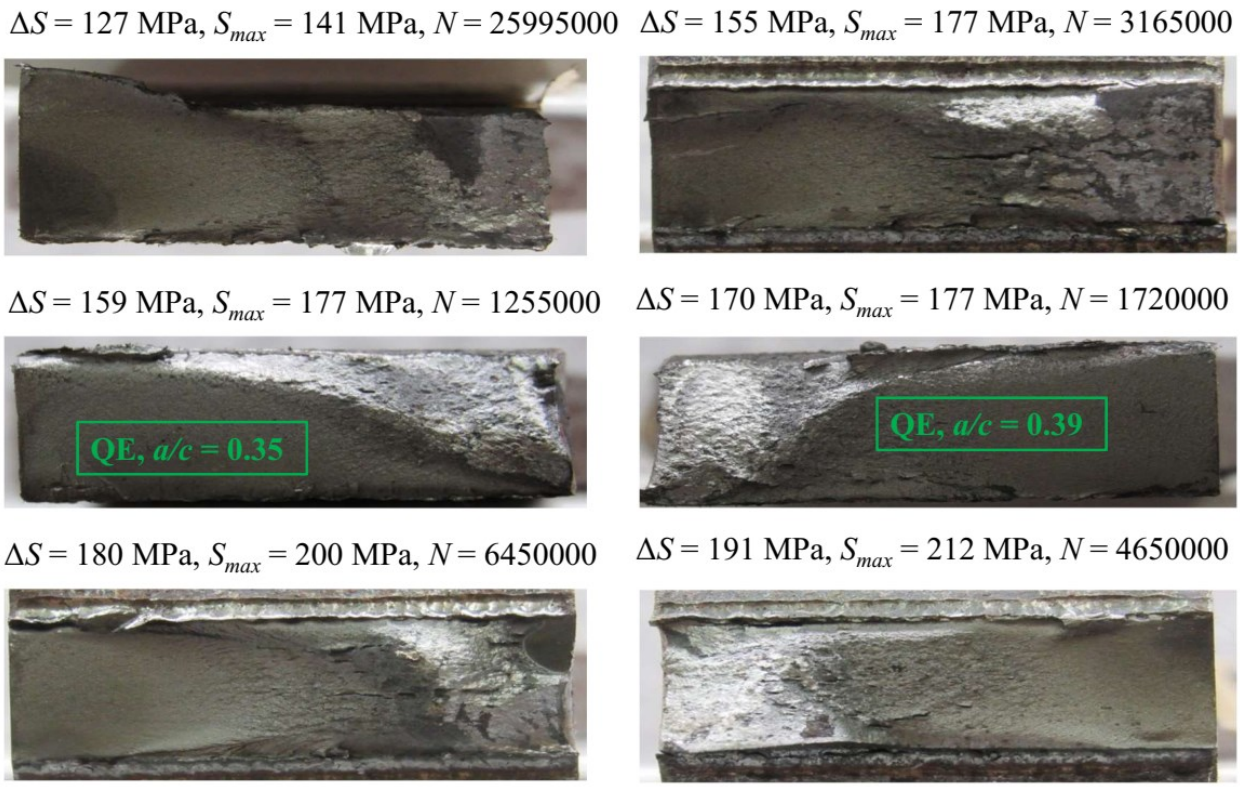

Figure 4.34: Fracture surfaces for HFMI treated 350W steel specimens under CA loading

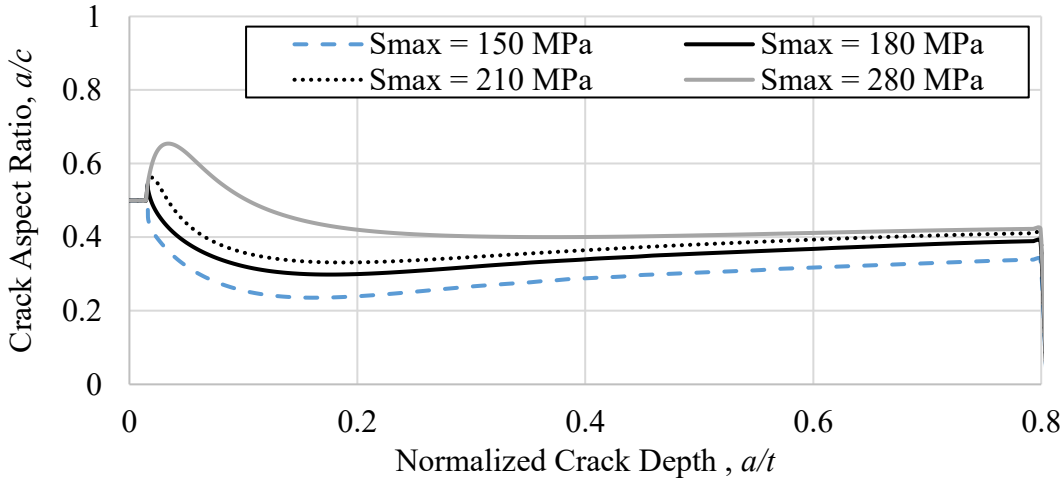

Figure 4.35: Crack shape evolution for QE crack under CA loading for HFMI treated 350W steel specimens with $(\sigma_r)_{toe} = -0.35 \cdot \sigma_y$

S-N curves for the 350W steel specimens in the as-welded condition under VA1 loading is shown in Figure 4.36. Since this is a case of VA loading, an equivalent stress range estimated using a Miner's sum has been plotted on the y-axis. It can be observed that at higher stress ranges (> 150 MPa), there is no effect of residual stress on fatigue life since all S-N curves converge with each other. A reasonably good estimation of the fatigue test results by the SBFM model can be observed for the as-welded specimen under VA1 loading except for one outlier.

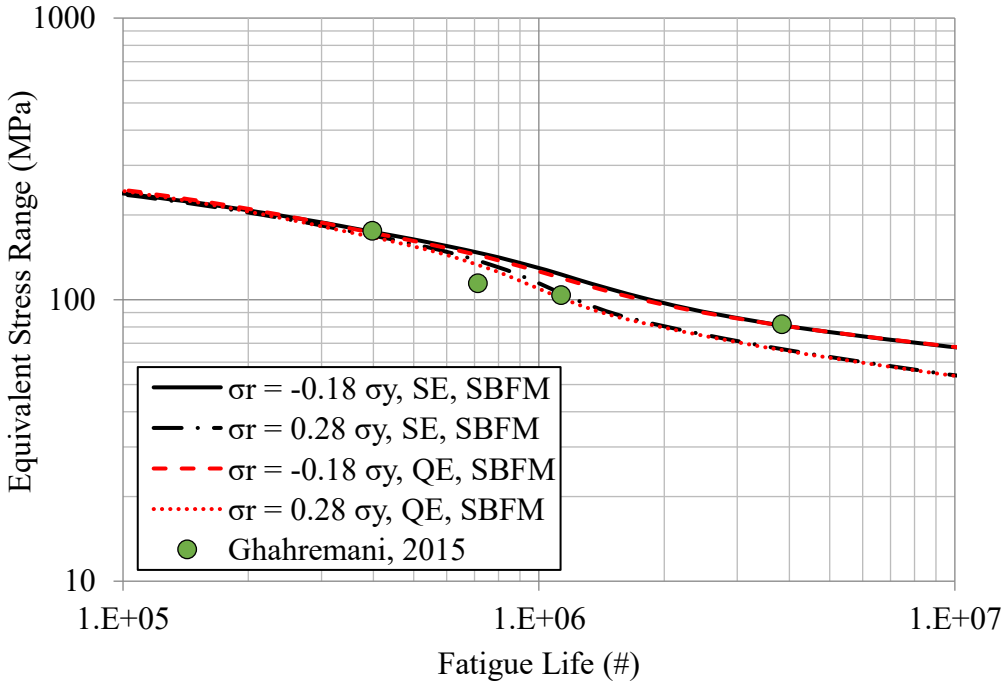

Figure 4.36: S-N curve for as-welded 350W steel specimens under VA1 loading

ΔS_{eq} = 104 MPa, S_{max} = 229 MPa, N = 1131000

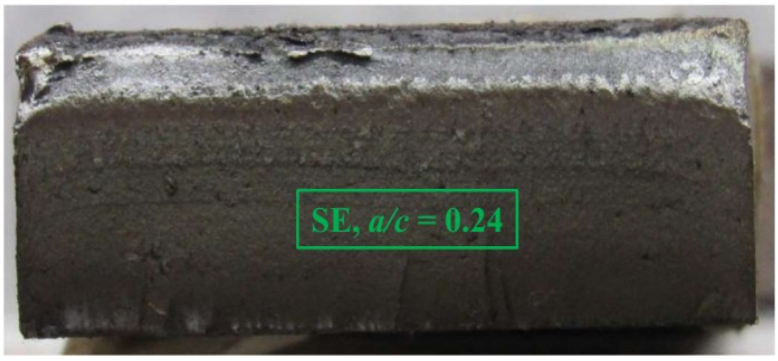

Figure 4.37: Fracture surface for the as-welded 350W steel specimen under VA1 loading

A fracture surface of the as-welded 350W steel specimen tested under VA1 loading is shown in Figure 4.37. In this case, a through-width crack was observed under VA1 loading at a maximum stress level of 229 MPa. The crack shape evolution in Figure 4.38 shows that for a maximum stress level of 230 MPa, a through-width crack is expected, which is shown with solid black crack shape evolution curve with a staircase shape around a normalized crack depth of 0.62. It can be observed from Figure 4.38 that at low-stress levels (≤ 230 MPa) a through-width crack is expected, and at higher stress levels, the final aspect ratio increases with an increase in stress level.

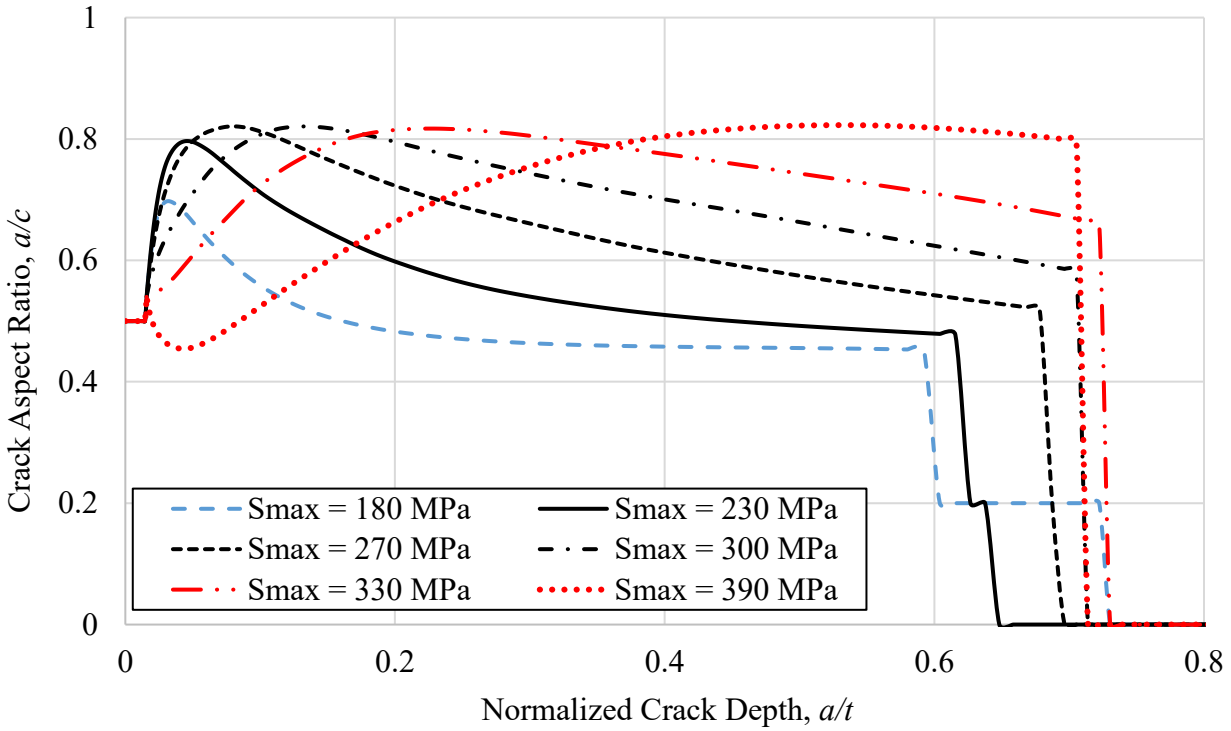

Figure 4.38: Crack shape evolution of SE crack under VA1 loading for as-welded 350W steel specimens with $(\sigma_r)_{toe} = 0.28 \cdot \sigma_y$

Figure 4.39 shows S-N curves for HFMI treated 350W specimens tested under VA1 loading. It can be observed from this figure that there is a large scatter in the fatigue test results. The envelope of S-N curves obtained by assuming $-0.80 \cdot \sigma_y$ and $-0.35 \cdot \sigma_y$ for the lower and upper bounds of the peak residual stress at the weld toe due to HFMI treatment contains most of the fatigue test data. As observed from the four S-N curves, there was no significant difference in fatigue life because of a semi-elliptical crack shape or a quarter elliptical crack shape assumption.

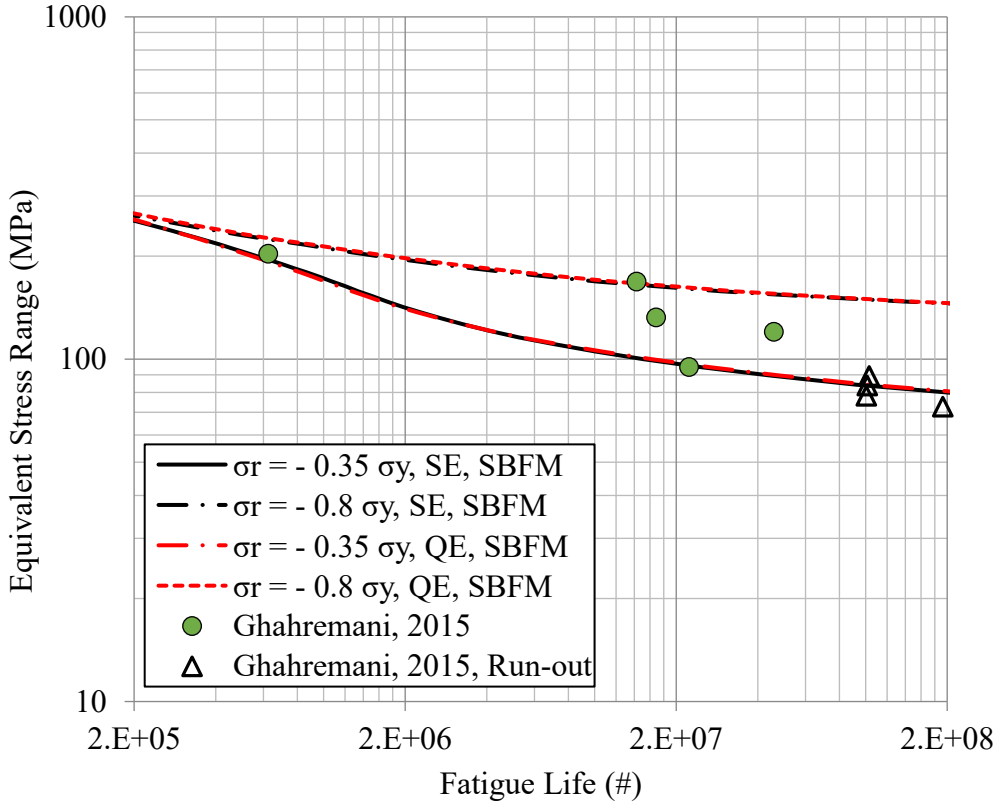

Figure 4.39: S-N curves for HFMI treated 350W steel specimens under VA1 loading

Fracture surfaces of the HFMI treated 350W specimens which were tested under VA1 loading are shown in Figure 4.40. For the maximum stress levels of 180 MPa, 229 MPa and 252 MPa, a crack initiated from an untreated edge, which is the left or right edge of the component cross-section as shown in the Figure 4.40. For other cases, a quarter elliptical crack was observed. For the maximum stress level of 320 MPa, the final crack aspect ratio observed from fracture surface is 0.45, which is very close to the value of 0.5 as predicted from SBFM model through crack shape evolution curve shown in Figure 4.41. In Figure 4.40, on each specimen cross-section, treated weld toe line, on the top and bottom edge of the cross-section can clearly be observed. For the case, when crack initiated from an untreated edge, the observed fatigue life improvement represents a lower bound of improvement in fatigue life because of impact treatment, since the failure location has shifted to the untreated edge (it may not happen in a wide structural component generally used in bridges).

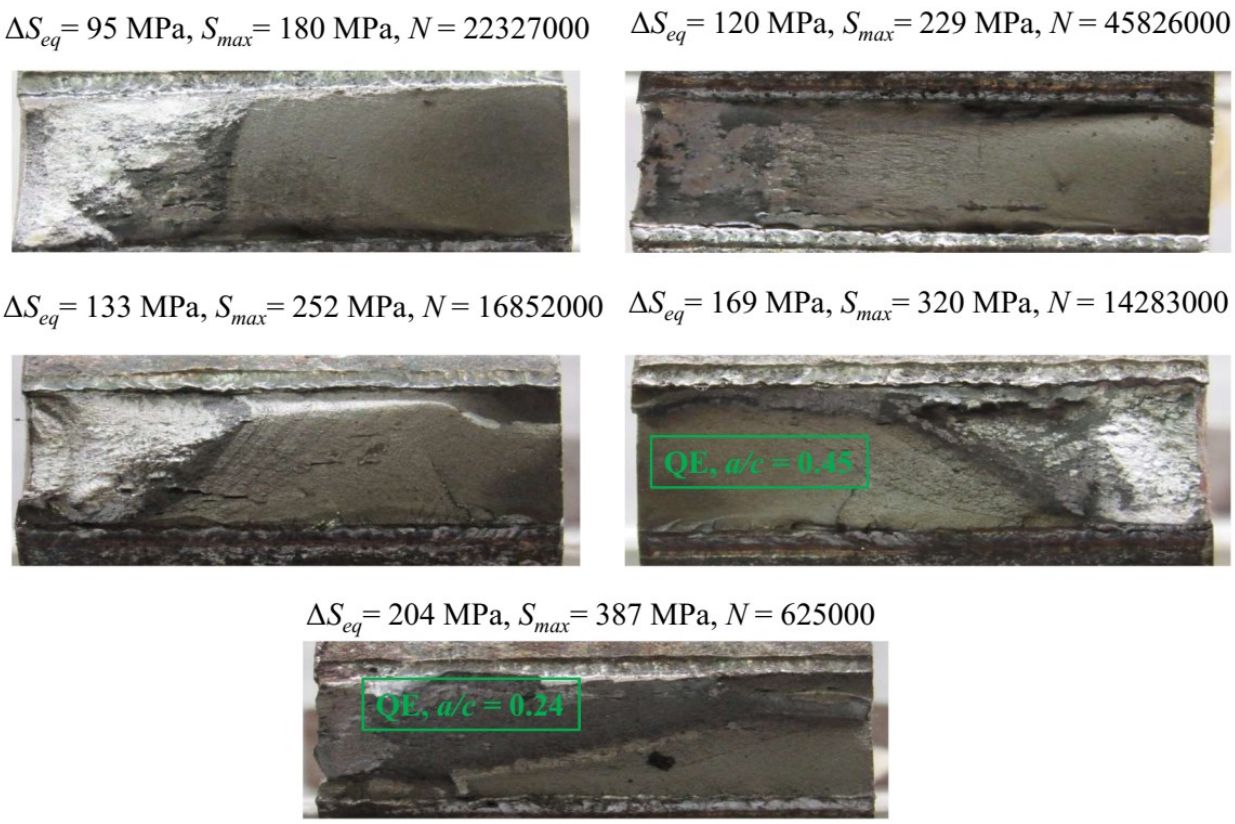

Figure 4.40: Fracture surfaces for HFMI treated 350W steel specimens under VA1 loading

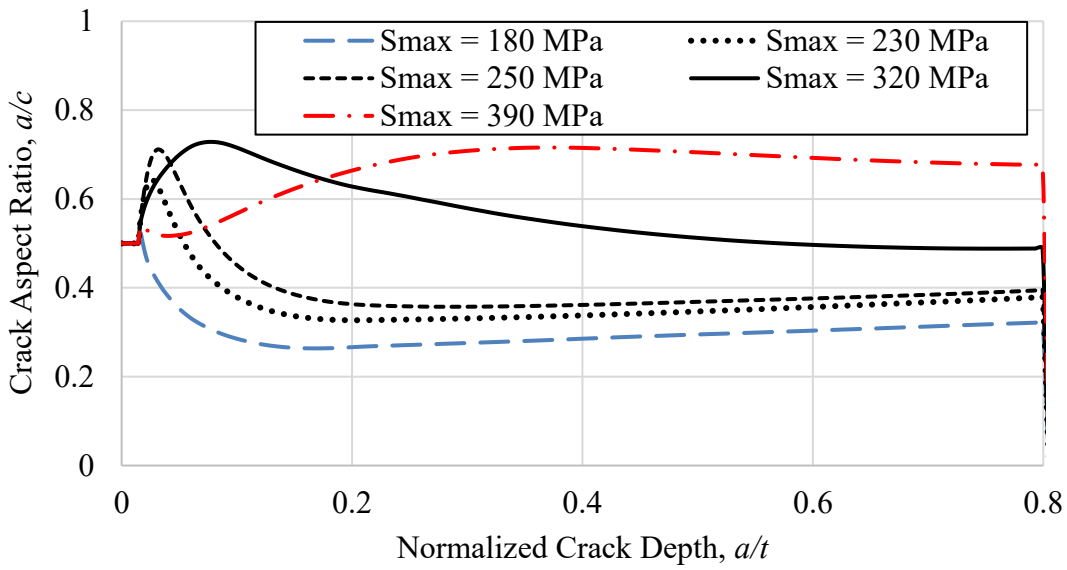

Figure 4.41: Crack shape evolution of QE crack under VA1 loading for HFMI treated 350W steel specimens with $(\sigma_r)_{toe} = -0.35 \cdot \sigma_y$

Figure 4.42 shows S-N curves for as-welded 350W specimens under VA2 loading. For this case, the S-N curves predicted by the SBFM model provide a close estimation of the experimental fatigue test results, with only one point falling substantially below the predicted S-N curves.

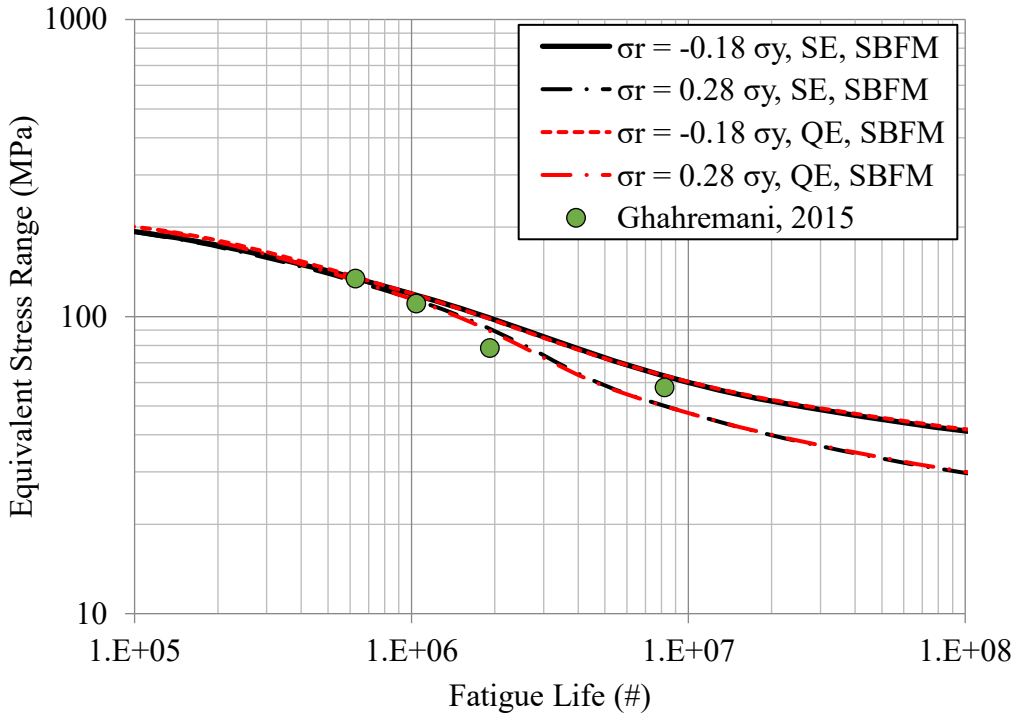

Figure 4.42: S-N curves for as-welded 350W steel specimens under VA2 loading

Fracture surfaces for as-welded 350W steel specimens tested under the VA2 loading are shown in Figure 4.43. As shown in this figure, for maximum stress levels less than 320 MPa, a through-width crack was observed while for higher stress levels a quarter elliptic crack shape was observed. The same pattern was predicted by the SBFM model through the crack shape evolution curves as shown in Figure 4.44. The through-width crack shape observed for all three specimens were well predicted by the SBFM model. For all as-welded specimens, it was observed that the crack initiated from the weld toe (bottom/top edge of cross-section) not from the unwelded region (left/right edge of cross-section) as shown in Figure 4.43.

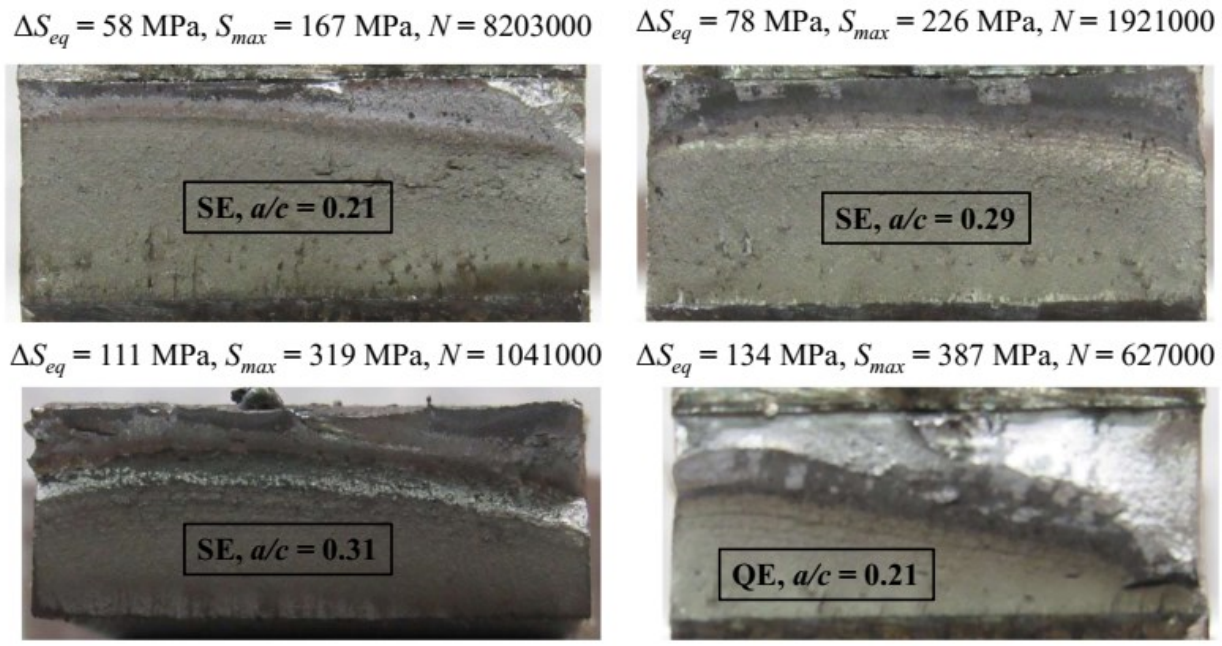

Figure 4.43: Fracture surfaces for as-welded 350W steel specimens under VA2 loading

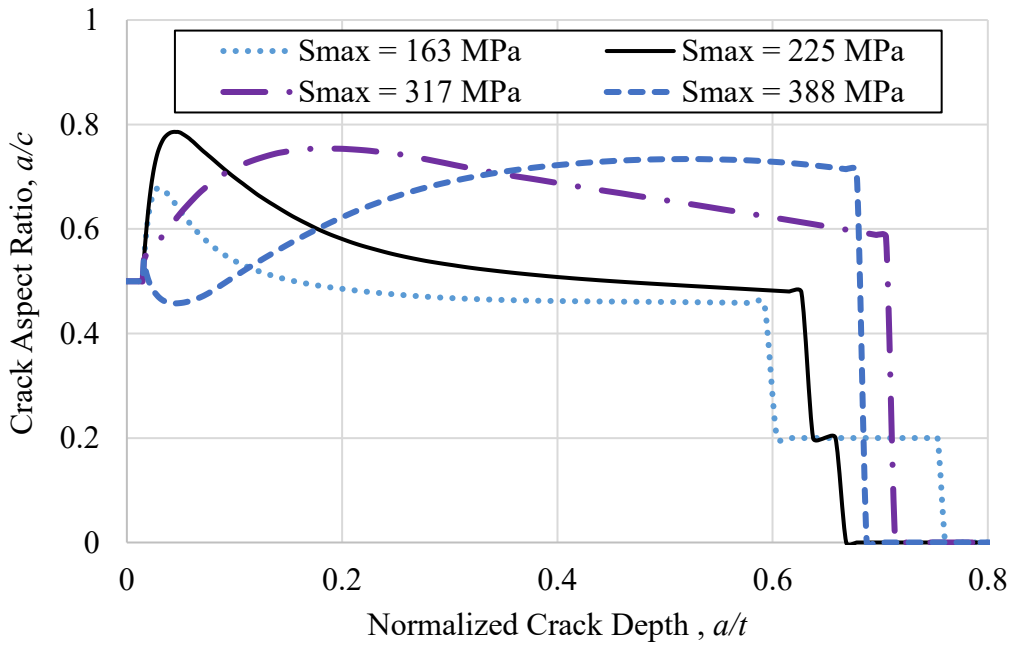

Figure 4.44: Crack shape evolution of SE crack under VA2 loading for as-welded 350W steel specimens with $(\sigma_r)_{toe} = 0.28 \cdot \sigma_y$

Figure 4.45 shows S-N curves for HFMI treated 350W steel specimens tested under the VA2 loading. A bound of peak residual stress varying from -0.80·σ_y to -0.35·σ_y provides an envelope of S-N curves, which contains all the experimental S-N data. The scatter in the fatigue test data was significant, possibly, because of large scatter in the residual stress resulting from the impact treatment process, which was observed in the residual stresses measured using the x-ray diffraction technique.

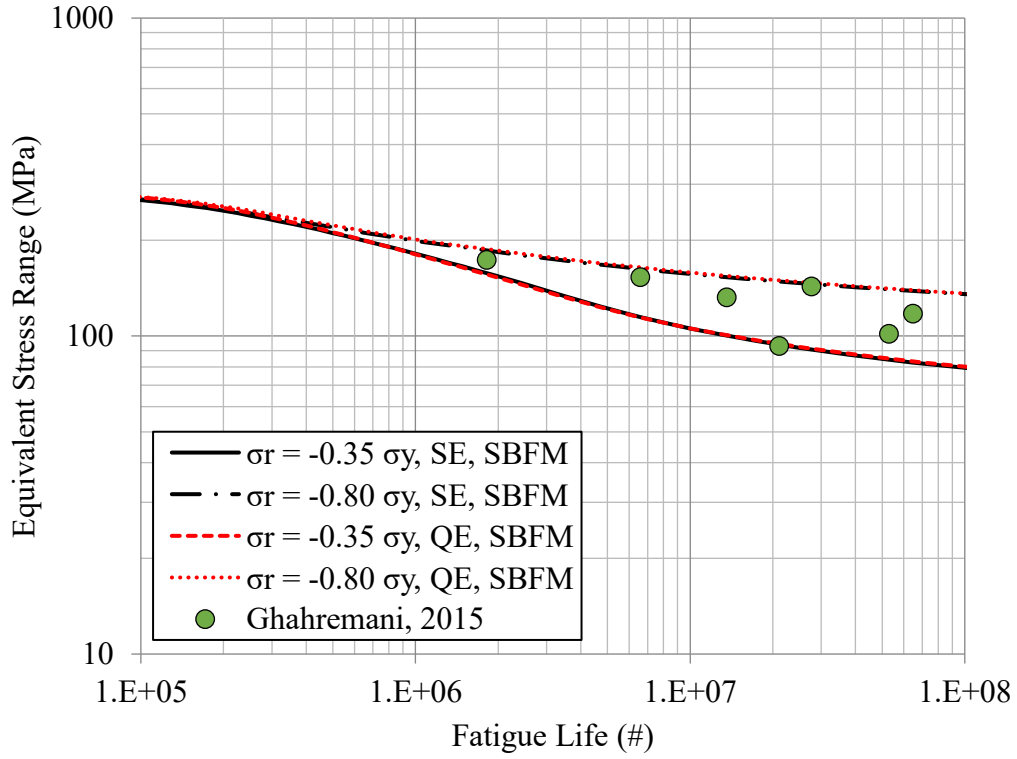

Figure 4.45: S-N curves for HFMI treated 350W steel specimens under VA2 loading

Fracture surfaces for HFMI treated 350W steel specimens tested under VA2 loading are presented in Figure 4.46. As observed from this figure, the final crack aspect ratio varied in between 0.41 to 0.62 which was predicted from SBFM model through the crack shape evolution curves as shown in Figure 4.47, where the final crack aspect ratio is varying from 0.40 to 0.60. For the particular case, when S_{max} is 319 MPa, the crack initiated from the corner and became a through-thickness crack. In the 2D SBFM model, the final crack depth was limited to 0.8·t because of the limitation of the used weight function method. Therefore, the predicted fatigue life will be

slightly lower than the experimentally obtained fatigue life. Since the crack growth rate at higher crack depths (> 0.8·t) is very high, the difference in fatigue life is expected to be negligible.

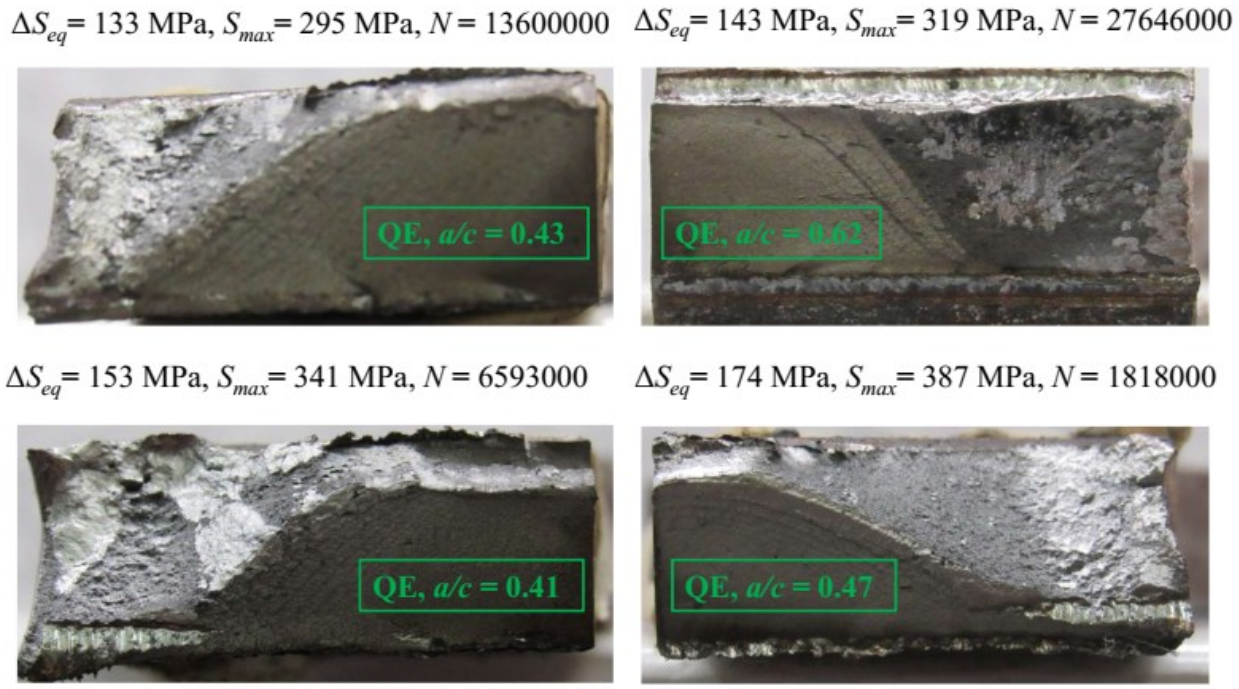

Figure 4.46: Fracture surfaces for HFMI treated 350W steel specimens under VA2 loading

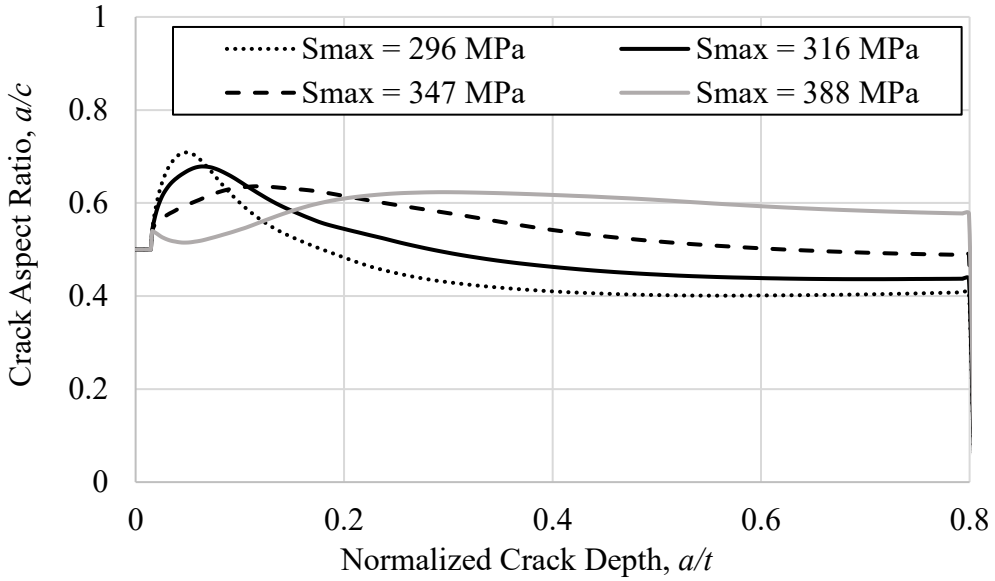

Figure 4.47: Crack shape evolution of QE crack under VA2 loading for HFMI treated 350W steel specimens with $(\sigma_r)_{toe}$ = -0.35·σ_y

4.8.2 SBFM analysis results for A514 steel specimens

The estimation of fatigue life and crack shape evolution curves by 2D SBFM model for A514 steel specimens in as-welded and HFMI treated condition is presented in this subsection. Figure 4.48 shows S-N curves for as-welded A514 steel specimens tested under CA loading. The assumed variation of residual stress distribution was similar to the case for 350W steel specimen in the as-welded condition, i.e. peak residual stress at the weld toe varied from -0.18·σ_y to +0.28·σ_y.

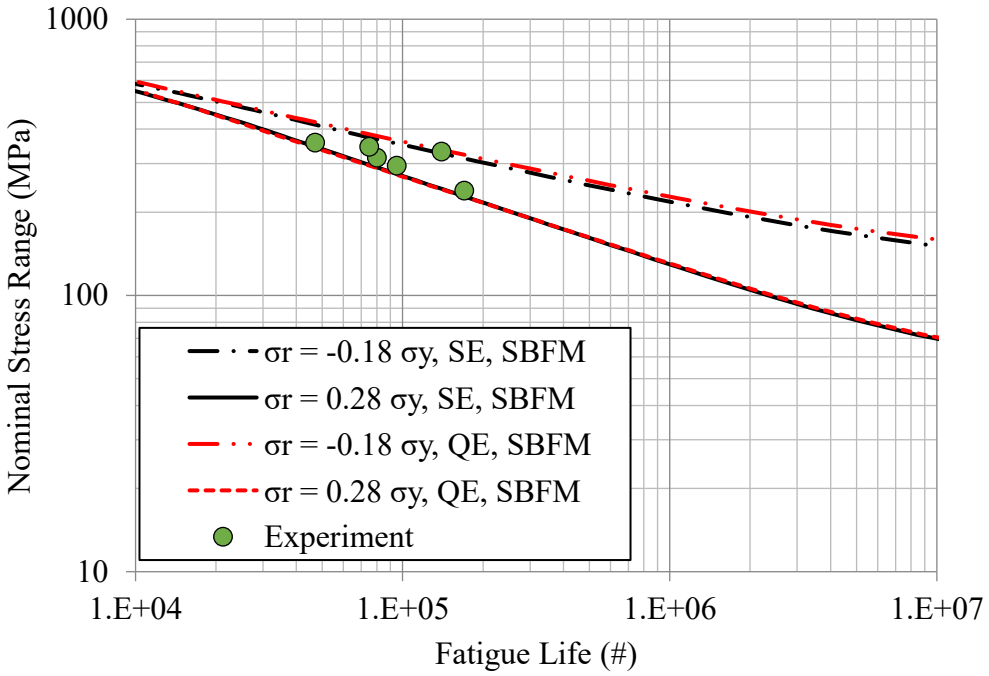

Figure 4.48: S-N curves for as-welded A514 steel specimens under CA loading

The comparison of the S-N curve predicted from SBFM model and experimental data shows that a reasonably good estimation of the fatigue test results is obtained using the SBFM model. Most of the data align along the S-N curve which was obtained with the assumption of 0.28·σ_y as the peak residual stress at the weld toe which shows that failure happened from the weld toe where tensile residual stress of magnitude of about 0.28·σ_y was present. The predicted S-N curves provide a reasonably good estimation for the fatigue life of the tested specimens with the assumed bounds of residual stress distributions. Figure 4.49 shows fracture surfaces for as-welded A514 steel specimen tested under the CA loading. Looking at the figure, it can be observed that at all stress levels, a through-width crack was observed.

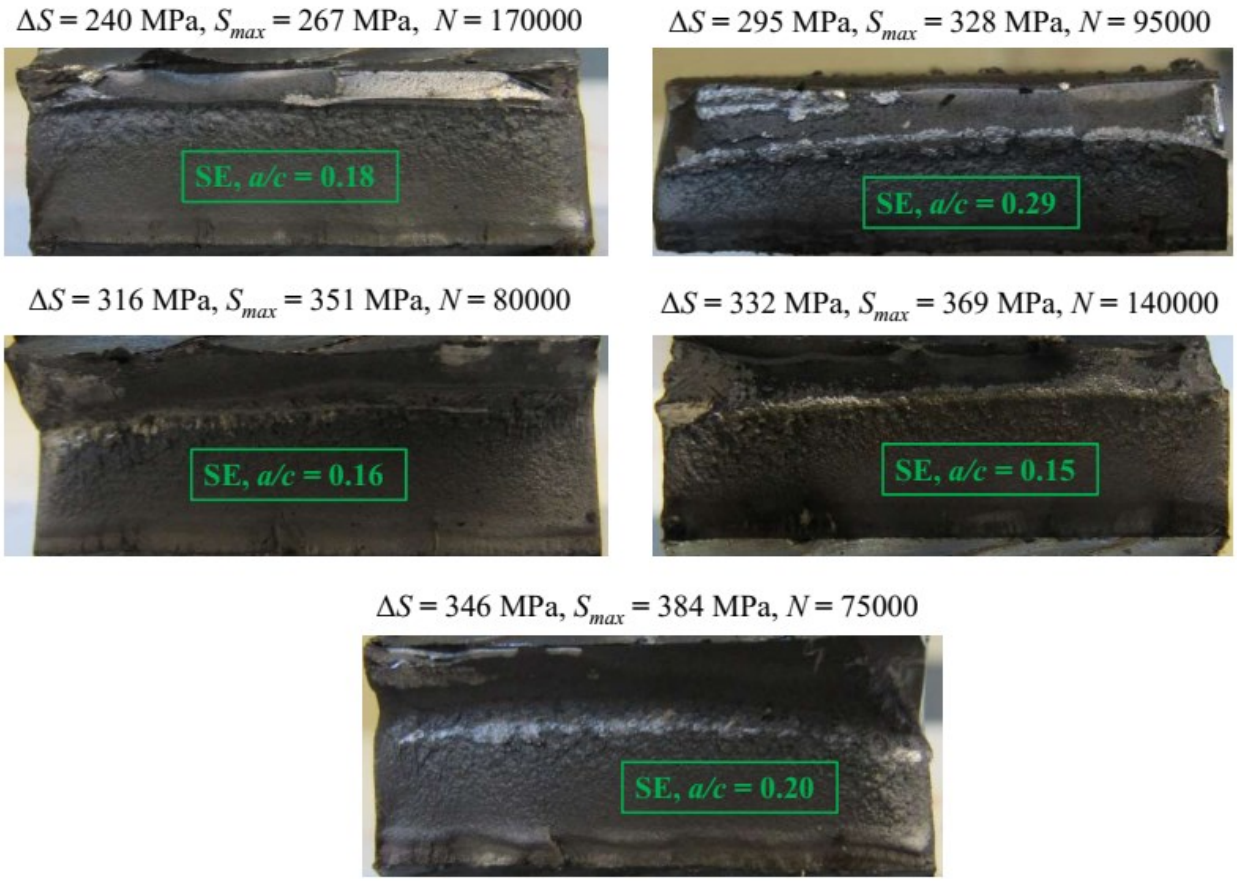

Figure 4.49: Fracture surfaces for as-welded A514 steel specimens under CA loading

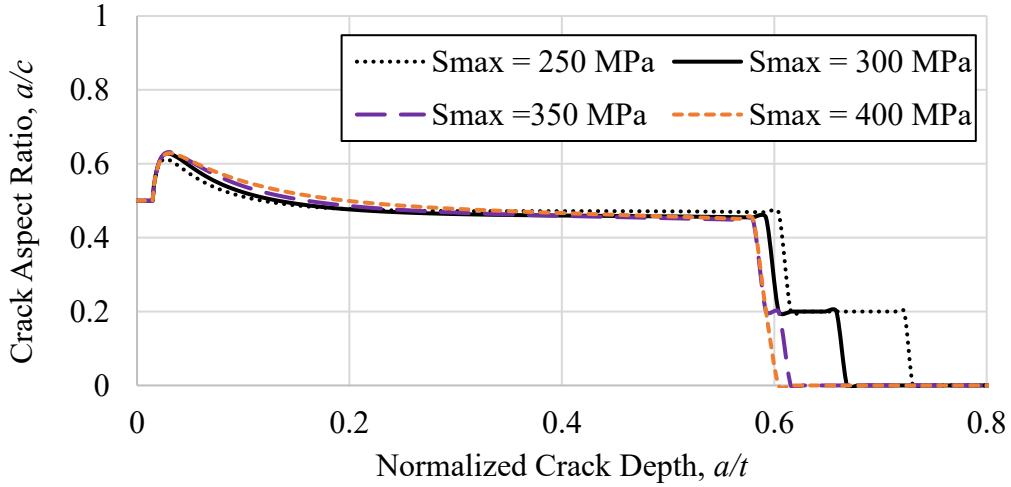

Figure 4.50: Crack shape evolution of SE crack under CA loading for as-welded A514 steel specimens with $(\sigma_r)_{toe} = 0.28 \cdot \sigma_y$

The crack shape evolution predicted by the SBFM model is shown in Figure 4.50, which also predicts that the final crack shape should be a through-width crack for the tested specimens. Another observation from Figure 4.50 is that the crack shape evolution is not as sensitive as it was for 350W specimens for a change of 50 MPa in maximum stress level. All the crack shape evolution curves are very close to each other for this case, while for 350W steel specimens, the crack shape evolution curves were significantly apart from each other (see Figure 4.32 for example) corresponding to a similar change in the stress level of 50 MPa.

Figure 4.51 shows S-N curves for HFMI treated A514 steel specimens tested under CA loading. The peak residual stress at the treated weld toe was assumed to vary from $-0.50 \cdot \sigma_y$ to $-0.35 \cdot \sigma_y$. The assumed bounds of the residual stress provided an envelope of S-N curves which contained all the experimental S-N data points except the run-out test data which has been shown with a diamond symbol. SE crack shape assumption provided a relatively conservative fatigue life estimation as compared to the QE crack shape assumption. Although, there was no significant difference in fatigue life corresponding to SE/ QE crack shape assumption.

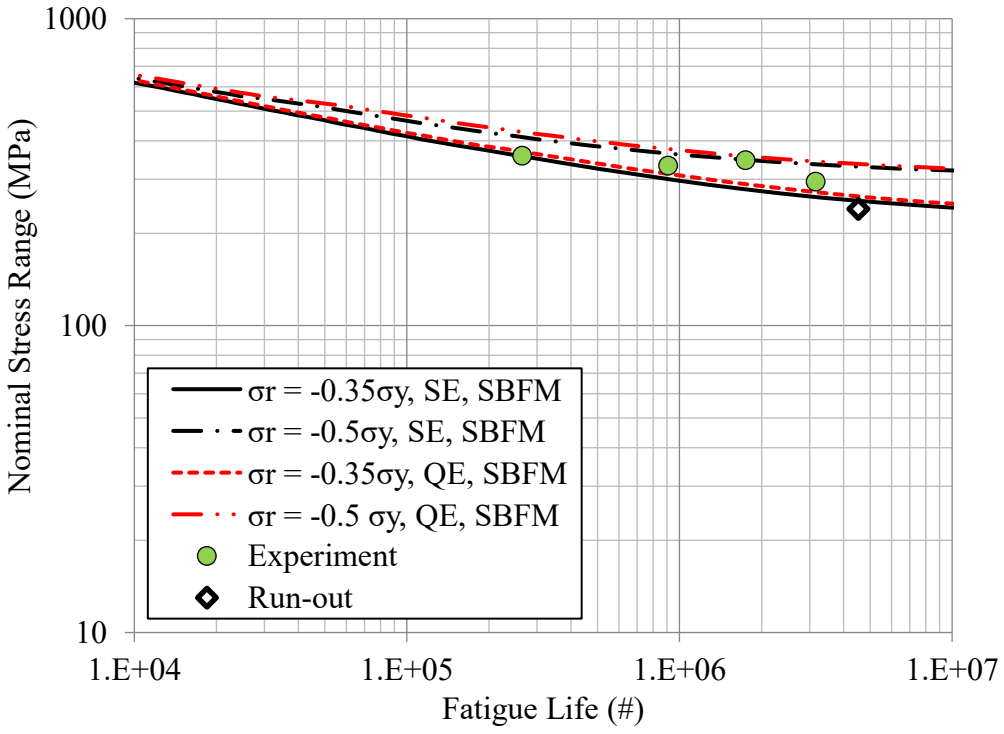

Figure 4.51: S-N curve for HFMI treated A514 steel specimens under CA loading

Figure 4.52 shows fracture surfaces of HFMI treated A514 steel specimens, which was tested under CA loading. For two cases, the maximum stress level of 328 MPa and 384 MPa, a crack initiated from the untreated edge (right/left edge in the cross-section shown) of the specimen. For the other two cases, one (top-right) is a well-rounded semi-elliptical crack and other (bottom-left) is a through-width crack.

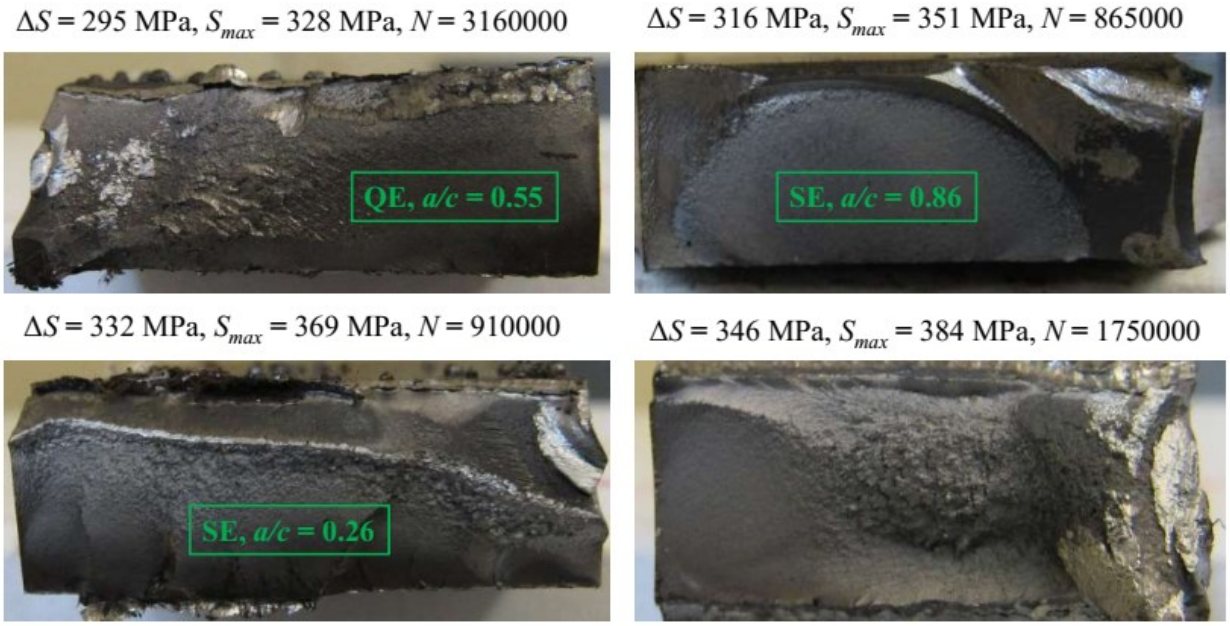

Figure 4.52: Fracture surfaces for HFMI treated A514 steel specimens under CA loading

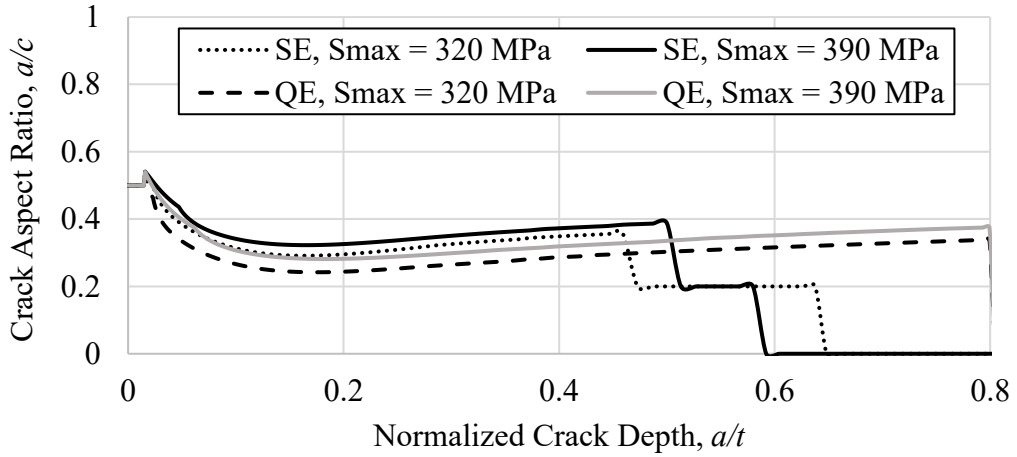

Figure 4.53: Crack shape evolution curves for HFMI treated A514 steel specimens under CA loading with $(\sigma_r)_{toe} = -0.35 \cdot \sigma_y$

Figure 4.53 shows crack shape evolution curves for HFMI treated A514 steel specimens tested under CA loading. As per crack shape evolution curves, a through-width crack should happen if a SE crack initiated from the treated edge which was evident from the fracture surface of the specimen tested at a maximum stress level of 369 MPa. If a QE crack initiates from the corner of the specimen cross-section, then the final crack aspect ratio of 0.38 is expected as shown in Figure 4.53. A well-rounded SE crack with *a/c* of 0.86 was not predicted by the SBFM model which happened in the specimen tested at a maximum stress level of 351 MPa. The possible reason behind such high aspect ratio may be a rounder initial defect than the assumed one and/or higher level of treatment which reduced the crack growth rate at the surface point.

S-N curves for as-welded A514 steel specimens tested under the CA-UL loading is shown in Figure 4.54. The assumed peak residual stress at the weld toe of $-0.18 \cdot \sigma_y$ provided a good estimation for the fatigue life of the tested specimens.

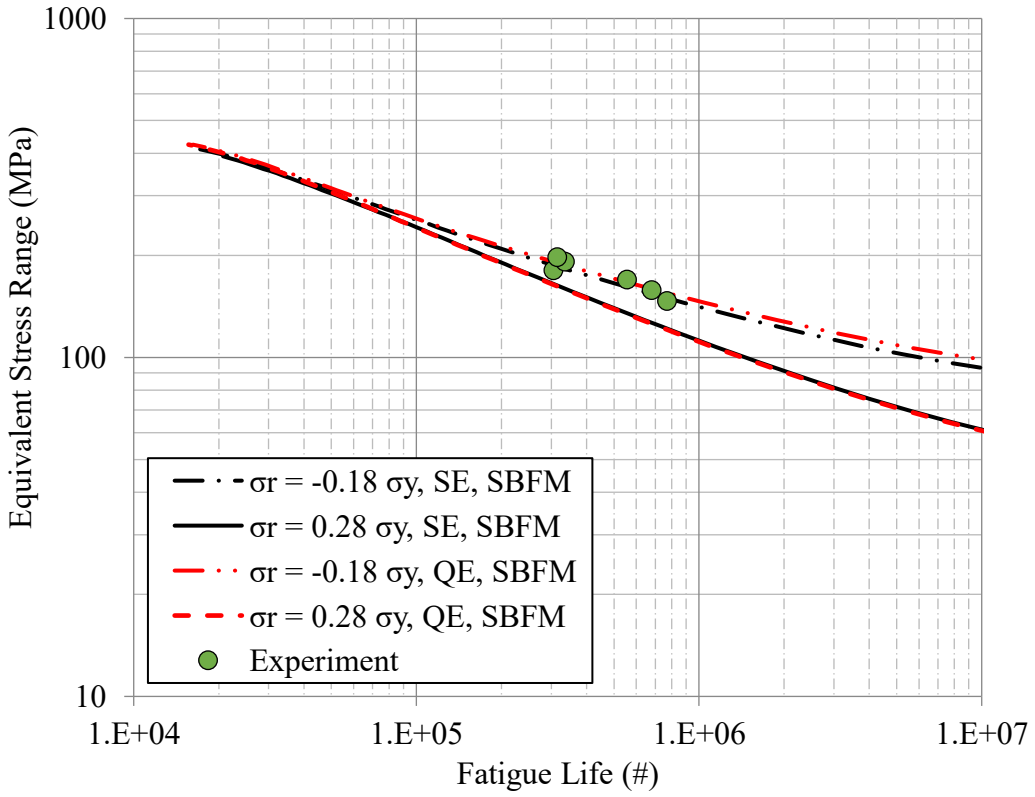

Figure 4.54: S-N curve for as-welded A514 steel specimens under CA-UL loading

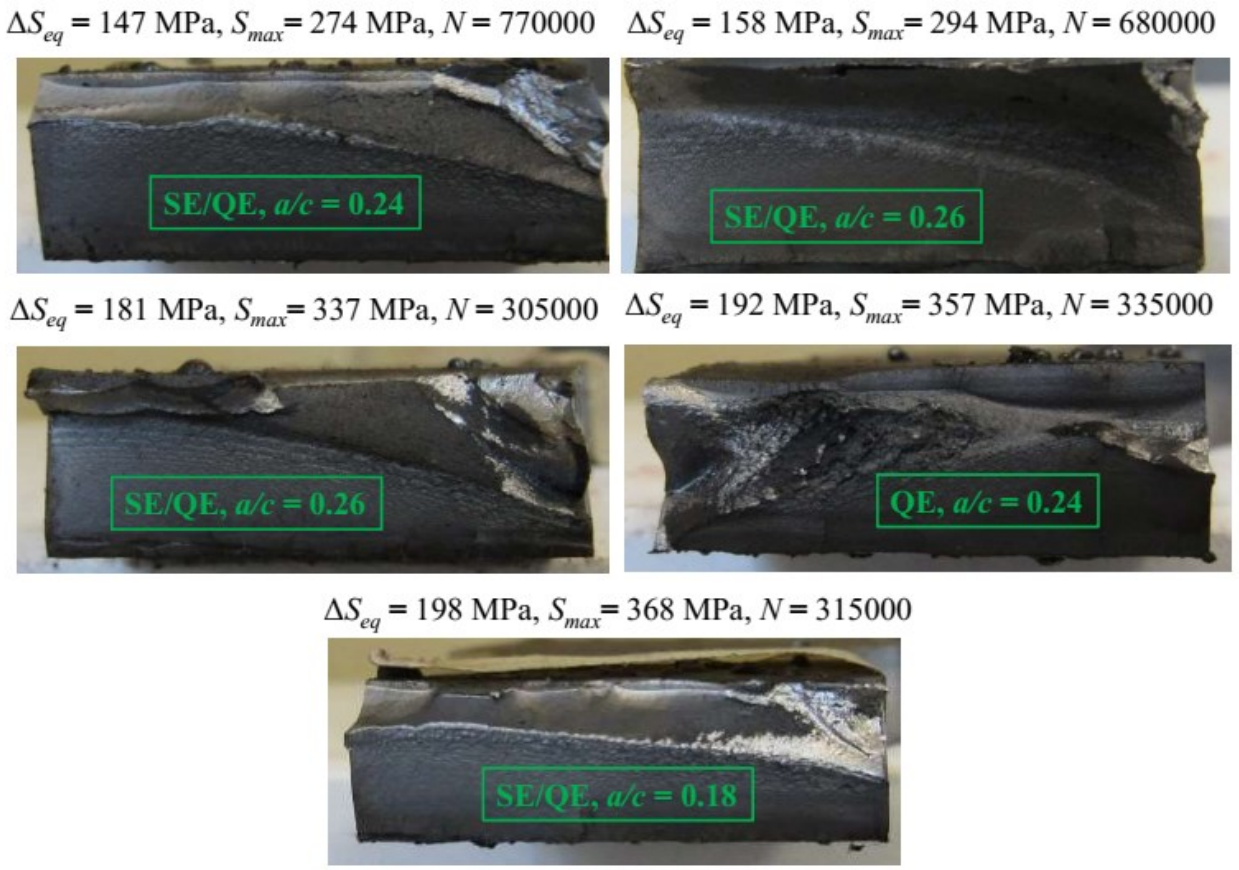

Figure 4.55: Fracture surfaces for as-welded A514 steel specimens under CA-UL loading

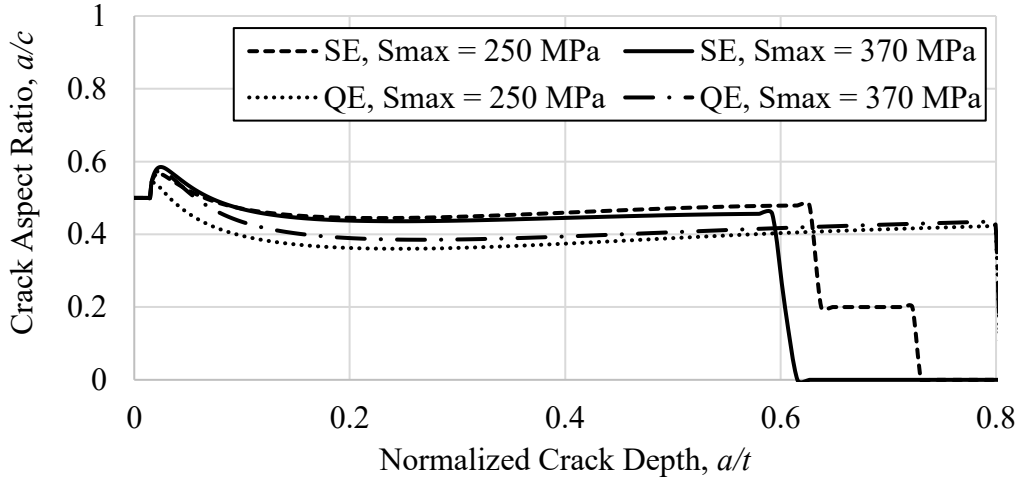

Figure 4.56: Crack shape evolution for as-welded A514 steel specimens under CA-UL loading with $(\sigma_r)_{toe} = -0.18 \cdot \sigma_y$

The fracture surfaces for as-welded A514 steel specimens tested under the CA-UL loading is shown in Figure 4.55. For all stress levels, a through-width crack was observed on the fracture surface with a varying aspect ratio of 0.18 to 0.26. Crack shape evolution curves predicted by the SBFM model with SE and QE crack shape assumption are shown in Figure 4.56. The predictions indicate that for all stress levels a through-width crack should happen if SE crack initiated from the welded edge, not from the corner. Crack shape evolution curves with a QE crack shape assumption shows that a final crack aspect ratio of 0.42 is expected if a crack initiated from the corner. For maximum stress levels of 357 MPa, a corner crack is observed in Figure 4.55 but the aspect ratio is 0.24 which is low as compared to the predicted value of 0.42. A precise defect geometry from non-destructive tests in these specimens would be helpful to predict more precise crack shape evolution curves and final crack aspect ratio.

Figure 4.57 shows S-N curves for HFMI treated A514 steel tested under CA-UL loading. An assumption of peak residual stress at the weld toe of value $-0.35 \cdot \sigma_y$ provided an excellent estimation for the fatigue life of tested specimens. Fracture surface for HFMI treated A514 steel specimens tested under CA-UL loading is shown in Figure 4.58. Looking at the fracture surface, it can be observed that the crack initiated from the untreated edge for all load levels which is not simulated with the SBFM model. However, when the cracking was simulated assuming crack initiating from treated weld toe and propagating along the thickness, then also estimated fatigue lives provided a reasonably good estimation for fatigue test results.

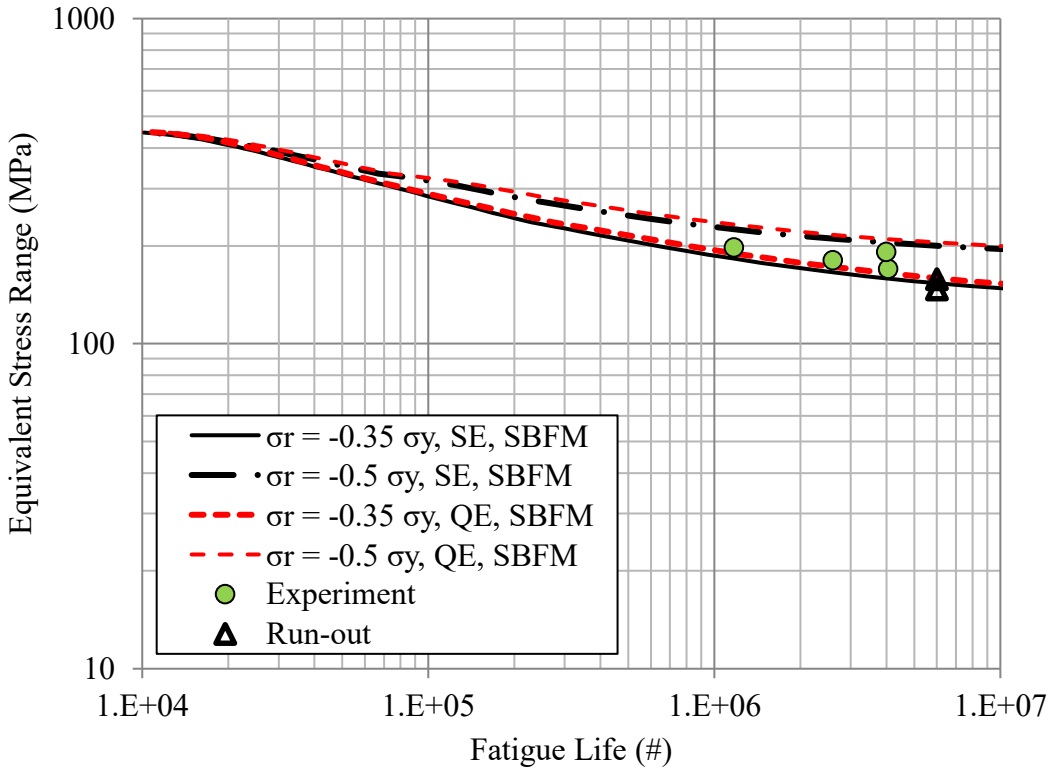

Figure 4.57: S-N curve for HFMI treated A514 steel specimens under CA-UL loading

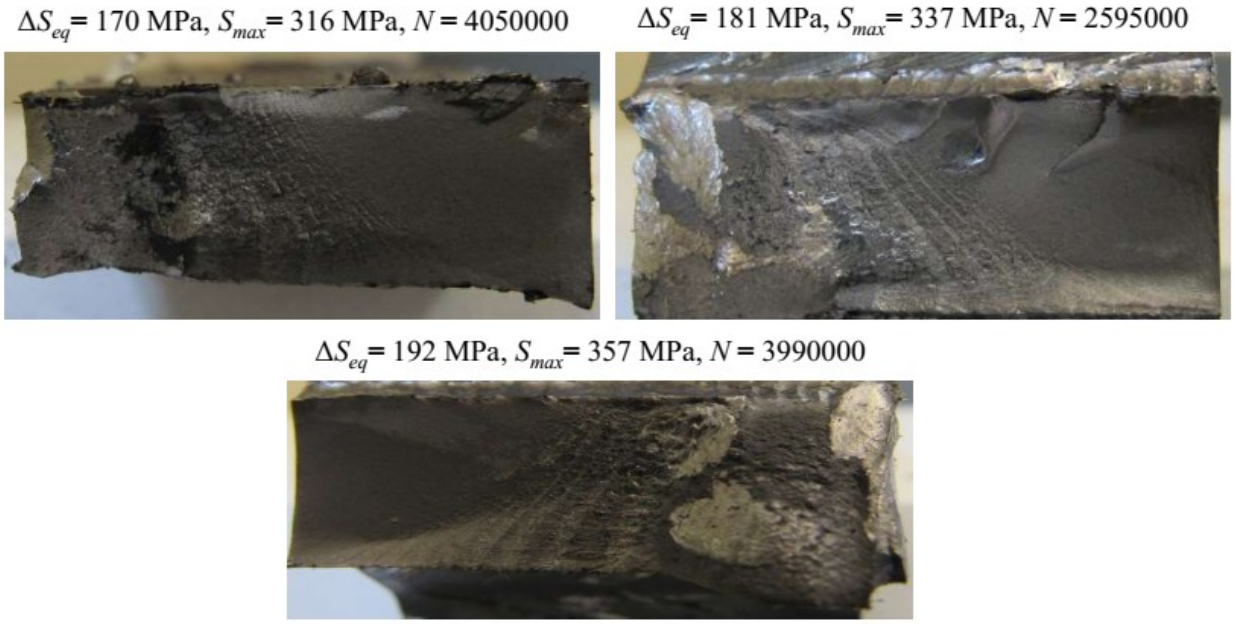

Figure 4.58: Fracture surfaces for HFMI treated A514 steel specimens under CA-UL loading

4.8.3 SBFM analysis results for 5083 aluminum specimens

S-N curves for as-welded aluminum specimens tested under the CA loading are shown in Figure 4.59. The peak residual stress at the weld toe was assumed to vary in between -0.18·σ_y to +0.28·σ_y and SE/QE crack shape assumptions were taken to come up with the four S-N curves shown in the figure. Looking at this figure, it is clear that assumed residual stress of -0.18 σ_y provided a good estimation for the fatigue life of the tested specimens. As discussed before, the four welds in the cruciform joints were performed sequentially rather than simultaneously which may have caused compressive residual stress at a few of the four weld toes. It is not very clear why a crack initiated from the location where compressive residual stress was present. The presence of welding defects or a higher SCF may have played a key role in the crack initiation. Fracture surfaces of the as-welded aluminum specimens tested under CA loading are shown in Figure 4.60. It can be observed that at all the stress levels, multiple cracks are present which is typical for aluminum especially at higher stress levels but the same was not observed in other materials (350W steel and A514 steel). In the case of multiple cracks, the aspect ratio mentioned on the fracture surface corresponds to the largest visible crack which would be dominating to cause the failure of the component. The presence of multiple cracks was not modelled in the SBFM model, still, a reasonably good estimation of fatigue life was obtained.

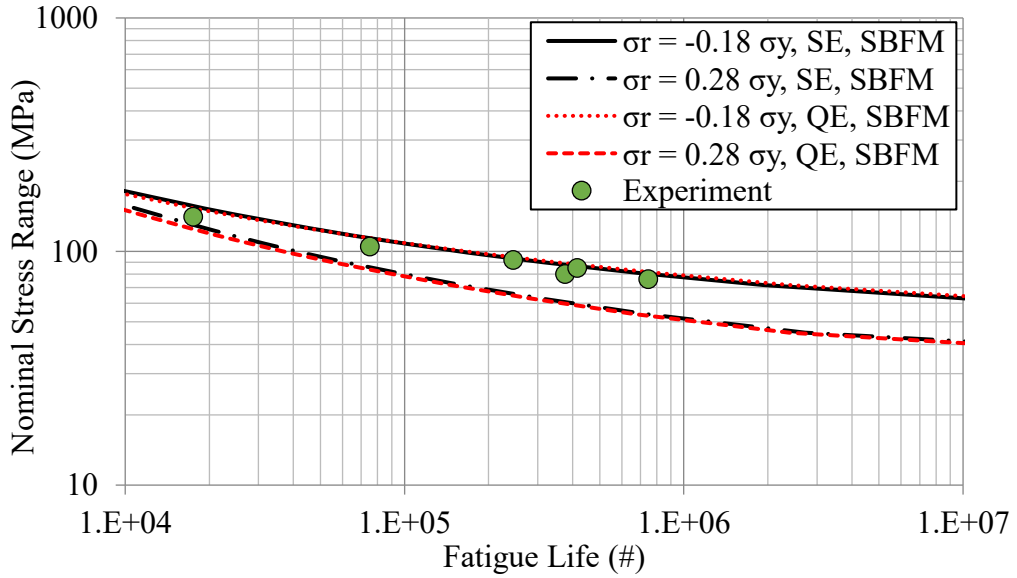

Figure 4.59: S-N curve for as-welded aluminum specimens under CA loading

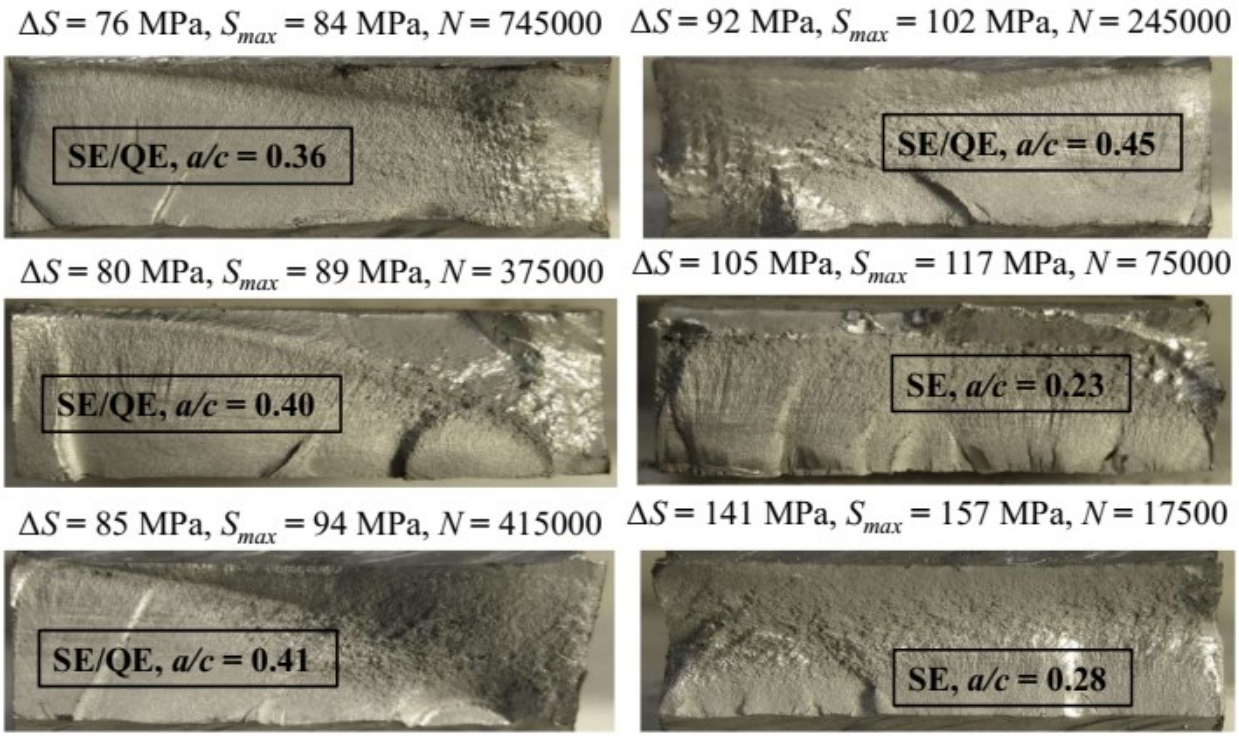

Figure 4.60: Fracture surfaces for as-welded aluminum specimens under CA loading

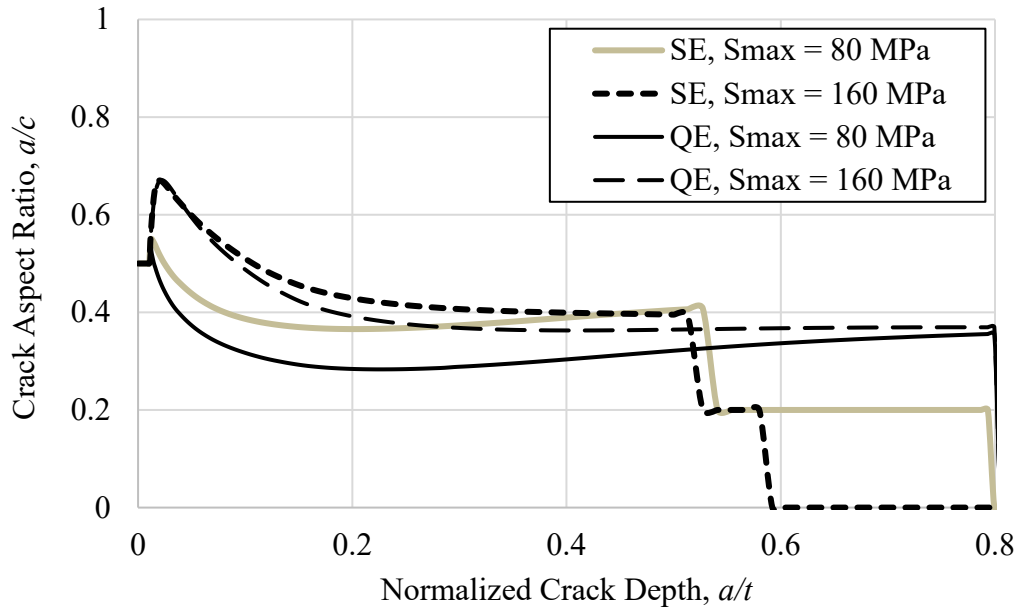

Figure 4.61: Crack shape evolution for as-welded aluminum specimens under CA loading with $(\sigma_r)_{toe} = -0.18 \cdot \sigma_y$

Crack shape evolution curves for as-welded aluminum specimens tested under CA loading are shown in Figure 4.61. It can be observed that a through-width crack is expected if SE crack initiated from the weld toe, which is observed on the fracture surface obtained for a maximum stress level of 117 MPa. As per the SBFM prediction of crack shape evolution with a QE crack shape assumption, the final crack aspect ratio for the QE crack should be close to 0.38 which is in between the values of 0.36 to 0.45 observed on the fracture surfaces shown in Figure 4.60.

Figure 4.62 shows S-N curves for the HFMI treated aluminum specimens tested under the CA loading. An assumed peak residual stress of $-0.05 \cdot \sigma_y$ provides a conservative estimation of the fatigue life for the experimental S-N data. As discussed before, the beneficial compressive residual stress in the HFMI treated aluminum specimen was found to be close to zero, as measured by the x-ray diffraction method, which is also evident from the S-N curve (with $\sigma_r = -0.05 \cdot \sigma_y$) as well.

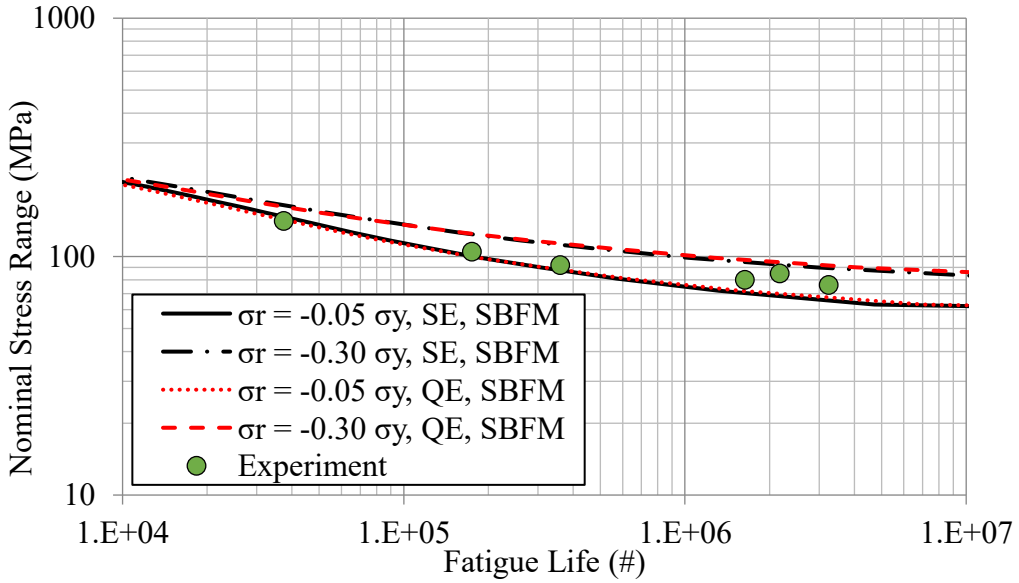

Figure 4.62: S-N curve for HFMI treated aluminum specimens under CA loading

The fracture surfaces of the HFMI treated aluminum specimen tested under the CA loading is shown in Figure 4.63. For the first fracture surface with a stress range of 80 MPa, corner crack appeared. For the second fracture surface on the left side with a stress range of 85 MPa, a large subsurface defect can be seen, which possibly caused the crack initiation from the untreated edge. For all other cases, multiple cracks can be seen to be present. Crack shape evolution curves predicted with the SBFM model are shown in Figure 4.64. For the case of a SE crack initiated

from the weld toe, either a through-width crack is expected or a final aspect ratio (a/c) of 0.54, which can also be seen from the fracture surface for maximum stress of 102 MPa. For corner cracks, the crack shape evolution curves show that the final aspect ratio should be in between 0.45 to 0.56 which is close to the value of 0.44 observed on fracture surface obtained at a maximum stress level of 89 MPa.

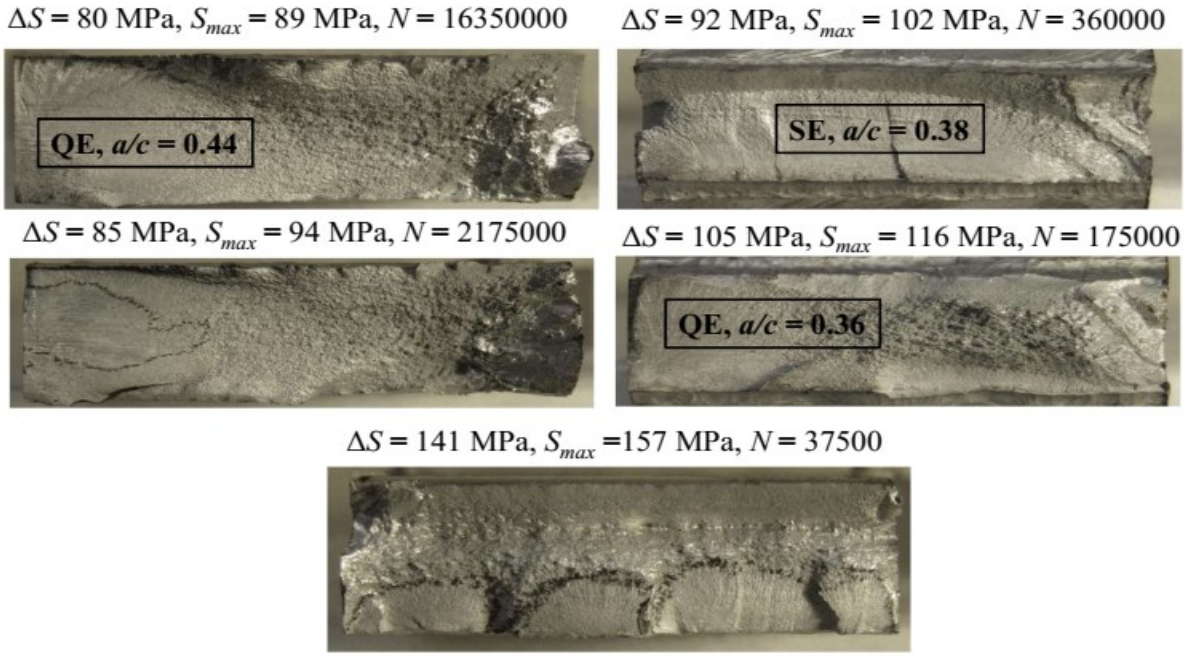

Figure 4.63: Fracture surfaces for HFMI treated aluminum specimens under CA loading

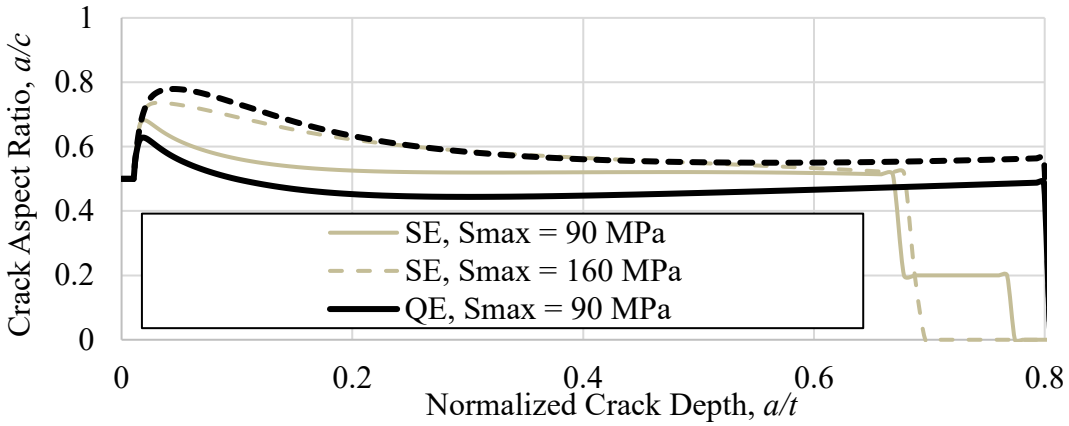

Figure 4.64: Crack shape evolution for HFMI treated aluminum specimens under CA loading, $(\sigma_r)_{toe} = -0.05 \cdot \sigma_y$

Figure 4.65 shows S-N curves for as-welded aluminum specimens tested under the CA-UL loading. The assumed bounds of peak residual stress at the weld toe varying from $-0.18 \cdot \sigma_y$ to $0.28 \cdot \sigma_y$ provides an envelope of S-N curves which contains all the experimental S-N data. After comparing S-N curves in Figure 4.59 and Figure 4.65, it can be observed that the effect of residual stress variation from $-0.18 \cdot \sigma_y$ to $+0.28 \cdot \sigma_y$ is less under the CA-UL loading than for the case of the CA loading, which is indicated by S-N curves that fall closer to each other in Figure 4.65 as compared to Figure 4.59. Fracture surfaces of the failed specimens for this case are shown in Figure 4.66. It can be observed that either a through-width crack appeared or a quarter-elliptical crack appeared for all tested stress levels. Crack shape evolution curves as predicted by the SBFM model are shown in Figure 4.67. It can be observed that if a SE crack initiated from the weld toe and propagated as a SE crack, then a through-width crack is expected at all tested stress levels which are observed on the fracture surface for maximum stress level of 84 MPa, 98 MPa, 108 MPa, and 126 MPa. Crack shape evolution curves obtained with a QE crack shape assumption show that the final crack aspect ratio should be about 0.42, which is close to the value of 0.40 observed on fracture surface for maximum stress level of 78 MPa.

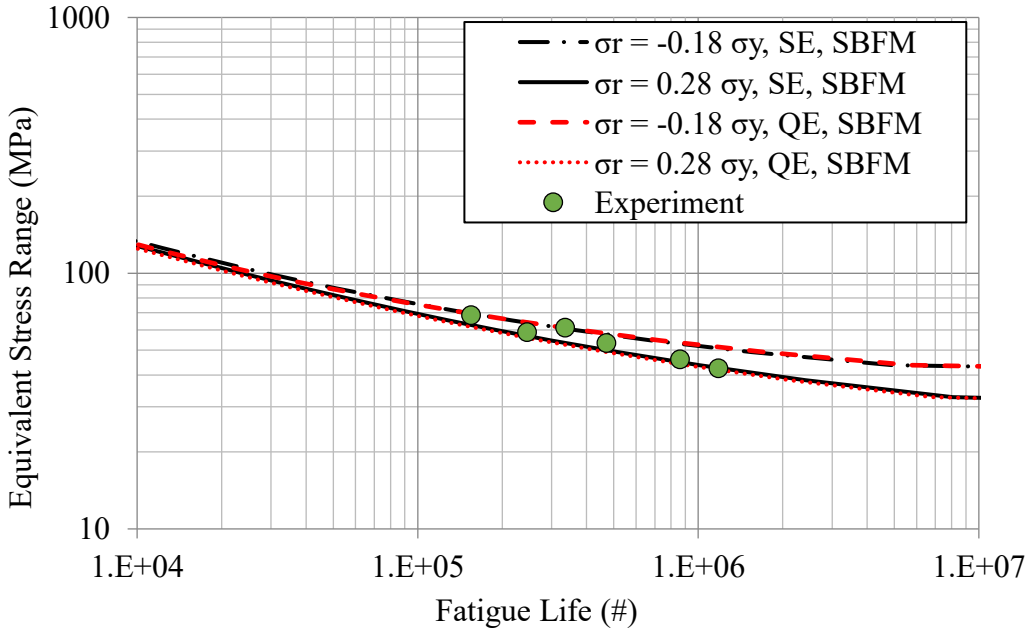

Figure 4.65: S-N curves for as-welded aluminum specimens under CA-UL loading

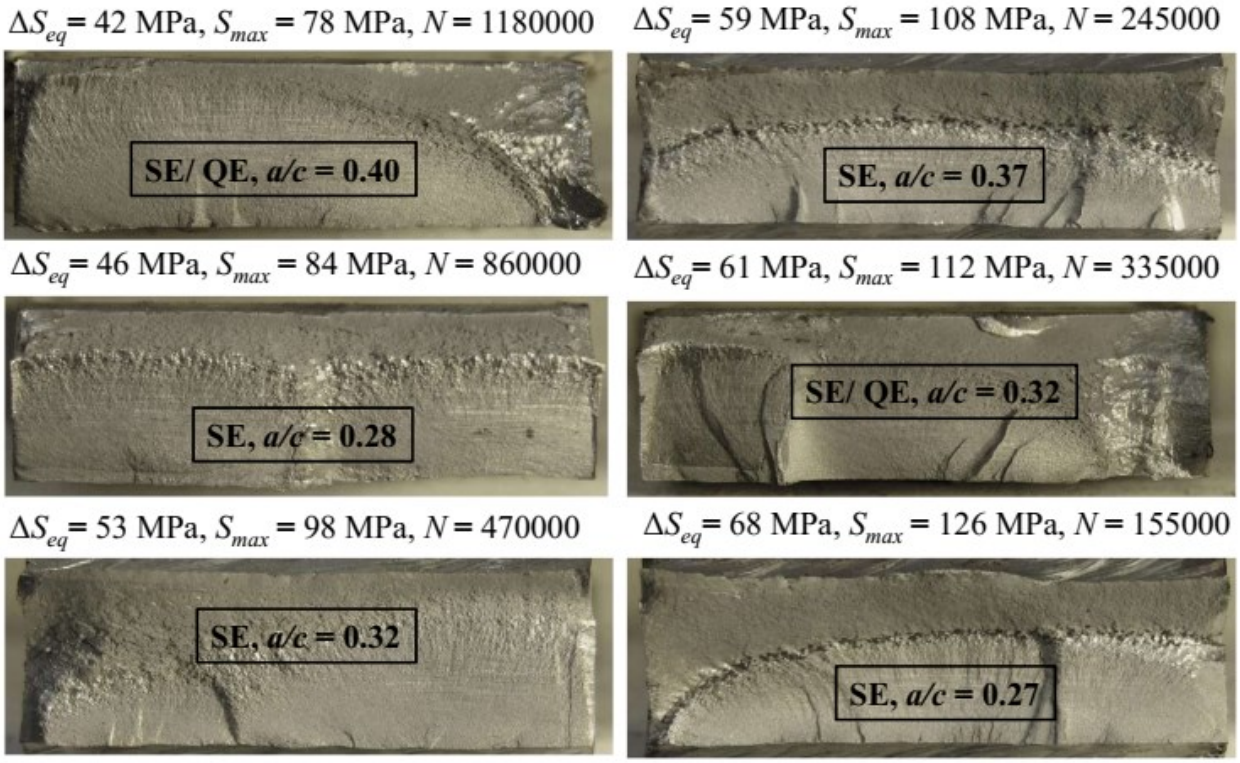

Figure 4.66: Fracture surfaces for as-welded aluminum specimens under CA-UL loading

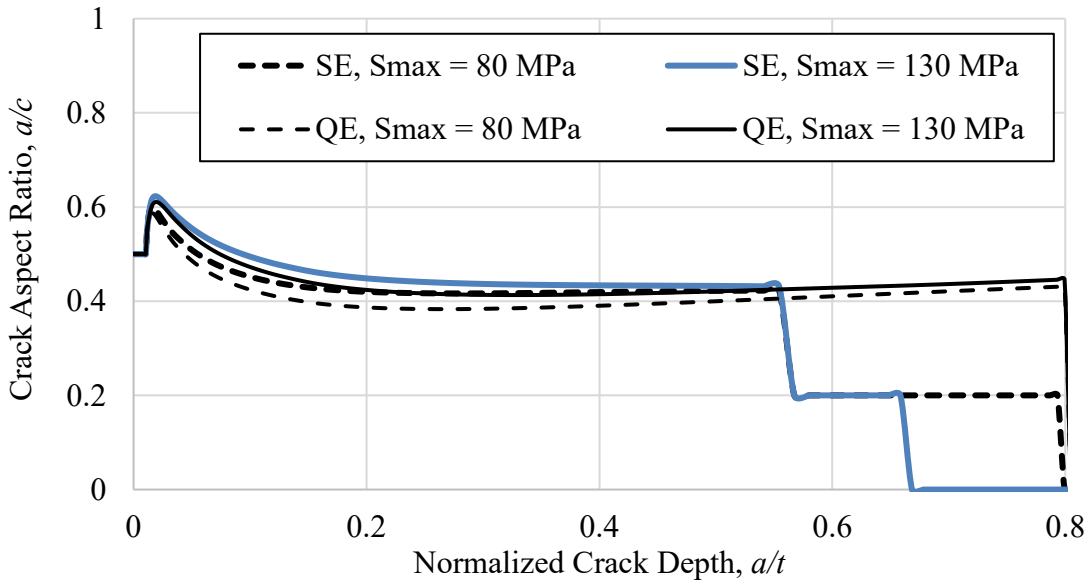

Figure 4.67: Crack shape evolution for as-welded aluminum specimens under CA-UL loading with $(\sigma_r)_{toe} = 0.28 \cdot \sigma_y$

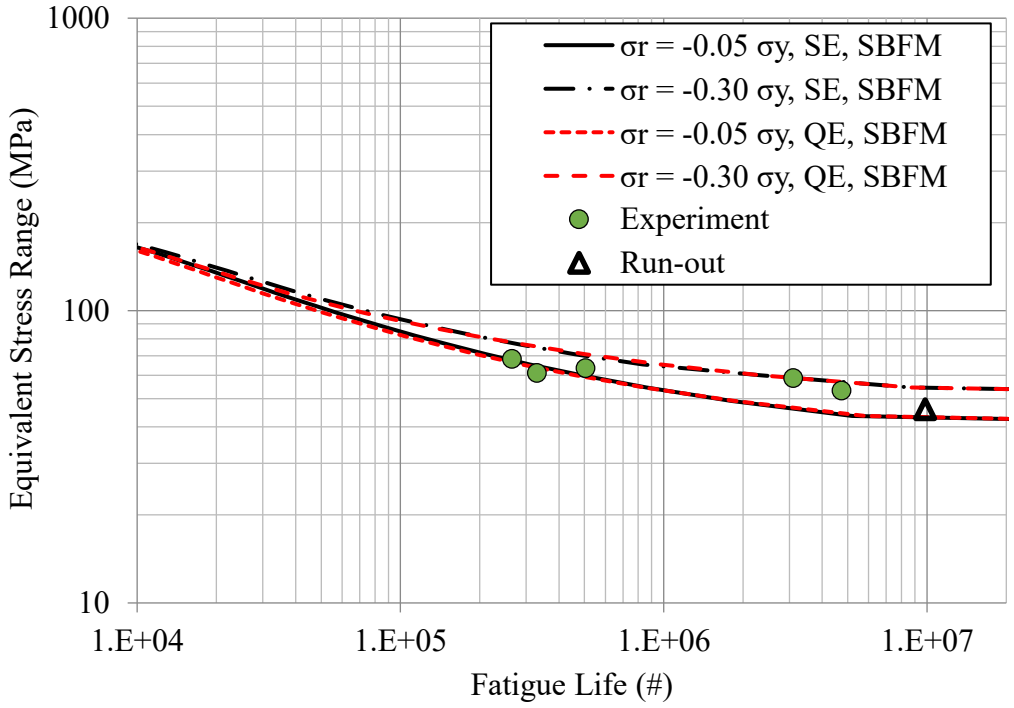

Figure 4.68: S-N curves for HFMI treated aluminum specimens under CA-UL loading

Figure 4.68 shows S-N curves for HFMI treated 5083 aluminum specimens tested under the CA-UL loading. Assumed bounds of residual stress varying from -0.30·σ_y to -0.05·σ_y provide an excellent estimation for the fatigue test results. Fracture surfaces for HFMI treated 5083 aluminum specimens tested under CA-UL loading are shown in Figure 4.69. It can be observed that a quarter elliptical crack appeared in all the cases and final aspect ratio varied between 0.33 and 0.61. For a maximum stress level of 98 MPa, the fracture surface shows that the thickness of the component is higher on the left side. This is because of the two weld toe locations, which are not exactly in front of each other on both sides of the main plate of the cruciform welded joint. Therefore, the crack initiated from one weld toe and propagated into the filler material of the weld on the other side of the main plate, which is reflected here as an increased thickness of the component. Crack shape evolution as predicted by SBFM for the different magnitude of maximum stress levels is shown in Figure 4.70. As per the crack shape evolution curves for QE crack, the final crack aspect ratio should be about 0.5 which is very close to the average value of final crack aspect ratios of 0.33 and 0.61 observed on the fracture surfaces.

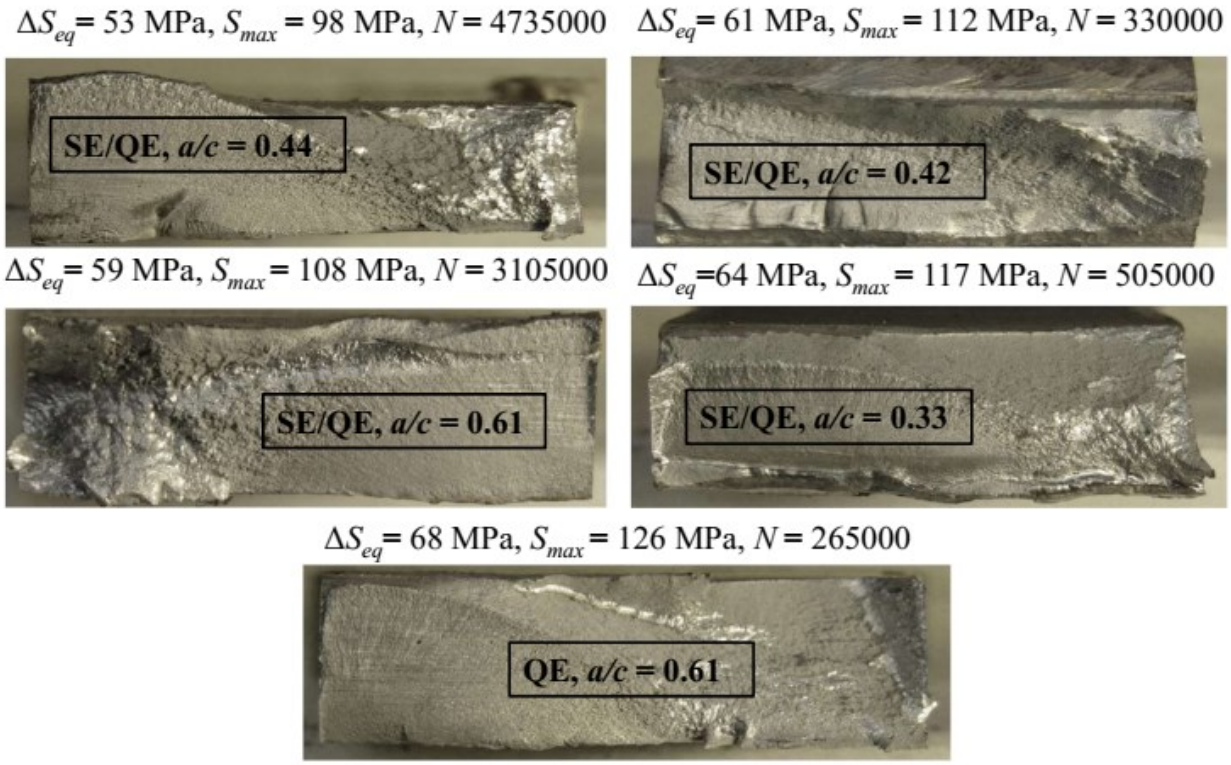

Figure 4.69: Fracture surfaces for HFMI treated aluminum specimens under CA-UL loading

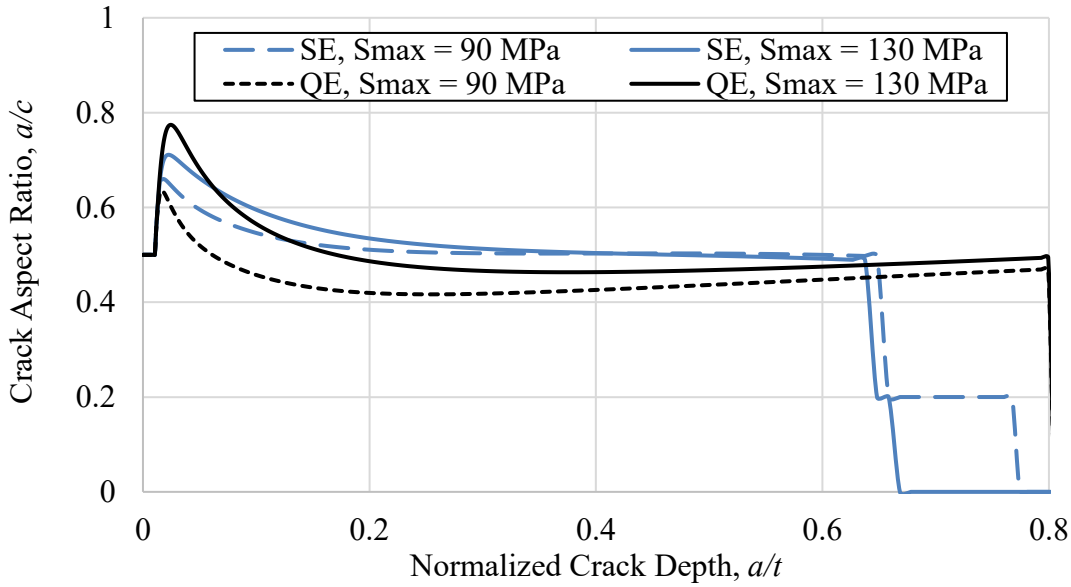

Figure 4.70: Crack shape evolution curves for HFMI treated aluminum specimens under CA-UL loading with $(\sigma_r)_{toe} = -0.05 \cdot \sigma_y$

In this section, the 2D SBFM model was validated with not only experimental S-N data but also with the final crack shape available from the fracture surface of the specimen. Reasonably good predictions were achieved with the 2D SBFM model for all three material types, which were fatigue tested under four different loading conditions. In the next section, a study of the variable amplitude loading effect on three material types is discussed followed by quantification of fatigue strength improvement for each material type.

4.9 Study of VA loading effect on fatigue life of tested specimens

In this section, S-N results from the SBFM model as well as from experimental tests are presented to assess the effect of VA loading on the fatigue life of the 350W steel, A514 steel, and 5083 aluminum welded specimens.

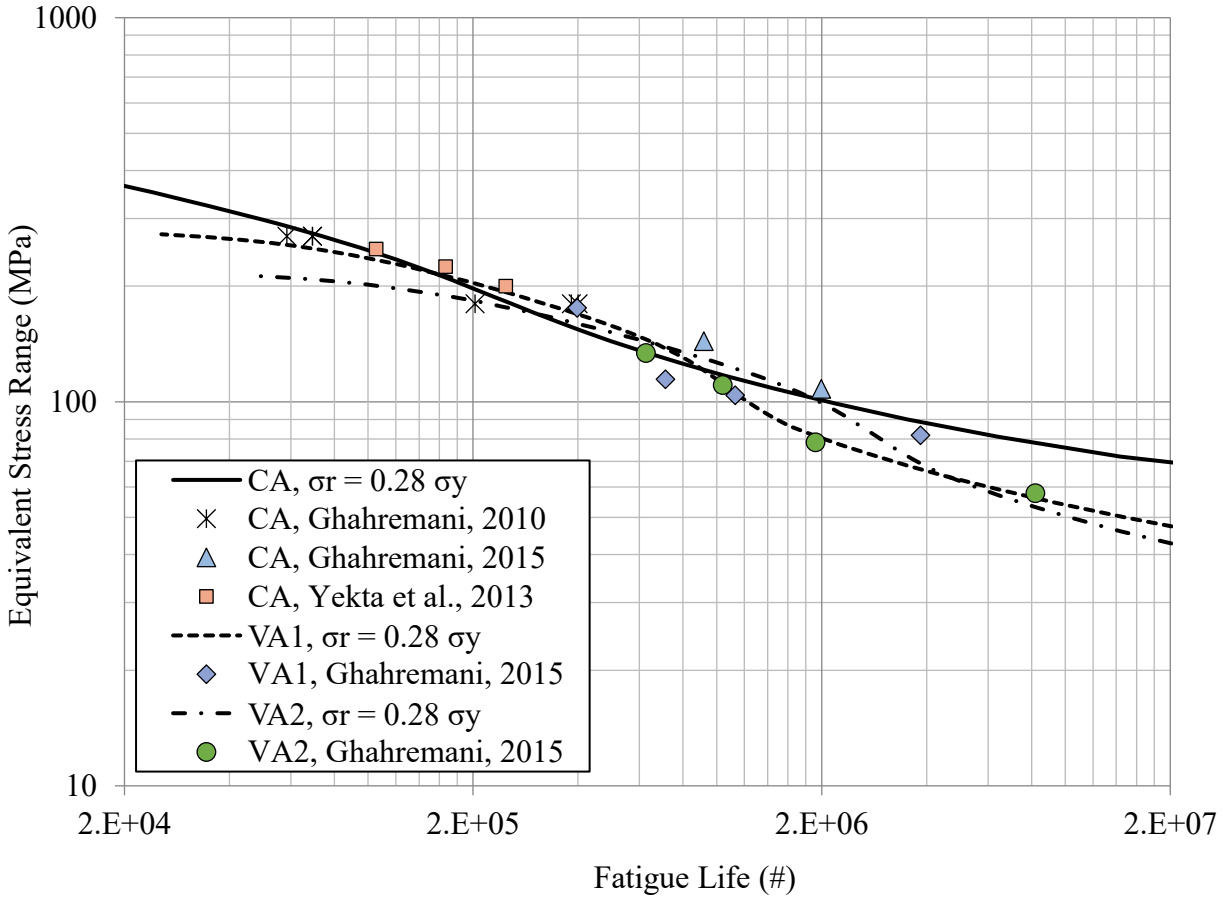

Figure 4.71: S-N curves for as-welded 350W steel specimens under various loading conditions

Figure 4.71 shows S-N curves and experimental data for "as welded" 350W steel specimens under CA, VA1 and VA2 loading conditions. The presented S-N curves from the SBFM model have been obtained for the assumption of a semi-elliptical crack shape and a peak residual stress at the weld toe of $+0.28 \cdot \sigma_y$. This figure shows that there is no significant effect on fatigue life because of the VA loading for the range of fatigue life 10^5 to 10^6. For a fatigue life of more than two million cycles, the estimated fatigue life from SBFM model is lower under the VA1 and the VA2 loading as compared to fatigue life under the CA loading ($R = 0.1$).

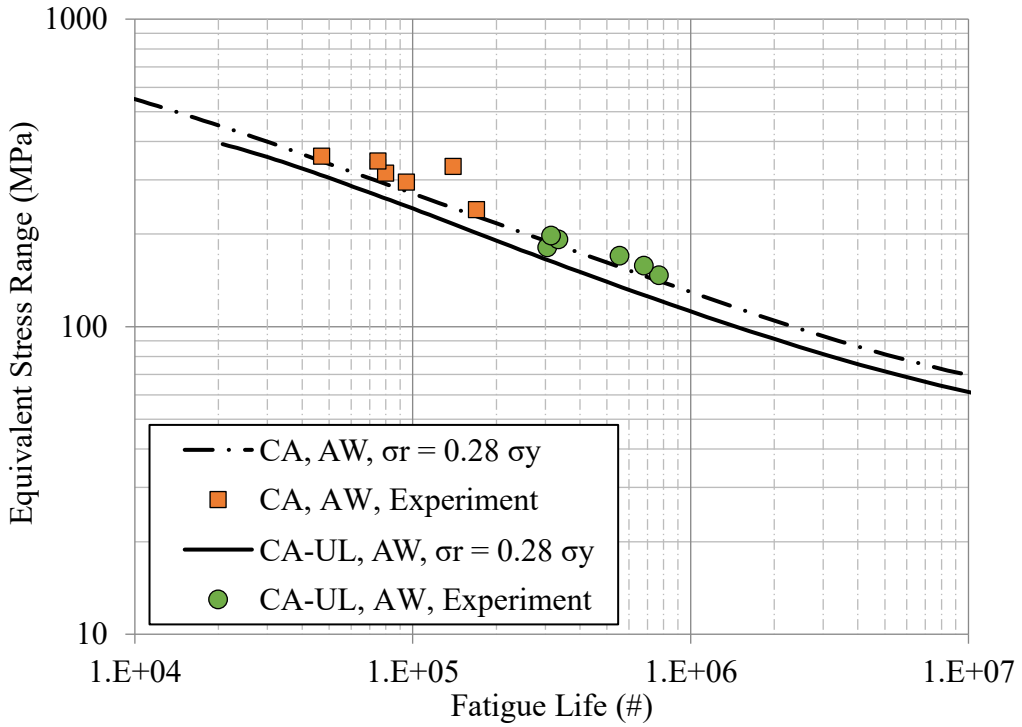

Figure 4.72: S-N curves for as-welded A514 steel specimens under various loading conditions

Figure 4.72 shows S-N curves and fatigue test data for "as welded" A514 steel specimens under CA and CA-UL loading conditions. It can be observed from the S-N curves that the fatigue life under the CA-UL loading is slightly less than the fatigue life under the CA loading. Although, the experimental S-N data does not show any significant variation under two different loading conditions. It can be concluded from Figure 4.71 and Figure 4.72 that there is no VA loading effect on the fatigue life of as-welded specimens if the fatigue life is less than 10^6 cycles for the employed VA loading histories.

Figure 4.73 shows S-N curves and experimental data for HFMI treated 350W steel specimens under CA, VA1 and VA2 loading conditions. The S-N curves show a significant difference in fatigue life for specimens tested under the three loading histories. Though there is no significant difference in fatigue life under the VA1 & VA2 loading histories, the fatigue life under the VA loading is less than under the CA loading according to the SBFM-derived S-N curves for the same magnitude of peak residual stress at the weld toe. This conclusion would have been difficult to draw based on only experimental S-N data because of the significant scatter in the fatigue test data. The study of VA loading effects made here by SBFM analysis is an important result, which is made possible by the 2D SBFM model. The ability to understand these effects may be important for assessing the benefit of HFMI treatment over a wide range of fatigue lives and variable amplitude loading conditions.

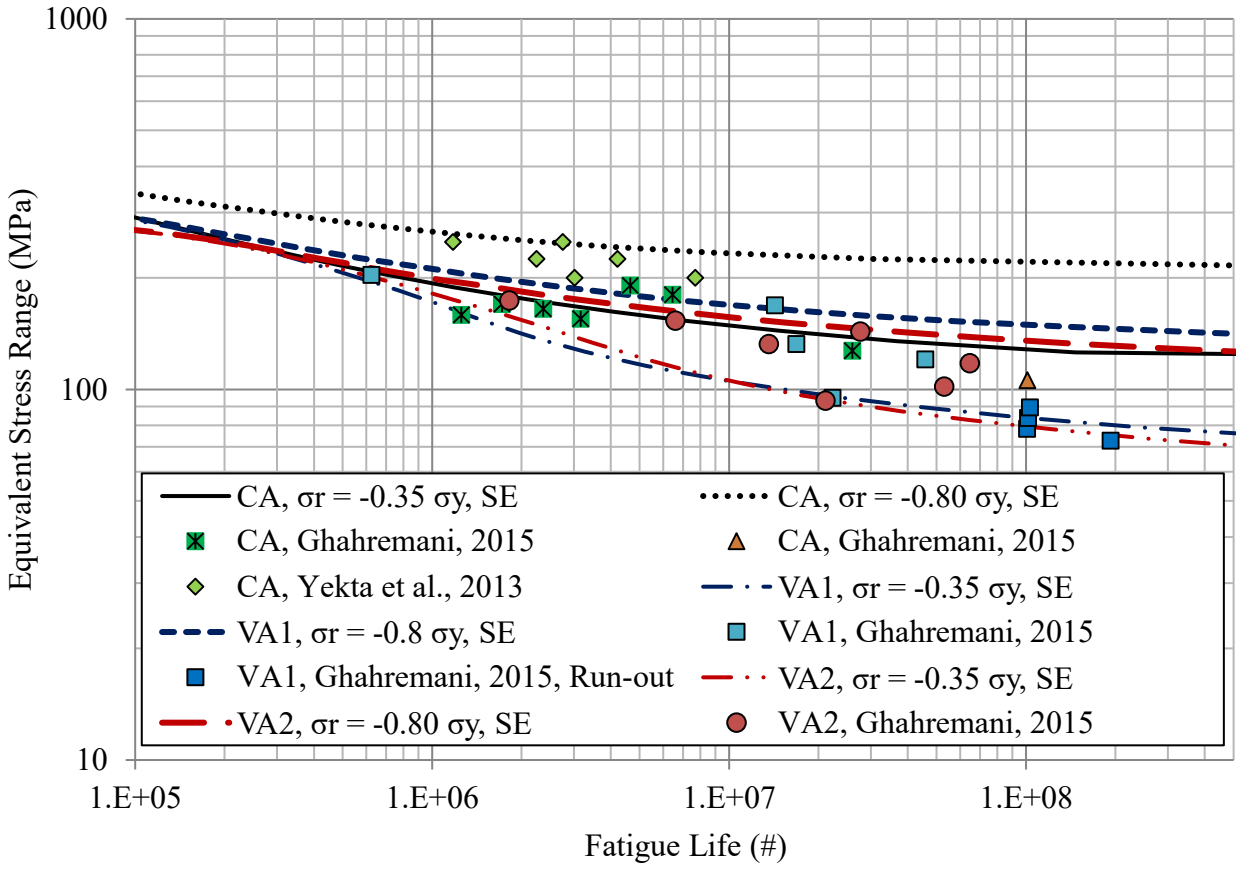

Figure 4.73: S-N curves for HFMI treated 350W steel specimens under various loading conditions

Figure 4.74 and Figure 4.75 shows S-N curves and experimental S-N data for treated A514 steel and aluminum specimens respectively. It can be observed from these two figures that fatigue life under CA-UL loading is lower than fatigue life under the CA loading. The difference in fatigue life under the two loading conditions is very much uniform in all fatigue life ranges which was not observed for 350W steel specimens. The VA loading effect was lower in low cycle fatigue regime and higher in high cycle fatigue regime for 350W steel specimens.

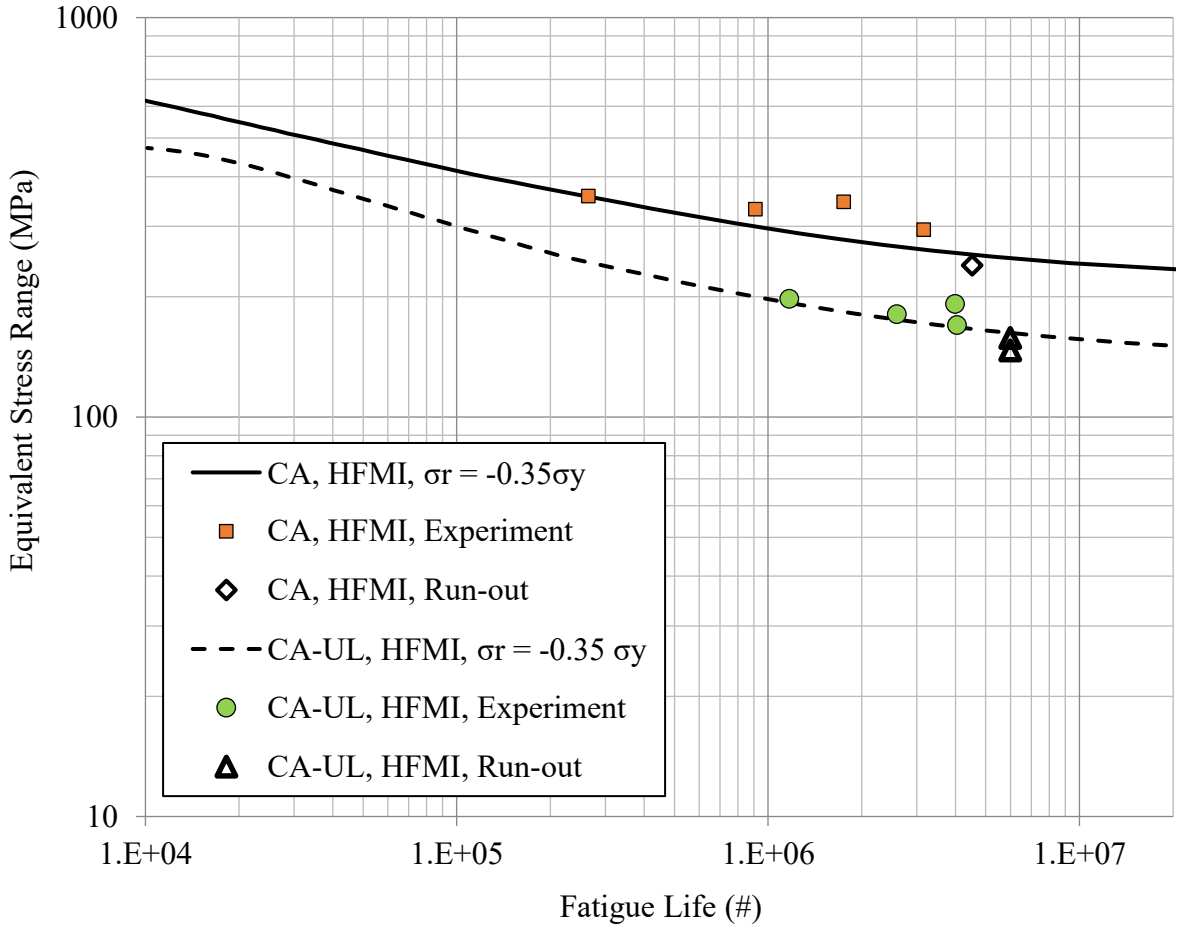

Figure 4.74: S-N curves for treated A514 steel specimens under various loading conditions

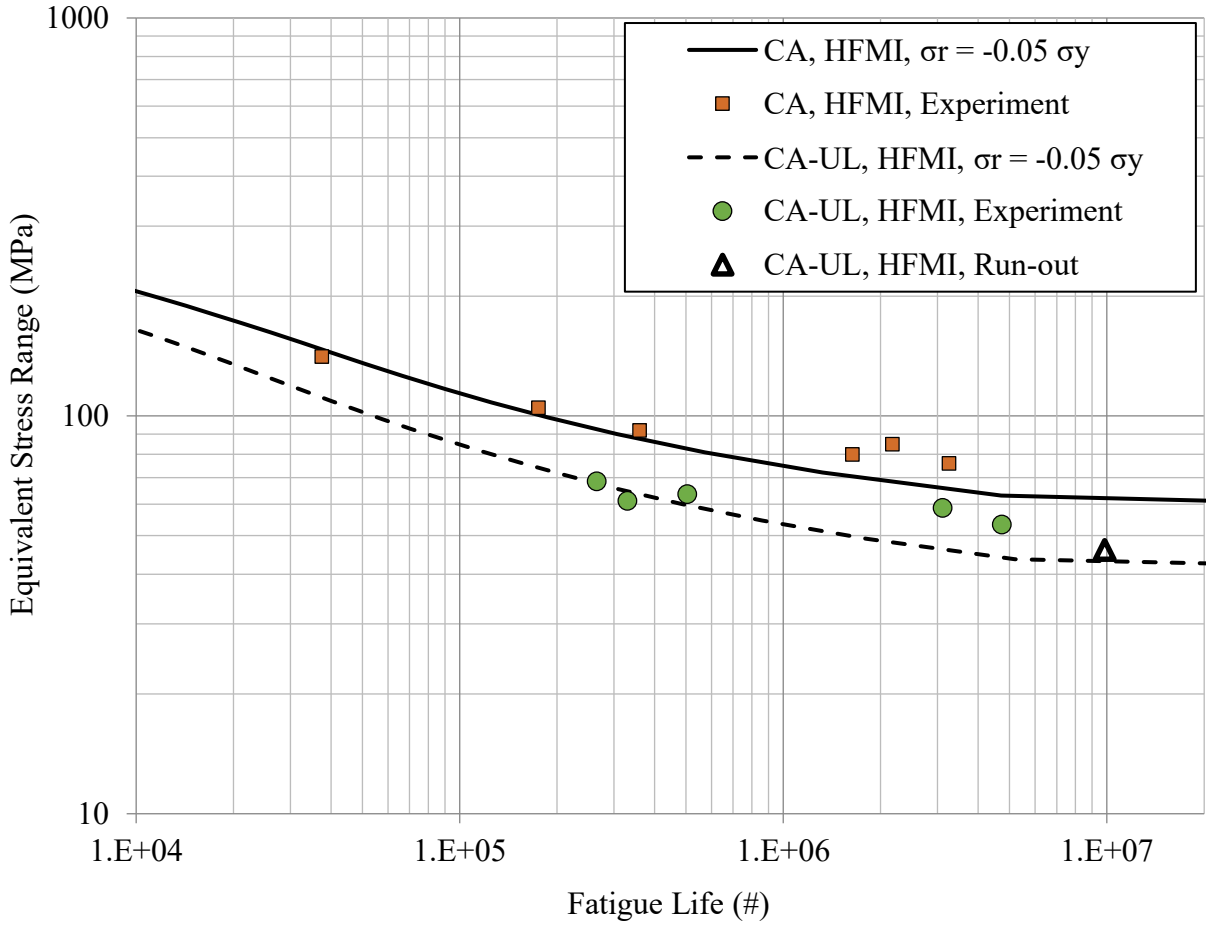

Figure 4.75: S-N curves for treated aluminum specimens under various loading conditions

4.10 Quantification of the fatigue strength improvement in the tested specimens

Figure 4.76 shows S-N curves for as-welded and HFMI treated 350W steel specimens under three loading conditions. The purpose of this figure is to estimate fatigue strength improvement because of HFMI treatment under different loading conditions. (Marquis and Barsoum 2016) quantifies the fatigue strength improvement in terms of an increase in the nominal stress range at 2 million cycles of fatigue life.

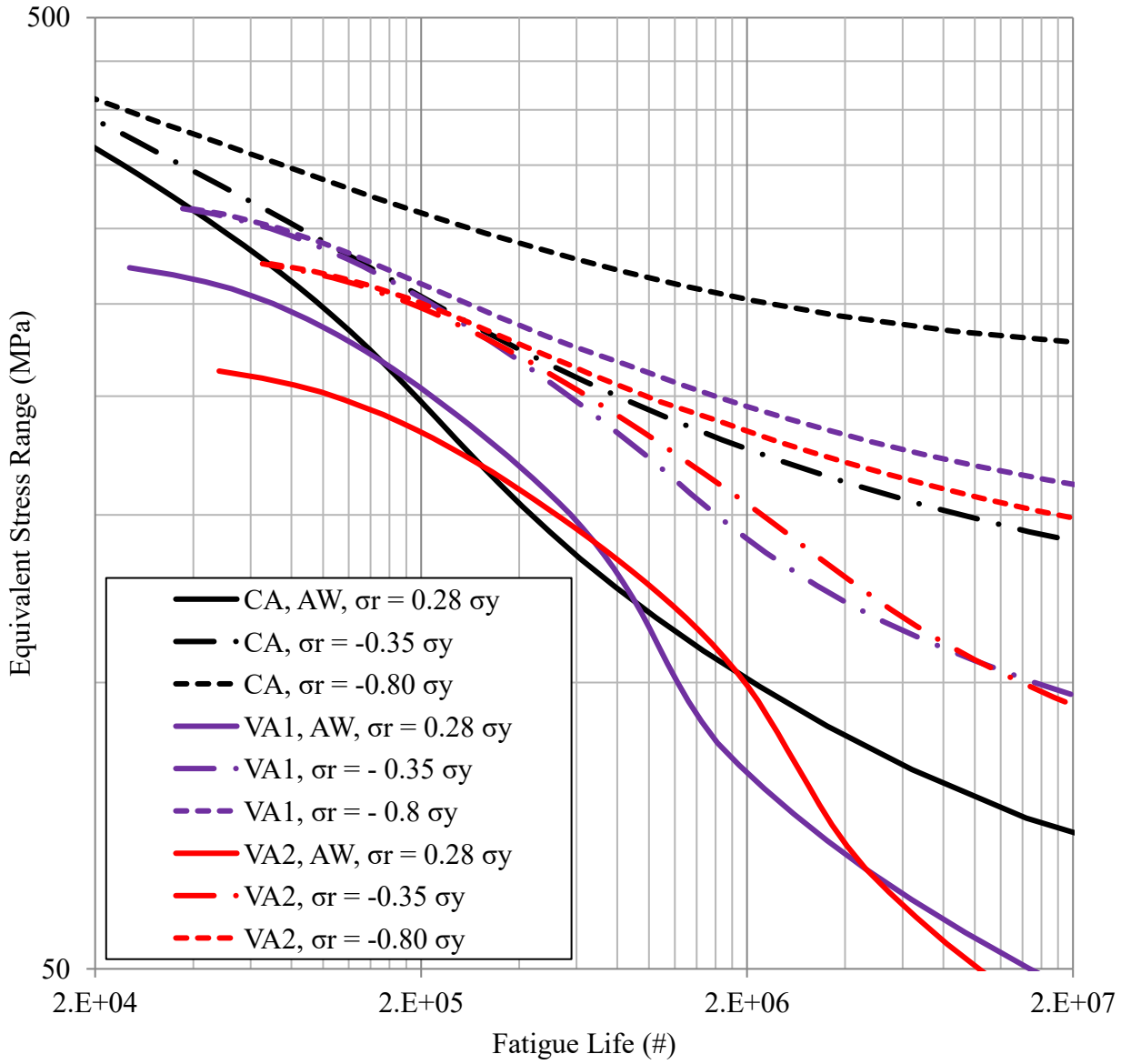

Figure 4.76: S-N curves for as-welded and HFMI treated 350W steel specimens

For CA loading, the nominal stress range (fatigue strength) at 2 million cycles increased from 101 MPa in the as-welded condition to 177 MPa and 253 MPa in the HFMI treated condition corresponding to a lower and an upper bound of the treatment levels (residual stress) respectively. For VA1 loading, the equivalent stress range increased from 81 MPa in the as-welded condition to 142 – 195 MPa in the treated condition. For VA2 loading, equivalent stress range increased from 99 MPa in the as-welded condition to 154 – 184 MPa in the treated condition.

The fatigue strength for as-welded and treated 350W specimens under CA, VA1, and VA2 loading conditions are summarized in Figure 4.77. It can be observed that with HFMI treatment the highest fatigue strength of 253 MPa is achieved under the CA loading and the lowest fatigue strength of 184 MPa is achieved under VA2 loading (corresponding to upper bound of treatment effectiveness).

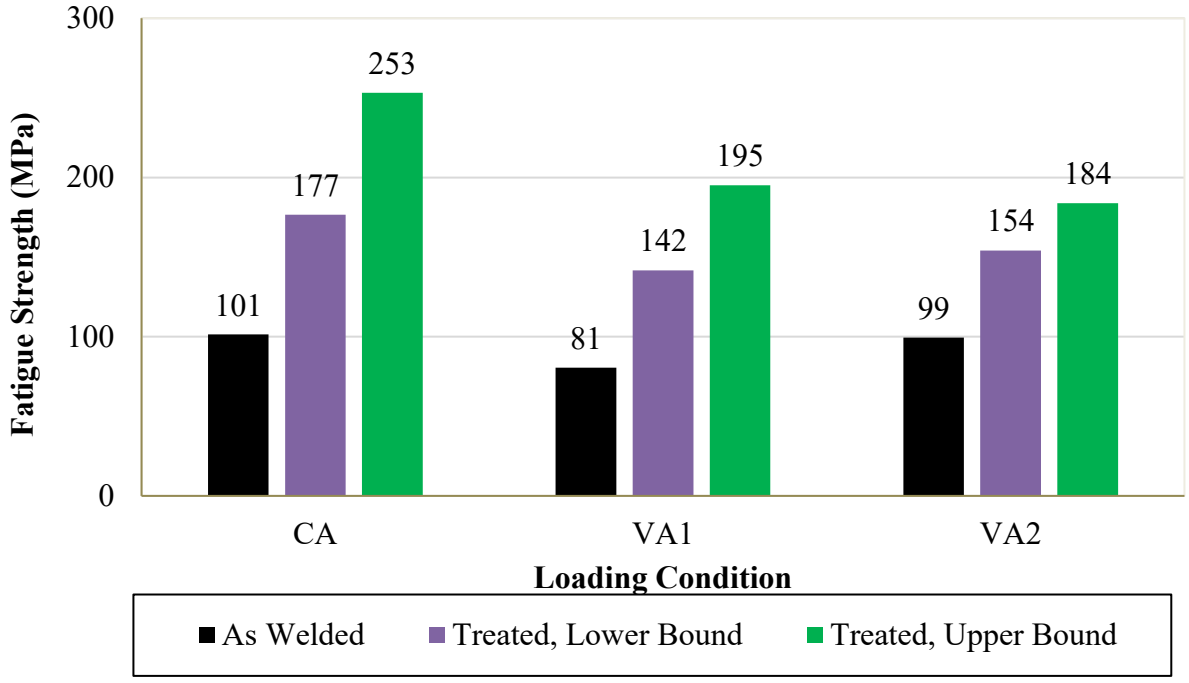

Figure 4.77: Fatigue strength of 350W steel specimens under different loading conditions

The percentage increase in fatigue strength can be calculated based on the difference between the equivalent stress ranges for the as-welded and impact treated specimens at two million cycle of fatigue life. Figure 4.78 summarizes the percentage increase in fatigue strength under different loading conditions for the HFMI treated 350W steel specimens. The increase in fatigue strength was similar for the CA and VA1 loading conditions but lower for the VA2 loading condition. The minimum fatigue strength increase was found to be 55% under VA2 loading (lower bound of treatment effectiveness).

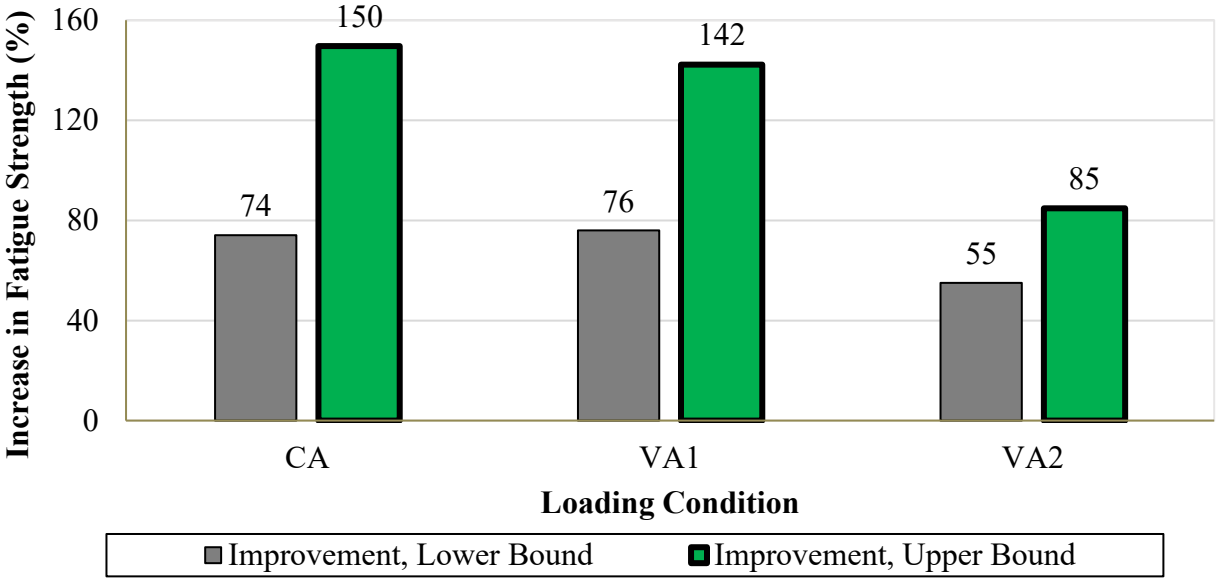

Figure 4.78: Percentage improvement in fatigue strength for 350W steel cruciform specimens

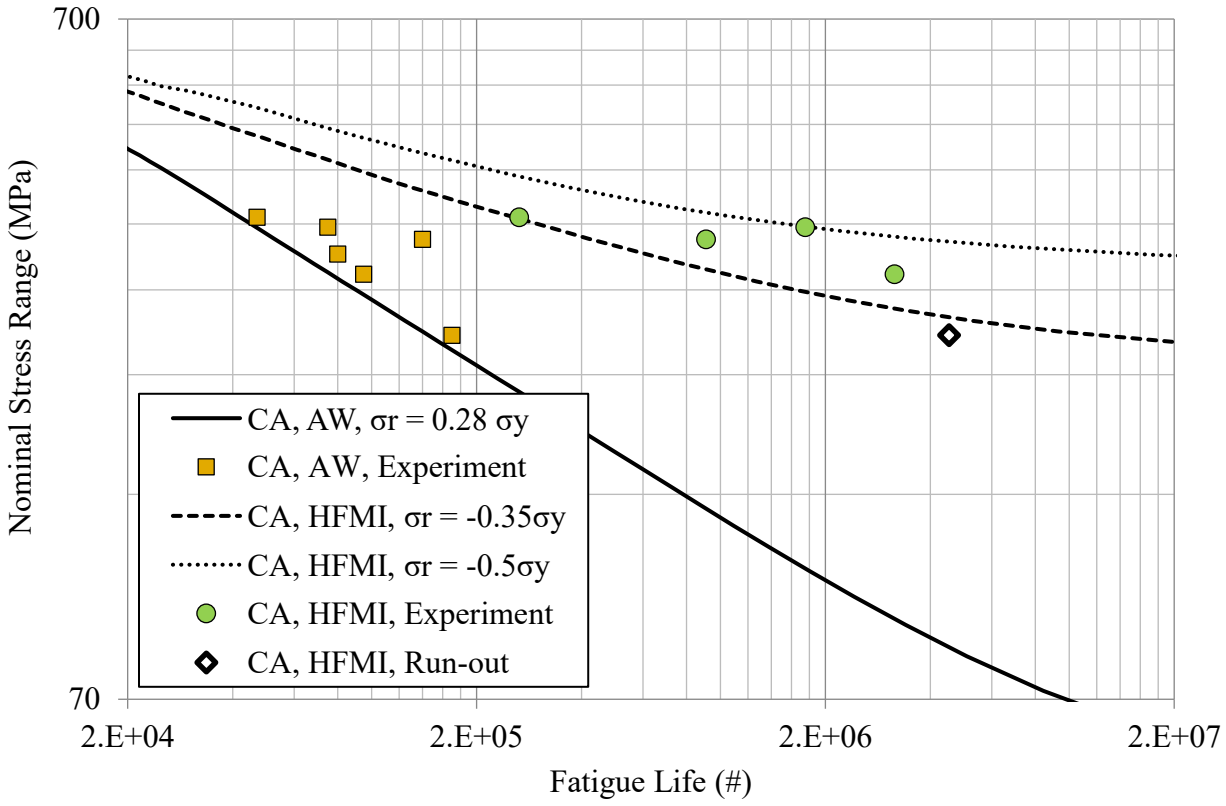

Figure 4.79: S-N curves for A514 steel specimens under CA loading

Figure 4.79 shows S-N curves and experimental S-N data for the A514 steel specimens in the as-welded and HFMI treated conditions subjected to CA loading. It can be observed that at two million cycles of fatigue life, the nominal stress range increased from 105 MPa in the as-welded condition to 275 – 344 MPa in the treated condition. Similarly, under CA-UL loading, it can be observed in Figure 4.80 that the equivalent stress range increased from 122 MPa in the as-welded condition to 171 – 215 MPa in the treated condition. The fatigue strengths at 2 million cycles under different loading conditions for the A514 steel specimens are summarized in Figure 4.81.

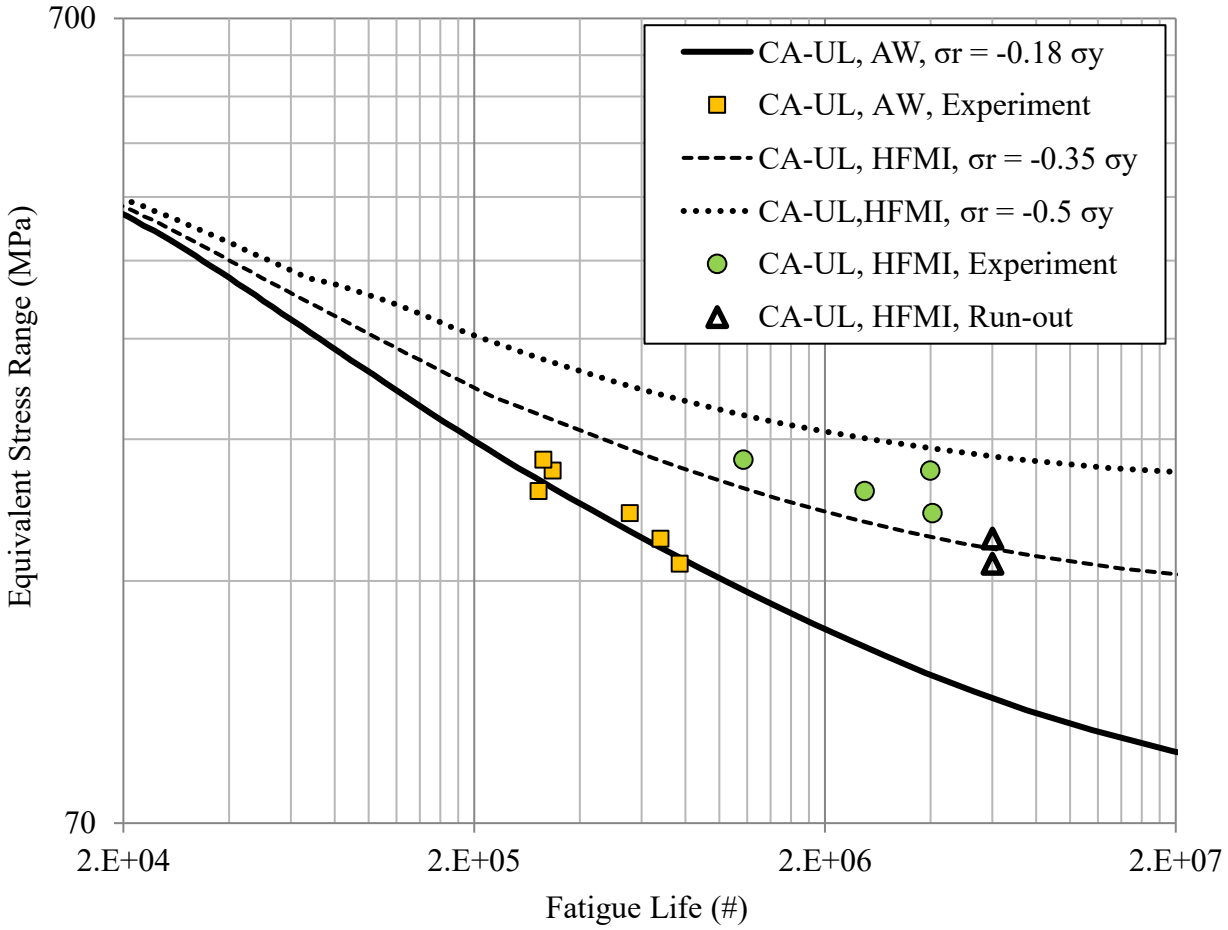

Figure 4.80: S-N curves for A514 steel specimens under CA-UL loading

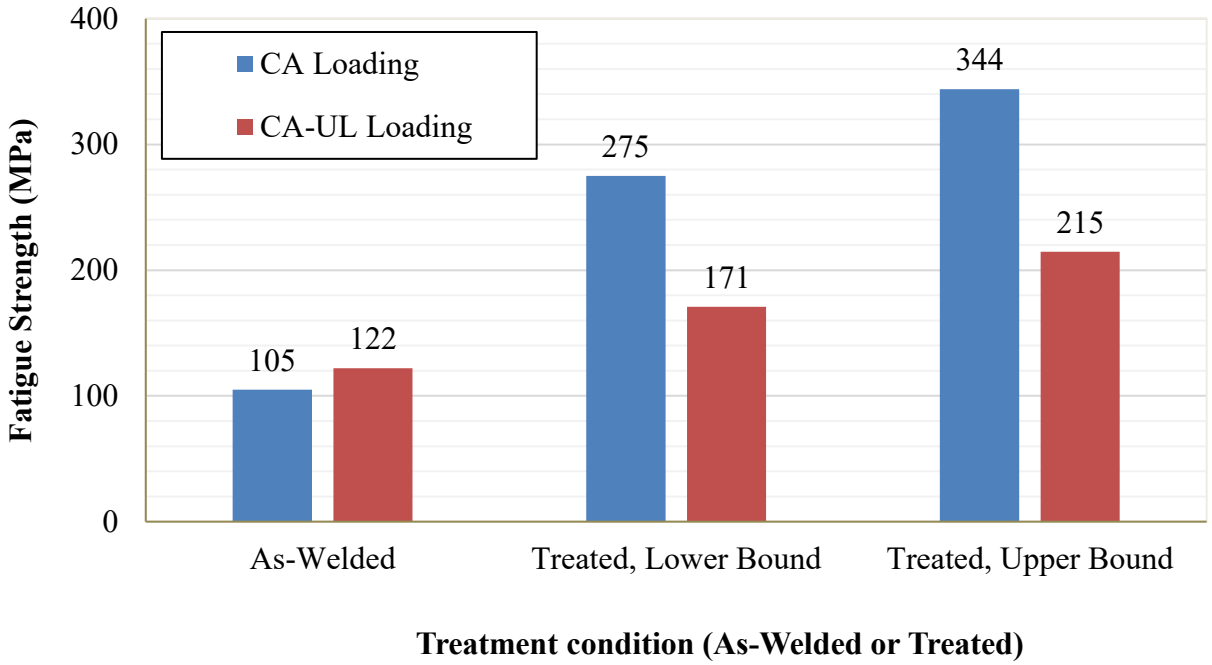

Figure 4.81: Fatigue strength of A514 steel specimens at 2 million cycles of fatigue life

Figure 4.82 shows S-N curves and experimental S-N data for the aluminum specimens in the as-welded and HFMI treated condition under the CA loading. As discussed before, the impact treatment on aluminum specimens was not very effective compared to steel, since the magnitude of residual stress at the weld toe was found to vary between $-0.30 \cdot \sigma_y$ to $-0.05 \cdot \sigma_y$. Therefore, the fatigue strength improvement under CA loading was found to be almost zero for a peak residual stress of $-0.05 \cdot \sigma_y$. For a higher magnitude of beneficial compressive residual stress with a peak value of $-0.30 \cdot \sigma_y$, the nominal stress range increased from 72 MPa to 94 MPa. Figure 4.83 shows S-N curves and experimental S-N data for the aluminum specimens in the as-welded and HFMI treated condition under CA-UL loading. Under this loading, the equivalent stress range increased from a value of 40 MPa in the as-welded condition to 61 MPa for HFMI treated condition at fatigue life of two million cycles, for the upper bound residual stress case.

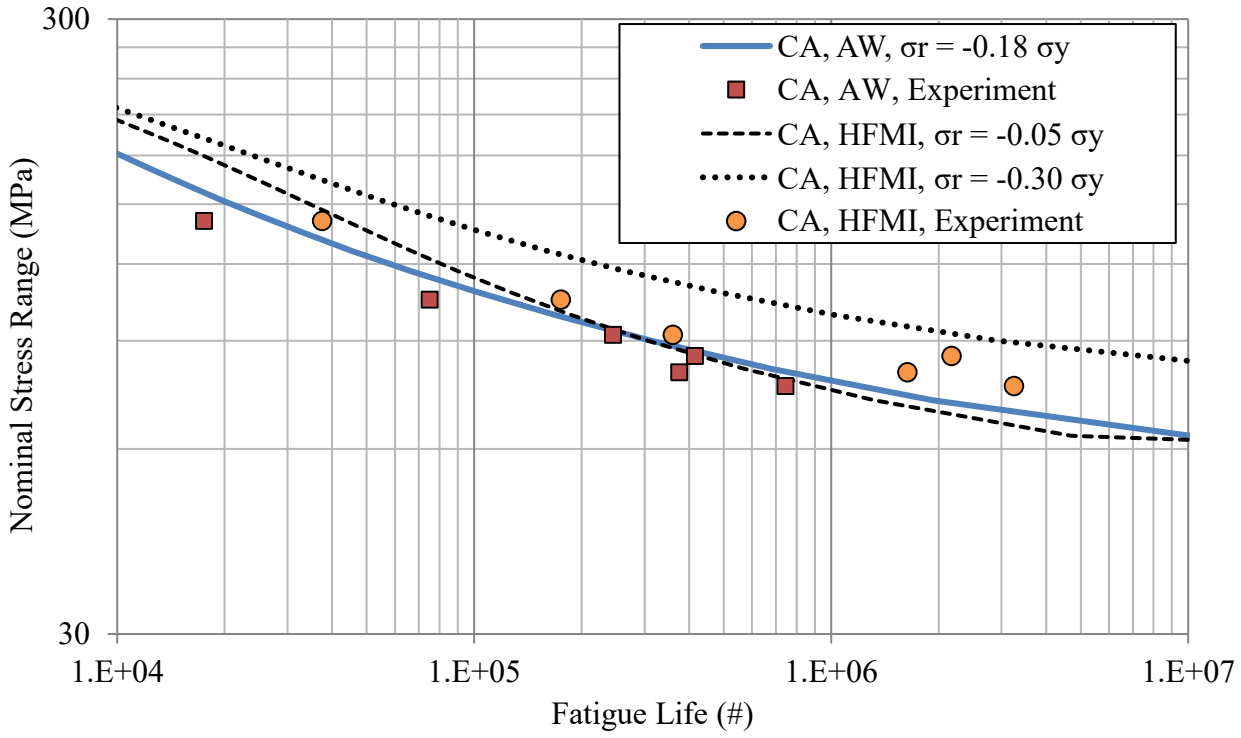

Figure 4.82: S-N curves for aluminum specimens under CA loading

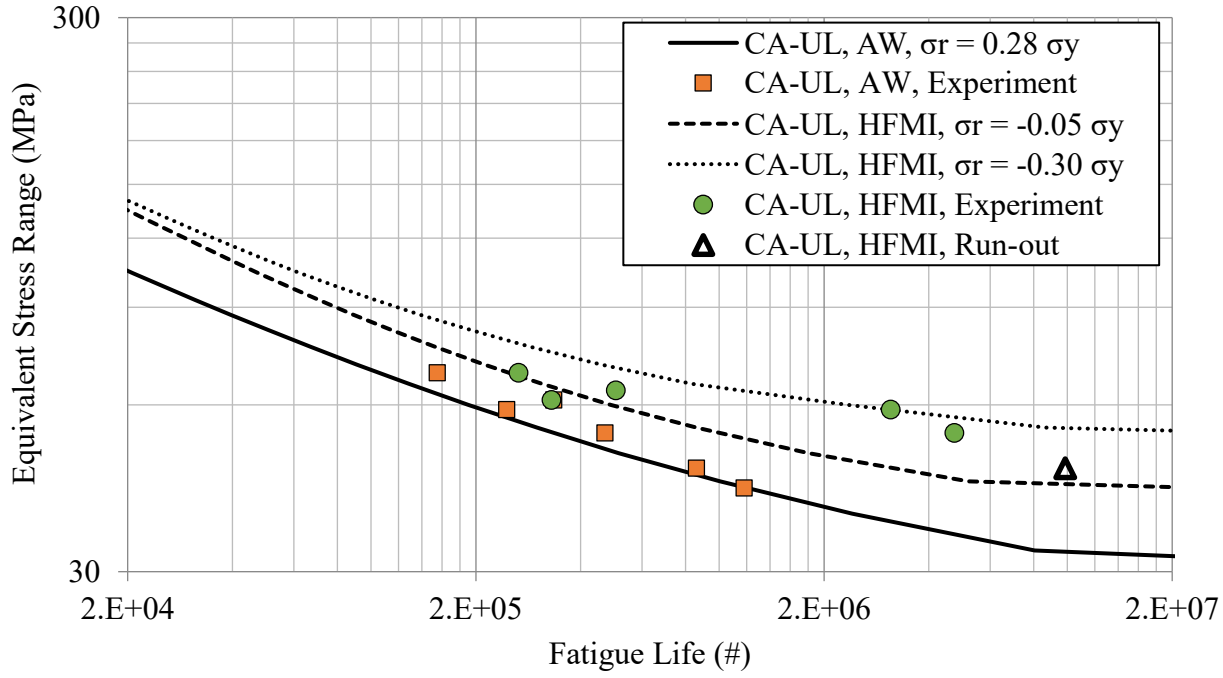

Figure 4.83: S-N curves for aluminum specimens under CA-UL loading

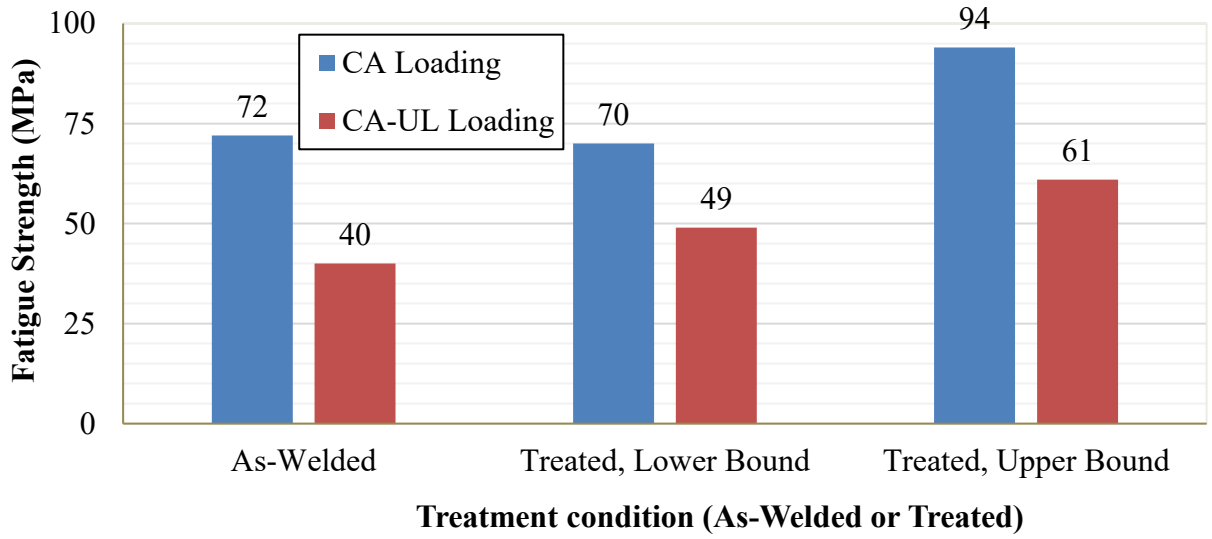

Figure 4.84: Fatigue strength of 5083 aluminum specimens at 2 million cycles of fatigue life

Figure 4.84 summarizes fatigue strength of aluminum specimens under CA and CA-UL loading conditions and in as-welded and HFMI treatment conditions. The percentage increase in fatigue strength for the A514 steel and 5083 aluminum specimens is shown in Figure 4.85. As observed in Figure 4.85, the percentage improvement in fatigue life for the A514 steel under CA loading had a range of 161% – 228%. However, a lower fatigue strength for A514 steel was observed under CA-UL loading, which varied from 48% – 86%. For the case of aluminum specimens, almost no fatigue strength increase was found with the lower bound of the compressive residual stress. For the upper bound of beneficial residual stress, the increase in fatigue strength for the 5083 aluminum was found to be 31% and 54% under CA and CA-UL loading respectively.

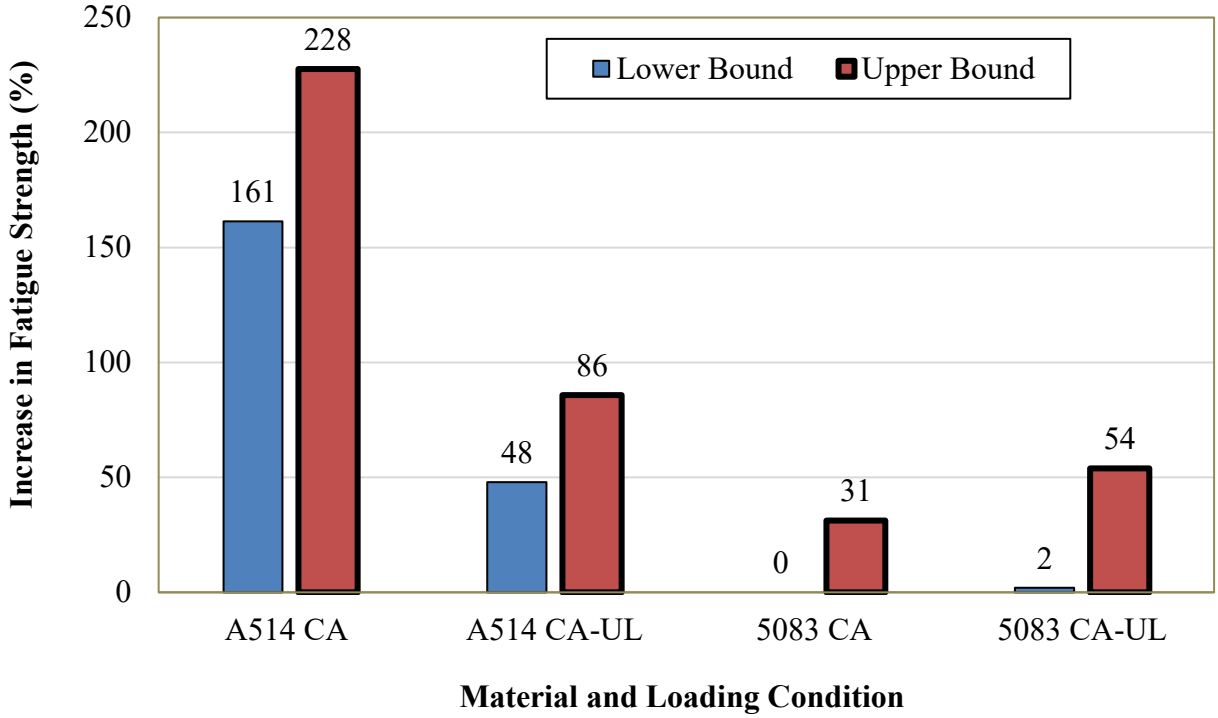

Figure 4.85: Fatigue strength improvements in A514 steel and 5083 aluminum specimens

In general, the model is seen to yield excellent estimations of the test results for the three materials subjected to several loading histories considered in the current study. The fact that this model provides good estimations for several investigated loading histories and for three different material suggests that it has a strong potential to be a useful tool for investigating loading history effects on the treatment effectiveness and to perform a study to observe the effect of a variation in the residual stress on fatigue life. This was also demonstrated in a previous study on needle peening of mild steel (Ghahremani and Walbridge 2011) wherein a similarly validated 1D SBFM model was used to conduct parametric studies investigating the treatment effectiveness under 20 complex VA loading histories typical of highway bridge structures. The model may also serve as a useful tool for studies investigating the effects of defects and quality control on the treatment effectiveness, similar to what was done in (Tehrani Yekta et al. 2013) with a 1D version of the SBFM model for HFMI treated mild steel welds.

4.11 Conclusions

Based on the research presented in the previous sections of this chapter, the following conclusions are drawn:

- HFMI results in a reliable fatigue life increase in steel (CSA 350 and ASTM A514) specimens, under constant as well as variable amplitude loading conditions.
- In general, the fatigue life increase due to HFMI was seen to increase with an increase in material strength. The actual increase depends on the applied loading and magnitude of compressive residual stress because of the HFMI treatment.
- A statistical analysis of the test results confirms that the fatigue life increase can be seen when comparisons are made over a range of survival probabilities (50% or 95%).
- A nonlinear fracture mechanics analysis, wherein the material monotonic and cyclic strength properties are considered, is capable of estimating the fatigue performance of the HFMI treated welds for a broad range of material properties and loading conditions.

Going forward, it is recommended that further research should be conducted to extend these results to more complex variable amplitude loading histories, with a focus on the high cycle fatigue (HCF) regime. A more comprehensive study of the effectiveness of HFMI treatment on aluminum welds is also recommended, with a focus on varying the indent depth to study the effect of this parameter on fatigue performance and the fatigue testing of large-scale welded aluminum components.

Chapter 5

Probabilistic SBFM Analysis of 350W Steel Cruciform Welded Joints

In this chapter, first, an overview of the design guidelines available in various design codes for the fatigue assessment of fusion-welded joints is presented, followed by a presentation of sensitivity study results, performed using the 2D SBFM model, for as-welded and HFMI treated 350W steel cruciform welded joints. Probabilistic distributions for the various SBFM input parameters are then defined. Lastly, probabilistic SBFM analysis results are presented with a comparison of the SBFM-derived survival probability curves and comparable code-based design S-N curves.

5.1 Introduction

Several standards (Eurocode 3, IIW(Hobbacher 2009), CSA S6 (Canadian Standards Association 2014), and AISC (American Institute of Steel Construction 2016)) include design curves for the fatigue assessment of cruciform welded joints. These are compared in Figure 5.1.

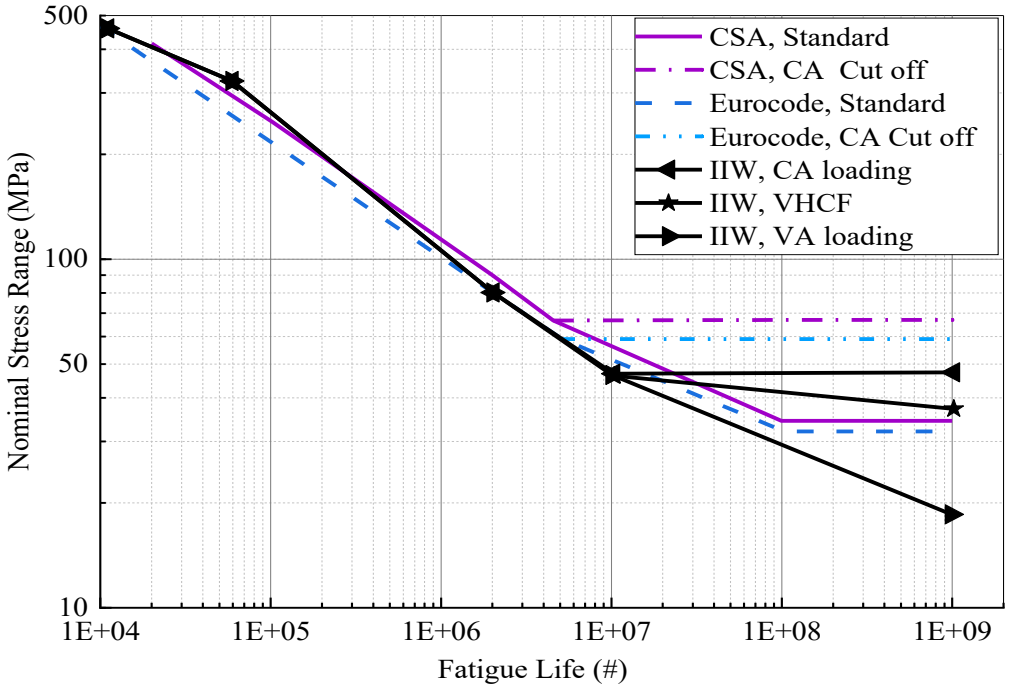

Figure 5.1: Design S-N curves for cruciform arc welded mild steel joints

The design S-N curves in the CSA S6 and AISC codes are the same, therefore, only the CSA S6 design curve is shown in Figure 5.1. The IIW provides one design curve for the LCF regime and three design curves for the HCF regime: 1) for CA loading, 2) for the very high cycle fatigue (VHCF) regime, and 3) for VA loading as shown in Figure 5.1. Overall, the design curves in these codes are very close to each other except for the CA cut off level, which is highest for the CSA and lowest for the IIW design curve. Experimental S-N data obtained from fatigue testing of as-welded 350W steel cruciform welded joints under CA loading from (Ghahremani 2015) is compared with the three design S-N curves for this detail in Figure 5.2.

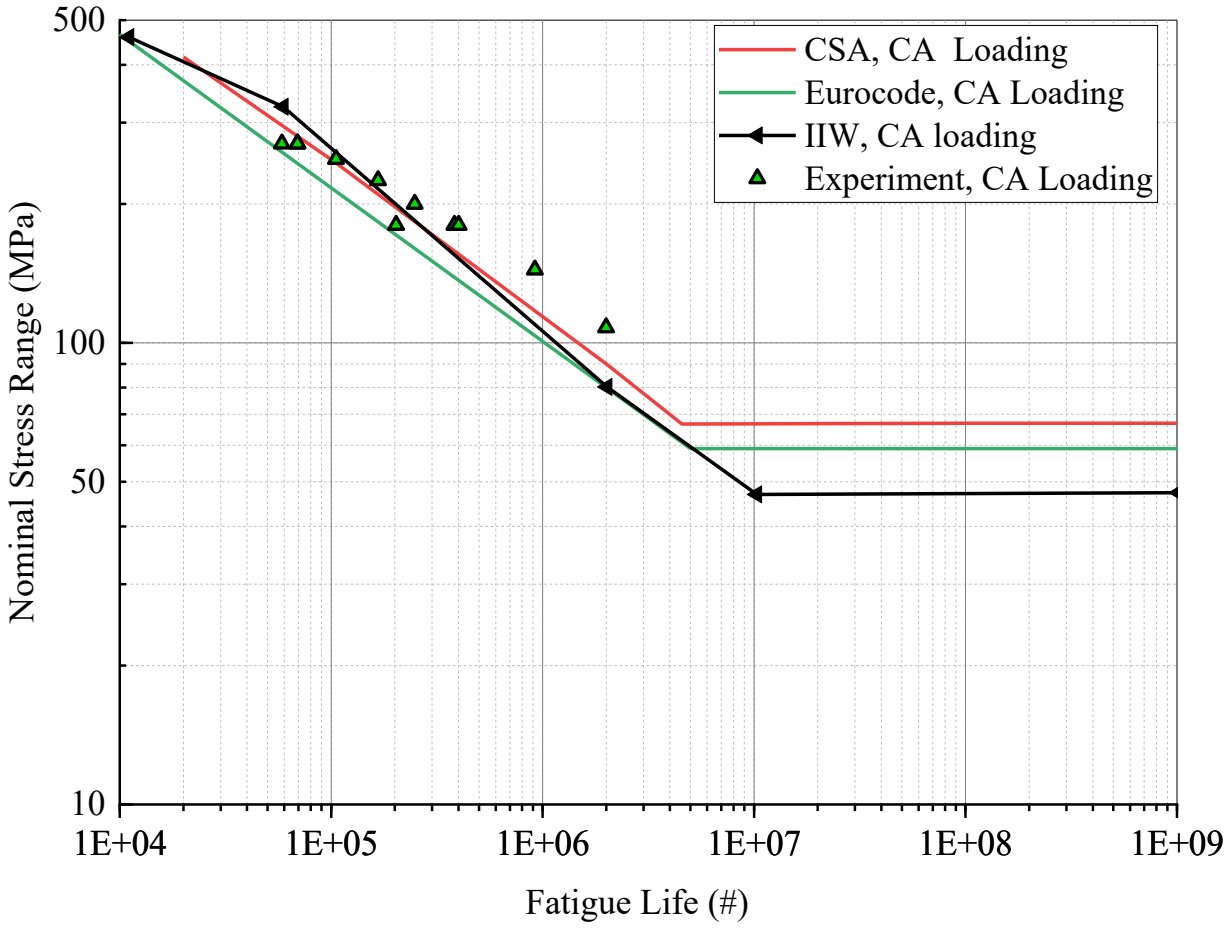

Figure 5.2: Comparison of experimental S-N data obtained under CA loading with design S-N curves

It can be observed in Figure 5.2 that some of the experimental S-N data points are below the CSA and IIW design curves. However, all of the S-N data points are above the Eurocode design

curve. Figure 5.3 shows a comparison of fatigue test results obtained under VA loading condition from (Ghahremani 2015) with code-based design S-N curves. It can be observed that several of the test results are below the design S-N curves.

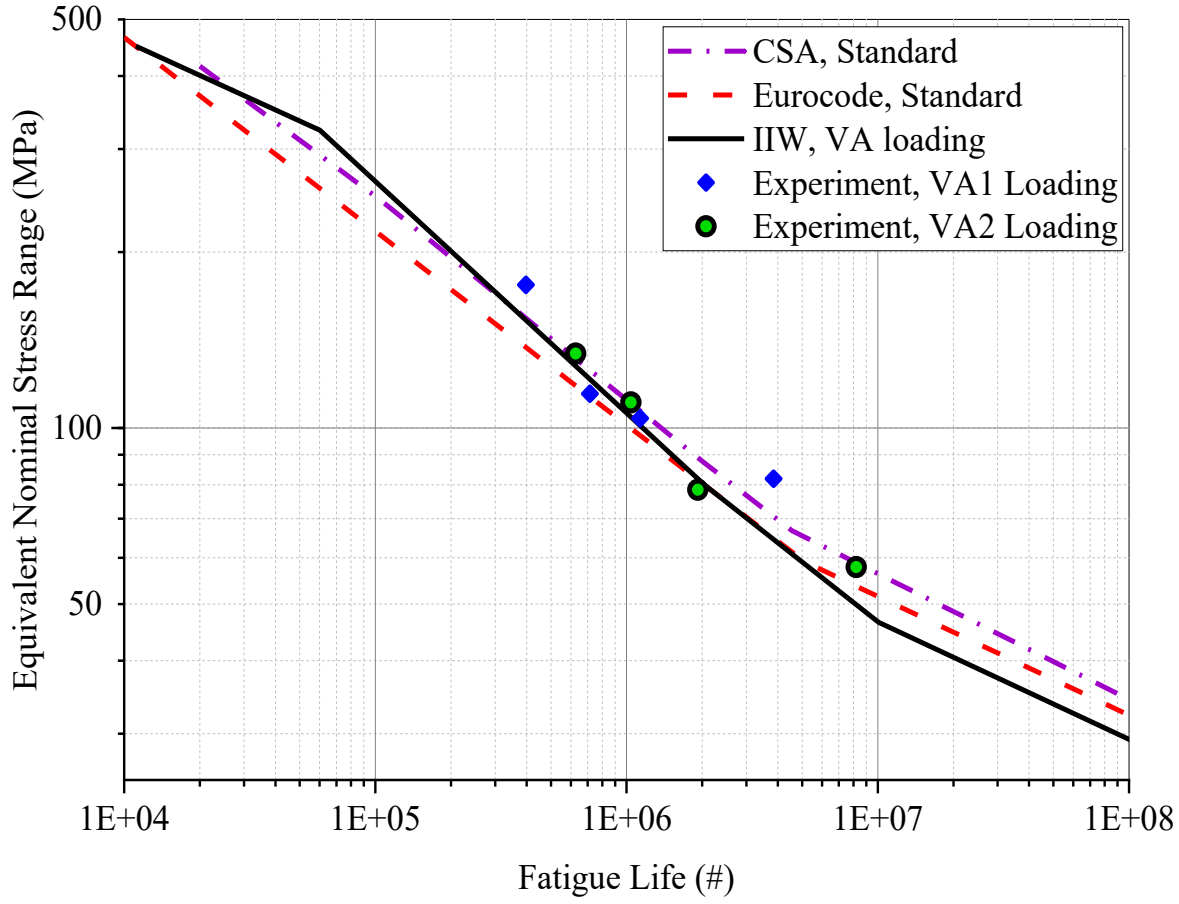

Figure 5.3: Comparison of experimental S-N data obtained under VA loading with design S-N curves

The IIW (Marquis and Barsoum 2016) provides guidelines for estimating fatigue life improvement in HFMI treated welds. In the IIW code, fatigue strength improvement is quantified in terms of the number of FAT classes depending on material strength as shown in Figure 5.4. Design S-N curves provided in the IIW document are named as FAT X, where X is the nominal stress range (in MPa) at two million cycles of fatigue life on the design S-N curve. There are several IIW FAT classes for welded steel joints, namely: 50, 56, 63, 71, 80, 90, 100, 112, 125, 140, 160, 180, 200, 225 and 250. Cruciform welded joints made of 350W steel in as-welded condition

belong to FAT 80 class as per the recommendation of IIW. The maximum possible improvement because of HFMI can be 8 FAT classes, which may be obtained for steel with yield strength more than 950 MPa as seen in Figure 5.4. For 350W steel, with a yield strength of 355 MPa, the maximum possible improvement because of HFMI treatment should be in the range of 4-5 FAT classes. Therefore, the FAT class for HFMI treated cruciform welded joint should be FAT 125 or FAT 140. The intermediate FAT classes between FAT 80 and FAT 125 are FAT 90, FAT 100, and FAT 112. It should be noted that S-N curves corresponding to different FAT classes are not equally spaced.

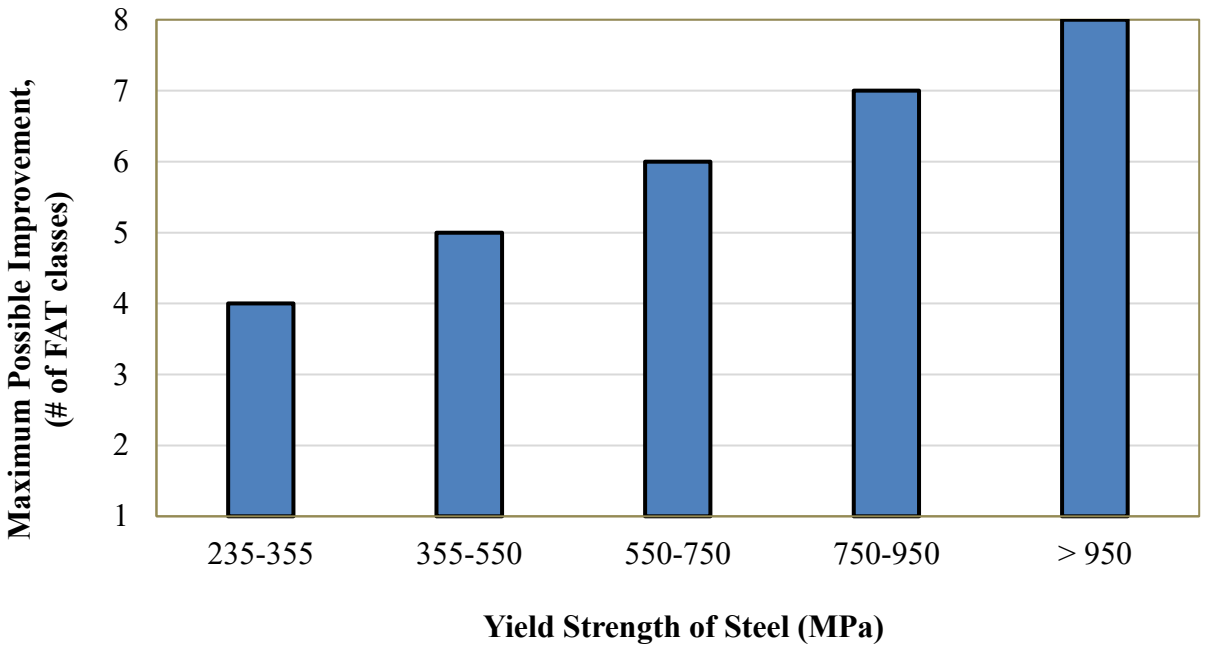

Figure 5.4: IIW recommended fatigue strength improvement due to HFMI treatment

The guidelines provided in IIW are applicable for steel structures of plate thicknesses of 5-50 mm and yield strength ranging from 235 MPa to 960 MPa. The IIW recommendation is applicable for structural steel only. The maximum nominal stress in the nominal stress history should not be more than 80% of the yield strength to achieve reliable fatigue strength improvement. The exact level of improvement depends on the applied load ratio or VA loading history. The recommendation is applicable for the joints, which belong to FAT 50-90 in the as-welded condition.

Against this background, the current study was undertaken with the following objectives:

- to perform a sensitivity analysis using the 2D SBFM model in its deterministic form to identify the most important parameters affecting the fatigue strength of as-welded and HFMI treated mild steel joints under VA loading conditions,
- to use the available test data for laboratory-scale specimens to validate a probabilistic 2D SBFM model, based on the previously-described deterministic model,
- to use the validated model to study scale effects and then establish design curves for HFMI-treated welds in real or large-scale structures such as bridge girders, and
- to quantify the design fatigue strength improvement due to HFMI treatment under CA loading at different load ratios and under various VA loading histories.

5.2 Sensitivity analysis using 2D SBFM model

The following sensitivity analysis has been performed for laboratory(small) scale specimens under the VA2 loading condition with the same component geometry and the mean input data as described in Chapter 4 for 350W steel cruciform welded joints. The variation in input material properties while performing this sensitivity analysis was kept to realistic upper and lower limits as observed during the laboratory tests.

5.2.1 Paris Erdogan law constants, *C* and *m*

For the deterministic analysis, the value of LN(C) and m was taken to be -27.5 and 3 based on the fitted curve passing through the experimental data as shown in Figure 5.5. For the sensitivity analysis, the value of m was kept constant at 3 and the lower and upper limit for LN(C) was estimated to be -29 and -26.5 respectively based on scatter in the test data. The effect of variation in LN(C) on the S-N curve for as-welded and HFMI treated specimens is shown in Figure 5.6 (left) and Figure 5.6 (right) respectively under the VA2 loading condition. It can be observed that the effect of variation in LN(C) on the S-N curve is relatively small for the treated specimens in comparison to the as-welded specimens. It has been observed previously that the SBFM model results are most sensitive to variations in LN(C).

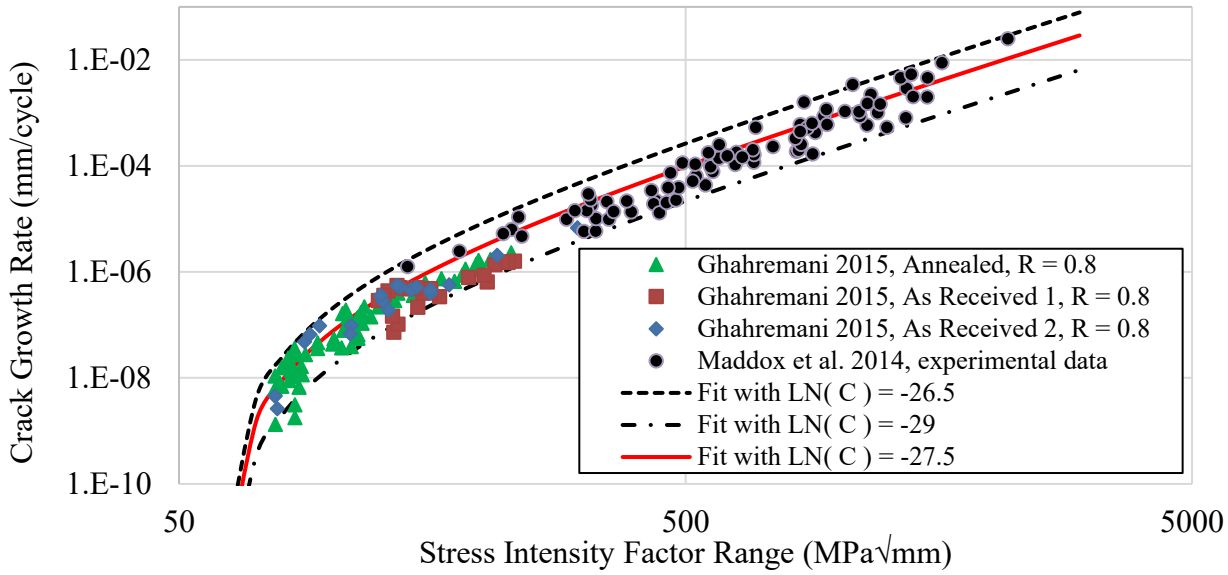

Figure 5.5: Bounds of crack growth rate curve obtained by varying LN(*C*)

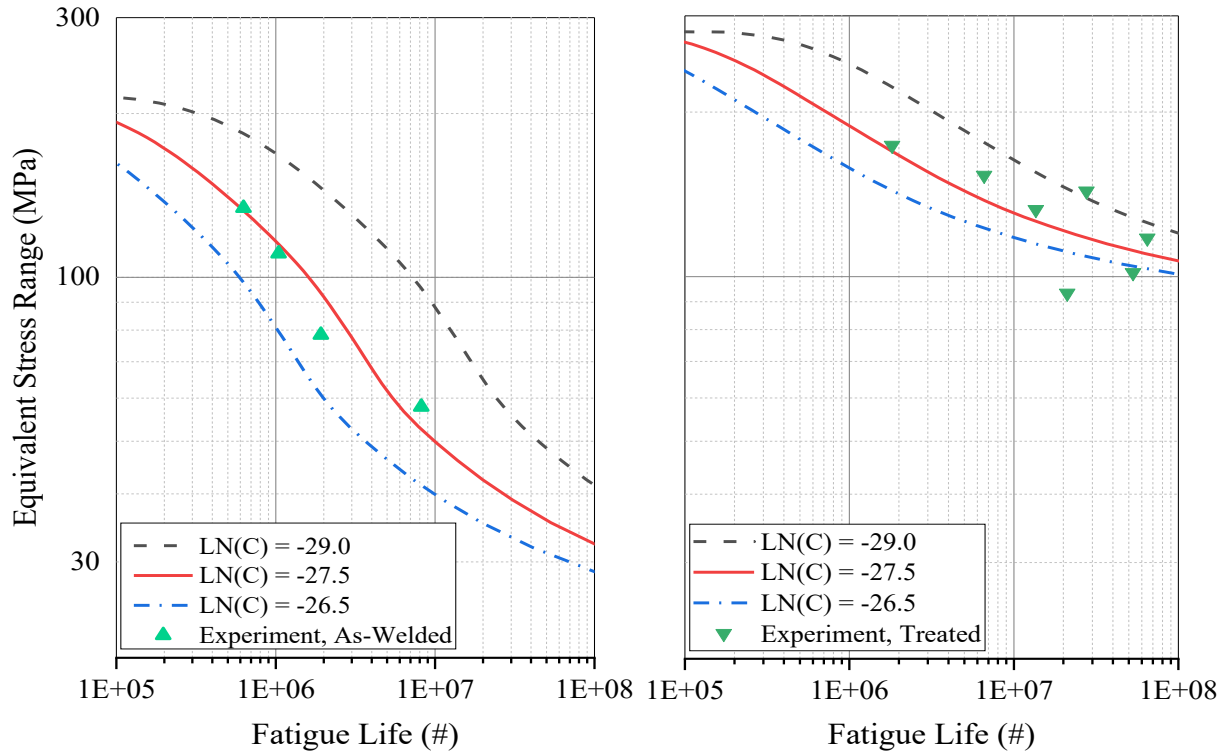

Figure 5.6: Effect of variation in LN(*C*) on the S-N curve for as-welded (left) and treated (right) specimens

5.2.2 Threshold stress intensity factor range, ΔK_{th}

For the deterministic analysis, the value of ΔK_{th} was assumed to be 60 MPa√mm and was adapted from (Ghahremani 2015). Here, based on scatter in the experimental test data, the variation in ΔK_{th} was estimated to be from 50 to 75 MPa√mm as shown in Figure 5.7. The effect of variation in ΔK_{th} on the S-N curve is shown in Figure 5.8. It can be observed that there is less effect of a variation in ΔK_{th} on the S-N curve for treated specimens than for the as-welded specimens.

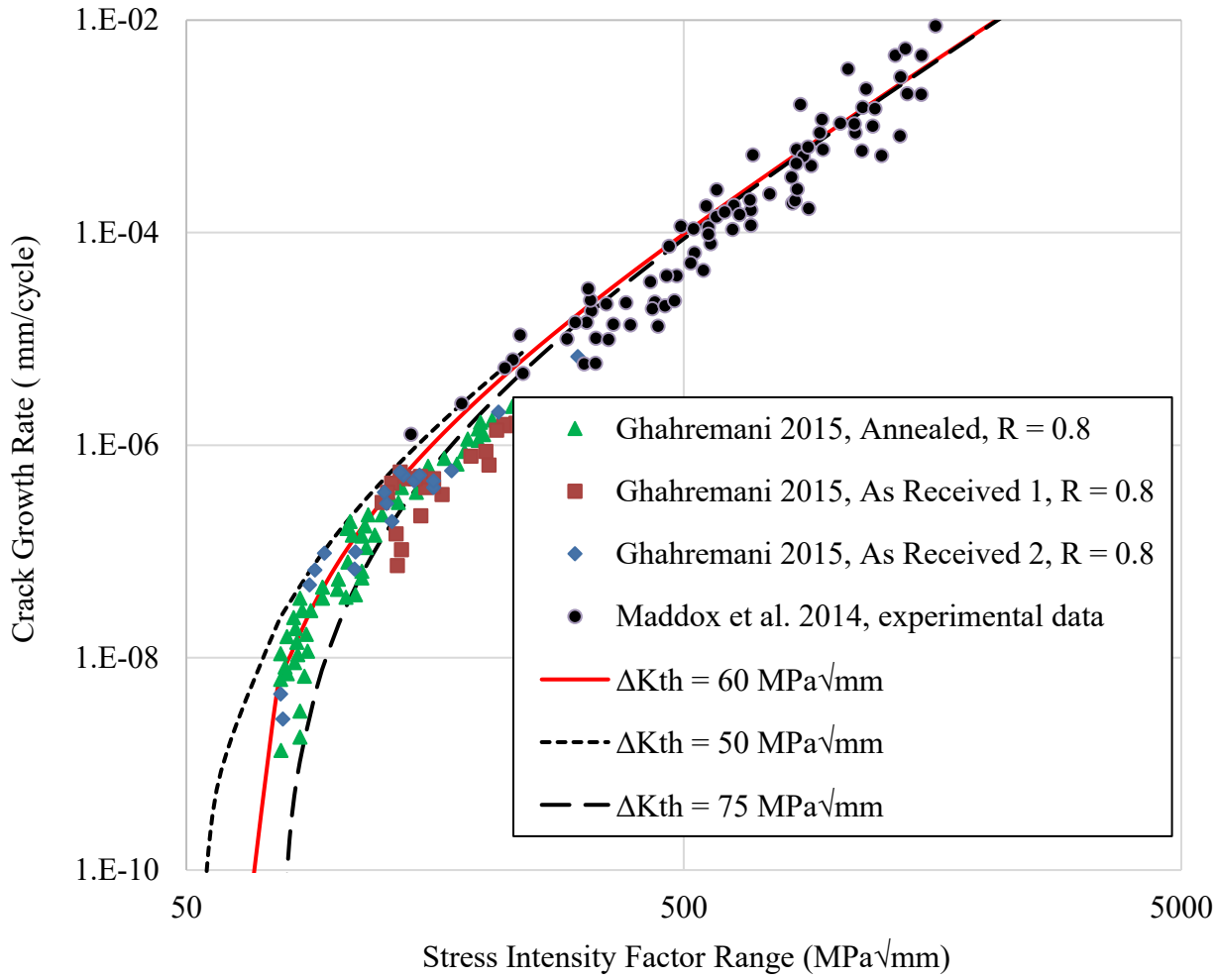

Figure 5.7: Bounds of crack growth rate curve obtained by varying ΔK_{th}

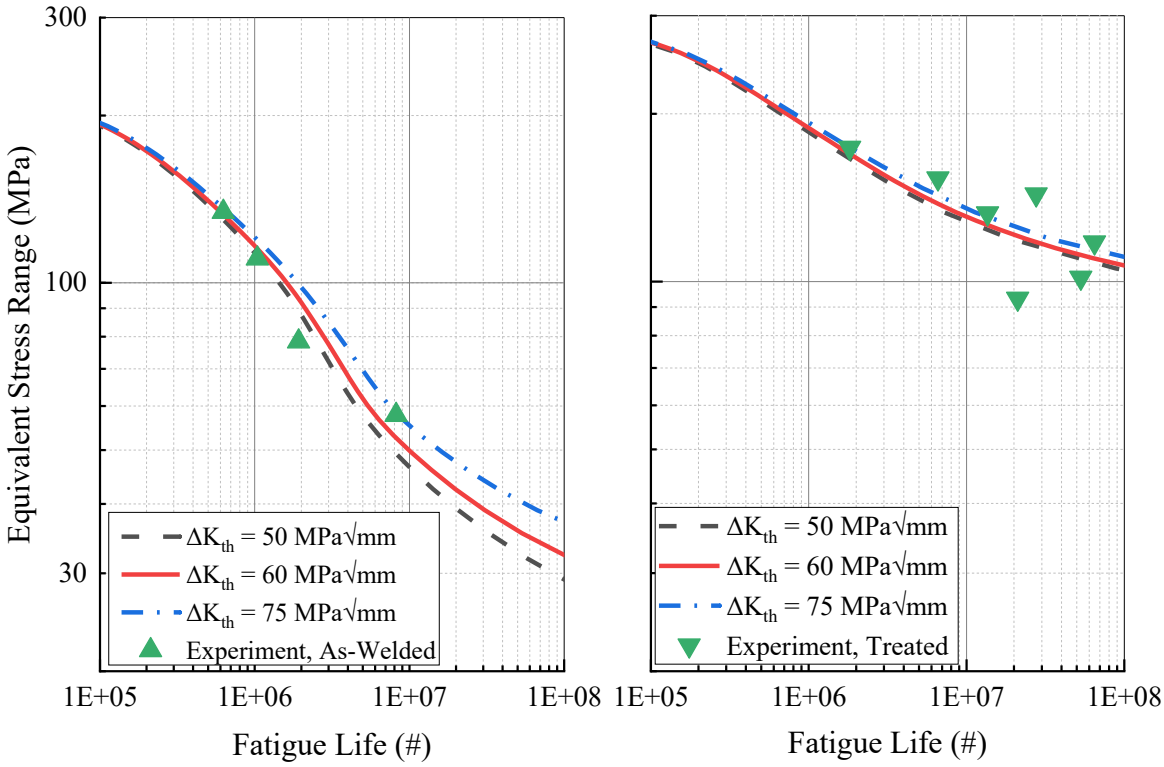

Figure 5.8: Effect of variation in ΔK_{th} on the S-N curve for as-welded (left) and treated (right) specimens

5.2.3 R-O material model parameters, *K'* and *n'*

The values of *K*' and *n*' were estimated to be 812 MPa and 0.108 respectively based on the fitted cyclic material test data curves available in (Ghahremani 2015), which are shown in Figure 5.9. For the sensitivity analysis, *n*' was kept at a constant value of 0.108 and the lower and upper limits of *K*' were estimated to be 700 MPa and 950 MPa to represent a realistic variation in cyclic material behaviour. Figure 5.10 shows the effect of variation in *K*' on the S-N curve for as-welded and HFMI treated specimens. It can be observed that the effect of variation in *K*' has a quantitatively similar effect on as-welded and treated specimens. The higher the fatigue life, the lower is the effect of a variation in *K*' until 10^7 cycles. Since, in the HCF regime, material behaviour is predominantly linear and governed by Hooke's law, therefore, there is no effect of *K'* on S-N curve in the high cycle fatigue (HCF) regime (>10^7 cycles).

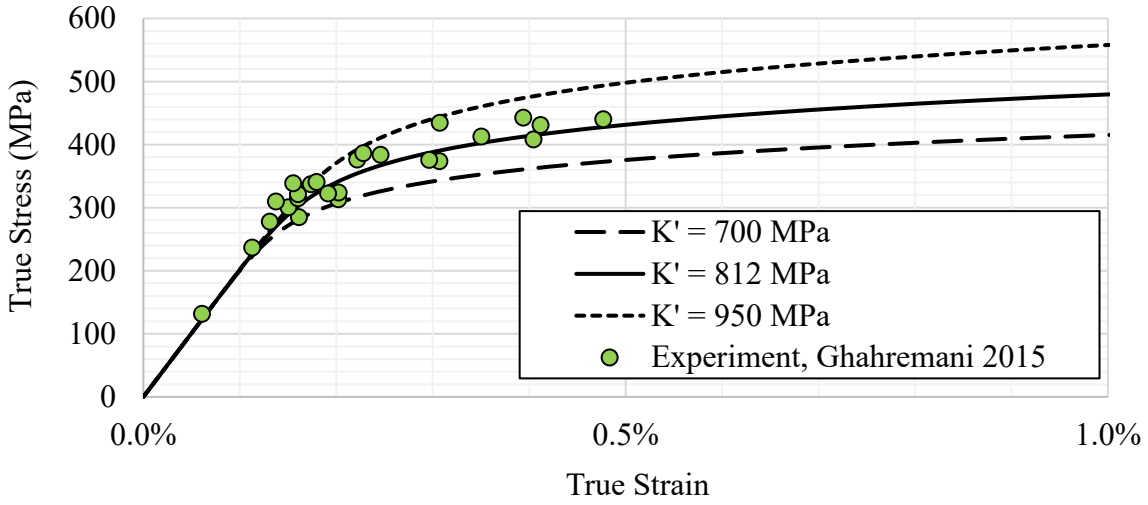

Figure 5.9: Bounds of the cyclic stress-strain curve obtained by varying *K*'

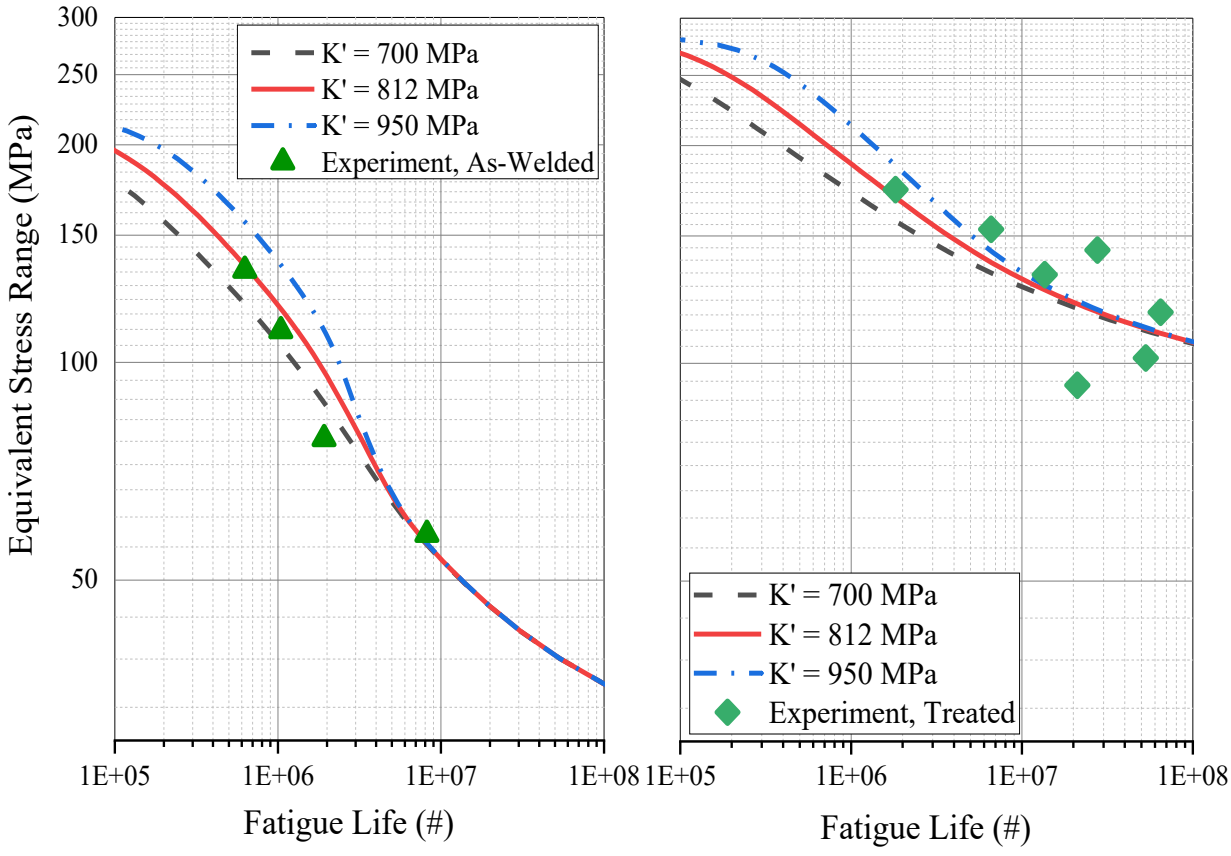

Figure 5.10: Effect of variation in *K*' on the S-N curve for as-welded (left) and treated (right) specimens

5.2.4 Ultimate strength, σ_u

For the deterministic SBFM analysis, the value of σ_u for 350W steel was estimated to be 616 MPa based on static tension test results available in (Ghahremani 2015). In general, ± 20 MPa of variation in ultimate strength was observed by the author while performing static tension tests of A514 steel and 5083 Aluminum specimens on three sets of specimens. Herein, the lower and upper limit of σ_u was arbitrarily taken to be 475 MPa and 840 MPa, so that an effect of variation in σ_u could be observed on the S-N curve as shown in Figure 5.11. It can be observed that there is a mild effect of variation in ultimate strength on the S-N curve in the LCF regime (< 10^6 cycles). In the LCF regime, the higher the ultimate strength, the higher is the fatigue strength.

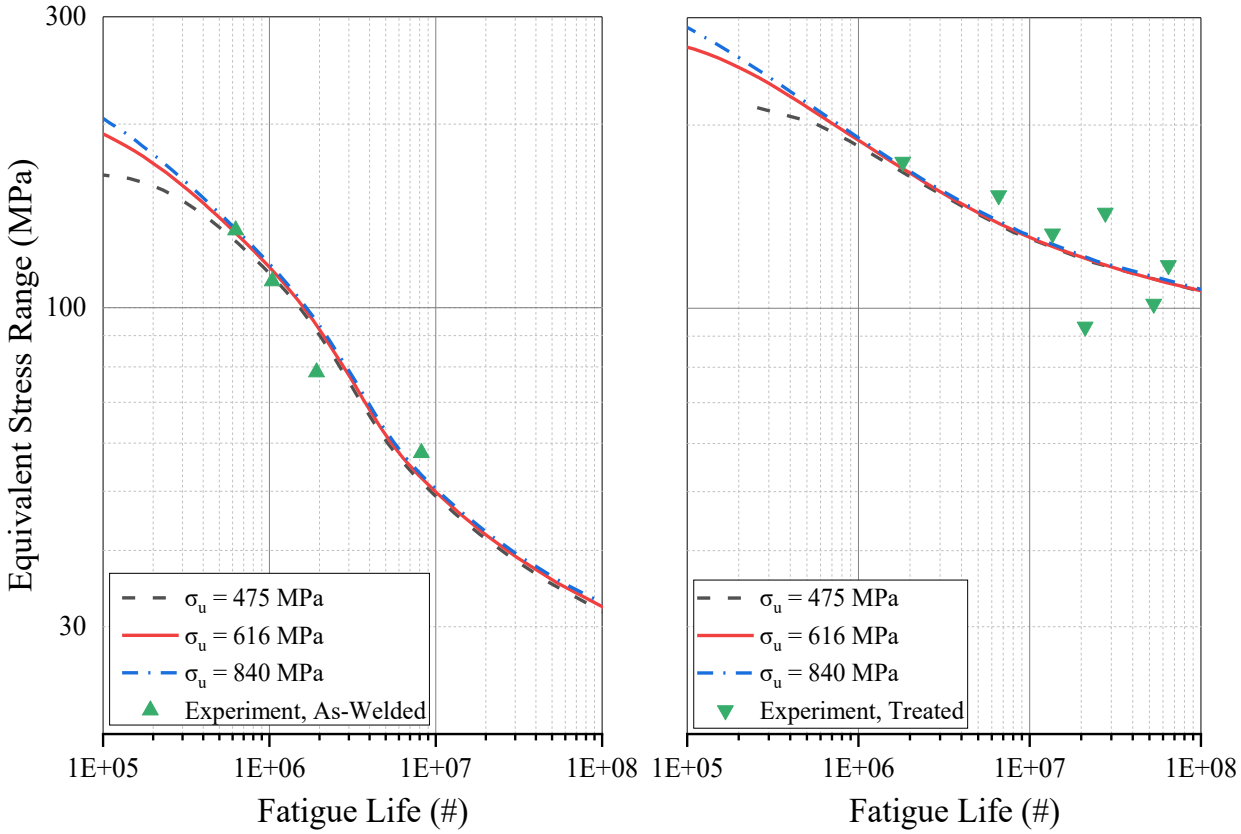

Figure 5.11: Effect of variation in σ_u on the S-N curve for as-welded (left) and treated (right) specimens

5.2.5 Stress concentration factor, *SCF*

Six weld toe geometries of the as-welded and HFMI treated specimens were modelled in finite element (FE) analysis software ABAQUS to estimate the SCF distribution along the expected crack path. FE analysis results for six weld toe geometries for as-welded and treated weld toes provided an estimate for variation in peak SCF at the weld toe. The six SCF distributions were used for SBFM analysis to observe the effect of variation in SCF on the S-N curve as shown in Figure 5.12. It can be observed that there is only a mild effect on the S-N curve because of this realistic variation in SCF.

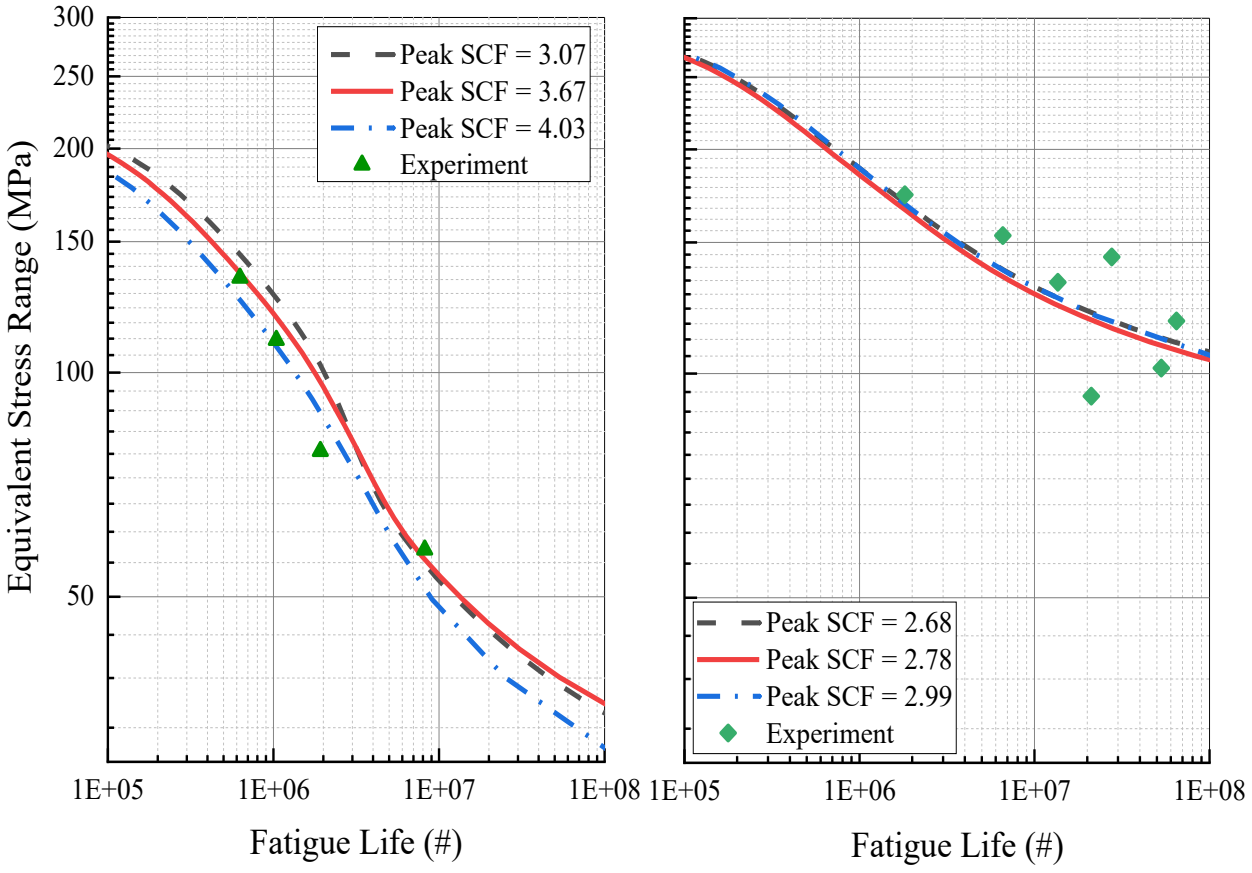

Figure 5.12: Effect of variation in *SCF* on the S-N curve for as-welded (left) and treated (right) specimens

5.2.6 Initial crack depth, a_i

The defect geometry for the studied specimen is not known, therefore a 0.15 mm deep defect with an aspect ratio of 0.5 was assumed for the deterministic SBFM analysis. Herein, four values of defect depth, specifically 0.045 mm, 0.15 mm, 0.25 mm, and 0.4 mm, were selected to observe the effect of variation in defect depth on the S-N curve for cruciform welded joints. Figure 5.13 shows S-N curves for as-welded and impact treated specimens at different values of defect depths. It can be observed that the effect of variation in a_i is significantly higher for as-welded specimens in comparison to treated specimens. For the as-welded specimens, fatigue strength can be significantly improved by reducing the defect size, especially in the HCF regime.

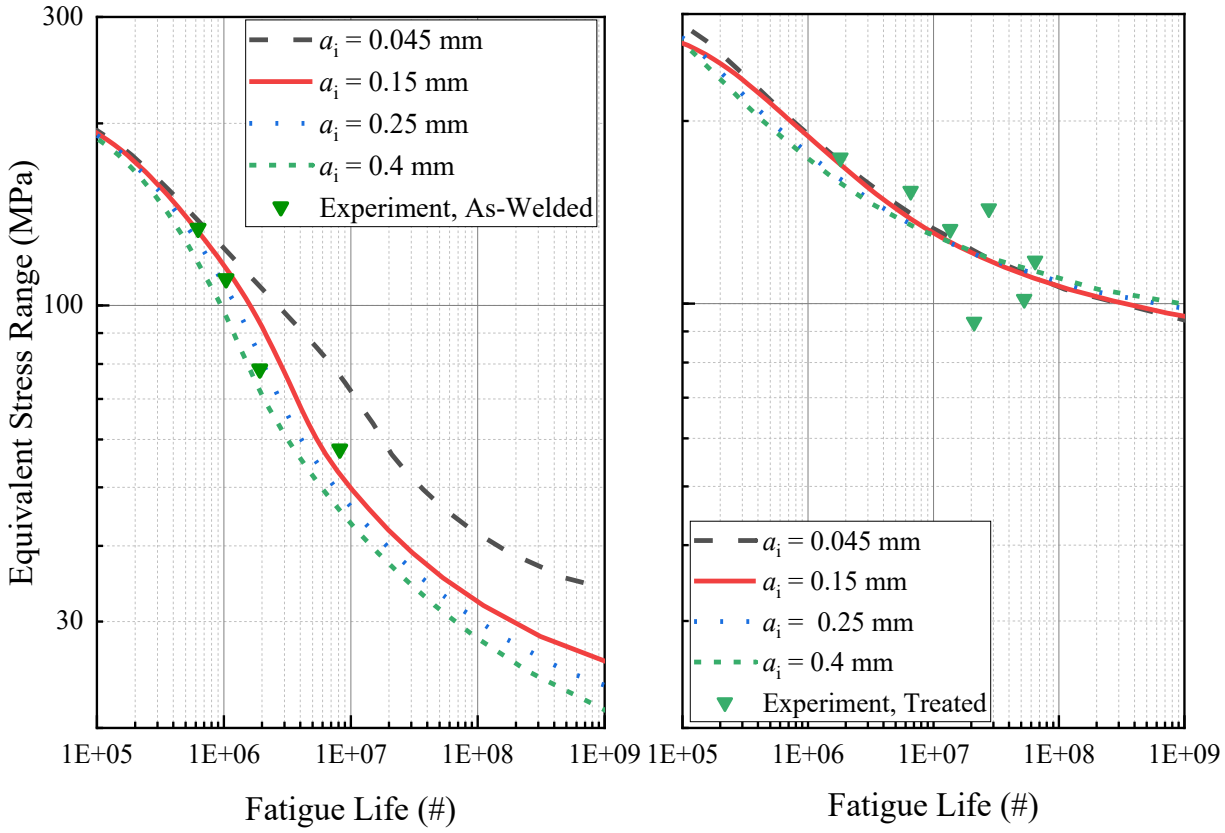

Figure 5.13: Effect of variation in a_i on the S-N curve for as-welded (left) and treated (right) specimens

5.2.7 Initial crack shape or defect aspect ratio, $(a/c)_{initial}$

For the deterministic analysis, the initial crack shape was assumed to be semi-elliptical with an aspect ratio of 0.5. To observe the effect of variation in a/c on the S-N curve, the lower and upper limit of the defect aspect ratio was taken to be 0.2 and 0.9. Figure 5.14 shows the effect of variation in the defect aspect ratio on the S-N curve for as-welded and impact treated specimens. It can be observed that there is a mild effect of variation in $(a/c)_{initial}$ on the as-welded specimens and relatively lower effect on the S-N curve for the treated specimens. In general, the lower the aspect ratio (wide defect), the lower is the fatigue life at a particular level of stress range for both as-welded and treated specimens.

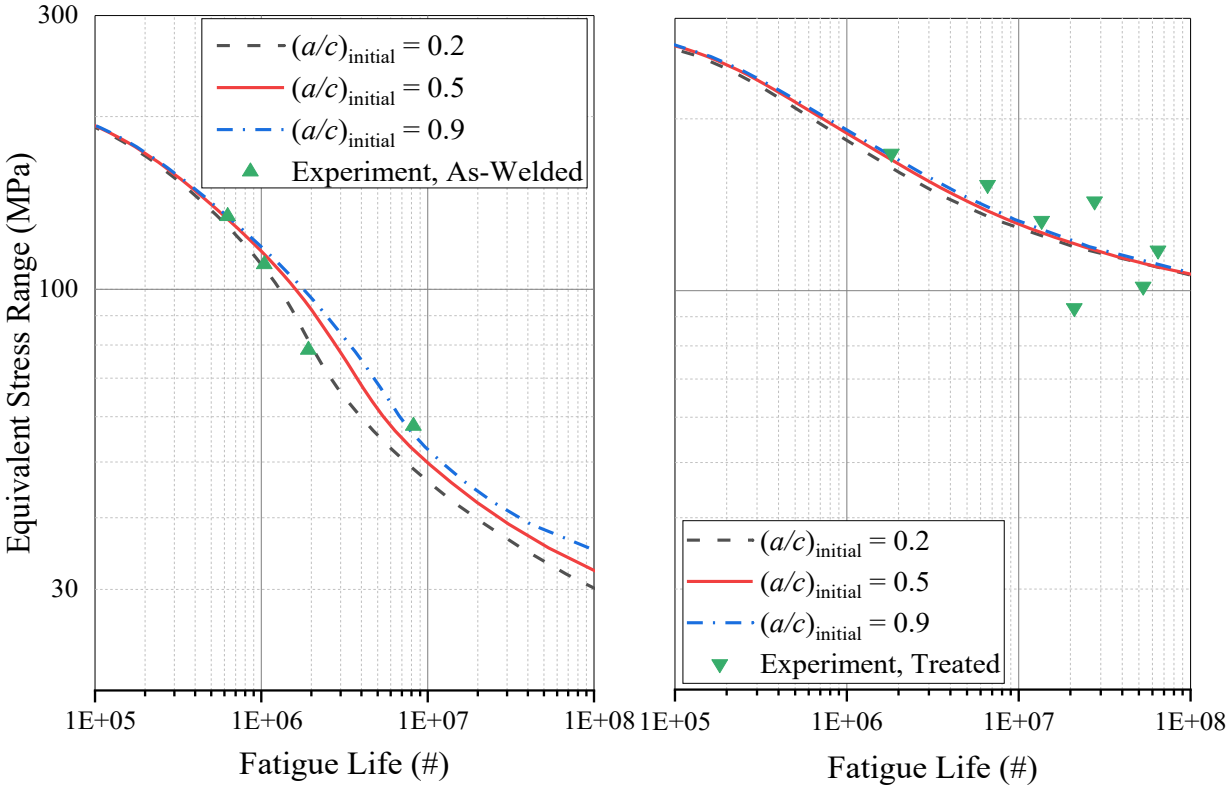

Figure 5.14: Effect of variation in $(a/c)_{initial}$ on the S-N curve for as-welded (left) and treated (right) specimens

5.2.8 Residual stress, σ_r

For the deterministic SBFM analysis, two weld toe peak residual stresses of -0.18·σ_y and +0.28·σ_y were considered for as-welded specimens to obtain the envelope of S-N curves which contained all the fatigue test data points. Herein, three peak residual stress values of -0.23·σ_y, -0.05·σ_y and +0.28·σ_y are considered as shown in Figure 5.15 to observe the effect of variability in residual stress distribution on S-N curve for as-welded specimens. For the treated specimens, while performing the deterministic analysis, two peak residual stresses of -0.80·σ_y and -0.35·σ_y were considered to obtain the envelope of two S-N curves which contained all the fatigue test data points. Herein, for sensitivity analysis, three peak residual stress values at the weld toe of -1.31·σ_y, -0.58·σ_y and -0.15·σ_y are considered as shown in Figure 5.16 to observe the effect of variability in residual stress distribution on S-N curve for impact treated specimens.

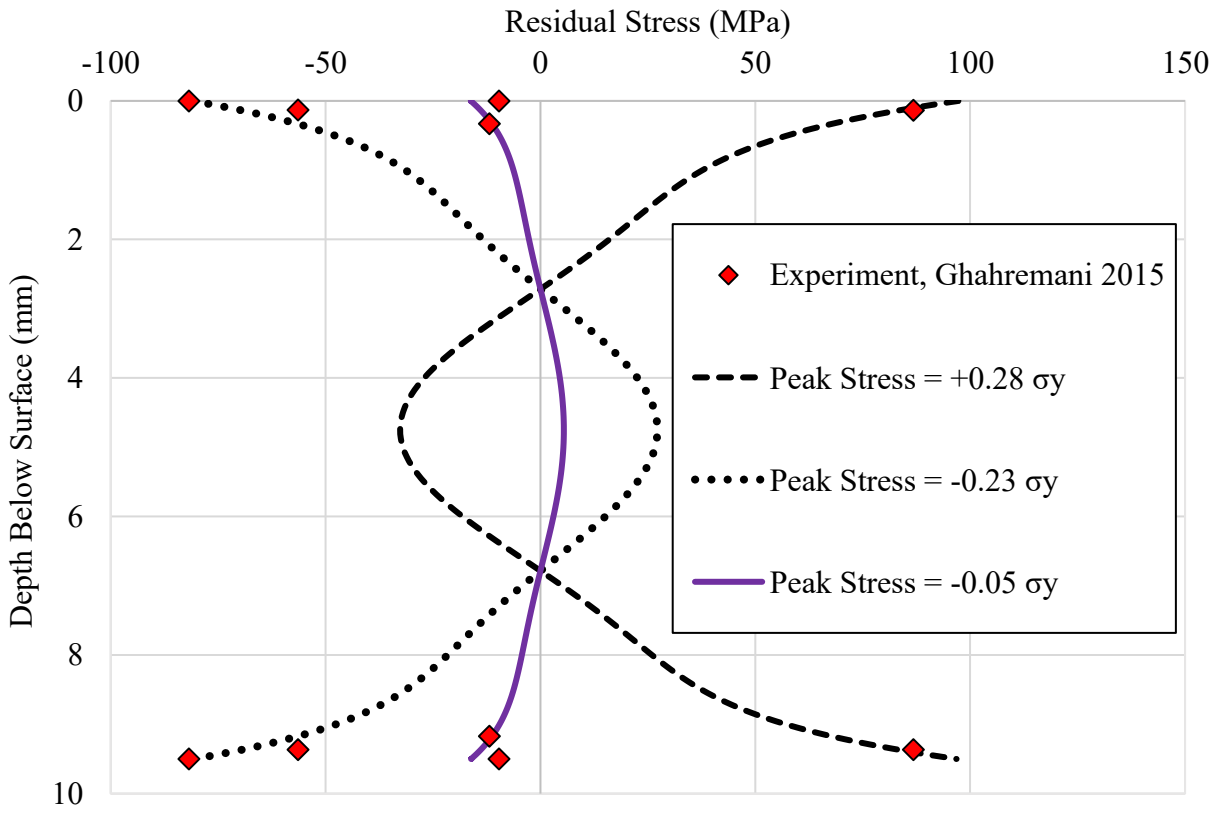

Figure 5.15: Bounds of residual stress distribution for as-welded specimens

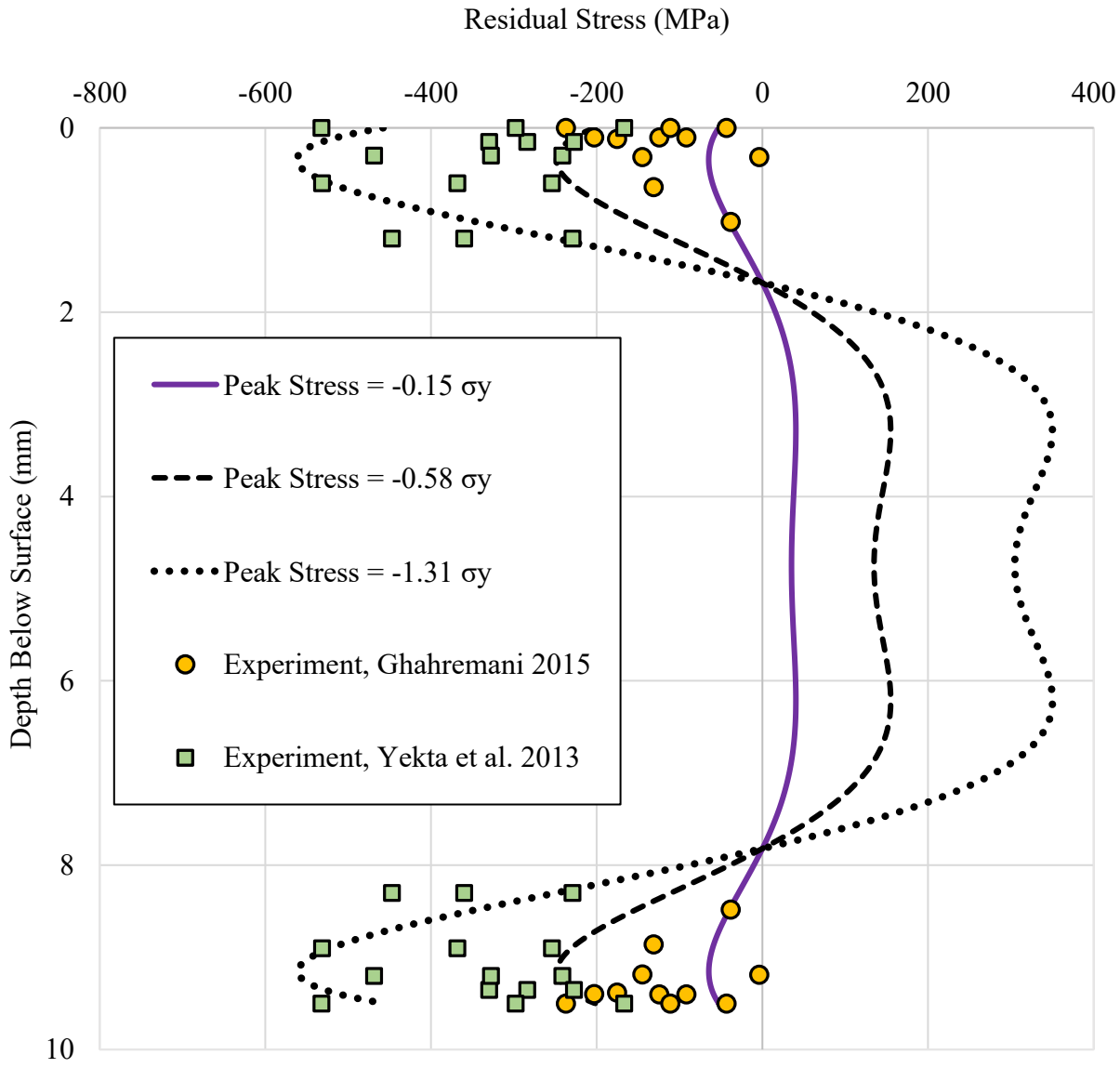

Figure 5.16: Bounds of residual stress distribution for treated specimens

Figure 5.17 shows the effect of variation in residual stress distribution on S-N curves for as-welded and impact treated specimens. It can be observed that there is a significant effect of variation in residual stress distribution on treated specimens in comparison to as-welded specimens.

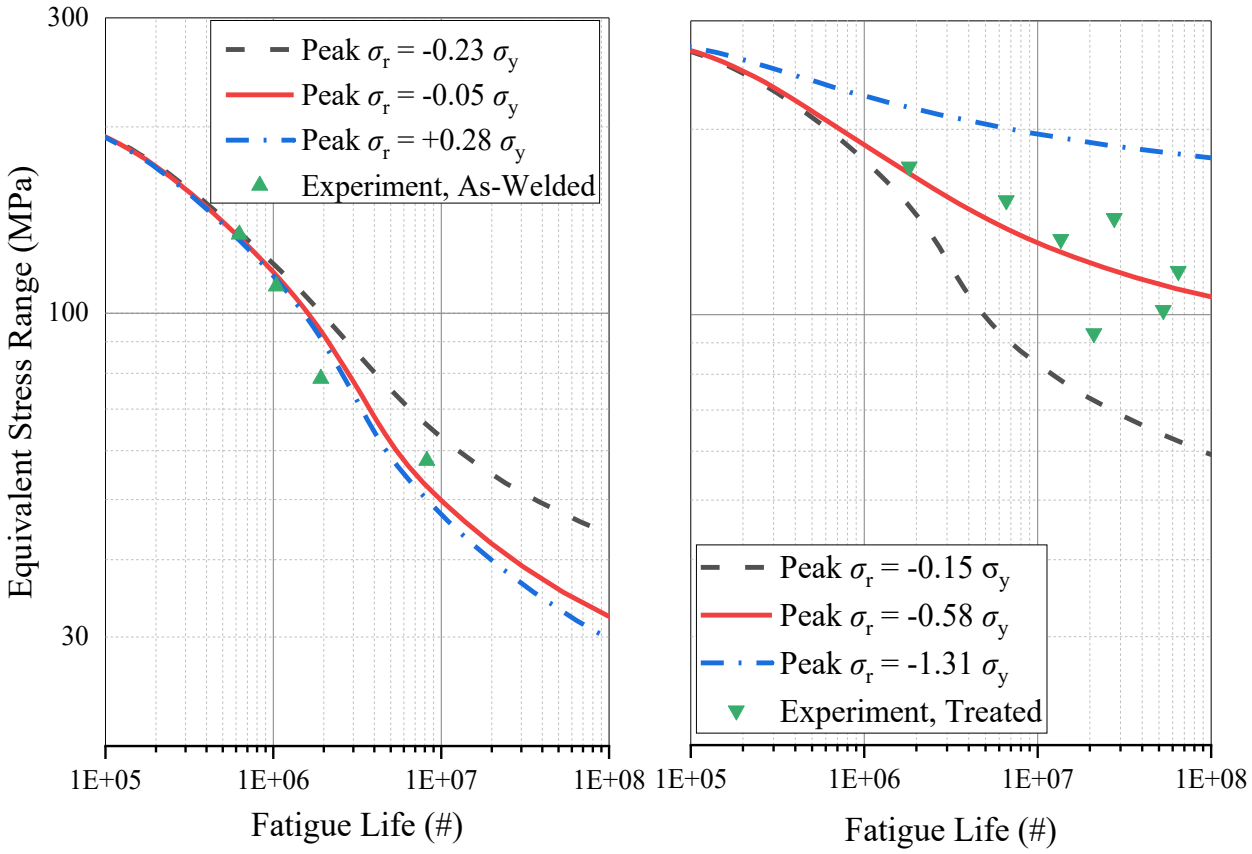

Figure 5.17: Effect of variation in σ_r on the S-N curve for as-welded (left) and treated (right) specimens

5.2.9 Crack closure build up parameter, μ_{op}

In the SBFM model, the load interaction effect has been considered using the crack closure model. While modelling crack closure, crack opening stress under VA loading was estimated from Equation (2.15), which involves the parameter μ_{op}. For the deterministic SBFM analysis, the value of μ_{op} was taken to be 0.018 for 350W steel based on experimental data available in (Ghahremani 2015). The uncertainty in μ_{op} is not known, therefore, an arbitrary variation was considered with a lower limit of 0.002 and an upper limit of 0.1 to observe the effect of variation in μ_{op} on the S-N curve as shown in Figure 5.18. It can be observed that there is less effect of a variation in μ_{op} on the S-N curve for treated specimens than for the as-welded specimens.

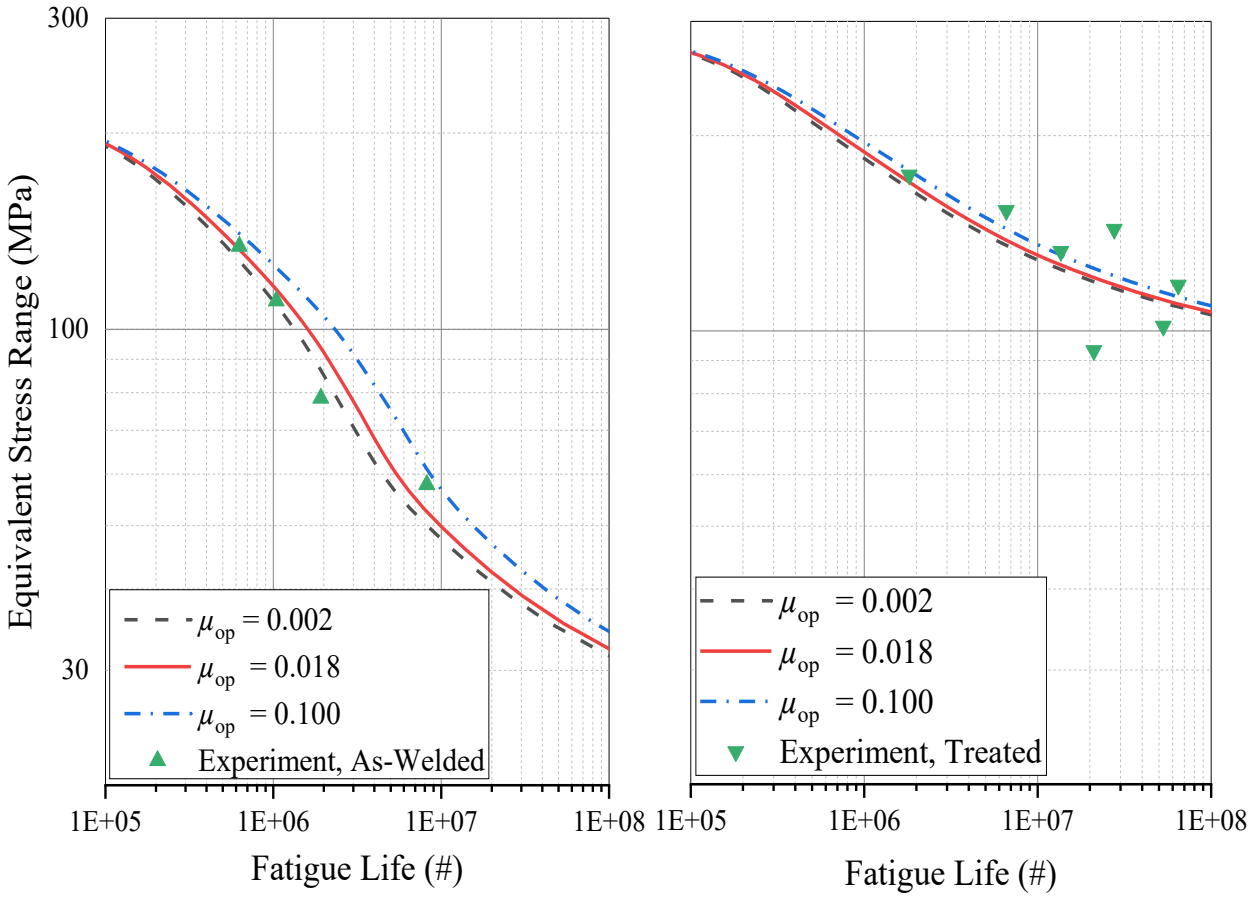

Figure 5.18: Effect of variation in μ_{op} on the S-N curve for as-welded (left) and treated (right) specimen

5.2.10 Plastic constraint factor, α

In the crack closure model, the steady-state crack opening stress under CA loading is calculated using Equations (2.15) and (2.16) taken from (Newman 1984). The crack opening stress equation involves the parameter, α (plastic constraint factor), through which three-dimensional constraint effects are considered. The parameter α with a value of 1 corresponds to a plane stress condition and with a value of 3 corresponds to a plane strain condition. Figure 5.19 shows the effect of a variation in α at the deepest point of the crack on the S-N curve for as-welded and treated specimens. It can be observed that there is a mild effect of variation in α on the S-N curve for as-welded specimens but there is a lower effect of α on the S-N curve for treated specimens. Similarly, at the surface point of the specimen, the effect of variation in α has been observed on

the S-N curve for as-welded and treated specimens as shown in Figure 5.20. Again, it can be observed that there a mild effect of variation in α (at the surface point) on the S-N curve for as-welded specimens and a relatively lower effect of the variation in α on the S-N curve for treated specimens. It can be observed that fatigue strength of as-welded specimens is higher in plane stress condition as compared to plane strain condition because there is relatively more closure effect (higher crack opening stress) in plane stress condition as compared to plane strain condition.

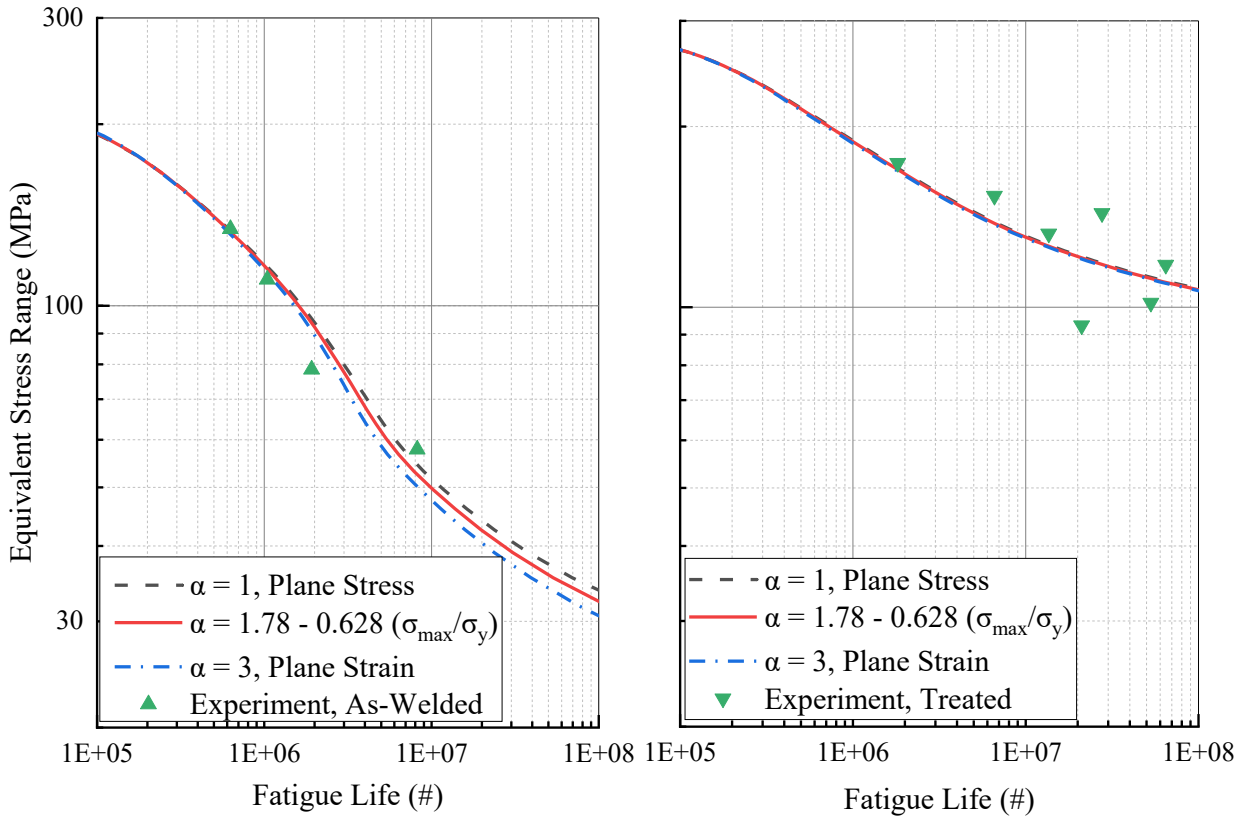

Figure 5.19: Effect of variation in α at the deepest point of a semi-elliptical crack on the S-N curve

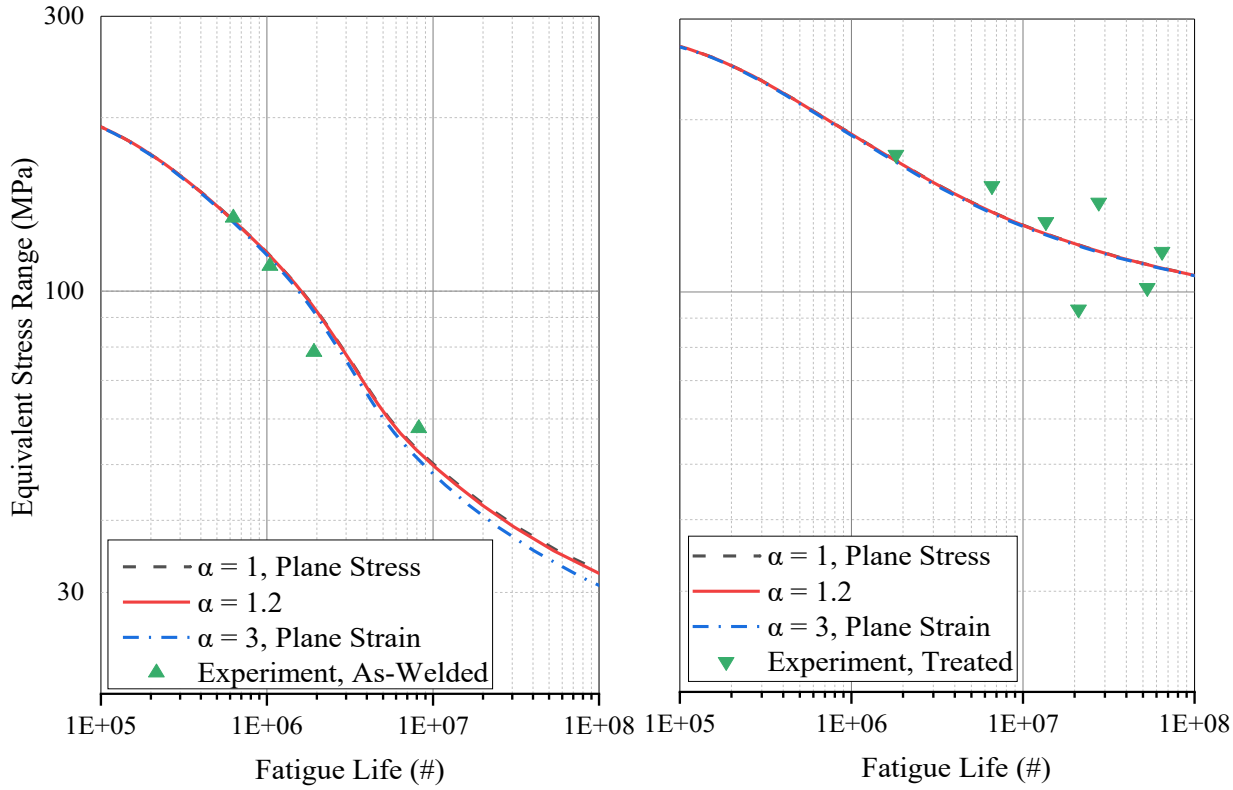

Figure 5.20: Effect of variation in α at the surface point of a semi-elliptical crack on the S-N curve

5.3 Probability distribution parameters for various SBFM input parameters

The probability distribution parameters for SBFM input parameters were decided based on data available in the existing literature as well as variability observed in the laboratory test results for the measurement of material properties in the current study. For σ_u, *SCF* distribution and σ_r distribution, scalar variables Var(σ_u), Var (*SCF*), and Var(σ_r) respectively were taken as random variables. These are essentially multipliers or scaling factors for the specific input parameter. The mean values for the σ_u, peak *SCF* for as-welded specimens, peak *SCF* for treated specimens, peak σ_r for as-welded specimen and peak σ_r for treated specimen were 616 MPa, 3.67, 2.78, $+0.05 \cdot \sigma_y$ and $-0.58 \cdot \sigma_y$ respectively. The distribution of *SCF* and σ_r were the same as the one presented in Chapter 4 which was scaled in this chapter based on the magnitude of the scaling factor. The resulting probability distribution parameters are presented in Table 5.1.

Table 5.1: Probability distribution parameters for various SBFM input parameters

Material Properties	**Symbol**	**Mean**	**COV**	**Distribution Type**	**Reference**
Paris Law Constant	LN(C)	-27.5	0.42	Lognormal	(Lotsberg et al. 2002)
Threshold Stress Intensity Factor	ΔK_{th}	60	0.07	Lognormal	(BS-7910 2005; Shetty, N.K.;Baker 1990)
R-O cyclic material model parameter	K'	812	0.05	Lognormal	Assumed
Ultimate strength	Var(σ_u)	1.0	0.07	Lognormal	(BS-7910 2005)
Crack closure build up parameter	μ_{op}	0.018	0.5	Lognormal	(Walbridge et al. 2012)
Initial crack depth	a_i	0.15	0.3	Lognormal	(Brückner and Munz 1983)
Initial crack aspect ratio	$(a/c)_{initial}$	0.5	0.2	Lognormal	(Righiniotis and Chryssanthopoulos 2003)
Stress concentration factor	Var (SCF)	1.0	0.07	Lognormal	(JCSS 2011)
Residual stress (as-welded specimens)	Var (σ_r)	1.0	1.25	Normal	Assumed
Residual stress (treated specimens)	Var (σ_r)	1.0	0.3	Lognormal	Assumed

Some of the parameters mentioned in Table 5.1 are expected to be correlated with each other, especially the parameters that are obtained from the same set of material test data. For example, the parameters C, m and ΔK_{th} are estimated from the same set of crack growth rate test data, therefore, these parameters should be correlated. However, the correlation among the parameters has been ignored in this study as a simplification. For the probabilistic analysis, C and ΔK_{th} were treated as random variables but m was assumed to be constant. The parameters K' and n' were estimated from cyclic material test data and are expected to be correlated. Herein, K' has been treated as a random variable but n' has been treated as constant to represent the variability in cyclic material behaviour. The SBFM input parameters such as yield strength, elastic modulus, width, and thickness of the specimen are treated as constant for the probabilistic SBFM analysis. Final crack depth has been estimated based on the failure criterion discussed in Section 2.7 rather than treated as a random variable. Variability in local weld toe geometry (weld toe angle and toe radius) was considered indirectly through variability in the *SCF*.

5.4 Probabilistic SBFM analysis for small-scale specimens

For the probabilistic SBFM analysis, Monte-Carlo Simulation was performed in which random numbers from the probability distribution of each random variable mentioned in Table 5.1 were simulated, which were used as input for the 2D SBFM model for fracture mechanics analyses. At 25 fixed values of stress level, SBFM analysis was performed to obtain ~2000 fatigue lives at each stress level, which provided overall 50000 S-N data points for estimation of each design S-N curve. The median and 97.7th percentile values of fatigue lives at each 25 fixed stress levels were calculated, which provided median and design S-N curves respectively. It was observed that the mean S-N curve was biased because of the specific assumed value (10^{10} cycles) to represent infinite life, therefore the median S-N curve has been presented rather than the mean S-N curve. Here, the design S-N curve corresponds to a 97.7 % survival probability which is normally the target level of survival probability in international design codes. Figure 5.21 shows the median and design S-N curve for as-welded specimens under CA loading (R = 0.1).

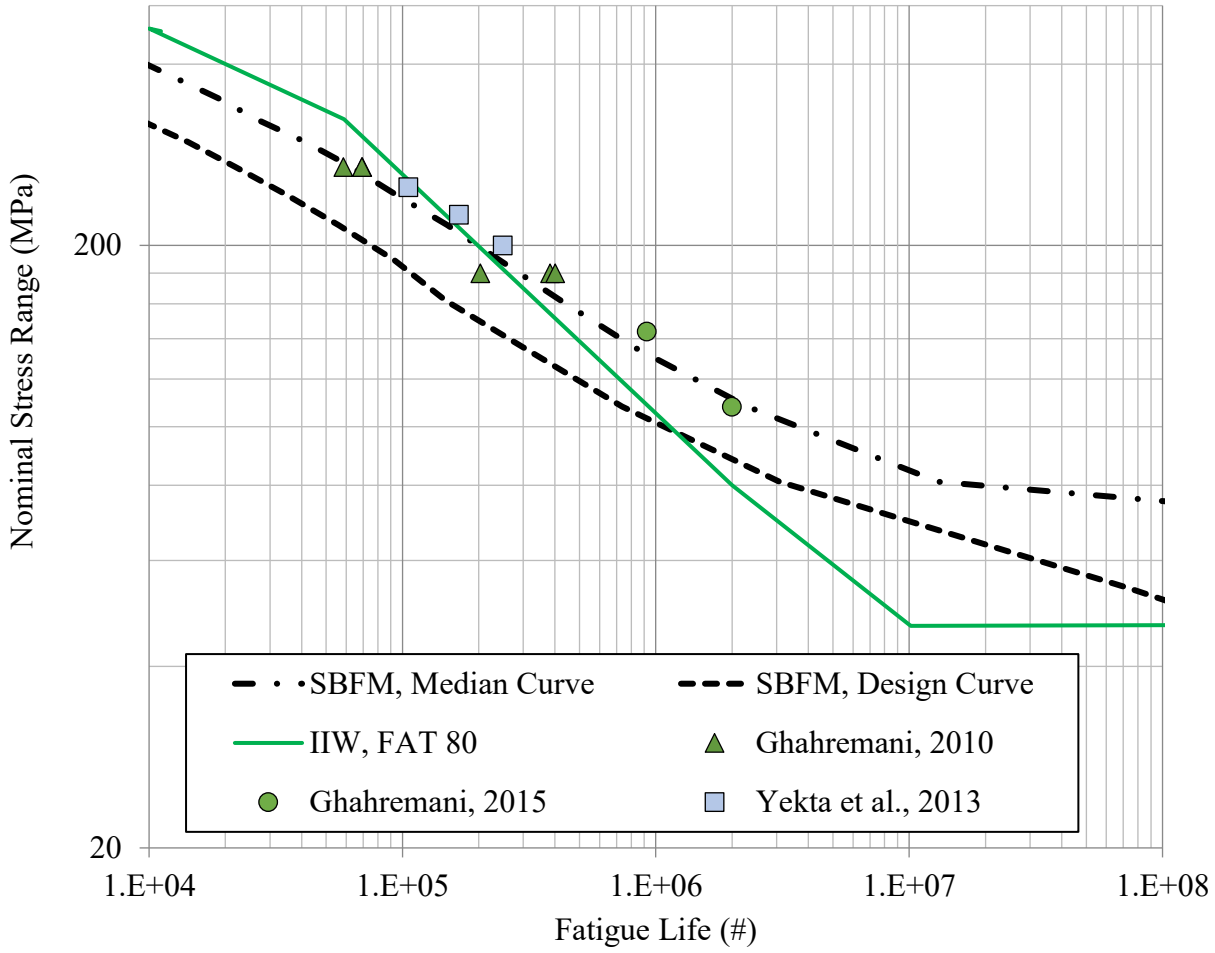

Figure 5.21: Probabilistic SBFM analysis results for as-welded specimens under CA loading

For comparison purposes, the experimental fatigue test results and the IIW design S-N curve have also been plotted in Figure 5.21. In this figure, the FAT 80 design curve and SBFM-derived design S-N curve are close to each other around one million cycles. Therefore, for the small-scale as-welded specimens, FAT 80 can be considered as a design S-N curve, which is also the FAT class suggested by IIW for mild steel cruciform welded joints. Although, it should be noted that four test data points are below the FAT 80 curve which shows that FAT 80 design curve is non-conservative in low cycle fatigue regime ($< 10^5$ cycles). FAT 80 design curve will provide a lower magnitude of fatigue strength improvement compared to any other lower FAT class than FAT 80, therefore, for quantification of fatigue strength improvement, this is a conservative

decision to assume that as-welded specimens belong to FAT 80 class i.e. overestimating the fatigue strength of as-welded specimens will provide lower magnitude of fatigue strength improvement in treated specimens.. It can be observed that the slope of the SBFM-derived design S-N curve is shallower than the relatively steeper IIW design S-N curve. The difference in slope is mainly because of the presence of low magnitude of residual stress in as-welded small-scale (laboratory) specimens. For small-scale specimens, the assumed mean value of the peak residual stress at the weld toe was $+0.05 \cdot \sigma_y$. It can also be observed that in the HCF regime, the SBFM-derived design curve for small-scale specimens is above the IIW design curve, which is also because of the assumed low magnitude of residual stress in the as-welded small-scale specimens. Figure 5.22 shows the median and design S-N curves for small-scale HFMI treated specimens under CA loading (R = 0.1).

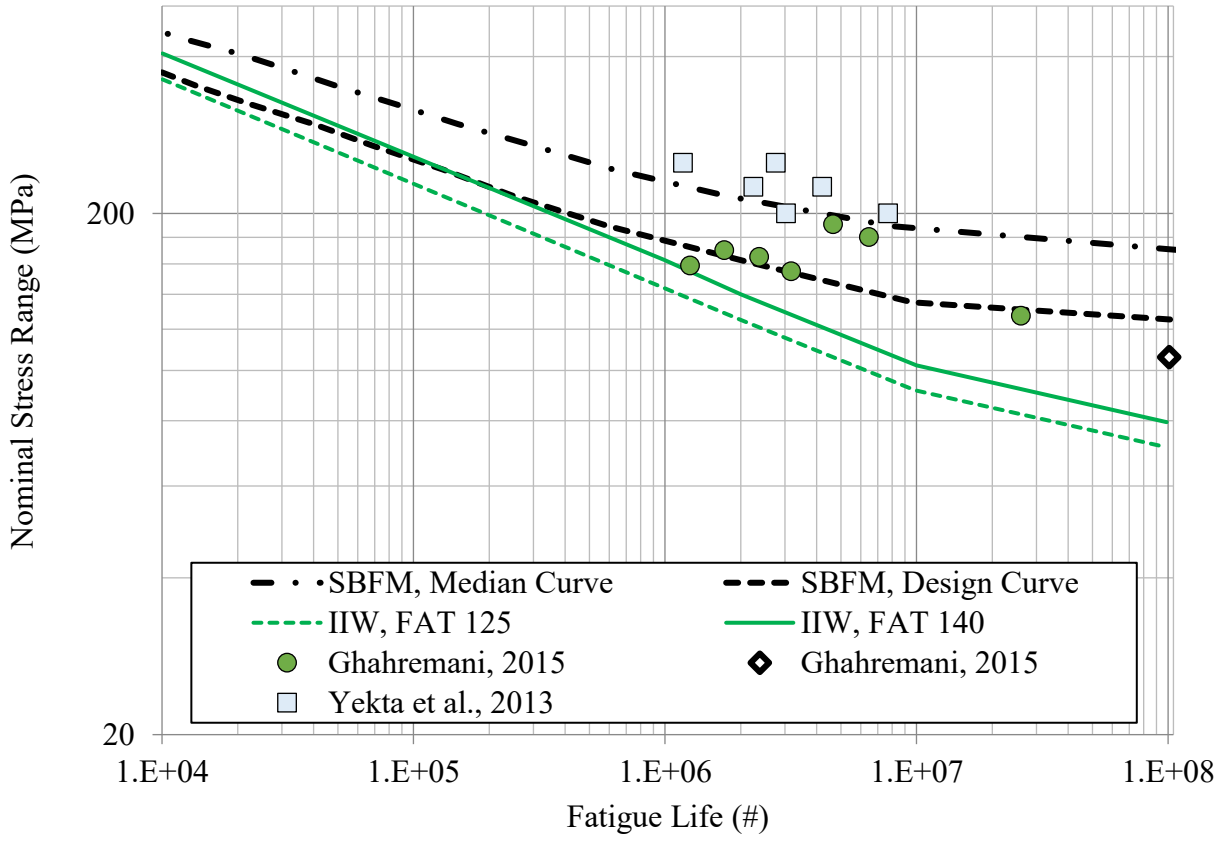

Figure 5.22: Probabilistic SBFM analysis results for treated specimens under CA loading

In this figure, the SBFM-derived design S-N curve and the FAT 140 design S-N curves are close to each other until one million cycles, therefore, FAT 140 can be treated as a design S-N curve for small-scale treated specimens. It can be observed that the SBFM-derived design S-N curve is above the IIW design S-N curves in the HCF regime (>10^6 cycles). The reason behind this is mainly because of the specific assumption for the mean value of peak residual stress (-0.58·σ_y) at the weld toe for the treated specimens.

Figure 5.23 shows the median and design S-N curves for as-welded specimens under VA1 loading. It can be observed that SBFM-derived design S-N curve and FAT 63 design S-N curve are close to each other, therefore, the FAT 63 (two FAT classes lower than FAT 80) curve can be treated as a design S-N curve for as-welded specimens under VA1 loading.

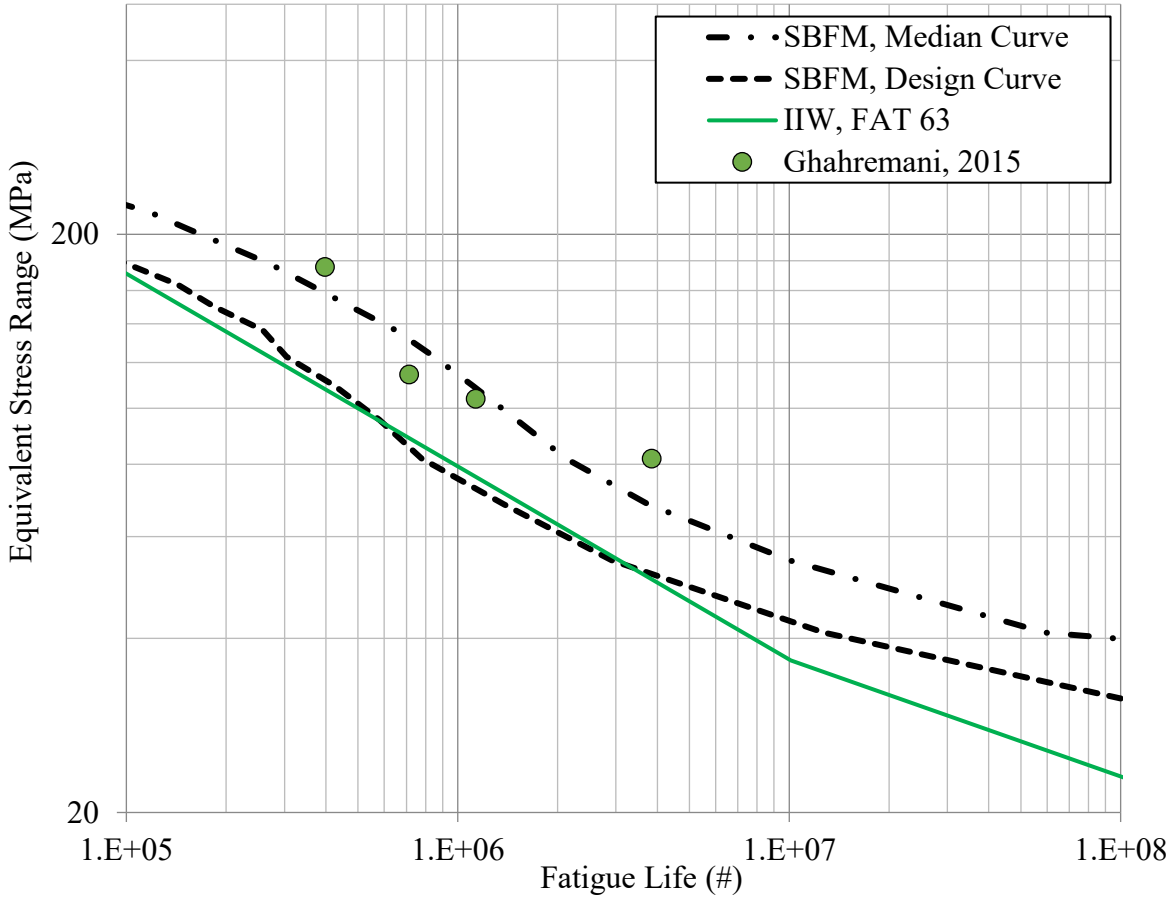

Figure 5.23: Probabilistic SBFM analysis results for as-welded specimens under VA1 loading

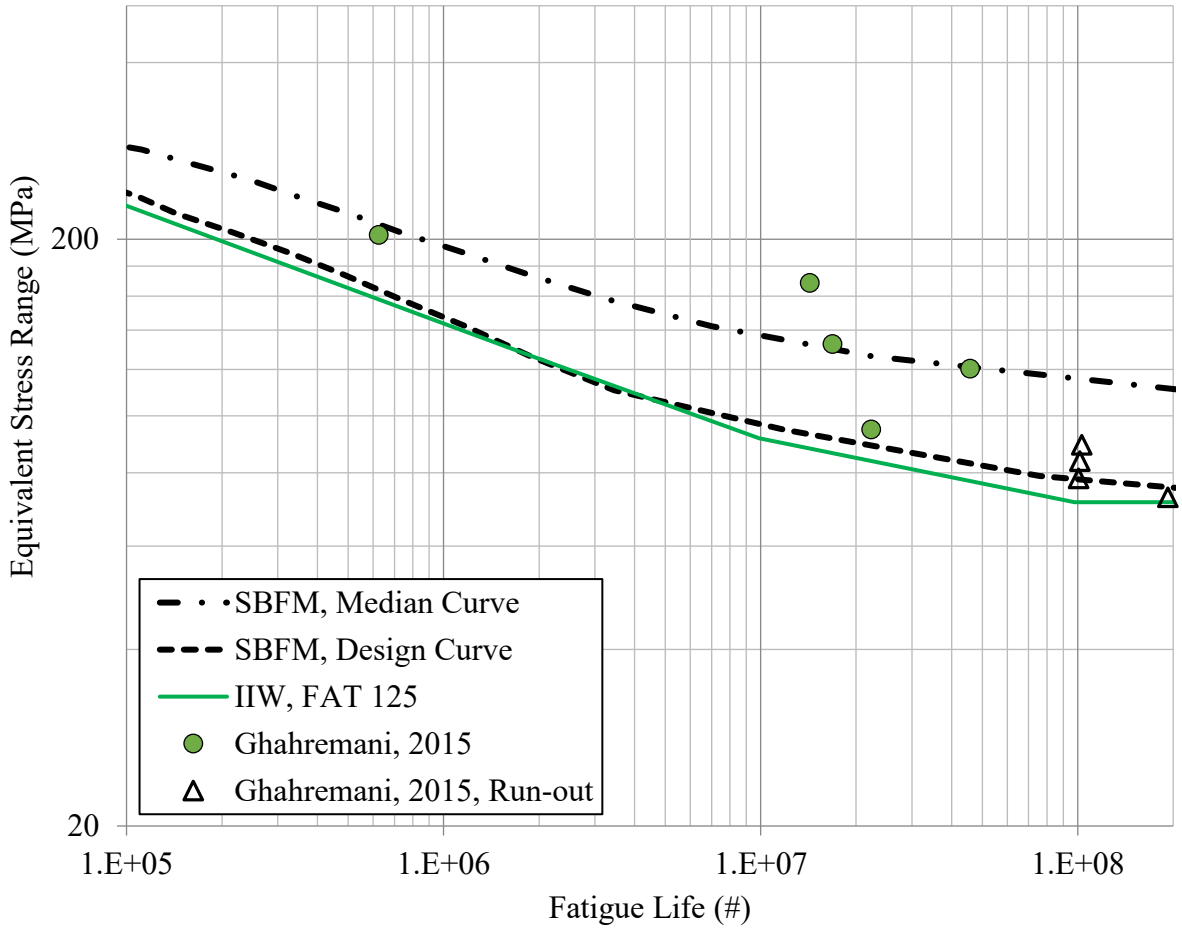

Figure 5.24: Probabilistic SBFM analysis results for treated specimens under VA1 loading

Figure 5.24 shows median and design S-N curves for treated specimens under VA1 loading. It can be observed that the SBFM-derived design S-N curve is close to IIW FAT 125 design S-N curve, therefore, FAT 125 can be treated as a design S-N curve for small-scale treated specimens under VA1 loading. Here, the slope of the IIW design curve and SBFM-derived design S-N curve is the same for the entire range of fatigue life as shown in Figure 5.24.

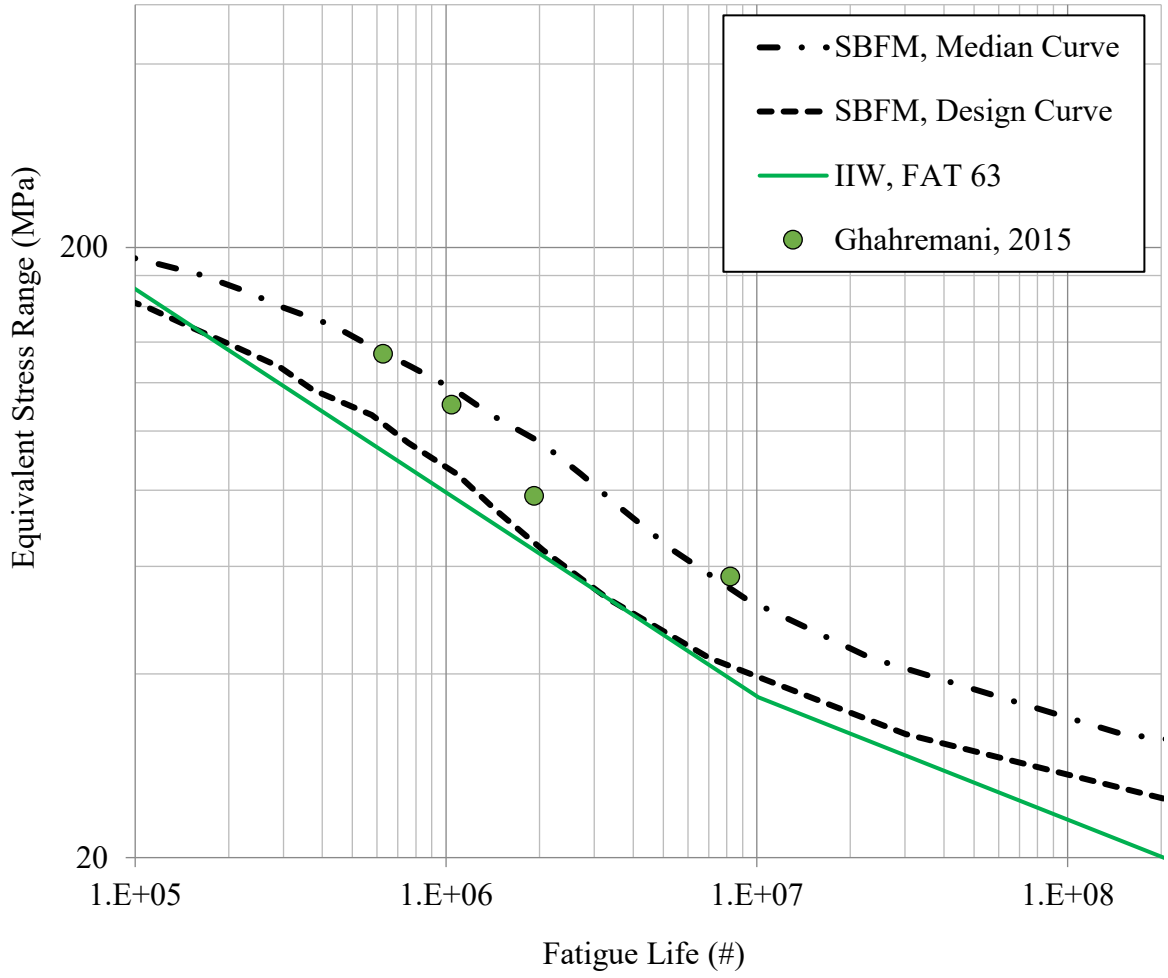

Figure 5.25: Probabilistic SBFM analysis results for as-welded specimens under VA2 loading

Figure 5.25 shows the median and design S-N curves for as-welded specimens under the VA2 loading. It can be observed that the SBFM based design S-N curve is close to IIW FAT 63 design curve, therefore, FAT 63 can be taken as a design S-N curve for as-welded small-scale specimens under the VA2 loading. Here, the slope of the IIW design curve and SBFM-derived design curve is the same for the entire range of fatigue life as shown in Figure 5.25.

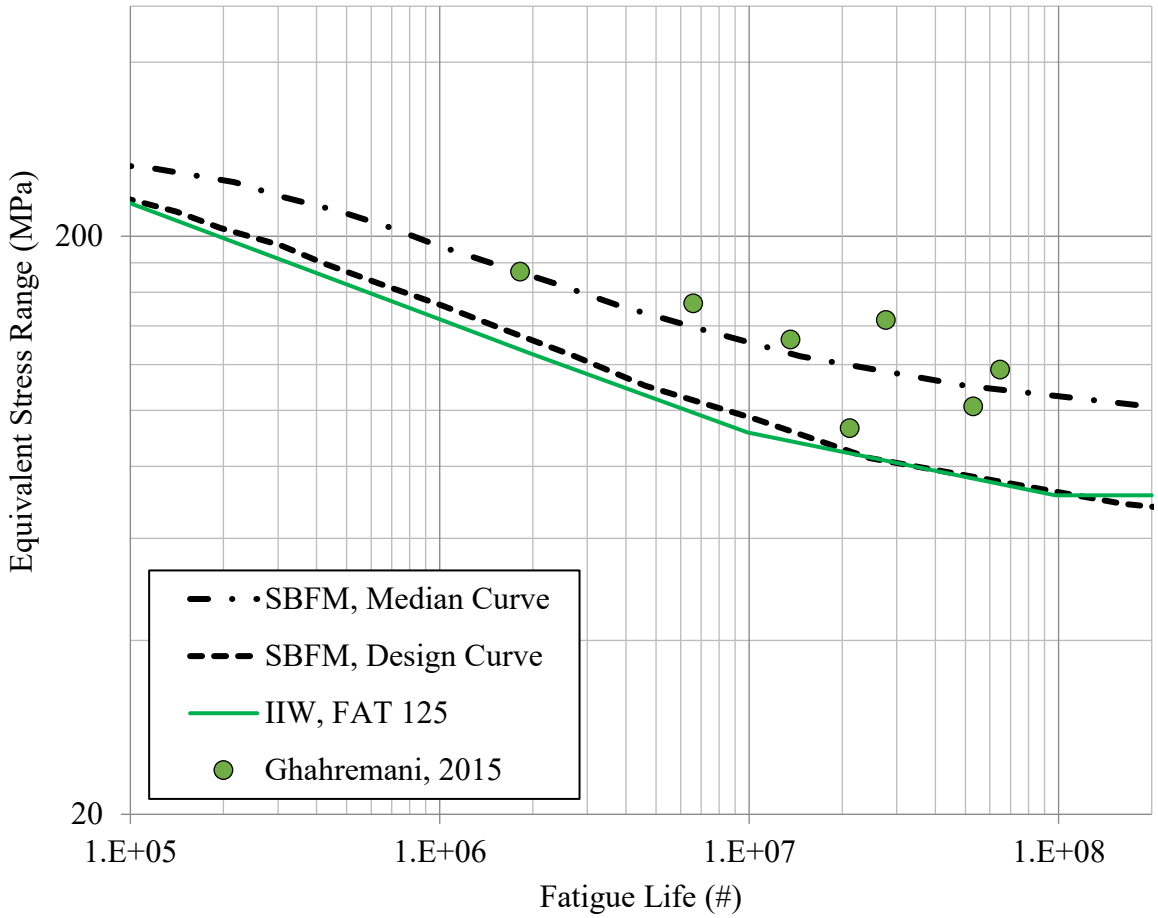

Figure 5.26: Probabilistic SBFM analysis results for treated specimens under VA2 loading

Figure 5.26 shows median and design S-N curve for treated 350W steel specimens under VA2 loading condition. It can be observed in this figure that the SBFM-derived design S-N curve is close to IIW FAT 125 design S-N curve. The slope and intercept of SBFM-derived design curve matches with the slope and intercept of the IIW FAT 125 design curve, therefore, FAT 125 can be taken as a design S-N curve for small-scale treated specimens under VA2 loading.

Figure 5.27 shows the comparison of design S-N curves under various loading conditions with IIW design S-N curves for as-welded specimens. FAT class for as-welded specimens was recommended to be FAT 80 according to IIW. It can be observed from Figure 5.27 that the FAT classes for as-welded small-scale specimens are ~FAT80, FAT63, and FAT 63 under CA, VA1, and VA2 loading conditions respectively. There is a reduction of 2 FAT classes for the design

curve under VA loading in comparison to FAT class under CA loading. IIW provides guidelines for the reduction in FAT class considering the load ratio effect under CA loading but not for any specific VA loading history. The average load ratio for the VA1 and VA2 loading histories is 0.15 and 0.59 respectively. IIW recommends no reduction in FAT class at a load ratio of 0.15 (VA1 loading) and there is no recommendation available in IIW for a reduction in FAT class at the load ratio of 0.59 (VA2 loading).

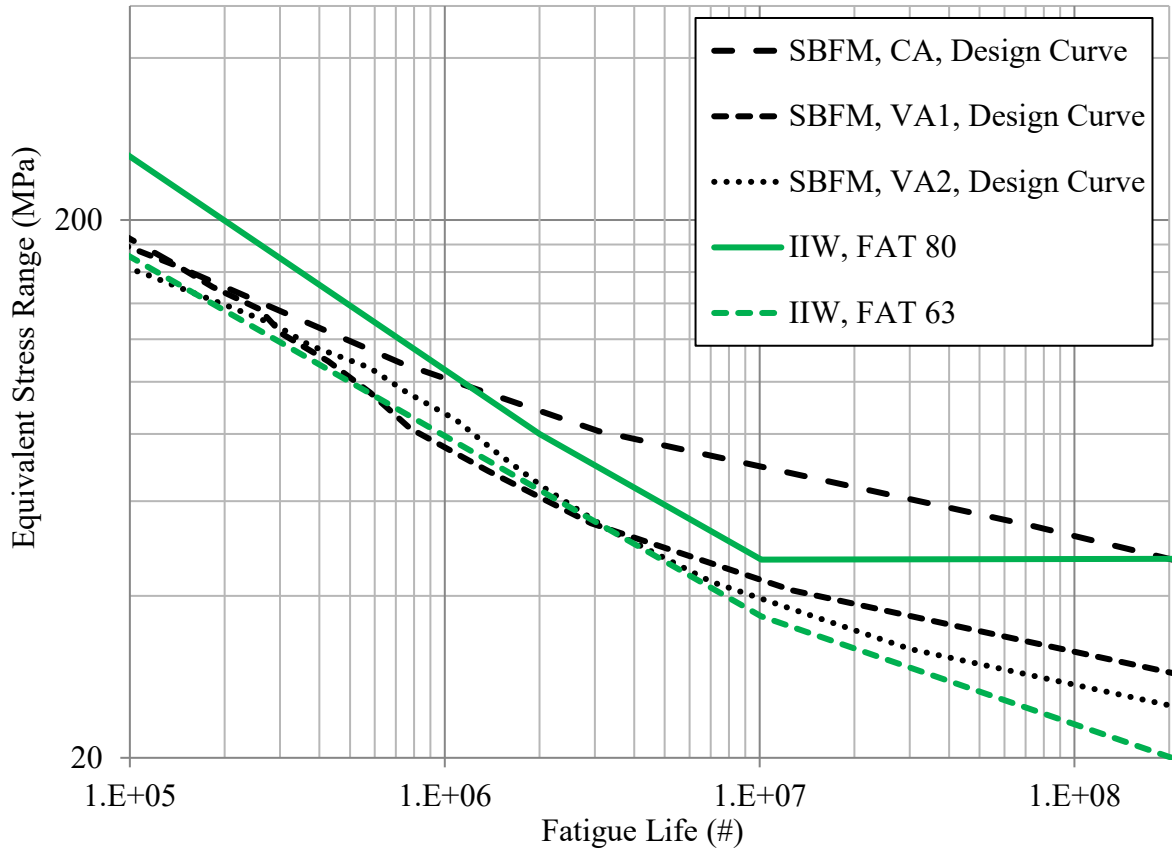

Figure 5.27: Comparison of design curves for as-welded specimens under various loading conditions

Figure 5.28 shows the comparison of SBFM-derived design S-N curves for treated specimens under various loading conditions along with IIW design curves. It can be observed that under VA loading, fatigue strength reduces significantly in the HCF regime as compared to fatigue strength under CA loading. From this figure, it can be concluded that FAT class for small-scale treated specimens are FAT 140, FAT 125, and FAT 125 under CA, VA1, and VA2 loading respectively.

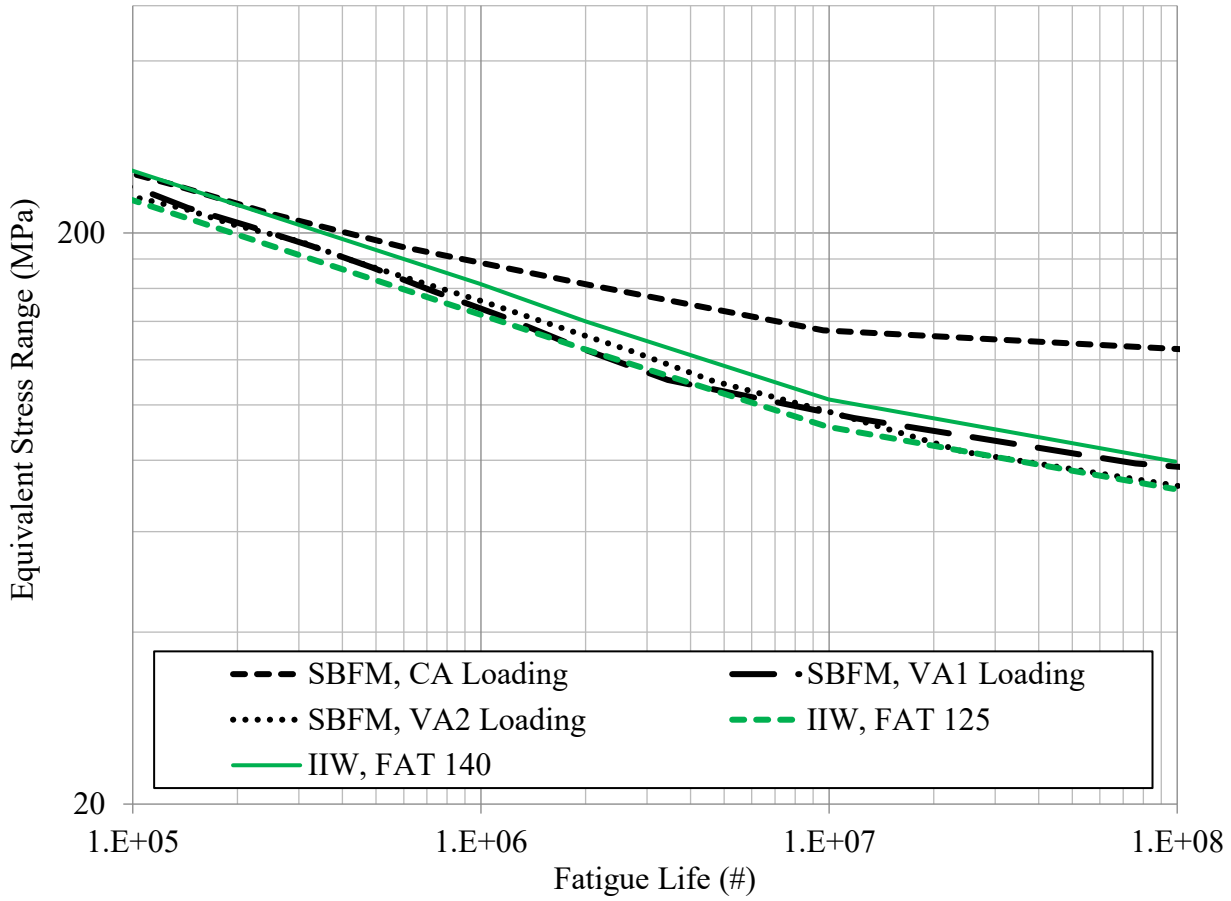

Figure 5.28: Comparison of design curves for treated specimens under various loading conditions

Figure 5.29 shows the comparison of SBFM-derived design S-N curves for as-welded and impact treated specimens. Fatigue strength improvement because of HFMI treatment can be visually observed by comparing the S-N curves under a specific loading condition at a fatigue life of 2 million cycles (see inside the box shown in Figure 5.29). To quantify the characteristic fatigue strength increase, the difference in equivalent stress range at two million cycles of fatigue life can be calculated for a specific loading condition (CA/VA1/VA2). It can be observed that FAT class for small-scale specimens under CA loading has increased from FAT 80 for as-welded specimens to FAT 140 for impact treated specimens, which is an improvement of five FAT classes. Under VA1 and VA2 loading, the FAT class for small-scale specimens has increased from FAT 63 for as-welded specimens to FAT 125 for impact treated specimens, which is an improvement of six FAT classes.

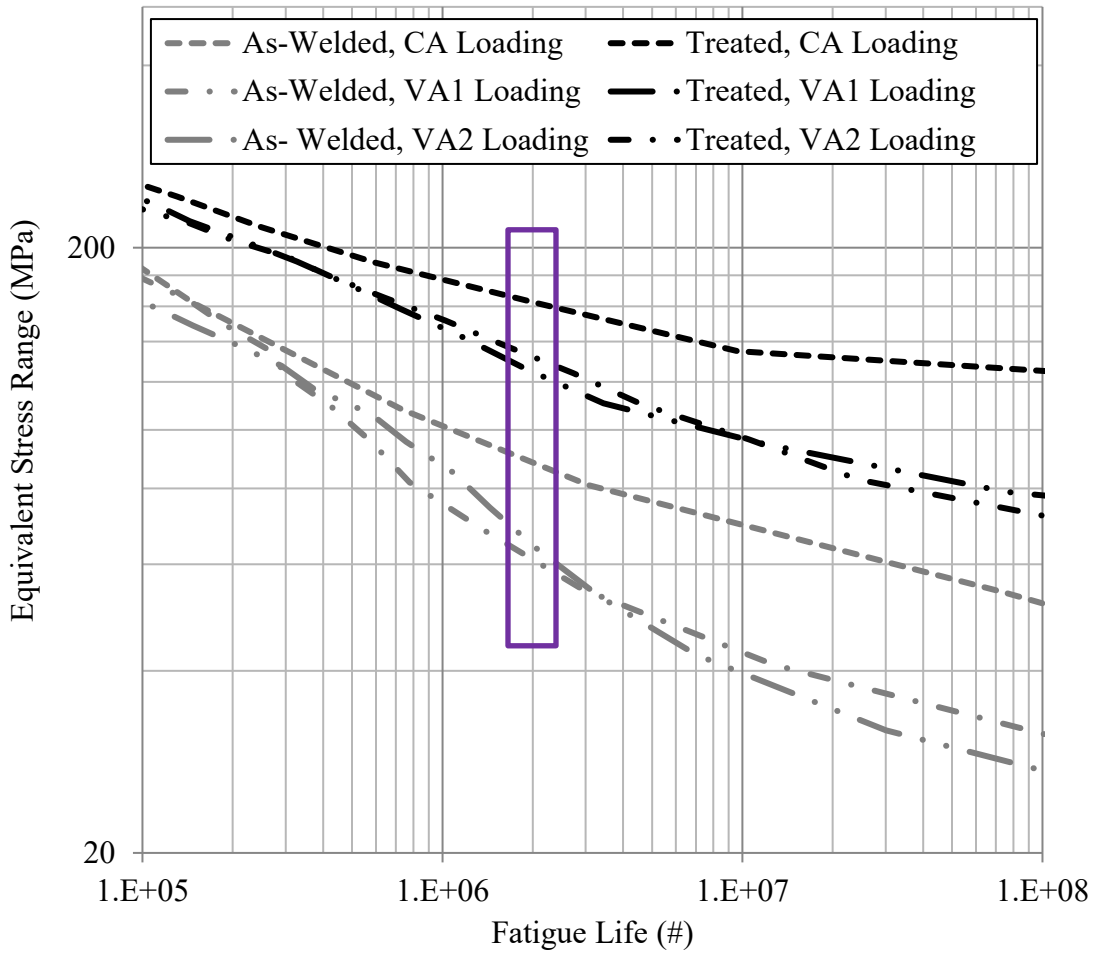

Figure 5.29: Comparison of design curves for as-welded and treated specimen under CA, VA1, and VA2 loading conditions

As per the IIW recommendation, it was expected that a FAT80 detail will have a fatigue improvement of 4-5 FAT classes after HFMI treatment. Therefore, it was expected that the FAT class for treated specimens would be FAT 125 or Fat 140. It was found from the probabilistic analysis results also that the FAT class for treated specimens is FAT 140 under CA loading and FAT125 under VA1 and VA2 loading, which confirms the recommendation of the IIW for treated specimens. It should be noted that the HFMI treatment is a local effect at the weld toe and the magnitude of residual stress distribution depends on the indent depth rather than the size or thickness of the component in general, therefore, for small-scale specimens, the FAT class for treated specimens is as expected based on the IIW recommendations.

5.5 Probabilistic SBFM analysis for studying scale effects on HFMI treatment benefit

There are four main differences that could be considered in the input parameters used for the analysis of large-scale structures in comparison to that used for the analysis of small-scale laboratory specimens, which are summarized below:

1. The mean value of peak residual stress for as-welded large-scale structures will typically be larger. A value on the order of $+0.5 \cdot \sigma_y$ would be more typical, in comparison with the $+0.05 \cdot \sigma_y$ assumed for as-welded small-scale specimens. The distribution of $\mathrm{Var}(\sigma_r)$ for large-scale as-welded specimens was assumed to be lognormal with COV of 0.2 rather than normal with COV of 1.25 for as-welded small-scale specimens. On the other hand, it is not expected that the residual stress because of HFMI treatment would be affected by the size of the structure being treated, so no change in the peak compressive stress due to treatment need to be considered.

2. The thickness of the component (i.e. the main plate of a cruciform joint) will vary widely in large-scale structural applications, and the design S-N curves for real structures often ignore this as a simplification. Thus, for applying the probabilistic model to large-scale structures, the thickness of the component was taken as a random variable with a uniform probability distribution and range from 5 mm to 50 mm. The IIW design guideline for HFMI treatment is applicable for the thickness range of 5 mm to 50 mm, therefore, the range of thickness was selected to be from 5 mm to 50 mm.

3. It is widely recognized that as plate thickness increases, the stress concentration factor (*SCF*) will also increase, since the local weld notch remains unchanged (i.e. does not scale up with plate thickness), thus resulting in a sharper or more severe local notch. To consider this possibility, finite element (FE) analyses were performed in ABAQUS to estimate this size effect on the stress concentration factor (*SCF*) for as-welded and impact treated cruciform joints. Cruciform joints with five main plate thicknesses (9.5, 16, 27, 45 and 60 mm) were modelled during linear elastic FE analysis. Attachment size and weld toe geometry were kept constant during the FE analysis. Variations in the SCF distribution with the thickness of the main plate for as-welded and impact treated specimens are shown in Figure 5.30 and

Figure 5.31 respectively. Since there is geometric and loading symmetry in the studied cruciform joints, therefore, the distribution is shown till the normalized depth (depth below weld toe / thickness of the component) of value 0.5. The SCF distribution for an intermediate thickness value was obtained by interpolating between the two SCF distributions closest to the desired thickness. The SCF distribution for a component with a thickness less than 9.5 mm was assumed to be the same as the SCF distribution for the 9.5 mm thick component.

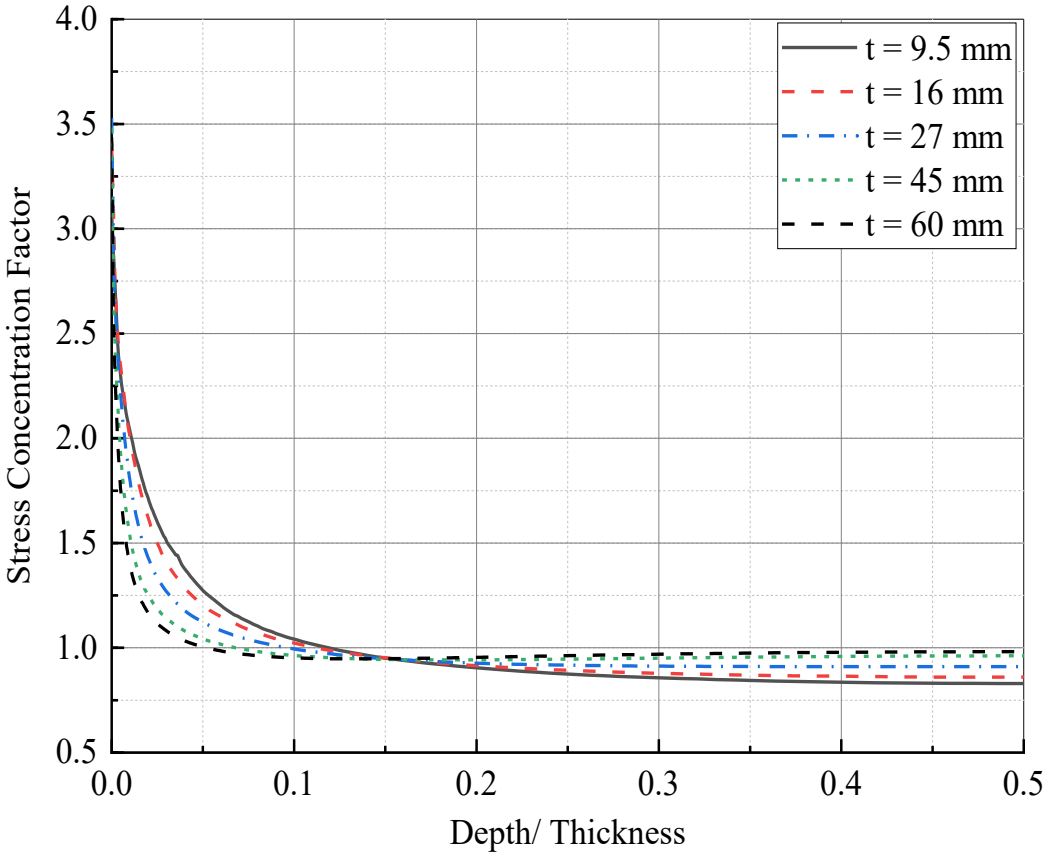

Figure 5.30: Variation of SCF with thickness for as-welded cruciform joints

4. Welded details in actual structures tend to be much wider than the 25.4 mm specimen width investigated experimentally in the current thesis. Thus, the possibility of a semi-elliptic surface crack turning into a through-width crack is considerably delayed in wide components. This can be considered in the current modelling framework by assuming a larger plate width – e.g. 254 mm, versus the 25.4 mm, assumed for the small-scale

specimens. A larger width for modelling large-scale structures was selected in the current study to simulate real-life components for bridge applications where the width of the component is large. For a component with a small width, when a semi-elliptical crack originates at the weld toe and propagates further along the surface, eventually the surface point of the crack reaches the free surface or width of the component. In this stage, a semi-elliptical crack becomes a through-width crack, which is simulated in the SBFM model with a small crack aspect ratio, *a/c*, of 0.2.

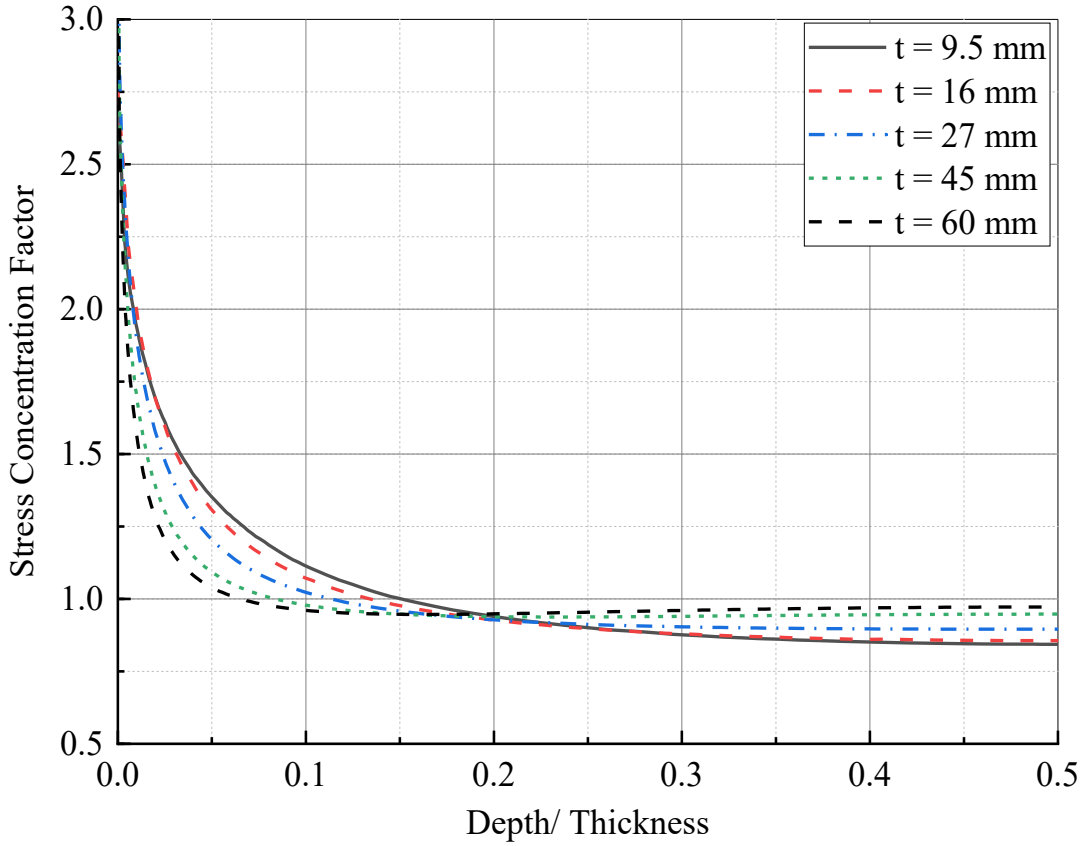

Figure 5.31: Variation of SCF with thickness for impact treated cruciform joints

With these changes, probabilistic SBFM analyses were performed for large-scale structures, to study the identified scale effects on the benefit of HFMI treatment. Figure 5.32 shows the resulting design S-N curves for as-welded cruciform joints in large structures under CA, VA1, and VA2 loading. In this figure, the SBFM-derived design S-N curves are compared with the FAT 63 and FAT 56 design curves. It can be observed that the SBFM-derived design curve under CA

loading is close to the FAT 63 design curve, which is two class lower than FAT 80 (the recommended FAT class for cruciform mild steel welded joints). The SBFM-derived design curves under VA1 and VA2 loading are close to FAT 56 curve, which is one class lower than FAT 63.

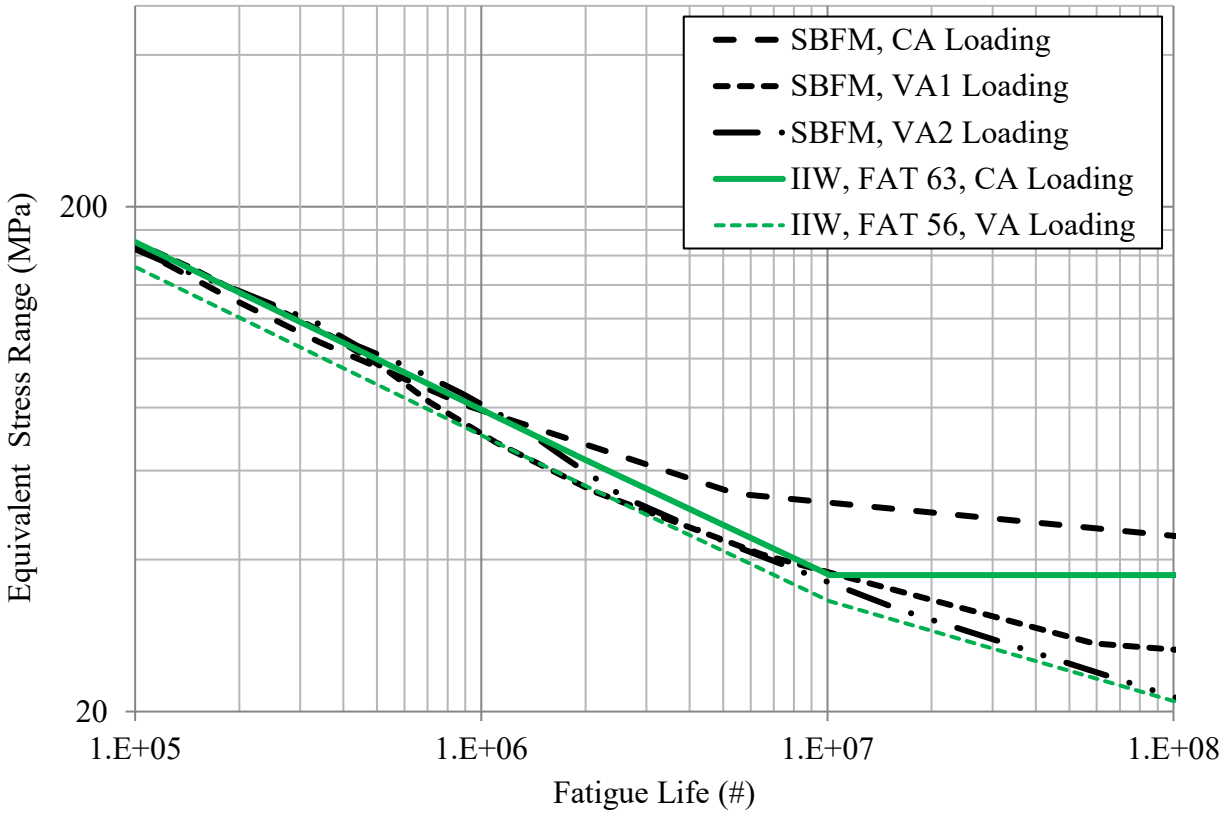

Figure 5.32: Comparison of SBFM-derived design S-N curves for large-scale as-welded joints with IIW design curves

Figure 5.33 shows the design S-N curves for treated cruciform welded joints in large structures under the same set of loading conditions. Here, the SBFM-derived design S-N curves are compared with the FAT 125 and FAT 140 IIW design curves. It can be observed that the SBFM-derived design S-N curve for the HFMI treated detail under CA loading is close to the FAT 140 curve, while the SBFM-derived design S-N curves under VA1 and VA2 loading are close to the FAT 125 curve. From this figure, it can be concluded that the FAT class for the large-scale treated joints is as per the IIW recommendation, which is 4-5 FAT classes higher than FAT 80. In other words, the FAT class for the large-scale as-received weld detail is 2-3 FAT class lower than

the suggested FAT class, but FAT class for large-scale treated joints is as per the recommendation of IIW.

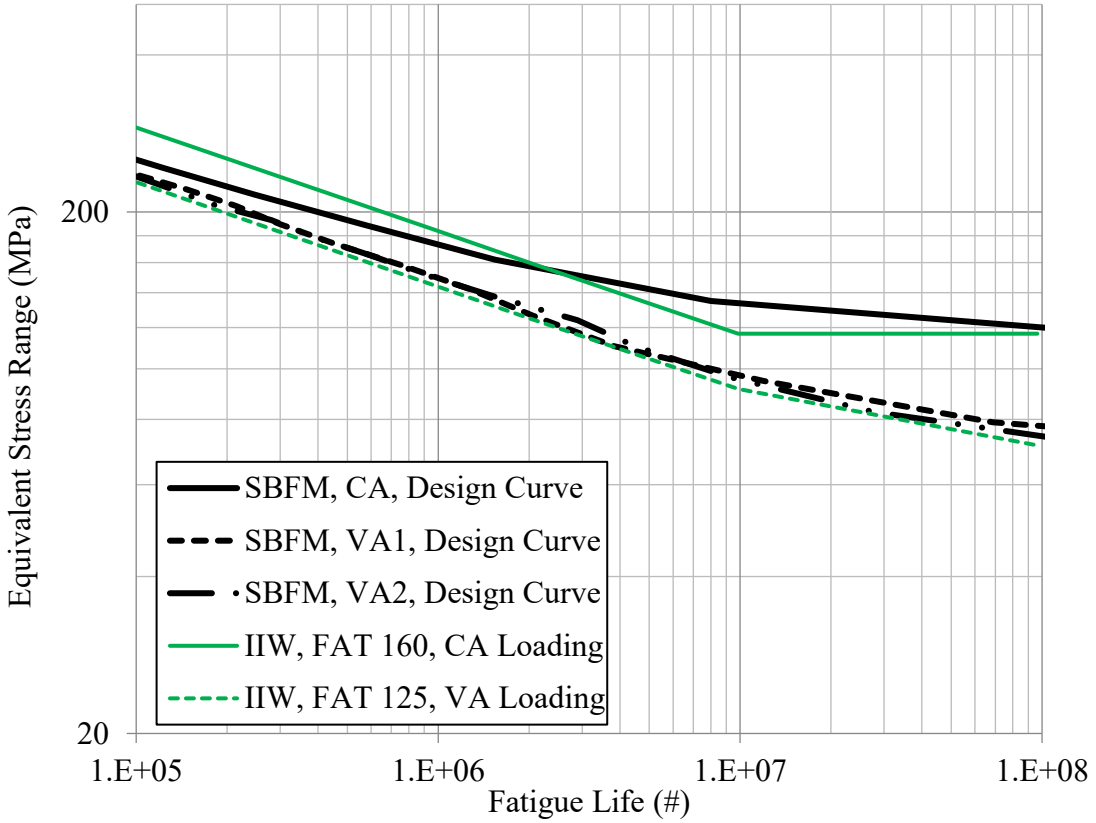

Figure 5.33: Comparison of SBFM-derived design S-N curves for large-scale treated joints with IIW design curves

5.6 Load ratio effect on fatigue strength improvement

In this section, fatigue strength improvement is quantified under CA loading at several load ratios, as well as under two VA loading histories. At first, design S-N curves for as-welded and impact treated joints under CA loading were obtained at different load ratios, as shown in Figure 5.34. For this analysis, the scale effects discussed in the previous section were considered, so the results are applicable to large-scale structures. It can be observed that the effect of load ratio on the design S-N curve for the treated joints is significantly more than for the as-welded joints. As the load ratio increases, the fatigue strength decreases significantly for the treated joints as compared to as-welded joints. This trend can be explained by the fact that the as-welded joints

have high tensile residual stresses at the surface, which means that the effective local strain ratio is already high, regardless of the load ratio associated with the externally applied cyclic load. For the treated joints, it should be noted that the analysis assumes that the treatment is applied before the externally applied load. In real structures such as bridges, the load ratio is often heavily influenced by permanent loads. It has been suggested by others (e.g. Walbridge, 2004) that the negative effect of load ratio can be largely negated if the treatment is applied after the permanent loads are introduced. However, this possibility is not explored in the presented load ratio study in the current thesis.

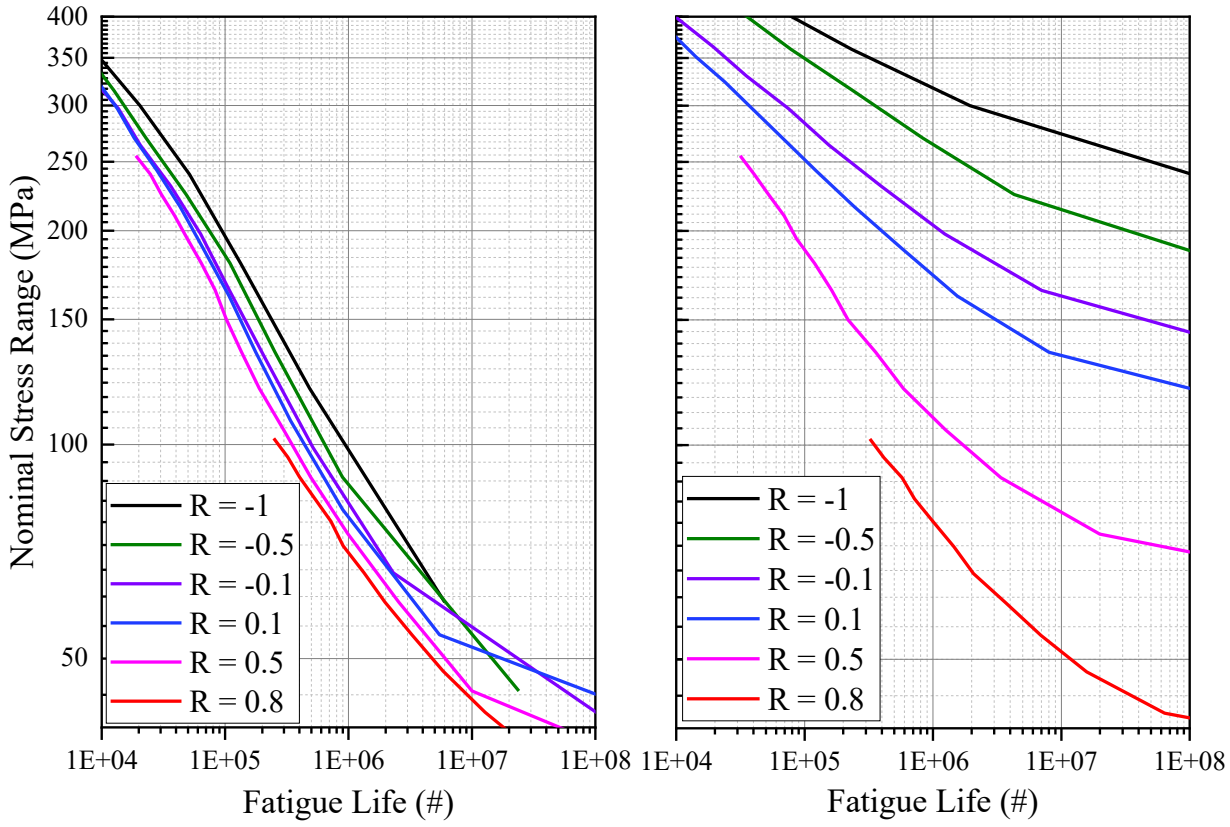

Figure 5.34: Load ratio effect on design S-N curve for as-welded (left) and impact treated (right) large-scale cruciform welded joints

To quantify the effect of load ratio on the treatment benefit, for a range of fatigue life, the change in the nominal stress range associated with the design S-N curve for as-welded and treated

joints was calculated to estimate the increase in fatigue strength due to HFMI treatment. The resulting percentage increase in fatigue strength under CA loading at different load ratios is shown in Figure 5.35. The range of the percentage increase in fatigue strength varies from ~0% to 400%. The higher the load ratio, the lower the percentage increase in fatigue strength. At a load ratio of 0.8, the percentage increase in fatigue strength varies from ~0% to 18% which is very low or almost negligible.

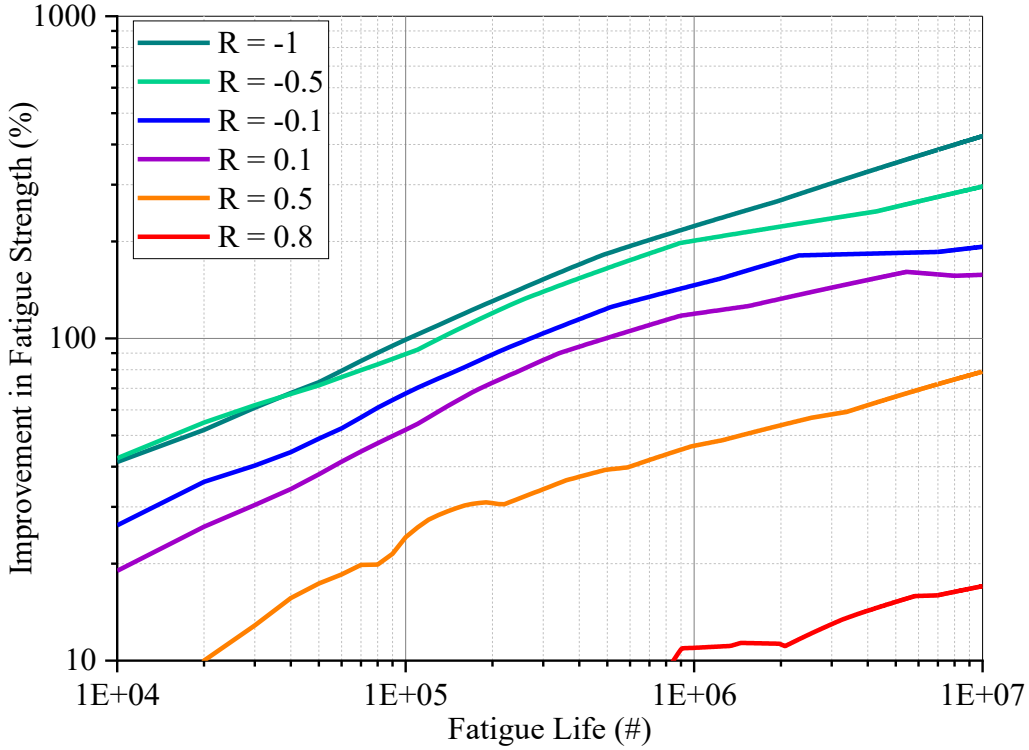

Figure 5.35: Load ratio effect on fatigue strength improvement

The IIW does not appear to explicitly consider an increase in the treatment benefit for negative R ratios, even though Figure 5.35 points to this possibility. Rather, the IIW suggests considering the treatment benefit to be the same for all load ratios, $R < 0.15$. According to the IIW (Marquis and Barsoum 2016), for a load ratio of 0.5, there should be a three FAT class reduction in fatigue strength of treated joints, however from Figure 5.34, it can be observed that FAT class for $R = 0.5$ and $R = 0.1$ is ~FAT 100 and ~FAT 160, which is a reduction of four FAT classes. The

percentage increase in the fatigue strength under CA loading (at $R = 0.1$), VA1 and VA2 loading is presented in Figure 5.36 for a range of possible fatigue lives.

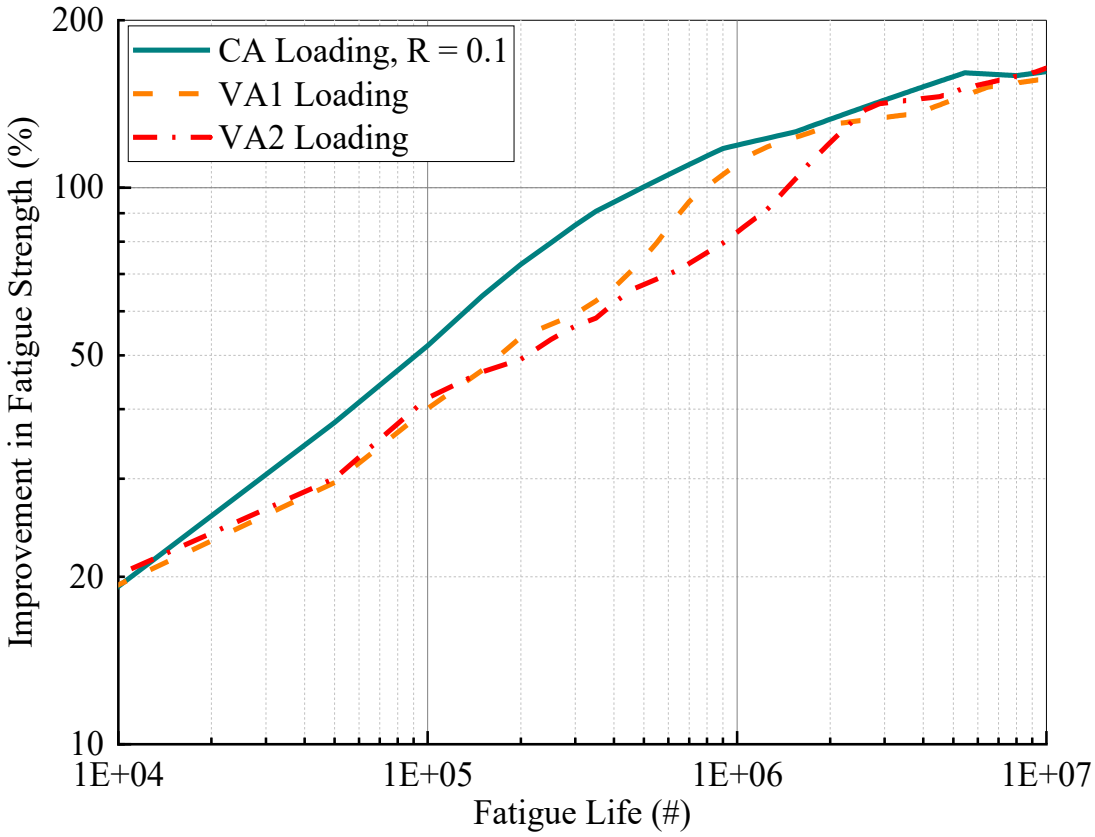

Figure 5.36: Load ratio and VA loading effect on fatigue strength improvement

It can be observed in Figure 5.36 that there is not much of a VA loading effect on fatigue strength improvement for the fatigue life of as-welded joints in between 10^4 and 10^7 cycles. The average and maximum load ratio for VA1 loading are 0.15 and 0.77 respectively. Based on the average load ratio of 0.15 for VA1 loading, the difference in percentage increase in fatigue strength under VA1 loading and CA loading ($R = 0.1$) is expected to be small. However, for the VA2 loading, the average and maximum load ratio are 0.59 and 0.94 respectively. Therefore, a larger reduction in fatigue strength is expected under VA2 loading. It is intriguing to observe that there is not a significant difference between the increase in fatigue strength under VA1 and VA2 loading. The possible reason behind this trend may be that a significant percentage (30-35%) of the VA2

loading history contains cycles with $R \approx 0.1$ as shown in Figure 2.7 of Chapter 2. It is also noteworthy that, upon closer inspection, it was found that the larger cycles in the VA1 and VA2 loading history tend to be the ones with the lower R ratios.

5.7 Summary and conclusions

In this chapter, a sensitivity study was carried out to observe the effects of variations in the SBFM input parameters on the resulting S-N curve for the tested specimens. A probabilistic SBFM model was then validated using the available fatigue test data. The validated model was then used to study scale effects. Finally, the improvement in fatigue strength because of HFMI treatment was assessed under CA loading at several load ratios and under several VA loading histories. The following conclusions are drawn based on the results presented in this chapter:

1. Some of the fatigue test data under CA and VA loading was found to be below the code-based design S-N curve for the as-welded specimens. The suggested FAT class for the cruciform welded joint made of 350W steel is FAT 80 according to the IIW. However, it was observed that while the fatigue performance of tested specimens is FAT 80 in the HCF regime under CA loading, only FAT 63 class fatigue performance is achieved under VA loading. The possible explanations for this result include: 1) possible issues with weld quality, 2) possible issues with specimen alignment during a fatigue test, and 3) possible issues with the narrow specimen width, which may have resulted in fatigue cracks prematurely growing into through-width cracks.

2. Based on the sensitivity analysis results for the as-welded and treated specimens, it was observed that variations in LN(C) and a_i had the greatest influence on the fatigue life for the as-welded specimens. Variations in LN(C) and the magnitude of the peak compressive residual stress had the greatest influence for the HFMI treated specimens.

3. The design fatigue strength of the as-welded laboratory-scale specimens estimated by the probabilistic SBFM model under CA, VA1, and VA2 loading was found to be equivalent to FAT 80, FAT 63, and FAT 63 respectively. The design fatigue strength of the treated laboratory-scale specimens under CA, VA1, and VA2 loading was found to be equivalent to FAT 140, FAT 125, and FAT 125 respectively. In other words, the fatigue strength

improvement due to HFMI treatment on the small-scale laboratory specimens was found to be 5 FAT classes under CA loading and 6 FAT classes under VA loading conditions.

4. When scale effects were considered, the fatigue strength of the cruciform detail in real structures (large-scale) under CA, VA1, and VA2 loading were found to be FAT 63, FAT 56, and FAT 56 respectively. The fatigue strength of HFMI treated large-scale welds under CA, VA1, and VA2 loading is equivalent to FAT 160, FAT 125 and FAT 125 respectively. In other words, the fatigue strength improvement due to HFMI treatment was found to be 7 FAT classes under all three loading conditions for cruciform weld joints in a real structure. The higher improvement for real structures is because of the higher residual stress expected in real, large-scale structures in the as-welded condition, which reduces the fatigue strength of as-welded joints and impact treatment becomes a more effective means to improve the fatigue strength in this situation.

5. The load ratio effect on fatigue strength improvement was found to be significant. It was observed that for $R > 0.8$, almost no fatigue strength improvement happens because of HFMI treatment. The effect of VA loading on the benefit of HFMI treatment was found to be relatively small for the two investigated VA loading histories.

Chapter 6

Summary, Conclusions, and Recommendations for Future Work

6.1 Summary and conclusions

The research summary and conclusions presented in this chapter are divided according to the four main projects carried out for this thesis including: (i) the study of the effects of angular misalignment on the fatigue performance of FSW joints under bending and tension load, (ii) the study of the effects of intentionally introduced welding defects on the fatigue performance of FSW joints, (iii) the fatigue testing and deterministic 2D SBFM analysis of HFMI treated weldments, and (iv) the probabilistic 2D SBFM analysis of HFMI treated weldments.

6.1.1 Effects of angular misalignment on the fatigue performance of FSW joints

In this project, new fatigue tests under cyclic four-point bending and tension loading were performed to investigate the fatigue behaviour of aluminum FSW butt joints with a significant angular misalignment. The test results were analyzed statistically using an approach recommended by the IIW. Also, the test results were estimated with a reasonable accuracy using an improved 1D SBFM model. An angular misalignment defect due to inadequate clamping during the welding process was seen to have a significant effect on the fatigue test results conducted under axial (tensile) loading. The significance of the angular misalignment defect, observed in the specimens fabricated for the current study, was assessed using a simple equation and strain gauges and was also confirmed by the fracture mechanics analysis results. The following conclusions are drawn based on fatigue testing and 1D deterministic SBFM analysis results:

- It was observed that even a slight misalignment of the order of 0.5° can create secondary stresses of ±38 MPa or more. Ignoring these secondary stresses can result in non-conservative estimates of fatigue life for properly welded specimens.
- It was observed that the favourable misalignment increased the fatigue strength of specimens tested under a tension loading from 71.0 MPa to 97.9 MPa.
- It was also observed that under a bending loading, the fatigue performance of the top side of the weld is better than that of the bottom side of the weld.

6.1.2 Effects of welding defects on the fatigue performance of FSW joints

In this project, the fatigue performance of FSW joints with intentionally introduced welding defects was studied experimentally as well as using the 1D SBFM model. Welding defects including toe flash, wormhole, and kissing bond defects were intentionally introduced in specimens, which were tested under cyclic axial loading to observe the effects of the defects on the fatigue performance. Defect geometry was measured based on microscopic images as well as from digital pictures of the fracture surface. The 1D SBFM model provided a reasonably accurate estimation of the fatigue test results when the observed defect geometry was used as input for the SBFM model. Based on the fatigue tests, metallurgical analysis, and nonlinear fracture mechanics (1D SBFM) analysis completed for this project, the following conclusions are drawn:

- The properly welded FSW butt joints were generally seen to achieve fatigue performance above the ADM Cat. B (similar arc welded joints) design curve.
- Kissing bond defects on the order of 0.3-1.0 mm in depth, in the 6061-T651 alloy specimens, generally resulted in a significant fatigue life reduction and a shift in the failure mode from crack initiation on the weld top to the weld root.
- The investigated toe-flash defect had a less significant effect on the fatigue performance of the FSW butt joint compared to the tested kissing bond defects.
- The tested lap joint detail resulted in a lower fatigue performance than that of the butt joint detail, which can be safely estimated using ADM Cat. D design curve.
- It is shown that the fatigue test results can be predicted reasonably well, using a nonlinear fracture mechanics (SBFM) model with typically assumed input parameters for 5xxx and 6xxx series aluminum alloys and knowledge of the initial defect geometry.

6.1.3 Testing and deterministic 2D SBFM analysis of HFMI treated weldments

In this project, new fatigue tests were conducted on as-welded and HFMI treated A514 steel and 5083 aluminum cruciform welded joints. Several SBFM model input parameters were estimated based on a comprehensive materials test program, finite element analysis, and direct measurements. The effectiveness of the SBFM model in estimating the fatigue test results for three

materials, including the two tested materials and CSA 350W steel, was assessed. In general, the model was seen to yield excellent estimations of the test results for the three materials subjected to several CA and VA loading histories. The fact that this model provides good estimations for several investigated loading histories and three materials suggests that it has strong potential to serve as a useful tool for investigating loading history effects on treatment effectiveness and for studies to observe the effects of variations in other model parameters on the fatigue life. Based on the fatigue tests and SBFM analysis results for this project, the following conclusions are drawn:

- HFMI results in a reliable fatigue life increase in steel (CSA 350 and ASTM A514) specimens, under constant (CA) as well as variable amplitude (VA) loading conditions.
- In general, the fatigue life increase due to HFMI treatment was seen to increase with an increase in material strength. The actual increase depends on the applied loading history and magnitude of compressive residual stress due to HFMI treatment near the weld toe.
- A statistical analysis of the test results confirms that the fatigue life increase can be seen when comparisons are made over a range of survival probabilities (i.e. 50% or 95%).
- A nonlinear fracture mechanics analysis, wherein the material monotonic and cyclic strength properties are considered, is capable of estimating the fatigue performance of the HFMI treated welds for a broad range of material properties and loading conditions.

6.1.4 Probabilistic 2D SBFM analysis of HFMI treated weldments

In this project, an overview of the design guidelines available in various design codes for the fatigue assessment of fusion-welded joints was first presented. A sensitivity analysis was performed to identify the important parameters affecting the fatigue strength of as-welded and HFMI treated joints. Probability distributions for various SBFM model input parameters were then defined based on statistical data available in the existing literature and on observed variation in material properties. Probabilistic 2D SBFM analyses were then performed to obtain the median and the design S-N curves for the small-scale laboratory specimens. The design S-N curves obtained from the probabilistic analysis were compared with the fatigue test data to provide a validation of the probabilistic 2D SBFM model. The validated 2D SBFM model was then used to investigate scale and loading history effects on the benefit of HFMI treatment.

The presented probabilistic analysis demonstrates how the 2D SBFM model can serve as a useful analytical tool for developing reliability-based design curves for the HFMI treatment technology, which are applicable to a broad range of materials (e.g. various grades of steel and aluminum), scales, and loading conditions, beyond what can be practically investigated in a purely experimental program. The following conclusions are drawn based on this research:

- Some of the fatigue test data under CA as well as VA loading was found to be below the code-based design S-N curve for as-welded specimens. The suggested FAT class for the cruciform welded joint made of 350W steel is FAT 80 according to IIW. However, it was observed that the fatigue performance of tested specimens is equivalent to FAT 80 (in the HCF regime only) under CA loading but FAT 63 under VA loading histories. The possible explanations for this result include: 1) possible issues with weld quality, 2) possible issues with specimen alignment during a fatigue test, and 3) possible issues with the narrow specimen width, which may have resulted in fatigue cracks prematurely growing into through-width cracks.
- Based on the sensitivity analysis results for the as-welded and treated specimens, it was observed that variations in LN(C) and a_i had the greatest influence on fatigue life for the as-welded specimens. Variations in LN(C) and the magnitude of the peak compressive residual stress had the greatest influence for the HFMI treated specimens.
- The design fatigue strength of the as-welded laboratory specimens estimated by the probabilistic SBFM model under CA, VA1, and VA2 loading was found to be equivalent to FAT 80, FAT 63, and FAT 63 respectively. The design fatigue strength of the treated specimens under CA, VA1, and VA2 loading was found to be equivalent to FAT 140, FAT 125, and FAT 125 respectively. In other words, the fatigue strength improvement due to HFMI treatment on the small-scale laboratory specimens was found to be five FAT classes under CA loading and six FAT classes under VA loading conditions.
- When scale effects were considered, the fatigue strength of the cruciform detail in real structures (large-scale) under CA, VA1, and VA2 loading were found to be FAT 63, FAT 56, and FAT 56 respectively. The fatigue strength of HFMI treated welds in real structures

under CA, VA1, and VA2 loading is equivalent to FAT 160, FAT 125 and FAT 125 respectively. In other words, the fatigue strength improvement due to HFMI treatment was found to be seven FAT classes under all three loading conditions. The higher improvement for real structures is because of the higher residual stress expected in real, large-scale structures in the as-welded condition.

- The load ratio effect on fatigue strength improvement was found to be significant. It was observed that for $R > 0.8$, almost no fatigue strength improvement happens because of HFMI treatment. The effect of VA loading on the benefit of HFMI treatment was found to be relatively small for the two investigated VA loading histories.

6.2 Recommendations for future work

The following subsections outline a number of recommendations for future work, which would complement the research presented in this thesis. The recommendations are again categorized based on four main projects carried out for this thesis.

6.2.1 Effects of angular misalignment on the fatigue performance of FSW joints

- Further research is recommended to investigate other kinds of joint misalignment (e.g. linear misalignment or "offset") that can result from the FSW process and relate the misalignment defect magnitude to fatigue performance.

6.2.2 Effects of welding defects on the fatigue performance of FSW joints

- Further work is recommended to quantify the effects of uncertainties related to defect geometry and material properties on the fatigue performance of FSW joints through a probabilistic SBFM analysis, similar to what was done in the current thesis for HFMI treated weldments.
- The combinations of two or more defect types can also be studied experimentally, as well as using a fracture mechanics model, such as the SBFM model employed herein, to identify worst-case scenarios from a fatigue perspective.

- Further efforts could be made to conduct an experimental program including specimens fabricated with continuous/consistent wormhole defects to study the effect of wormhole defects on fatigue performance of FSW joints more comprehensively.

6.2.3 Testing and deterministic 2D SBFM analysis of HFMI treated weldments

- The 2D SBFM model employed in this project can be improved to model subsurface defects, and to simulate bullet shape cracks, which initiates from the untreated edge of the component, and to simulate through-width cracks more precisely.
- It is recommended that further research should be conducted to extend these fracture mechanics analysis to a broader range of more complex variable amplitude loading histories, with a focus on the high cycle fatigue domain.
- A more comprehensive study of the effectiveness of HFMI treatment on aluminum welds is also recommended, with a focus on varying the indent depth to study the effect of this parameter on fatigue performance and the testing of larger-scale aluminum components.
- Emerging ultrasonic non-destructive evaluation techniques such as high-frequency stress wave propagation can be used to observe the defect geometry in the components similar to the tested specimen, which would increase the accuracy of the fracture mechanics analysis results.

6.2.4 Probabilistic 2D SBFM analysis of HFMI treated weldments

- Probabilistic 2D SBFM analysis can be performed to quantify the benefit of HFMI treatment on materials other than 350W steel, such as A514 steel and 5083 aluminum.
- Probabilistic 2D SBFM analysis can be performed to assess VA loading effects on the benefit of HFMI treatment with a wider range of VA loading histories.
- A more comprehensive collection of data on residual stress and other SBFM input parameters, such as C, ΔK_{th}, K', a_i and $(a/c)_{initial}$, will provide necessary data to model uncertainty in these parameters during probabilistic fracture mechanics analysis.

Bibliography

Albrecht, Pedro, Yamada, Kentaro. 1977. “Rapid Calculation of Stress Intensity Factors.” *Journal of the Structural Division, ASCE* 103(ST2):377–89.

American Institute of Steel Construction. 2016. *Code of Standard Practice for Steel Buildings and Bridges*. American Institute of Steel Construction.

Anderson, Ted L. and Grzegorz Glinka. 2006. “A Closed-Form Method for Integrating Weight Functions for Part-through Cracks Subject to Mode I Loading.” *Engineering Fracture Mechanics*.

Anon. 2006. *Canadian Institute of Steel Construction (CISC), Handbook of Steel Construction: 9th Ed., Toronto*.

Anon. 2010. *Aluminum Association. ADM-10: Aluminum Design Manual – Specifications and Guidelines for Aluminum Structures*.

ASTM B209M. 2014. “ASTM B209M-14 Standard Specification for Aluminum and Aluminum-Alloy Sheet and Plate (Metric).” *ASTM International*.

ASTM B918/B918M-17a. 2017. *Standard Practice for Heat Treatment of Wrought Aluminium Alloys*.

ASTM E1097 - 12. 2017. *Standard Guide for Determination of Various Elements by Direct Current Plasma Atomic Emission Spectrometry*. American Society for Testing and Materials.

ASTM E1479 – 99. 2011. *Standard Practice for Describing and Specifying Inductively-Coupled Plasma Atomic Emission Spectrometers*. American Society for Testing and Materials.

ASTM E647-13. 2013. “Standard Test Method for Measurement of Fatigue Crack Growth Rates.” *American Society for Testing and Materials (ASTM)*.

ASTM E647, ASTM Standard. 2016. “ASTM E647 - Standard Test Method for Measurement of Fatigue Crack Growth Rates.” *ASTM Book of Standards*.

ASTM E8. 2010. *E8/E8M Standard Test Methods for Tension Testing of Metallic Materials*.

AWS-D17.3/D17.3M:200X. 2010. "Specification for Friction Stir Welding of Aluminum Alloys for Aerospace Applications." *American Welding Society*.

AWS D1.2/D1.2M. 2014. *AWS D1.2/D1.2M:2014 Structural Welding Code--Aluminum*.

Aydin, Hakan, Ali Bayram, M. Tahir Yildirim, and Kurtuluş Yiğit. 2010. "Influence of Welding Parameters on the Fatigue Behaviours of Friction Stir Welds of 3003-O Aluminum Alloys." *Medziagotyra*.

Barsom, J. M., & Novak, S. R. 1977. *Subcritical Crack Growth and Fracture of Bridge Steels*.

Brückner, A. and D. Munz. 1983. "Curve Fitting to Defect Size Distributions for the Calculation of Failure Probabilities." *Nuclear Engineering and Design*.

BS-7910. 2005. "Guide to Methods for Assessing the Acceptability of Flaws in Metallic Structures." *BSI Standards Publication*.

CAN/CSA W59.2. 2018. *Welded Aluminum Construction*. Canadian Standards Association.

Canadian Standards Association. 2014. *Canadian Highway Bridge Design Code*.

Cavaliere, P., G. Campanile, F. Panella, and A. Squillace. 2006. "Effect of Welding Parameters on Mechanical and Microstructural Properties of AA6056 Joints Produced by Friction Stir Welding." *Journal of Materials Processing Technology*.

Cavaliere, P., A. De Santis, F. Panella, and A. Squillace. 2009. "Effect of Welding Parameters on Mechanical and Microstructural Properties of Dissimilar AA6082-AA2024 Joints Produced by Friction Stir Welding." *Materials and Design*.

Cavaliere, P., A. Squillace, and F. Panella. 2008. "Effect of Welding Parameters on Mechanical and Microstructural Properties of AA6082 Joints Produced by Friction Stir Welding." *Journal of Materials Processing Technology*.

Conle, A., Oxland, T.R., and Topper, T. H. 1988. "Computer-Based Prediction of Cyclic Deformation and Fatigue Behavior." *American Society for Testing and Materials (ASTM)* Low Cycle(ASTM STO 942):1218–36.

Coughlin, R. and S. Walbridge. 2012. “Fatigue Testing and Analysis of Aluminum Welds under In-Service Highway Bridge Loading Conditions.” *Journal of Bridge Engineering*.

Dalle Donne, C., G. Biallas, T. Ghidini, and G. Raimbeaux. 2000. “Effect of Weld Imperfections and Residual Stresses on the Fatigue Crack Propagation in Friction Stir Welded Joints.” *2nd International Conference on Friction Stir Welding*.

Das, Hrishikesh, Debayan Chakraborty, and Tapan Kumar Pal. 2014. “High-Cycle Fatigue Behavior of Friction Stir Butt Welded 6061 Aluminium Alloy.” *Transactions of Nonferrous Metals Society of China (English Edition)*.

Development, Draft F. O. R. 2000. “Eurocode 9 : Design of Aluminium Structures Ð Part 2 : Structures Susceptible to Fatigue.” *Update*.

Dialami, N., M. Chiumenti, M. Cervera, and C. Agelet de Saracibar. 2017. “Challenges in Thermo-Mechanical Analysis of Friction Stir Welding Processes.” *Archives of Computational Methods in Engineering*.

Dickerson, T. L. and J. Przydatek. 2003. “Fatigue of Friction Stir Welds in Aluminium Alloys That Contain Root Flaws.” *International Journal of Fatigue*.

Dugdale, D. S. 1960. “Yielding of Steel Sheets Containing Slits.” *Journal of the Mechanics and Physics of Solids*.

El-Zeghayar, Maria. 2010. “The Introduction of Crack Opening Stress Modeling into Strain-Life And Small Crack Growth Fatigue Analysis.” University of Waterloo, Ontario, Canada.

Elber, W. 2009. “The Significance of Fatigue Crack Closure.” in *Damage Tolerance in Aircraft Structures*.

Ericsson, Mats, Lai Z. Jin, and Rolf Sandström. 2007. “Fatigue Properties of Friction Stir Overlap Welds.” *International Journal of Fatigue*.

Fowler, Steven, Athanasios Toumpis, and Alexander Galloway. 2016. “Fatigue and Bending Behaviour of Friction Stir Welded DH36 Steel.” *International Journal of Advanced Manufacturing Technology*.

G. Josi. 2010. “Reliability-Based Management of Fatigue Failures.” University of Alberta.

Gerster, P., F. Schäfers, and M. Leitner. 2013. “Pneumatic Impact Treatment (PIT) - Application and Quality Assurance.” *International Institute of Welding*.

Ghahremani, Kasra. 2010. “Predicting the Effectiveness of Post-Weld Treatments Applied under Load.” University of Waterloo.

Ghahremani, Kasra. 2015. “Fatigue Assessment of Repaired Highway Bridge Welds Using Local Approaches.” University of Waterloo.

Ghahremani, Kasra, Mahdi Safa, Jamie Yeung, Scott Walbridge, Carl Haas, and Sebastien Dubois. 2015. “Quality Assurance for High-Frequency Mechanical Impact (HFMI) Treatment of Welds Using Handheld 3D Laser Scanning Technology.” *Welding in the World*.

Ghahremani, Kasra and Scott Walbridge. 2011. “Fatigue Testing and Analysis of Peened Highway Bridge Welds under In-Service Variable Amplitude Loading Conditions.” *International Journal of Fatigue*.

Ghahremani, Kasra, Scott Walbridge, and Tim Topper. 2015. “High Cycle Fatigue Behaviour of Impact Treated Welds under Variable Amplitude Loading Conditions.” *International Journal of Fatigue*.

Glinka, G. and G. Shen. 1991. “Universal Features of Weight Functions for Cracks in Mode I.” *Engineering Fracture Mechanics*.

Grujicic, M., G. Arakere, B. Panduragan, A. Hariharan, C. F. Yen, B. A. Cheeseman, and C. Fountzoulas. 2011. “Statistical Analysis of High-Cycle Fatigue Behavior of Friction Stir Welded AA5083-H321.” *Journal of Materials Engineering and Performance*.

Guo, S., L. Shah, R. Ranjan, S. Walbridge, and A. Gerlich. 2019. “Effect of Quality Control Parameter Variations on the Fatigue Performance of Aluminum Friction Stir Welded Joints.” *International Journal of Fatigue* 118.

Guo, Shi. 2018. “Fatigue Behaviour of Aluminum Friction Stir Welds Under Highway Bridge

Loading Conditions." University of Waterloo.

Haagensen, P. J. and S. J. Maddox. 2013. *IIW Recommendations on Methods for Improving the Fatigue Strength of Welded Joints*.

El Haddad, M. H., T. H. Topper, and K. N. Smith. 1979. "Prediction of Non Propagating Cracks." *Engineering Fracture Mechanics*.

El Haddad, M. H., T. H. Topper, and T. N. Topper. 1981. "Fatigue Life Predictions of Smooth and Notched Specimens Based on Fracture Mechanics." *Journal of Engineering Materials and Technology*.

HAGISAWA, Nobuyasu and Ichiro OKURA. 2009. "Influence of Stress Ratios on Fatigue Strength of A6005C-T5 Aluminum Alloy and Friction Stir Welded Joints." *Doboku Gakkai Ronbunshuu A*.

He, Xiaocong, Fengshou Gu, and Andrew Ball. 2014. "A Review of Numerical Analysis of Friction Stir Welding." *Progress in Materials Science*.

Hobbacher, A. 2011. *Fatigue Design of Welded Joints and Components*.

Hobbacher, A. F. 2009. "The New IIW Recommendations for Fatigue Assessment of Welded Joints and Components - A Comprehensive Code Recently Updated." *International Journal of Fatigue*.

ISO 25239. 2011. *Friction Stir Welding- Aluminum*.

JCSS. 2011. *JCSS Probabilistic Model Code Part 3: Resistance Models*.

Kadlec, Martin, Roman Růžek, and Lucie Nováková. 2015. "Mechanical Behaviour of AA 7475 Friction Stir Welds with the Kissing Bond Defect." *International Journal of Fatigue*.

Kainuma, Shigenobu, Hiroto Katsuki, Ichiro Iwai, and Masaki Kumagai. 2008. "Evaluation of Fatigue Strength of Friction Stir Butt-Welded Aluminum Alloy Joints Inclined to Applied Cyclic Stress." *International Journal of Fatigue*.

Khalil, M. and T. H. Topper. 2003. "Prediction of Crack-Opening Stress Levels for 1045 as-Received Steel under Service Loading Spectra." *International Journal of Fatigue*.

Kobayashi, Y., M. Sakuma, Y. Tanaka, and K. Matsuoka. 2007. “Fatigue Strength of Friction Stir Welding Joints of Aluminium Alloy 6082 Extruded Shape.” *Welding International*.

Kuhlmann, U., A. Dürr, and H. Günther. 2017. “Application of Post-Weld Treatment Methods to Improve the Fatigue Strength of High Strength Steels in Bridges.”

Kuhlmann, Ulrike, Joachim Bergmann, André Dürr, Rayk Thumser, Hans Peter Günther, and Uwe Gerth. 2005. “Erhöhung Der Ermüdungsfestigkeit von Geschweißten Höherfesten Baustählen Durch Anwendung von Nachbehandlungsverfahren.” *Stahlbau*.

Lam, T. S., T. H. Topper, and F. A. Conle. 1998. “Derivation of Crack Closure and Crack Growth Rate Data from Effective-Strain Fatigue Life Data for Fracture Mechanics Fatigue Life Predictions.” *International Journal of Fatigue*.

Leitner, M., W. Mössler, A. Putz, and M. Stoschka. 2015. “Effect of Post-Weld Heat Treatment on the Fatigue Strength of HFMI-Treated Mild Steel Joints.” *Welding in the World*.

Lohwasser, D. and Z. Chen. 2009. *Friction Stir Welding: From Basics to Applications*.

Lomolino, S., R. Tovo, and J. Dos Santos. 2005. “On the Fatigue Behaviour and Design Curves of Friction Stir Butt-Welded Al Alloys.” *International Journal of Fatigue*.

Lotsberg, Inge, Gudfinnur Sigurdsson, and Per Terje Wold. 2002. “Probabilistic Inspection Planning of the Åsgard A FPSO Hull Structure With Respect to Fatigue.” *Journal of Offshore Mechanics and Arctic Engineering*.

Maddox, S. J. 1975. “An Analysis of Fatigue Cracks in Fillet Welded Joints.” *International Journal of Fracture*.

Mahdavi Shahri, Meysam, Torsten Höglund, and Rolf Sandström. 2012. “Eurocode 9 to Estimate the Fatigue Life of Friction Stir Welded Aluminium Panels.” *Engineering Structures*.

Marquis, Gary B. and Zuheir Barsoum. 2016. “IIW Recommendations on High Frequency Mechanical Impact (HFMI) Treatment for Improving the Fatigue Strength of Welded Joints.”

Marquis, Gary B., Eeva Mikkola, Halid Can Yildirim, and Zuheir Barsoum. 2013. “Fatigue

Strength Improvement of Steel Structures by High-Frequency Mechanical Impact: Proposed Fatigue Assessment Guidelines." *Welding in the World*.

McClung, R. C. 1994. "Finite Element Analysis of Specimen Geometry Effects on Fatigue Crack Closure." *Fatigue & Fracture of Engineering Materials & Structures*.

Miranda, Antonio Carlos de Oliveira, Adrian Gerlich, and Scott Walbridge. 2015. "Aluminum Friction Stir Welds: Review of Fatigue Parameter Data and Probabilistic Fracture Mechanics Analysis." *Engineering Fracture Mechanics*.

Moreira, P. M. G. P., M. A. V de Figueiredo, and P. M. S. T. de Castro. 2007. "Fatigue Behaviour of FSW and MIG Weldments for Two Aluminium Alloys." *Theoretical and Applied Fracture Mechanics*.

Newman, J. C. 1984. "A Crack Opening Stress Equation for Fatigue Crack Growth." *International Journal of Fracture*.

Newman, JC. 2009. "A Finite-Element Analysis of Fatigue Crack Closure." in *Mechanics of Crack Growth*.

Okura, Ichiro, Nobuyasu Hagisawa, Makoto Naruo, and Hitoshi Toda. 2005. "Fatigue Behaviour of Aluminum Deck Fabricated by Friction Stir Welding." *Structural Engineering / Earthquake Engineering*.

Parry, M., Nordberg, H., & Hertzberg, R. W. 1972. "Fatigue Crack Propagation in A514 Base Plate and Welded Joints." *Welding Journal Research Supplement, 51(10)* 485s-490s.

Pedersen, M. M., O. Mouritsen, M. R. Hansen, J. G. Andersen, and J. Wenderby. 2010. "Comparison of Post-Weld Treatment of High-Strength Steel Welded Joints in Medium Cycle Fatigue." *Welding in the World*.

Raimbault, Jeremie. 2016. "Modelling Fatigue Deterioration and Retrofitting in Bridge Management Systems." University of Waterloo, Ontario, Canada.

Ranjan, R., K. Ghahremani, S. Walbridge, and A. Ince. 2016. "Testing and Fracture Mechanics Analysis of Strength Effects on the Fatigue Behavior of HFMI-Treated Welds." *Welding in*

the World.

Righiniotis, T. D. and M. K. Chryssanthopoulos. 2003. “Probabilistic Fatigue Analysis under Constant Amplitude Loading.” *Journal of Constructional Steel Research*.

Roy, Sougata, John W. Fisher, and Ben T. Yen. 2003. “Fatigue Resistance of Welded Details Enhanced by Ultrasonic Impact Treatment (UIT).” in *International Journal of Fatigue*.

Shetty, N.K.;Baker, M. J. 1990. “Fatigue Reliability of Tubular Joints in Offshore Structures-Reliability Analysis.” *Proceedings of the 9th International Conference on Offshore Mechanics and Arctic Engineering-OMAE* 2:33–40.

SINTEC, Structural Integrity Technologies Inc. 2019. “HFMI.” Retrieved September 20, 2005 (http://www.sintec.ca/).

Smallbone, C. 2008. “Improving the Global Quality of Life through Optimum Use of Welding Technology.” *Welding in the World*.

Sonsino, CM. 2008. “Principles of Variable Amplitude Fatigue Design and Testing.” in *Fatigue Testing and Analysis Under Variable Amplitude Loading Conditions*.

Suzuki, Tamaki, Teppei Okawa, Hiroshi Shimanuki, Tetsuro Nose, Noriaki Ohta, Hiroshi Suzuki, and Atsushi Moriai. 2014. “Effect of Ultrasonic Impact Treatment (UIT) on Fatigue Strength of Welded Joints.” *Advanced Materials Research*.

Svensson, L.-E., Karlsson, L., Larsson, H., Fazzini, M., & Karlsson, J. 2000. “Microstructure and Mechanical Properties of Friction Stir Welded Aluminum Alloys with Special Reference to AA5083 and AA6082.” *Science and Technology of Welding and Joining* 285–96.

Tehrani Yekta, Rana, Kasra Ghahremani, and Scott Walbridge. 2013. “Effect of Quality Control Parameter Variations on the Fatigue Performance of Ultrasonic Impact Treated Welds.” *International Journal of Fatigue*.

The Aluminum Association. 2015. “Aluminum Design Manual Part I: Spedification for Aluminum Structures.”

Thomas, W. M. 1991. “Friction Stir Butt Welding.”

Tobler, R. L. and R. P. Reed. 2010. “Fracture Mechanics Parameters for a 5083-0 Aluminum Alloy at Low Temperatures.” *Journal of Engineering Materials and Technology*.

U. Kuhlmann, J. Bergmann, A. Dürr, R. Thumser, H.-P. Günther, U. Gerth. 2005. “Enhancement of the Fatigue Strength of Welded High Strength Steels by Application of Post-Weld Treatment Methods.” *Stahlbau, 74* 358–65.

Uzun, Huseyin, Claudio Dalle Donne, Alberto Argagnotto, Tommaso Ghidini, and Carla Gambaro. 2005. “Friction Stir Welding of Dissimilar Al 6013-T4 To X5CrNi18-10 Stainless Steel.” *Materials and Design*.

V.-M. Lihavainen. 2006. “A Novel Approach for Assessing the Fatigue Strength of Ultrasonic Impact Treated Welded Structures.” Lappeenranta University of Technology.

Vidal, Catarina, Virgínia Infante, and Pedro Vilaça. 2014. “Fatigue Behaviour at Elevated Temperature of Friction Stir Channelling Solid Plates of AA5083-H111 Aluminium Alloy.” *International Journal of Fatigue*.

Vigh, László Gergely and Ichiro Okura. 2013. “Fatigue Behaviour of Friction Stir Welded Aluminium Bridge Deck Segment.” *Materials and Design*.

Vormwald, M. and T. Seeger. 1991. “The Consequences of Short Crack Closure on Fatigue Crack Growth Under Variable Amplitude Lading.” *Fatigue & Fracture of Engineering Materials & Structures*.

Walbridge, Scott. 2008. “Fatigue Analysis of Post-Weld Fatigue Improvement Treatments Using a Strain-Based Fracture Mechanics Model.” *Engineering Fracture Mechanics*.

Walbridge, Scott, Dilum Fernando, and Bryan T. Adey. 2012. “Probabilistic Models to Evaluate Effectiveness of Steel Bridge Weld Fatigue Retrofitting by Peening.” *Transportation Research Record: Journal of the Transportation Research Board*.

Wang, C. H., L. R. F. Rose, and J. C. Newman. 2002. “Closure of Plane-Strain Cracks under Large-Scale Yielding Conditions.” *Fatigue and Fracture of Engineering Materials and*

Structures.

Weich, Imke, Thomas Ummenhofer, Thomas Nitschke-Pagel, Hamdollah Eslami Chalandar, and Klaus Dilger. 2009. “Fatigue Behaviour of Welded High-Strength Steels after High Frequency Mechanical Post-Weld Treatments.” *Welding in the World*.

Yildirim, Halid Can and Gary B. Marquis. 2013. “A Round Robin Study of High-Frequency Mechanical Impact (HFMI)-Treated Welded Joints Subjected to Variable Amplitude Loading.” *Welding in the World*.

Yıldırım, H. C., G. Marquis, and C. M. Sonsino. 2016. “Lightweight Design with Welded High-Frequency Mechanical Impact (HFMI) Treated High-Strength Steel Joints from S700 under Constant and Variable Amplitude Loadings.” *International Journal of Fatigue*.

Yuan, K. L. and Y. Sumi. 2015. “Modelling of Ultrasonic Impact Treatment (UIT) of Welded Joints and Its Effect on Fatigue Strength.” *Frattura Ed Integrita Strutturale*.

Zheng, X. J., G. Glinka, and R. N. Dubey. 1996. “Stress Intensity Factors and Weight Functions for a Corner Crack in a Finite Thickness Plate.” *Engineering Fracture Mechanics*.

Zhou, Caizhi, Xinqi Yang, and Guohong Luan. 2005. “Fatigue Properties of Friction Stir Welds in Al 5083 Alloy.” *Scripta Materialia*.

Zhou, Caizhi, Xinqi Yang, and Guohong Luan. 2006a. “Effect of Kissing Bond on Fatigue Behavior of Friction Stir Welds on Al 5083 Alloy.” *Journal of Materials Science*.

Zhou, Caizhi, Xinqi Yang, and Guohong Luan. 2006b. “Investigation of Microstructures and Fatigue Properties of Friction Stir Welded Al-Mg Alloy.” *Materials Chemistry and Physics*.

Albrecht, Pedro, Yamada, Kentaro. 1977. “Rapid Calculation of Stress Intensity Factors.” *Journal of the Structural Division, ASCE* 103(ST2):377–89.

American Institute of Steel Construction. 2016. *Code of Standard Practice for Steel Buildings and Bridges*. American Institute of Steel Construction.

Anderson, Ted L. and Grzegorz Glinka. 2006. “A Closed-Form Method for Integrating Weight

Functions for Part-through Cracks Subject to Mode I Loading." *Engineering Fracture Mechanics*.

Anon. 2006. *Canadian Institute of Steel Construction (CISC), Handbook of Steel Construction: 9th Ed., Toronto*.

Anon. 2010. *Aluminum Association. ADM-10: Aluminum Design Manual – Specifications and Guidelines for Aluminum Structures*.

ASTM B209M. 2014. "ASTM B209M-14 Standard Specification for Aluminum and Aluminum-Alloy Sheet and Plate (Metric)." *ASTM International*.

ASTM B918/B918M-17a. 2017. *Standard Practice for Heat Treatment of Wrought Aluminium Alloys*.

ASTM E1097 - 12. 2017. *Standard Guide for Determination of Various Elements by Direct Current Plasma Atomic Emission Spectrometry*. American Society for Testing and Materials.

ASTM E1479 – 99. 2011. *Standard Practice for Describing and Specifying Inductively-Coupled Plasma Atomic Emission Spectrometers*. American Society for Testing and Materials.

ASTM E647-13. 2013. "Standard Test Method for Measurement of Fatigue Crack Growth Rates." *American Society for Testing and Materials (ASTM)*.

ASTM E647, ASTM Standard. 2016. "ASTM E647 - Standard Test Method for Measurement of Fatigue Crack Growth Rates." *ASTM Book of Standards*.

ASTM E8. 2010. *E8/E8M Standard Test Methods for Tension Testing of Metallic Materials*.

AWS-D17.3/D17.3M:200X. 2010. "Specification for Friction Stir Welding of Aluminum Alloys for Aerospace Applications." *American Welding Society*.

AWS D1.2/D1.2M. 2014. *AWS D1.2/D1.2M:2014 Structural Welding Code--Aluminum*.

Aydin, Hakan, Ali Bayram, M. Tahir Yildirim, and Kurtuluş Yiğit. 2010. "Influence of Welding Parameters on the Fatigue Behaviours of Friction Stir Welds of 3003-O Aluminum Alloys." *Medziagotyra*.

Barsom, J. M., & Novak, S. R. 1977. *Subcritical Crack Growth and Fracture of Bridge Steels*.

Brückner, A. and D. Munz. 1983. "Curve Fitting to Defect Size Distributions for the Calculation of Failure Probabilities." *Nuclear Engineering and Design*.

BS-7910. 2005. "Guide to Methods for Assessing the Acceptability of Flaws in Metallic Structures." *BSI Standards Publication*.

CAN/CSA W59.2. 2018. *Welded Aluminum Construction*. Canadian Standards Association.

Canadian Standards Association. 2014. *Canadian Highway Bridge Design Code*.

Cavaliere, P., G. Campanile, F. Panella, and A. Squillace. 2006. "Effect of Welding Parameters on Mechanical and Microstructural Properties of AA6056 Joints Produced by Friction Stir Welding." *Journal of Materials Processing Technology*.

Cavaliere, P., A. De Santis, F. Panella, and A. Squillace. 2009. "Effect of Welding Parameters on Mechanical and Microstructural Properties of Dissimilar AA6082-AA2024 Joints Produced by Friction Stir Welding." *Materials and Design*.

Cavaliere, P., A. Squillace, and F. Panella. 2008. "Effect of Welding Parameters on Mechanical and Microstructural Properties of AA6082 Joints Produced by Friction Stir Welding." *Journal of Materials Processing Technology*.

Conle, A., Oxland, T.R., and Topper, T. H. 1988. "Computer-Based Prediction of Cyclic Deformation and Fatigue Behavior." *American Society for Testing and Materials (ASTM)* Low Cycle(ASTM STO 942):1218–36.

Coughlin, R. and S. Walbridge. 2012. "Fatigue Testing and Analysis of Aluminum Welds under In-Service Highway Bridge Loading Conditions." *Journal of Bridge Engineering*.

Dalle Donne, C., G. Biallas, T. Ghidini, and G. Raimbeaux. 2000. "Effect of Weld Imperfections and Residual Stresses on the Fatigue Crack Propagation in Friction Stir Welded Joints." *2nd International Conference on Friction Stir Welding*.

Das, Hrishikesh, Debayan Chakraborty, and Tapan Kumar Pal. 2014. "High-Cycle Fatigue Behavior of Friction Stir Butt Welded 6061 Aluminium Alloy." *Transactions of Nonferrous*

Metals Society of China (English Edition).

Development, Draft F. O. R. 2000. "Eurocode 9 : Design of Aluminium Structures Ð Part 2 : Structures Susceptible to Fatigue." *Update*.

Dialami, N., M. Chiumenti, M. Cervera, and C. Agelet de Saracibar. 2017. "Challenges in Thermo-Mechanical Analysis of Friction Stir Welding Processes." *Archives of Computational Methods in Engineering*.

Dickerson, T. L. and J. Przydatek. 2003. "Fatigue of Friction Stir Welds in Aluminium Alloys That Contain Root Flaws." *International Journal of Fatigue*.

Dugdale, D. S. 1960. "Yielding of Steel Sheets Containing Slits." *Journal of the Mechanics and Physics of Solids*.

El-Zeghayar, Maria. 2010. "The Introduction of Crack Opening Stress Modeling into Strain-Life And Small Crack Growth Fatigue Analysis." University of Waterloo, Ontario, Canada.

Elber, W. 2009. "The Significance of Fatigue Crack Closure." in *Damage Tolerance in Aircraft Structures*.

Ericsson, Mats, Lai Z. Jin, and Rolf Sandström. 2007. "Fatigue Properties of Friction Stir Overlap Welds." *International Journal of Fatigue*.

Fowler, Steven, Athanasios Toumpis, and Alexander Galloway. 2016. "Fatigue and Bending Behaviour of Friction Stir Welded DH36 Steel." *International Journal of Advanced Manufacturing Technology*.

G. Josi. 2010. "Reliability-Based Management of Fatigue Failures." University of Alberta.

Gerster, P., F. Schäfers, and M. Leitner. 2013. "Pneumatic Impact Treatment (PIT) - Application and Quality Assurance." *International Institute of Welding*.

Ghahremani, Kasra. 2010. "Predicting the Effectiveness of Post-Weld Treatments Applied under Load." University of Waterloo.

Ghahremani, Kasra. 2015. "Fatigue Assessment of Repaired Highway Bridge Welds Using Local Approaches." University of Waterloo.

Ghahremani, Kasra, Mahdi Safa, Jamie Yeung, Scott Walbridge, Carl Haas, and Sebastien Dubois. 2015. “Quality Assurance for High-Frequency Mechanical Impact (HFMI) Treatment of Welds Using Handheld 3D Laser Scanning Technology.” *Welding in the World*.

Ghahremani, Kasra and Scott Walbridge. 2011. “Fatigue Testing and Analysis of Peened Highway Bridge Welds under In-Service Variable Amplitude Loading Conditions.” *International Journal of Fatigue*.

Ghahremani, Kasra, Scott Walbridge, and Tim Topper. 2015. “High Cycle Fatigue Behaviour of Impact Treated Welds under Variable Amplitude Loading Conditions.” *International Journal of Fatigue*.

Glinka, G. and G. Shen. 1991. “Universal Features of Weight Functions for Cracks in Mode I.” *Engineering Fracture Mechanics*.

Grujicic, M., G. Arakere, B. Panduragan, A. Hariharan, C. F. Yen, B. A. Cheeseman, and C. Fountzoulas. 2011. “Statistical Analysis of High-Cycle Fatigue Behavior of Friction Stir Welded AA5083-H321.” *Journal of Materials Engineering and Performance*.

Guo, S., L. Shah, R. Ranjan, S. Walbridge, and A. Gerlich. 2019. “Effect of Quality Control Parameter Variations on the Fatigue Performance of Aluminum Friction Stir Welded Joints.” *International Journal of Fatigue* 118.

Guo, Shi. 2018. “Fatigue Behaviour of Aluminum Friction Stir Welds Under Highway Bridge Loading Conditions.” University of Waterloo.

Haagensen, P. J. and S. J. Maddox. 2013. *IIW Recommendations on Methods for Improving the Fatigue Strength of Welded Joints*.

El Haddad, M. H., T. H. Topper, and K. N. Smith. 1979. “Prediction of Non Propagating Cracks.” *Engineering Fracture Mechanics*.

El Haddad, M. H., T. H. Topper, and T. N. Topper. 1981. “Fatigue Life Predictions of Smooth and Notched Specimens Based on Fracture Mechanics.” *Journal of Engineering Materials and Technology*.

HAGISAWA, Nobuyasu and Ichiro OKURA. 2009. “Influence of Stress Ratios on Fatigue Strength of A6005C-T5 Aluminum Alloy and Friction Stir Welded Joints.” *Doboku Gakkai Ronbunshuu A*.

He, Xiaocong, Fengshou Gu, and Andrew Ball. 2014. “A Review of Numerical Analysis of Friction Stir Welding.” *Progress in Materials Science*.

Hobbacher, A. 2011. *Fatigue Design of Welded Joints and Components*.

Hobbacher, A. F. 2009. “The New IIW Recommendations for Fatigue Assessment of Welded Joints and Components - A Comprehensive Code Recently Updated.” *International Journal of Fatigue*.

ISO 25239. 2011. *Friction Stir Welding- Aluminum*.

JCSS. 2011. *JCSS Probabilistic Model Code Part 3: Resistance Models*.

Kadlec, Martin, Roman Růžek, and Lucie Nováková. 2015. “Mechanical Behaviour of AA 7475 Friction Stir Welds with the Kissing Bond Defect.” *International Journal of Fatigue*.

Kainuma, Shigenobu, Hiroto Katsuki, Ichiro Iwai, and Masaki Kumagai. 2008. “Evaluation of Fatigue Strength of Friction Stir Butt-Welded Aluminum Alloy Joints Inclined to Applied Cyclic Stress.” *International Journal of Fatigue*.

Khalil, M. and T. H. Topper. 2003. “Prediction of Crack-Opening Stress Levels for 1045 as-Received Steel under Service Loading Spectra.” *International Journal of Fatigue*.

Kobayashi, Y., M. Sakuma, Y. Tanaka, and K. Matsuoka. 2007. “Fatigue Strength of Friction Stir Welding Joints of Aluminium Alloy 6082 Extruded Shape.” *Welding International*.

Kuhlmann, U., A. Dürr, and H. Günther. 2017. “Application of Post-Weld Treatment Methods to Improve the Fatigue Strength of High Strength Steels in Bridges.”

Kuhlmann, Ulrike, Joachim Bergmann, André Dürr, Rayk Thumser, Hans Peter Günther, and Uwe Gerth. 2005. “Erhöhung Der Ermüdungsfestigkeit von Geschweißten Höherfesten Baustählen Durch Anwendung von Nachbehandlungsverfahren.” *Stahlbau*.

Lam, T. S., T. H. Topper, and F. A. Conle. 1998. “Derivation of Crack Closure and Crack

Growth Rate Data from Effective-Strain Fatigue Life Data for Fracture Mechanics Fatigue Life Predictions." *International Journal of Fatigue*.

Leitner, M., W. Mössler, A. Putz, and M. Stoschka. 2015. "Effect of Post-Weld Heat Treatment on the Fatigue Strength of HFMI-Treated Mild Steel Joints." *Welding in the World*.

Lohwasser, D. and Z. Chen. 2009. *Friction Stir Welding: From Basics to Applications*.

Lomolino, S., R. Tovo, and J. Dos Santos. 2005. "On the Fatigue Behaviour and Design Curves of Friction Stir Butt-Welded Al Alloys." *International Journal of Fatigue*.

Lotsberg, Inge, Gudfinnur Sigurdsson, and Per Terje Wold. 2002. "Probabilistic Inspection Planning of the Åsgard A FPSO Hull Structure With Respect to Fatigue." *Journal of Offshore Mechanics and Arctic Engineering*.

Maddox, S. J. 1975. "An Analysis of Fatigue Cracks in Fillet Welded Joints." *International Journal of Fracture*.

Mahdavi Shahri, Meysam, Torsten Höglund, and Rolf Sandström. 2012. "Eurocode 9 to Estimate the Fatigue Life of Friction Stir Welded Aluminium Panels." *Engineering Structures*.

Marquis, Gary B. and Zuheir Barsoum. 2016. "IIW Recommendations on High Frequency Mechanical Impact (HFMI) Treatment for Improving the Fatigue Strength of Welded Joints."

Marquis, Gary B., Eeva Mikkola, Halid Can Yildirim, and Zuheir Barsoum. 2013. "Fatigue Strength Improvement of Steel Structures by High-Frequency Mechanical Impact: Proposed Fatigue Assessment Guidelines." *Welding in the World*.

McClung, R. C. 1994. "Finite Element Analysis of Specimen Geometry Effects on Fatigue Crack Closure." *Fatigue & Fracture of Engineering Materials & Structures*.

Miranda, Antonio Carlos de Oliveira, Adrian Gerlich, and Scott Walbridge. 2015. "Aluminum Friction Stir Welds: Review of Fatigue Parameter Data and Probabilistic Fracture Mechanics Analysis." *Engineering Fracture Mechanics*.

Moreira, P. M. G. P., M. A. V de Figueiredo, and P. M. S. T. de Castro. 2007. "Fatigue

Behaviour of FSW and MIG Weldments for Two Aluminium Alloys." *Theoretical and Applied Fracture Mechanics*.

Newman, J. C. 1984. "A Crack Opening Stress Equation for Fatigue Crack Growth." *International Journal of Fracture*.

Newman, JC. 2009. "A Finite-Element Analysis of Fatigue Crack Closure." in *Mechanics of Crack Growth*.

Okura, Ichiro, Nobuyasu Hagisawa, Makoto Naruo, and Hitoshi Toda. 2005. "Fatigue Behaviour of Aluminum Deck Fabricated by Friction Stir Welding." *Structural Engineering / Earthquake Engineering*.

Parry, M., Nordberg, H., & Hertzberg, R. W. 1972. "Fatigue Crack Propagation in A514 Base Plate and Welded Joints." *Welding Journal Research Supplement, 51(10)* 485s-490s.

Pedersen, M. M., O. Mouritsen, M. R. Hansen, J. G. Andersen, and J. Wenderby. 2010. "Comparison of Post-Weld Treatment of High-Strength Steel Welded Joints in Medium Cycle Fatigue." *Welding in the World*.

Raimbault, Jeremie. 2016. "Modelling Fatigue Deterioration and Retrofitting in Bridge Management Systems." University of Waterloo, Ontario, Canada.

Ranjan, R., K. Ghahremani, S. Walbridge, and A. Ince. 2016. "Testing and Fracture Mechanics Analysis of Strength Effects on the Fatigue Behavior of HFMI-Treated Welds." *Welding in the World*.

Righiniotis, T. D. and M. K. Chryssanthopoulos. 2003. "Probabilistic Fatigue Analysis under Constant Amplitude Loading." *Journal of Constructional Steel Research*.

Roy, Sougata, John W. Fisher, and Ben T. Yen. 2003. "Fatigue Resistance of Welded Details Enhanced by Ultrasonic Impact Treatment (UIT)." in *International Journal of Fatigue*.

Shetty, N.K.;Baker, M. J. 1990. "Fatigue Reliability of Tubular Joints in Offshore Structures-Reliability Analysis." *Proceedings of the 9th International Conference on Offshore Mechanics and Arctic Engineering-OMAE* 2:33–40.

SINTEC, Structural Integrity Technologies Inc. 2019. “HFMI.” Retrieved September 20, 2005 (http://www.sintec.ca/).

Smallbone, C. 2008. “Improving the Global Quality of Life through Optimum Use of Welding Technology.” *Welding in the World*.

Sonsino, CM. 2008. “Principles of Variable Amplitude Fatigue Design and Testing.” in *Fatigue Testing and Analysis Under Variable Amplitude Loading Conditions*.

Suzuki, Tamaki, Teppei Okawa, Hiroshi Shimanuki, Tetsuro Nose, Noriaki Ohta, Hiroshi Suzuki, and Atsushi Moriai. 2014. “Effect of Ultrasonic Impact Treatment (UIT) on Fatigue Strength of Welded Joints.” *Advanced Materials Research*.

Svensson, L.-E., Karlsson, L., Larsson, H., Fazzini, M., & Karlsson, J. 2000. “Microstructure and Mechanical Properties of Friction Stir Welded Aluminum Alloys with Special Reference to AA5083 and AA6082.” *Science and Technology of Welding and Joining* 285–96.

Tehrani Yekta, Rana, Kasra Ghahremani, and Scott Walbridge. 2013. “Effect of Quality Control Parameter Variations on the Fatigue Performance of Ultrasonic Impact Treated Welds.” *International Journal of Fatigue*.

The Aluminum Association. 2015. “Aluminum Design Manual Part I: Spedification for Aluminum Structures.”

Thomas, W. M. 1991. “Friction Stir Butt Welding.”

Tobler, R. L. and R. P. Reed. 2010. “Fracture Mechanics Parameters for a 5083-0 Aluminum Alloy at Low Temperatures.” *Journal of Engineering Materials and Technology*.

U. Kuhlmann, J. Bergmann, A. Dürr, R. Thumser, H.-P. Günther, U. Gerth. 2005. “Enhancement of the Fatigue Strength of Welded High Strength Steels by Application of Post-Weld Treatment Methods.” *Stahlbau, 74* 358–65.

Uzun, Huseyin, Claudio Dalle Donne, Alberto Argagnotto, Tommaso Ghidini, and Carla Gambaro. 2005. “Friction Stir Welding of Dissimilar Al 6013-T4 To X5CrNi18-10

Stainless Steel." *Materials and Design*.

V.-M. Lihavainen. 2006. "A Novel Approach for Assessing the Fatigue Strength of Ultrasonic Impact Treated Welded Structures." Lappeenranta University of Technology.

Vidal, Catarina, Virgínia Infante, and Pedro Vilaça. 2014. "Fatigue Behaviour at Elevated Temperature of Friction Stir Channelling Solid Plates of AA5083-H111 Aluminium Alloy." *International Journal of Fatigue*.

Vigh, László Gergely and Ichiro Okura. 2013. "Fatigue Behaviour of Friction Stir Welded Aluminium Bridge Deck Segment." *Materials and Design*.

Vormwald, M. and T. Seeger. 1991. "The Consequences of Short Crack Closure on Fatigue Crack Growth Under Variable Amplitude Lading." *Fatigue & Fracture of Engineering Materials & Structures*.

Walbridge, Scott. 2008. "Fatigue Analysis of Post-Weld Fatigue Improvement Treatments Using a Strain-Based Fracture Mechanics Model." *Engineering Fracture Mechanics*.

Walbridge, Scott, Dilum Fernando, and Bryan T. Adey. 2012. "Probabilistic Models to Evaluate Effectiveness of Steel Bridge Weld Fatigue Retrofitting by Peening." *Transportation Research Record: Journal of the Transportation Research Board*.

Wang, C. H., L. R. F. Rose, and J. C. Newman. 2002. "Closure of Plane-Strain Cracks under Large-Scale Yielding Conditions." *Fatigue and Fracture of Engineering Materials and Structures*.

Weich, Imke, Thomas Ummenhofer, Thomas Nitschke-Pagel, Hamdollah Eslami Chalandar, and Klaus Dilger. 2009. "Fatigue Behaviour of Welded High-Strength Steels after High Frequency Mechanical Post-Weld Treatments." *Welding in the World*.

Yildirim, Halid Can and Gary B. Marquis. 2013. "A Round Robin Study of High-Frequency Mechanical Impact (HFMI)-Treated Welded Joints Subjected to Variable Amplitude Loading." *Welding in the World*.

Yıldırım, H. C., G. Marquis, and C. M. Sonsino. 2016. "Lightweight Design with Welded High-

Frequency Mechanical Impact (HFMI) Treated High-Strength Steel Joints from S700 under Constant and Variable Amplitude Loadings." *International Journal of Fatigue*.

Yuan, K. L. and Y. Sumi. 2015. "Modelling of Ultrasonic Impact Treatment (UIT) of Welded Joints and Its Effect on Fatigue Strength." *Frattura Ed Integrita Strutturale*.

Zheng, X. J., G. Glinka, and R. N. Dubey. 1996. "Stress Intensity Factors and Weight Functions for a Corner Crack in a Finite Thickness Plate." *Engineering Fracture Mechanics*.

Zhou, Caizhi, Xinqi Yang, and Guohong Luan. 2005. "Fatigue Properties of Friction Stir Welds in Al 5083 Alloy." *Scripta Materialia*.

Zhou, Caizhi, Xinqi Yang, and Guohong Luan. 2006a. "Effect of Kissing Bond on Fatigue Behavior of Friction Stir Welds on Al 5083 Alloy." *Journal of Materials Science*.

Zhou, Caizhi, Xinqi Yang, and Guohong Luan. 2006b. "Investigation of Microstructures and Fatigue Properties of Friction Stir Welded Al-Mg Alloy." *Materials Chemistry and Physics*.

Appendix A: **FSW Misalignment Study- Bending Stress Calculation**

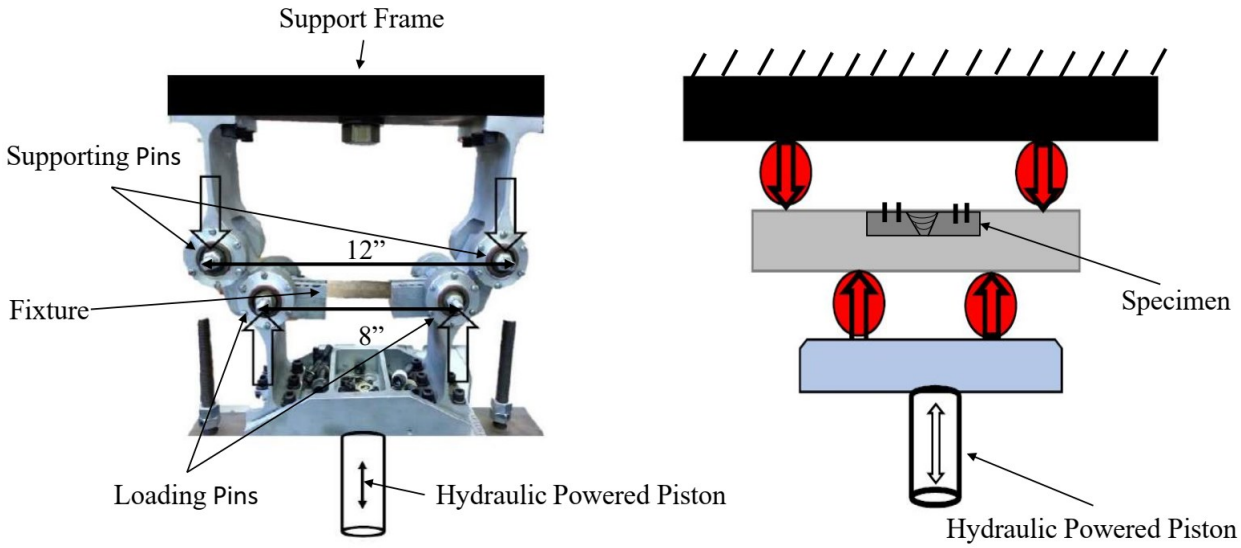

Figure 1: Actual four-point bending test frame (left) and simplified sketch of the frame (right)

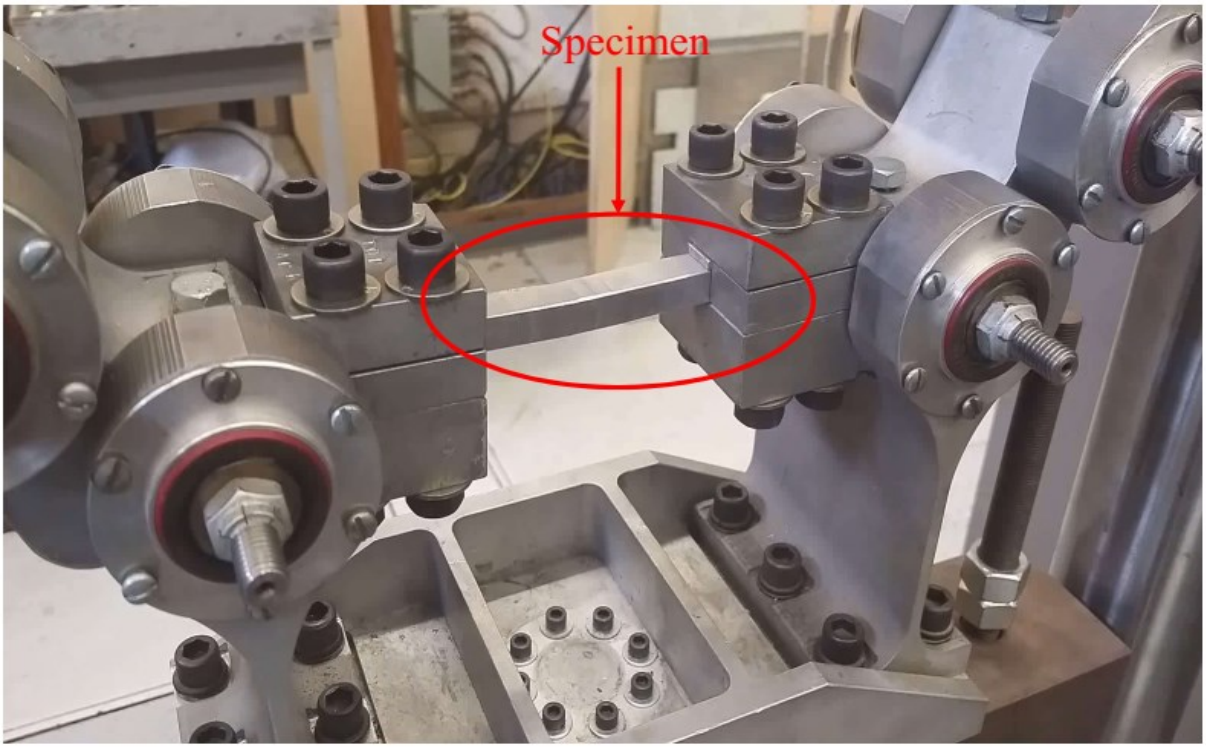

Figure 2: Close view of the four-point bending test fixture

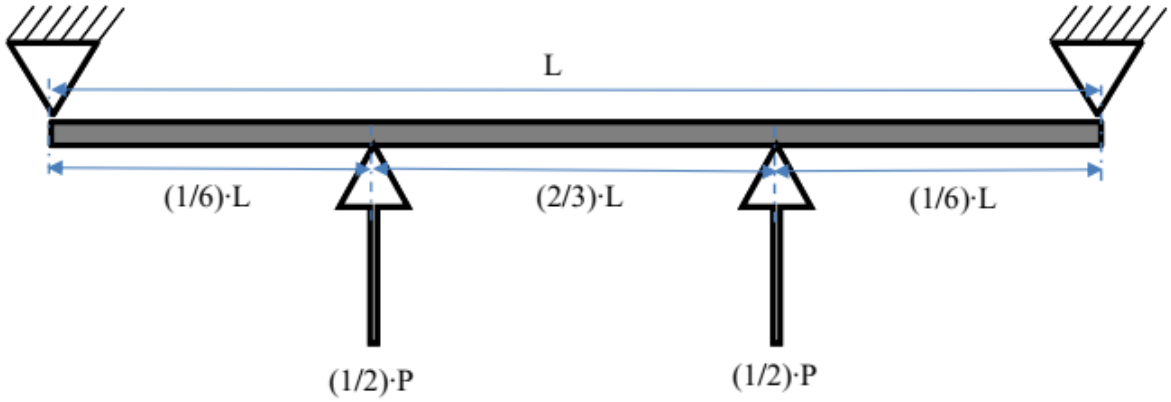

Figure 3: Simplified line diagram for the four-point bending test apparatus

There are four pins in four-point bending test frame as shown in Figure 1(left). The pins at the extreme end are called supporting pins and middle two pins are called loading pins. The spacing between the two supporting pins is 304.8 mm (12”) and the distance between two loading pins is 203.2 mm (8”).

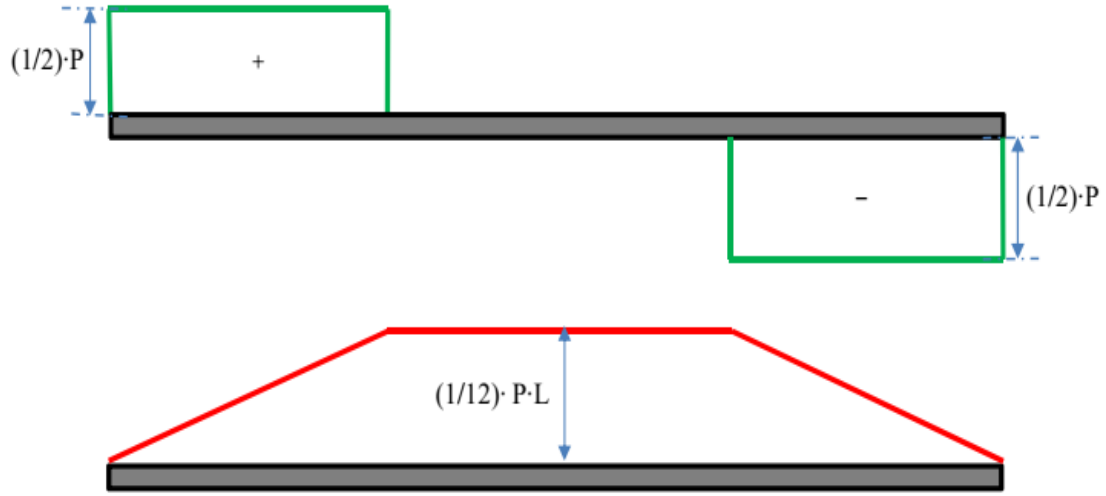

Figure 4: Shear force diagram (top) and bending moment diagram (bottom)

The moment (M) because of the applied load (P) through the piston is related according to the following equation:

$$M = \frac{P}{2} \times \frac{L}{6} = \frac{PL}{12}$$

Maximum stress at the top fiber of the specimen can be calculated from the following equation:

$$\sigma = \frac{M}{I} y = \frac{\left(\frac{1}{12} PL\right)}{\left(\frac{wt^3}{12}\right)} \times \left(\frac{t}{2}\right) = \frac{PL}{2wt^2}$$

For the four-point bending test frame at Waterloo, L = 304.8 mm

For FSW specimens tested under bending load, w = 12.57 mm, t = 9.5 mm

$$\sigma(MPa) = \frac{P \times 304.8 \times 1000}{2 \times 12.57 \times 9.5^2} = 134.34 \times P(kN)$$

Appendix B: **FSW Misalignment Study - Fatigue Test Results**

Test Configuration	Control type	Frequency (Hz)	Width (mm)	Thickness (mm)	Δ*S* (MPa)	Fatigue Life
Bending - Top	Stroke	30	12.60	9.85	119.03	3142463
Bending - Top	Stroke	30	12.56	10.40	125.91	3164372
Bending - Top	Stroke	30	12.56	10.08	118.66	592627
Bending - Top	Load	3	12.73	9.98	170.94	334263
Bending - Top	Load	3	12.58	9.88	219.53	60400
Bending - Top	Load	40	27.00	10.00	120.00	13000000
Bending - Top	Load	40	27.00	10.00	130.00	1184480
Bending - Top	Load	40	27.00	10.00	140.00	1170050
Bending - Top	Load	40	27.00	10.00	150.00	364559
Bending - Top	Load	40	27.00	10.00	160.00	371610
Bending - Top	Load	40	27.00	10.00	180.00	264508
Bending - Top	Load	40	27.00	10.00	220.00	78159
Bending - Top	Load	40	27.00	10.00	200.00	167390
Bending - Top	Load	40	27.00	10.00	240.00	69831
Bending - Bottom	Stroke	30	12.62	9.82	109.49	3851613
Bending - Bottom	Stroke	30	12.45	10.18	130.12	207383
Bending - Bottom	Stroke	30	12.61	9.74	126.46	3257716
Bending - Bottom	Load	3	12.63	9.86	178.19	132386
Bending - Bottom	Load	3	12.56	9.85	213.78	8616
Bending - Bottom	Load	3	27.00	10.00	200.00	55000
Bending - Bottom	Load	3	27.00	10.00	164.00	657000
Bending - Bottom	Load	3	27.00	10.00	230.00	16076
Bending - Bottom	Load	3	27.00	10.00	250.00	50000
Bending - Bottom	Load	3	27.00	10.00	180.00	48294
Bending - Bottom	Load	3	27.00	10.00	170.00	110603
Bending - Bottom	Load	3	27.00	10.00	140.00	308299
Bending - Bottom	Load	3	27.00	10.00	130.00	583107
Bending - Bottom	Load	3	27.00	10.00	120.00	355532
Bending - Bottom	Load	40	27.00	10.00	200.00	54000
Bending - Bottom	Load	40	27.00	10.00	160.00	44230
Tension	Load	40	27.00	10.00	96.3	10000000
Tension	Load	40	27.00	10.00	112.3	10000000
Tension	Load	40	27.00	10.00	168.3	29200
Tension	Load	40	27.00	10.00	188.3	20000
Tension	Load	40	27.00	10.00	135.3	170000
Tension	Load	40	27.00	10.00	155.3	75000
Tension	Load	40	27.00	10.00	94.3	19000000

Appendix C: **FSW Defect Study - Fatigue Test Results (Guo et al. 2019)**

Test ID	Loading	S_{max} (MPa)	ΔS_{eq} (MPa)	N (cycles)	Failure	Defect[1]	Defect[2]
6061 Butt Joints, Properly Welded							
A6PW01B	CA	158.4	142	61079	BM		
A6PW01C	CA	118.1	106.3	828642	AS		
A6PW01D	CA	109.2	98.3	741302	BM		
A6PW02A	CA	88.9	80	3255068	Run-out		
A6PW02B	CA	103.9	93.5	6017249	Run-out		
A6PW02C	CA	133	119.7	420979	AS/BM		
A6PW02D	CA	148.7	133.8	276560	WR/BM		
A6PW03A	CA	160.9	144.9	33235	WR	332 μm (JLR)	
A6PW03C	CA	178	160	48356	AS and WR	344 μm (JLR)	
A6PW04A	VA	166.3	65.0	492437	WR		
A6PW04B	VA	102.3	40.0	4112113	WR		
A6PW04C	VA	144.4	56.5	858770	WR		
A6PW05A	VA	127.9	50.0	7724571	AS		
A6PW05C	VA	166.3	65.0	5383609	RS		
6061 Butt Joints, Polished							
A6PO01A	CA	150.7	135.6	168458	BM		
A6PO01B	CA	135.6	122.0	835120	RS		
A6PO01C	CA	120.5	108.5	402093	BM		
A6PO01D	CA	105.5	94.9	544477	BM		
A6PO02A	CA	165.7	149.2	132631	BM/RS		
A6PO02B	CA	90.4	81.4	5020279	Run-out		
A6PO02D	VA	153.5	60	12132612	BM		
A6PO03A	VA	166.3	65	1111127	WR		
A6PO03B	VA	179	70	2935508	AS		
A6PO03C	VA	127.9	50	4063234	AS		
A6PO03D	VA	127.9	50	15077492	BM		
6061 Butt Joints, Kissing Bond Defect							
A6KB01A	CA	120.0	106.7	13506	WR	1.10±0.06 mm	1.05± 0.03 mm
A6KB01B	CA	90.0	80	57581	WR	1.11±0.08 mm	1.00±0.03 mm
A6KB01C	CA	60.0	53.4	5322591	Run-out	1.20±0.03 mm	
A6KB01D	CA	75.0	66.7	135466	WR		0.97±0.04 mm

A6KB02A	VA	127.9	50.0	342040	WR	1.00±0.02 mm	0.90±0.03 mm
A6KB02B	VA	76.8	30.0	10176309	Run-out	1.03±0.01 mm	
A6KB02C	VA	102.3	40.0	1692092	WR	1.01±0.03 mm	0.87±0.02 mm
A6KB02D	VA	89.5	35.0	4613013	WR		0.85±0.06 mm
A6KB03A	VA	153.5	60.0	213159	WR	1.02±0.04 mm	0.93±0.02 mm
A6KB03B	VA	127.9	50.0	458736	WR	1.02±0.04 mm	0.89±0.03 mm
A6KB03C	VA	102.3	40.0	2017588	WR	1.00±0.03 mm	0.85±0.02 mm
A6KB03D	VA	89.5	35.0	1791686	WR		0.8±0.03 mm
6061 Lap Joints							
Test ID	**Loading**	**S_{max} (MPa)**	**ΔS_{eq} (MPa)**	***N* (cycles)**	**Failure**	**Defect[1]**	**Defect[2]**
A6LJ01A	CA	120.0	108	13693	WR	453 µm	
A6LJ01B	CA	90.0	81.0	64970	WR	599 µm	
A6LJ01C	CA	75.0	67.5	126227	WR	449 µm	
A6LJ01D	CA	60.0	54.0	219378	WR		
A6LJ02A	CA	45.0	40.5	563711	WR	455 µm	
A6LJ02B	CA	30.0	27.0	5338486	WR	292 µm	
A6LJ02C	VA	76.8	30.0	2144792	WR	313 µm	
A6LJ02D	VA	51.2	20.0	9419241	WR		
A6LJ03A	VA	89.5	35.0	923005	WR	262 µm	
A6LJ03B	VA	89.5	35.0	1395342	WR	384 µm	
A6LJ03D	VA	115.1	45.0	494469	WR	376 µm	
6061 Butt Joints, Toe Flash Defect							
A6TF01A	CA	150.0	146.7	55846	AS		
A6TF01B	CA	120.0	117.8	114016	AS		
A6TF01C	CA	90.0	88.3	520841	AS		
A6TF01D	CA	105.0	103.1	418103	AS		
A6TF02B	CA	75.0	68.6	467218	WR	700 µm	0.62±0.04 mm
A6TF02C	VA	166.3	65.0	290734	WR	629 µm	0.63±0.03 mm
A6TF02D	VA	153.5	60.0	349585	WR		
A6TF03A	CA	78.8	70.9	1009218	WR	356 µm (JLR)	

A6TF03B	CA	63.5	57.2	5497205	Run-out	324 μm (JLR)	
A6TF03C	VA	102.3	40.0	10001506	Run-out		
A6TF03D	VA	115.1	45.0	11082046	Run-out		
5083 Butt Joints, Properly Welded							
A5PW02A	CA	125.6	113.0	92467	AS and WR		
A5PW02B	CA	109.9	98.9	5606722	Run-out		
A5PW02C	CA	141.3	127.2	2992566	Run-out		
A5PW02D	CA	172.7	155.4	94494	WR		
A5PW03A	CA	157.0	141.3	404680	WR	33 μm (JLR)	
A5PW03B	CA	164.8	148.4	238098	WR	160 μm (JLR)	
A5PW03C	CA	149.1	134.2	390320	WR	365 μm (JLR)	
A5PW03D	CA	149.1	134.2	99589	WR		
5083 Butt Joints, Wormhole Defect							
A5WH01A	CA	125.6	113.0	139337	WH		0-2.46 mm
A5WH01B	CA	109.9	98.9	408156	WR		
A5WH01C	CA	94.2	84.8	338064	WH		0-2.76 mm
A5WH01D	CA	78.5	70.6	2951	WH		3.18±0.16 mm

Notes: ΔS_{eq} shown in this table for VA tests is the nominal stress range value calculated using Palmgren-Miner sum with $m = 4.84$.

N = number of cycles required to fracture specimen into two pieces.

BM = base metal, AS = advancing side, RS = retreating side, WR = weld root

1 = cross section measurement, 2 = fracture surface measurement, JLR = joint line remnant

Appendix D: **HFMI Treatment Study - Fatigue Test Results**

As-welded, 350W Steel (Ghahremani et al. 2015)							
Test ID	***N* (10^3 cycles)**	**ΔS^a_{eq} (MPa)**	**S_{max} (MPa)**	**S_{min} (MPa)**	**ΔS_{max} (MPa)**	**ΔS_{min} (MPa)**	**ΔS^b_{min} (MPa)**
XAC-1	1,995	108	120	12			
XAC-2	920	144	160	16			
XAV-1	3,843	81.91	180	9	171	3	11
XAV-2	1,131	103.94	229	12	217	3	14
XAV-3	713	114.48	252	13	239	4	15
XAV-4	397	175.79	387	20	367	6	23
XAW-1	8,203	57.82	167	7	162	3	3
XAW-2	1,921	78.42	226	9	220	3	3
XAW-3	1,041	110.59	319	13	310	5	5
XAW-4	627	134.08	387	16	376	6	6
Treated, 350W Steel (Ghahremani, Walbridge, et al. 2015)							
Test ID	***N* (10^3 cycles)**	**ΔS^c_{eq} (MPa)**	**S_{max} (MPa)**	**S_{min} (MPa)**	**ΔS_{max} (MPa)**	**ΔS_{min} (MPa)**	**ΔS^b_{min} (MPa)**
XTC-1	101,080	106	118	12			
XTC-2	25,995	127	141	14			
XTC-3	3,165	155	177	22			
XTC-4	1,255	159	177	18			
XTC-5	2,365	165	177	11			
XTC-6	1,720	170	177	7			
XTC-7	6,450	180	200	20			
XTC-8	4,650	191	212	21			
XTV-1	192,686	72.705	138	7	131	2	8
XTV-2	100,685	78.26	148	7	141	2	9
XTV-3	101,545	83.80	159	8	151	2	10
XTV-4	103,020	89.36	170	9	161	3	10
XTV-5	22,327	94.91	180	9	171	3	11
XTV-6	45,826	120.44	229	12	217	3	14
XTV-7	16,852	132.65	252	13	239	4	15
XTV-8	14,283	168.72	320	16	304	5	19
XTV-9	625	203.69	387	20	367	6	23
XTW-1	21,103	93.25	207	8	201	3	3
XTW-2	52,989	101.68	226	9	220	3	3

Test ID	N (10^3 cycles)	ΔS^c_{eq} (MPa)	S_{max} (MPa)	S_{min} (MPa)	ΔS_{max} (MPa)	ΔS_{min} (MPa)	ΔS^b_{min} (MPa)
XTW-3	64,693	117.62	262	11	254	4	4
XTW-4	13,599	132.61	295	12	286	4	4
XTW-5	27,646	143.39	319	13	310	5	5
XTW-6	6,592	153.23	341	14	331	5	5
XTW-7	1,818	173.85	387	16	376	6	6
Note 1: the naming convention, X represent cruciform type joints, (A, T) represents toe condition (A= as welded, T = treated), (C, V, W) represents loading condition (C = CA, V = VA1, W =VA2), Digits represents specimen number							
Note 2: underline = runout (testing was discontinued after roughly 100 million cycles)							
[a] CA equivalent stress range with m' = 3							
[b] The minimum stress range present in the loading spectrum with at least 1% occurrence in the loading block.							
[b] The minimum stress range present in the loading spectrum with at least 1% occurrence in the loading block.							
[c] The equivalent stress range ΔS_{eq} for the treated specimen was calculated assuming $m' = 5$							

As-welded and HFMI treated 5083 Aluminum Specimens (Ranjan et al. 2016)						
Loading			As-Welded		HFMI Treated	
ΔS_{eq} (MPa)	ΔS_{max} (MPa)	Type	Cycles	Notes	Cycles	Notes
76	76	CA	745,000		3,250,000	
80	80	CA	375,000		1,635,000	
85	85	CA	415,000		2,175,000	
92	92	CA	245,000		360,000	
105	105	CA	75,000		175,000	
141	141	CA	17,500		37,500	
43	70	CA-UL	1,180,000			
46	76	CA-UL	860,000		9,860,000	runout
53	88	CA-UL	470,000		4,735,000	
59	97	CA-UL	245,000		3,105,000	
61	101	CA-UL	335,000		330,000	
64	105	CA-UL			505,000	
68	113	CA-UL	155,000		265,000	

As-welded and HFMI treated A514 Steel Specimens (Ranjan et al. 2016)						
Loading			As-Welded		HFMI Treated	
ΔS_{eq} (MPa)	ΔS_{max} (MPa)	Type	Cycles	Notes	Cycles	Notes
240	240	CA	170,000		4,530,000	runout
295	295	CA	95,000		3,160,000	
316	316	CA	80,000		*865,000**	*runout*
332	332	CA	140,000		910,000	
346	346	CA	75,000		1,750,000	
358	358	CA	47,000		265,000	
147	246	CA-UL	770,000		6,000,000	runout
158	265	CA-UL	680,000		6,000,000	runout
170	284	CA-UL	555,000		4,050,000	
181	303	CA-UL	305,000		2,595,000	
192	322	CA-UL	335,000		3,990,000	
198	332	CA-UL	315,000		1,170,000	

**Failed prematurely in the base metal away from the weld.*